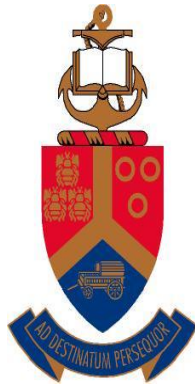


**Gas sensing properties of nanostructured vanadium oxide
semiconductors by chemoresistive and optical methods**

by

Akande Amos Adeleke

(MSc)



Submitted in partial fulfilment of the requirements for the degree

DOCTOR OF PHILOSOPHY (PhD) IN PHYSICS

In the Faculty of Natural and Agricultural Science

University of Pretoria

October 2017

Supervisor: Dr. A. G. J. Machatine

Co- supervisor: Dr. B. W. Mwakikunga

Co- supervisor: Dr. K. T. Roro

Declaration

I hereby declare that this thesis entitled “*Gas sensing properties of nanostructured vanadium oxide semiconductors by chemoresistive and optical methods*” is the result of my PhD research and that it has not been submitted elsewhere for the award of any degree or diploma at the University of Pretoria or any other institutions.

Signature:

Date:.....

Acknowledgements

I specially thank the Almighty God (the greatest teacher) for His unconditional love, mercy and grace (1 Corinthians 13, Luke 15: 11-22 and Ephesians 2: 8-9) and for seeing me through this journey.

I would like to express my heartfelt gratitude to Dr. B.W. Mwakikunga, I am fortunate to have known him and have him as one of my supervisors. Apart from given me the opportunity to work with him and his group, he has been a complete teacher, he has taught me to believe in myself and to be an independent researcher.

I am also grateful to Dr. A. G. J. Machatine and Dr. K. Roro for their invaluable scientific and career advice, experienced input, immense contribution and supervision throughout the period of this research. I really appreciate you.

I would like to specially thank the Council for Scientific and Industrial Research (CSIR) and National Centre for Nano-Structured Materials (NCNSM) for funding and hosting the research. It would not have been a success without your world class state of the art Nanotechnology facility. I am delighted to NCNSM manager Prof. S. S. Ray and all the staff members of the institution for providing excellent working environment and for their assistance. I am also grateful for the facilities at Department of Physics of the University of Pretoria under Prof. C. Theron.

I thank India-Brazil- South Africa (IBSA) trilateral scheme for funding my MSc studies and research visit and conferences to the Federal University of Parana, Curitiba, Brazil (2013) and Bharati Vidapeeth University, Pune India (2014).

I acknowledge National Research Foundation (NRF) through KIC grant 98510 for funding my trip to the World Academy of Science and Engineering and Technology (WASET) 19th

International Conference on Condensed Matter Physics (ICCMP) Sydney, Australia January (2017).

I sincerely acknowledge Ms Margaret Ward for taking time out of her busy schedule to correct and edit the spelling, grammar and general English issues of this thesis. I really appreciate your effort.

Special appreciation goes to my parents (Mr & Mrs Akande) for their love, support and prayers, my wife (Afolakemi) for her understanding, support and encouragement, my son (Williams) for been a source of joy to us and my siblings for their encouragement.

Dedication

This thesis is dedicated to the Omniscience, the Almighty God.

List of Publications and Presentations

Article in Peer-Reviewed Journals

1. **A.A. Akande**, E.C Liganiso, B.P Dhonge, K.E. Rammutla, A. Machatine, L. Prinsloo, H. Kunert, B.W. Mwakikunga, “Phase evolution of vanadium oxides obtained through temperature programmed calcinations of ammonium vanadate in hydrogen atmosphere and their humidity sensing properties” *Journal of Materials Chemistry and Physics* 151, (2015) 206–214. **(10 citations)**
2. **A.A. Akande**, K.E. Rammutla, T. Moyo, N.S.E. Osman, S.S. Nkosi, C.J. Jafta, B.W. Mwakikunga, “Magnetism Variation and Susceptibility Hysteresis at the Metal-Insulator Phase Transition Temperature of VO₂ in a Composite Film Containing Vanadium and Tungsten Oxides” *Journal of Magnetism and Magnetic Materials* 375 (2015) 1-9 **(12 citations)**
3. **A.A. Akande**, B.W. Mwakikunga, K.E. Rammutla, B.P Dhonge, A.G.J, Machatine “Room temperature Methane (CH₄) sensing by Vanadium oxide (VO_x) nanoparticles” *Adv. Sc. Lett* 22, 4 (2016) **(1 citations)**
4. **Amos Adeleke Akande**, Bonex Wakufwa Mwakikunga and Koena Erasmus Rammutla, Augusto Machatine “Larger Selectivity of the V₂O₅ nano-particles Sensitivity to NO₂ than NH₃” *Sensors & Transducers Vol. 192 Issue 9 (2015)* 61-65 **(1 citations)**
5. **A.A. Akande**, B.W. Mwakikunga, K.E. Rammutla, B.P Dhonge, A.G.J, Machatine, Gate Voltage Controlled Humidity Sensing Using MOSFET of VO₂ Particles, *Int. J. Chem. Mol. Nucl. Mat. Met. Eng. Vol: 11, No: 1 (2017)* 78-81 **(0 citations)**
6. **A. A Akande**, A. G. J. Machatine, B. Masina, G. Chimowa, B. Matsoso, K. Roro, M-M Duvenhage, H. Swart, S.S. Ray, B.W. Mwakikunga, Blue- and red- shifts of

- V₂O₅ phonons in NH₃ environment by in situ Raman Spectroscopy, *J. Phys. D: Applied Physics* (2018) [015106](#). (0 citations)
7. B.N. Masina, S. Lafane, L. Wu, [A.A. Akande](#), B. Mwakikunga, S. Abdelli-Messaci, T. Kerdja, and A. Forbes “Phase-selective vanadium dioxide (VO₂) nanostructured thin films by pulsed laser deposition” *Journal of Applied Physics* 118 165308 (2015) (9 citations)
 8. G. Chimowa, ZP Tshabalala, [A.A. Akande](#), G Bepete, B Mwakikunga, S.S. Ray, Improving methane gas sensing properties of multi-walled carbon nanotubes by vanadium oxide filling, *Sens Act B: Chemical* 247, 11-18 (2017) (5 citations)
 9. AA Khaleed, A Bello, JK Dangbegnon, DY Momodu, MJ Madito, FU Ugbo, [A.A. Akande](#), BP Dhonge, F Barzegar, BW Mwakikunga, N Manyala, Gas sensing study of hydrothermal reflux synthesized NiO/graphene foam electrode for CO sensing, *J. Mat. Sci.* 52, 4, (2017) 2035-2044. (5 citations)
 10. AA Khaleed, A Bello, JK Dangbegnon, DY Momodu, MJ Madito, FU Ugbo, [A.A. Akande](#), BP Dhonge, F Barzegar, O Olaniyan, BW Mwakikunga, N Manyala, Effect of activated carbon on the enhancement of CO sensing performance of NiO, *J. Alloy Com* 694 (2017) 155-162 (6 citations)
 11. [A.A. Akande](#), B.W. Mwakikunga, K. T. Roro, A.G.J, Machatine, C. N. M. Ouma, NH₃ gas sensing characteristics of multi-planer V₂O₅ nanostructure: A combined experimental and *ab initio* approach (**In preparation**)

International Conference Proceedings

1. [A.A. Akande](#), B.W. Mwakikunga, K.E. Rammutla, B.P Dhonge, A.G.J, Machatine, Gate Voltage Controlled Humidity Sensing Using MOSFET of VO₂ Particles, World Academy of Science and Engineering and Technology (WASET) 19th

International Conference on Condensed Matter Physics (ICCMP) Sydney, Australia Jan 27-28 (2017)

2. **A.A. Akande**, E.C Liganiso, B.P Dhonge, D.E. Motaung, K.E. Rammutla, B.W. Mwakikunga, “Microwave synthesis of vanadium oxide (VO_x) nanoparticles and their application in methane sensing”, 3rd International Conference NANOCON 014, Bharati Vidapeeth University, Pune India Oct. 2014. Oral Presentation
3. **A.A. Akande**, K.E. Rammutla, B.W. Mwakikunga, “Hydrothermal Synthesis and Gas Sensing Properties of Polycrystalline Vanadium Oxide”. 5th International Conference on Nanotechnology and Nanoscience NanoAfrica May 2014 South Africa. Oral Presentation
4. **A.A. Akande**, K.E. Rammutla, B.W. Mwakikunga, “Ammonia and Hydrogen Sulphide Sensing of Polycrystalline VO_x”. International India-Brazil-South Africa Advanced Materials Nanotechnology conference, Curitiba, Brazil, Nov. 2013. Oral Presentation

South African Institute of Physics Proceedings

1. **A.A. Akande**, K.E. Rammutla, B.W. Mwakikunga, “Chemiresistive Gas Sensing Properties of Vanadium Pentoxide nanoparticles”. South African Institute of Physics Conference 2014, University of Johannesburg, South Africa.
<http://events.saip.org.za/contributionListDisplay.py?confId=34>.
2. **A.A. Akande**, K.E. Rammutla, B.W. Mwakikunga. “Mott’s Variable Range Hopping Model: a Method for the Identification of Phase Transition”. South African Institute of Physics Conference 2013, University of Zululand Richard Bay South Africa.
<http://events.saip.org.za/contributionListDisplay.py?confId=32>.

3. **Amos A. Akande**, Bonex W. Mwakikunga Erasmus K, Rammutla, Funda Mpanza, Kittessa Roro, “VO₂ nanorods on p-type Si as new candidate for near infrared light harvesting devices” 6th South African Conference on Photonic Materials 2015, Mabula Game Lodge South Africa.

Abstract

The aims of this research thesis are to synthesise VO_2 , V_2O_5 and V_6O_{13} nanostructures and apply the materials on sensor electrodes for gas and humidity sensing. These materials were synthesised and optimised using chemical vapour deposition (CVD), microwave assisted and pulse laser deposition (PLD) techniques. Analyses with thermogravimetric (TGA), differential scanning calorimetry (DSC), X-ray diffraction (XRD), high resolution transmission electron microscope (HRTEM), energy dispersive spectroscopy (EDS), X-ray photoelectron spectroscopy (XPS), vibrating sample magnetometry (VSM), Raman and Fourier transform infrared (FTIR) spectroscopy showed VO_x phases order as $\text{NH}_4\text{VO}_3 \rightarrow \text{VO}_2 + \text{V}_2\text{O}_5$ (150 – 200 °C) $\rightarrow \text{V}_6\text{O}_{13}$ (300 °C) $\rightarrow \text{V}_2\text{O}_5$ (above 350 °C). This is when the precursor NH_4VO_3 was annealed in CVD between 100 – 350 °C in H_2 atmosphere for 2 hrs. Adsorption analysis of VO_x nanostructures showed a profile of Brunauer-Emmett-Teller (BET) surface areas which increased with the annealing temperature until 300 °C after which the transition occurred. Humidity (%) sensing response of VO_x showed high response for V_6O_{13} and V_2O_5 phase whereas, the Langmuir isotherm plot in the form of the response per BET surface area with respect to different levels of relative humidity showed high response for VO_2 . Phase evolution diagram based on these properties has been proposed.

Thermal CVD annealing of NH_4VO_3 at 500 °C in N_2 atmosphere for 2, 12 and 24 hours produced monoclinic V_6O_{13} (at 2 hrs) and α -orthorhombic V_2O_5 (at 12 and 24 hrs) nanorod structures using the above characterization techniques. Gas sensing application of these structures revealed that the H_2S gas is selective in adsorption to V_6O_{13} phase with 132 % response magnitude at 350 °C and 60 ppm, this response is 647.2 % higher than that of NH_3 , CH_4 , NO_2 , H_2 and CO . The response and recovery times are 32 and 129 s respectively which is remarkably short compared with the data in literatures. This V_6O_{13} sensor was ranked with

its V_2O_5 counterpart and still found to be 238.5 % higher for H_2S gas. Density functional theory (DFT) through *ab initio* molecular dynamics of (110) facet of monoclinic V_6O_{13} and α -orthorhombic V_2O_5 also showed high H_2S adsorption energy for V_6O_{13} than V_2O_5 with a profile which simulate the experimental findings.

Low temperature microwave assisted synthesis of VO_x from NH_4VO_3 without post-annealing treatment demonstrated small size homogeneous crystallite with high BET surface area and high adsorption and desorption pores. These properties translated to sub-ppm room temperature sensing of the flammable CH_4 and odorant NH_3 and toxic NO_2 with high sensitivity. The VO_2 (B) phase produced via the same microwave process applied for humidity sensing in the lateral gate metal oxide semiconductor field effect transistor (MOSFET) configuration for 0, 5, 8, 10, 12 and 15 V gate voltages. An optimum percentage humidity response observed at 5 V showed response and recovery times in the order of 60 – 70 s which is remarkably shorter than the ≥ 300 s response of the non-gated VO_2 humidity sensor reported in this thesis. Statistical information extracted from the non-linear S-curve Hill Dose rate showed that the VO_2 (B) sensor is very resilient to relative humidity by showing the humidity level of more than 100% where the response of the sensor could be reduced to 50%.

In-situ Raman spectroscopy sensing of NH_3 gas at the surface of PLD deposited V_2O_5 thin film was presented. The film crystal structure, depth profile and oxidation state was studied by cross section scanning electron microscope (SEM), time of flight secondary ion mass spectroscopy (TOF-SIMS), XPS and group theoretical analysis. Recoverable red shift of 194 cm^{-1} and blue shift of 996 cm^{-1} phonons upon the interaction with the NH_3 gas at 25 and 100 °C was observed. Decrease in the Raman scattered photons of the 145 cm^{-1} phonon was also observed for different levels of NH_3 exposure. The responses of these phonon properties in NH_3 environment compared to the chemoresistive sensing of the film at 40 ppm showed that

the in-situ Raman spectroscopy techniques is not only more sensitive but also demonstrated possibility for selective gas detection via blue and red shift of phonon frequencies.

Table of contents

Declaration	i
Acknowledgements	ii
Dedication	iv
List of publications and presentations.....	v
Abstract.....	ix
List of Figures.....	xvii
List of Tables.....	xxv
Chapter 1: Introduction.....	1
1.1 General Overview and Rationale of the Study	1
1.2 Aims and Objectives	6
References	7
Chapter 2: Literature Review.....	10
2.1 Properties of Nanostructures Materials	10
2.2 Group Theory Aspect of this work	13
2.3 Correlated Vanadium Oxides Systems	14
2.4 Vanadium dioxide.....	19
2.5 Transition Mechanism of Vanadium dioxide	21
2.5.1 Crystal Structure of VO ₂	21

2.5.2 <i>Electronic Structure of VO₂</i>	23
2.5.3 <i>Phonon band structure of VO₂</i>	25
2.6 Vanadium pentoxide (V ₂ O ₅)	26
2.6.1 <i>V₂O₅ Crystallographic, Electronic and Phonon structures</i>	26
2.7 Vanadium oxide (V ₆ O ₁₃)	31
2.7.1 <i>Crystallographic, Electronic and Phonon structures of V₆O₁₃</i>	31
2.8 Surface Structures of VO ₂ , V ₂ O ₅ and V ₆ O ₁₃	34
References	35
Chapter 3: Methodology and sensing mechanisms	44
3.1 Preparation Methods	44
3.1.1 <i>Chemical Vapour Deposition</i>	44
3.1.2 <i>Microwave Assisted Techniques</i>	45
3.1.3 <i>Pulse Laser Deposition</i>	46
3.2 Sensing Mechanism	47
3.2.1 <i>Chemoresistors Sensing Mechanism</i>	47
3.2.2 <i>Mechanism of Gas Sensing using Optical Spectroscopy</i>	51
References	57
Chapter 4: Phase evolution of VO₂, V₂O₅ and V₆O₁₃ nanostructures from NH₄VO₃ and their humidity sensing properties	61

4.1 Introduction.....	61
4.2 Experimental techniques	62
4.2.1 Powder Synthesis	62
4.2.2 Powder Characterization	63
4.3 Results and Discussions	65
4.3.1 Thermal Analysis (DSC/TGA)	65
4.3.2 X-Ray diffraction Spectra	68
4.3.3 Transmission Electron Microscope	69
4.3.4 Phase Diagram	71
4.3.5 Raman Spectroscopy	72
4.3.6 Fourier Transform Infrared Spectroscopy (FT-IR)	73
4.3.7 X-ray Photoelectron Spectroscopy and Energy Dispersive Spectroscopy (XPS and EDX)	74
4.3.8 Vibrating Sample Magnetometry (VSM)	78
4.3.9 Brunauer-Emmett-Teller (BET)	82
4.3.10 Applications: Humidity Sensing.	84
4.4 Conclusion	85
References	87
Chapter 5: Selective adsorption of H₂S gas to vanadium mixed valence state V₆O₁₃ nanorods particle	93
5.1 Introduction.....	93

5.2 Experimental and Computational techniques	94
5.2.1 Powder Synthesis	94
5.2.2 Powder Characterization	94
5. 2.3 Gas sensing measurement/test	95
5.2.4 Computational procedures	96
4.3. Results and Discussions	97
5.4 Conclusion	113
References	114

Chapter 6: Room temperature sensing of CH₄ and selectivity of NO₂ than NH₃ of nanospherical VO_x particles

6.1 Introduction.....	117
6.2 Experimental Details.....	118
6.3 Results and Discussion.....	119
6.4 Conclusions ...	132
References	134

Chapter 7: Gate voltage controlled humidity sensing using MOSFET of VO₂ nanoflowers.

7.1 Introduction.....	137
7.2 Experimental Details.....	138

7.2.1 <i>Material preparation and characterization</i>	138
7.2.2 <i>VO₂ MOSFET fabrication and Humidity sensing Measurements</i>	139
7.3 Results and Discussion.....	141
7.4 Conclusions	148
References	149
Chapter 8: Blue- and red- shifts of V₂O₅ phonons in NH₃ environment by in situ Raman spectroscopy.....	151
8.1 Introduction.....	151
8.2 Experimental	153
8.3 Results and Discussion.....	155
8.3.1 <i>In-situ Raman spectroscopy with gas sensing at 25 °C</i>	160
8.3.2 <i>In-situ Raman spectroscopy with gas sensing at 100 °C</i>	164
8.3.3 <i>Comparison of in-situ Raman spectroscopy-gas-sensor tester and the traditional chemoresistive gas-sensor testing station</i>	167
8.4 Conclusions	171
References	173
Chapter 9: Concluding Remarks and Recommendations	177
9.1 Summary	177
9.2 Future research work and recommendations	180
Appendix.....	183

Lists of figures

Figure 1.1 Review of the various screening areas and the respective target gases	4
Figure 2.1: Evolution of band gap and density of states as function of number of atoms as the materials is reduced from bulk to nano regime, (a) Band gap scheme form single atom to bulk, and (b) Kubo's gaps scheme showing effects of the size on metal-to insulator transition.	12
Figure 2.2: Phase diagram of Vanadium oxygen systems	15
Figure 2.3: (a) Transition temperatures of a selected number of vanadium oxide phases as function of the oxygen to vanadium ratio.....	17
Figure 2.4: Resistance and Conductance, (b) Transmittance and Reflectance, (c) Roughness (d) Scattering, (e) Raman relative intensity of 618 cm^{-1} phonon frequency and (f) Surface Plasmon resonance wavelength	20
Figure 2.5: VO_2 monoclinic (M_1) $P2_1/c$ (insulator) below 340 K	22
Figure 2.6: VO_2 Tetragonal (T) $P4_2/mnm$ (metallic) above or at 340 K	23
Figure 2.7: VO_2 Tetragonal (T) $P4_2/mnm$ (metallic) above or at 340 K	24
Figure 2.8: First Brillouin zone of (a) tetragonal, and (b) monoclinic structures	26
Figure 2.9: Local coordination of vanadium and oxygen atoms in the $Pmnm$ (D_{2h}^{13} No. 59) lattice indicating the crystal axes and nearest-neighbour distances	28

Figure 2.10: (a) Unit cell of Orthorhombic $Pmnm$ (D_{2h}^{13} No. 59) lattice. The atoms with the grey colours are the vanadium atoms why the one with red colours are oxygen atoms. (b) Brillouin Zone of the structure.....29

Figure 2.11: Band structure and partial density of states (PDOS) profiles of Figure (2.10)..30

Figure 2.12: (a) Unit cell of monoclinic lattice $C2/m$ C_{2h}^3 . The atoms with the grey colours are the vanadium atoms why the one with red colours are oxygen atoms. (b) 2D structure in a-c plane showing the local coordination of vanadium and oxygen atoms33

Figure 3.1: Schematic diagram of thermal chemical vapour deposition system.....45

Figure 3.2: (a) Precursors for microwave synthesis (b) Schematic diagram of the microwave reactor46

Figure 3.3: Schematic diagram of the pulse laser deposition system47

Figure 3.4: Band bending schematic diagram of n-type MOS after ionosorption of oxygen49

Figure 3.5: Schematic diagram for change of the sensor resistance upon exposure to the target gas (reducing gas) in the cases of n-type and p-type MOS sensors49

Figure 3.6: Schematic diagram of the in-situ Raman spectroscopy52

Figure 4.1 (a): DSC thermogram of the starting precursor (NH_4VO_3)66

Figure 4.1 (b): TGA/DTA thermogram of the starting precursor (NH_4VO_3)66

Figure 4.1 (c): TGA/DTA thermogram of the sample prepared at 400 °C.....66

Figure 4.2: DSC thermograms of the samples prepared by thermal annealing of NH_4VO_3 from 100 - 350 °C	68
Figure 4.3 (a): XRD spectra of the standard NH_4VO_3 and of the samples prepared by thermal annealing of NH_4VO_3 from 100 - 350 °C.....	69
Figure 4.3 (b): High resolution TEM image of sample annealed at 350 °C	70
Figure 4.4: Vanadium Oxides (VO_2 , V_6O_{13} and V_2O_5) Phase Evolution diagram.	71
Figure 4.5 (a): Raman spectra of the standard NH_4VO_3 and of the samples prepared by annealing of NH_4VO_3 from 100 - 350 °C.....	72
Figure 4.5 (b): FT-IR of the standard NH_4VO_3 and of the samples prepared by annealing of NH_4VO_3 from 100 - 350 °C.....	73
Figure 4.6: Proportions of V_2O_5 , VO_2 , and V_6O_{13} determined by EDS calibrated with XPS as they vary with annealing temperatures.....	77
Figure 4.7: Vibrating sample magnetometry (VSM) for VO_x samples annealed at 100, 150, 200, 250, 300 and 350 °C (a) Parameters definition for a hysteresis loop for bulk and nano materials (b) Hysteresis loops for VO_x samples annealed at 100, 150, 200, 250, 300 and 350 °C and (c) A plot of the hysteresis loop parameters against annealing temperatures.....	78
Figure 4.8: (a) N_2 adsorption and desorption isotherms profile of the powder annealed at 250 °C, insert is the BET plot.....	83
Figure 4.8: (b) BET surface area versus temperature for all the annealed powders and including NH_4VO_3	84
Figure 4.9: (a) Transient profiles of current through the VO_x samples in varying levels of humidity (b) Responses weighted against BET surface area for VO_x samples as function of humidity level.....	85

Figure 5.1: Schematic diagram of KSGA565 KENOSISTEC sensing station illustrating how the gas sensing measurement was performed.....	96
Figure 5.2: XRD spectra of the samples prepared by thermal annealing of NH_4VO_3 500 °C at for 2, 12, and 24 hours.....	98
Figure 5.3 (a): Low and HRTEM images of V_6O_{13} , (b) SAED of V_6O_{13} , (c) Low and HRTEM images of V_2O_5 (prepared for 12 hrs), (c) SAED of V_2O_5 (prepared for 12 hrs), and (e) corresponding EDX spectrum of (a).....	99
Figure 5.4: FE-SEM images of (a) V_6O_{13} , (b) V_2O_5 (prepared for 12 hrs), (c) V_2O_5 (prepared for 24 hrs).....	100
Figure 5.5: (a) Raman spectra of the samples prepared by thermal annealing of NH_4VO_3 at 500 °C for 2, 12, and 24 hours (b) Spectra in (a) between 100 – 250 cm^{-1} range.	101
Figure 5.6: VSM profile of the samples prepared by thermal annealing of NH_4VO_3 at 500 °C for 2, 12, and 24 hours.....	102
Figure 5.7: CL profile of the samples prepared by thermal annealing of NH_4VO_3 at 500 °C for 2, 12, and 24 hours.....	103
Figure 5.8: Conductometric sensing signal from 25 - 350 °C (a) of H_2S (b) of NH_3	106
Figure 5.9: Response profiles as a function of different gas concentrations (a) for H_2S , (b) for NH_3	107
Figure 5.10 (a) Conductometric sensing signal of H_2S at 350 °C (b) Response and recovery time calculations of 60 ppm of the profile in (a)	108

Figure 5.11 Gases response of 60 ppm at 350 °C, (a) Gases responses for the samples prepared at 2 hours (b) H ₂ S responses for the samples prepared at 2, 12 and 24 hours....	109
Figure 5.12 (a) V ₆ O ₁₃ (110) surface and H ₂ S molecules, (b) V ₂ O ₅ (110) surface and H ₂ S molecules.....	110
Figure 5.13 (a) Adsorption energies vs number of H ₂ S molecules of V ₆ O ₁₃ and V ₂ O ₅ (110) surfaces, (b) Absolute Adsorption energies per molecules vs number of H ₂ S molecules of V ₆ O ₁₃ and V ₂ O ₅ (110) surfaces	112
Figure 6.1 (a) XRD pattern of VO _x nanoparticles, (b) SEM micrograph of VO _x nanoparticles, (c) HRTEM of VO _x NPs, (d) SAED pattern of VO _x NPs..	121
Figure 6.2. (a) Raman spectrum of VO _x nanoparticles, (b) N ₂ adsorption/desorption isotherms. profile of VO _x nanoparticles, insert is the BET plot.	122
Figure 6.3 (a) Variation of the current flowing through VO _x nanoparticles recorded for different concentrations of CH ₄ gas, (b) Sensor response as a function of different CH ₄ gas concentrations (c) Profile of Dose response curve with variable Hill slope of the VO _x responses vs CH ₄ gas concentrations.....	123
Figure 6.4 (a) XRD spectrum of V ₂ O ₅ nanoparticles, (b) SEM micrograph of V ₂ O ₅ nanoparticles.....	126
Figure 6.5 N ₂ adsorption/desorption isotherms profile of V ₂ O ₅ NPs, insert is the BET plot.....	127
Figure 6.6 (a) The electrical response of V ₂ O ₅ NPs for different concentrations of NH ₃ , (b) Sensor response as a function of different NH ₃ gas concentrations.	128
Figure 6.7 (a) The electrical response of V ₂ O ₅ NPs for different concentrations of NO ₂ , (b) Sensor response as a function of different NO ₂ gas concentrations.....	129

Figure 6.8 Sensing mechanism of V_2O_5 NPs (Chemisorption effect is also observed rather than only Iono-sorption	130
Figure 7.1 (a) Pictorial image of the lateral-gate MOSFET (b) SEM micrograph of the lateral-gate MOSFET.	140
Figure 7.2 (a) XRD partern (b) SEM image, and (c) core level XPS spectrum of VO_2 nanoflowers particles.....	142
Figure 7.3 (a) Raman spectrum (b) BET - N_2 molecule adsorption and disorption isotherms of VO_2 nanoflowers particles.....	143
Figure 7.4 Current-time curves for the sensor response to varying levels of relative humidity concentrations (a) 0 V gate bias (b) 5 V gate bias (c) 10 V gate bias (d) 15 V gate bias.....	144
Figure 7.5 (a) Response of the VO_2 nanoflowers sensor versus levels of relative humidity (b) Response of the VO_2 nanoflowers sensor to relative humidity versus the respective gate voltages.	146
Figure 7.6 Non-linear profile of the response to humidity as a function of the level of the relative humidity for 5V gate bias	147
Figure 8.1. (a) XRD pattern of V_2O_5 film, (b) Williamson-Hull plot for the grains stain determination	156
Figure 8.2. SEM images of V_2O_5 film, (a) in-plane surface image (b) cross-section image at the edge of the film showing three distinct layers.	157
Figure 8.3. XPS spectra of the V_2O_5 film, (a) Broad survey scan spectrum (b) Higher resolution deconvoluted core level spectrum of V-2p and O-1s for the V_2O_5 film.	159

Figure 8.4. (a) TOF-SIMS depth profile of the negative ions of V, VO, Si and SiO species available in the film (b) is the TOF-SIMS depth profile spectrum showing the low counts SiO-, V- and VO₃H- species in (a) , (c) 3D overlays image of the ions of the film consisting of Si-, SiO₂- and VO- (d) 3D overlays image of the entire film displaying VO-, VO₂- and VO₃- as the surface ions.....160

Figure 8.5. (a) Raman spectra at 25 °C of V₂O₅ film in air, and covered with NH₃ molecule recorded at 6 minutes intervals, (b) Raman spectra at 25 °C of V₂O₅ film recovering from NH₃ molecule recorded at 6 and 12 minutes intervals.161

Figure 8.6. (a) Magnified images of 996 cm⁻¹ Raman lines when the film is exposed to NH₃ at 25° C (b) Magnified images of 996 cm⁻¹ Raman lines when the film is recovering from NH₃ at 25° C (c) Gaussian fitted data of the heights of low-frequencies 143 cm⁻¹ Raman lines when the film is exposed to and recovering from NH₃ at 25°, (d) Gaussian fitted data of peak-positions of high-frequencies 996 cm⁻¹ Raman lines when the film is exposed to and recovering from NH₃ at 25°.....162

Figure 8.7. (a) Raman spectra at 100 °C of V₂O₅ film in air, and covered with NH₃ molecule recorded at 6 minutes intervals, (b) Raman spectra at 100 °C of V₂O₅ film recovering from NH₃ molecule recorded at 6 and 12 minutes intervals.....165

Figure 8.8. (a) Magnified images of 996 cm⁻¹ Raman lines when the film is exposed to NH₃ at 100° C (b) Magnified images of 996 cm⁻¹ Raman lines when the film is recovering from NH₃ at 100° C (c) Gaussian fitted data of the heights of low-frequencies 143 cm⁻¹ Raman lines when the film is exposed to and recovering from NH₃ at 100° C, (d) Gaussian fitted data of peak-positions of high-frequencies 996 cm⁻¹ Raman lines when the film is exposed to and recovering from NH₃ at 100° C.....166

Figure 8.9. Conductometric sensing signal for NH₃ (a) at room temperature (b) at 100 °C.

.....168

Figure 8.10. (a) Response curve as a function of different NH_3 gas concentrations, (b) Plot of response time constant for different concentration of NH_3 gas169

Figure 9.1. (a) Optical microscope of the clean micro-nano transistors array, (b) Magnified image of (a) with VO_2 nanofibers deposited before resist deposition (c) Magnified image of the e-beam developed device after lifting (etching) the resist, and (d) Magnified image of clean transistor showing the device configurations (drain, source and gate pattern).181

List of Tables

Table 4.1 (a): XPS analysis for reference or standard sample containing VO ₂ , V ₂ O ₅ , V ₆ O ₁₃ and WO ₃	75
Table 4.1 (b): EDS analysis for reference or standard sample containing VO ₂ , V ₂ O ₅ , and V ₆ O ₁₃	75
Table 4.2: EDS analysis based on the calibrations in Tables 1 (a) and (b) and local composition for the VO _x samples annealed at 150, 200, 250, 300 and 350 °C.....	76
Table 4.3: A summary of the hysteresis loop parameters of remanent magnetization (M _R ⁺ and M _R ⁻), saturation magnetization (M _S ⁺ and M _S ⁻) and squareness (SQ) as well as hysteresis width and exchange bias width	81
Table 5.1: Summary of crystallite size, strain and magnetic properties of the samples prepared by thermal annealing of NH ₄ VO ₃ at 500 °C for 2, 12, and 24 hours.	102
Table 6.1: Summary of surface properties versus gas sensing responses (%) of ethanol and water synthesized VO _x	132
Table 7.1: List of known VO ₂ polymorphs alongside their major properties	138
Table 8.1: Summary of Raman signatures versus chemoresistive sensing of NH ₃ molecule at V ₂ O ₅ surface	171

CHAPTER 1

INTRODUCTION

1.1 General Overview and Rationale of the Study

The problem of air pollution is probably the number one challenge that is facing humanity in this present age. This problem emerged as a result of an increase in the concentration and release of airborne particulate matter and gases from oil exploration fields, motor vehicles, power plants, agricultural fields and other industrial activities [1-3]. Some of these pollutants are dust, dirt, soot, smoke, complex organic and inorganic substances such as the very offensive, combustible, and flammable methane (CH_4), sulphur dioxide (SO_2), hydrogen gas (H_2), the toxic and odorant hydrogen sulphide (H_2S), carbon dioxide (CO_2), carbon monoxide (CO), nitrogen monoxide (NO), nitrogen dioxide (NO_2), ammonia (NH_3) etc. Others are the volatile organic compounds (VOCs) which are benzene, ethanol, acetone, methanol, formaldehyde, tetrachloroethylene and hexamethyldisiloxane (HMDS) to mention a few [1-5]. These pollutants have been a major stumbling block to the world's desire for clean air, and a green and safe environment. According to the research conducted by the Global Burden of Disease project and reported by the BBC Science and Environment in 2013 [6], "polluted air causes 5.5 million deaths a year, EcoWatch also reported the International Energy Agency and America Lung Association's findings to be 6.5 million a year in 2015 [7]. The World Health Organisation (WHO) recorded 7 million in 2012 – a figure found to be one in eight of total global deaths [8].

Indoor and outdoor and long-time exposure to gases and VOCs have been reported to have negative effects such as damage to the respiratory system and skin irritations and are also the main cause of sick building syndrome [2, 9-10]. For example NO_2 and its by-products NO

and N_2O , are the most dangerous among inorganic gases forming a reddish-brown gas with a pungent and irritating odour and usually irritating the lungs and eyes which often causes problems in the human respiratory system [3, 9, 10]. They have been reported to be responsible for asthma, lung diseases, and kidney impairment and as a carcinogenic agent [9, 10]. Naturally occurring and toxic H_2S which is usually a by-product of crude petroleum, volcanic gas, natural gases etc. also causes problems in the human breathing system. Ammonia (NH_3) has a pungent odour, is colourless in nature and is a non-toxic gas, which negatively impacts the environment through irritating human eyes, causing liver failure and usually comes from the decomposition of animal manures. Methane (CH_4) gas is very important in homes and industries, and is highly combustible, flammable and explosive such that when it leaks or is trapped in storage; it can dangerously explode and cause fire. Sulphur dioxide (SO_2) is another gas that usually causes irritation in the human system. It has been severally reported to provoke nose and throat irritation, coughing, wheezing, a tight feeling around the chest and shortness of breath [10]. Carbon oxides gases (CO , CO_2) are colourless and odourless but very toxic and active in preventing oxygen from being absorbed into the blood stream when inhaled by man. They often cause non-functioning or malfunctioning of some vital organs, CO_2 ingestion has been reported to also lead to asphyxiation and suffocation. These gases are by-products of numerous organic materials and substances which we consume in our day to day activities.

Volatile organic compounds (VOCs) are organic/carbonaceous molecules originating from natural materials and artificial or processed materials. These compounds are also dangerous to human health; and have been suspected and proven to be carcinogenic, for example, formaldehyde, toluene, and benzene [3, 9, 10]. Molecules such as acetone, methanol, ethanol, formaldehyde, benzene, pentane, ethane, isoprene etc. are breath constituents and so

biomarkers for diseases like diabetes mellitus, ketonemia, oxidative stress and cholesterol metabolism [3, 9].

However, the precursors through which these gases and compounds emanate from are unavoidable for our daily survival, like crude petroleum and natural gas which are heavily relied upon by the entire world for her energy provision. Precursors such as animal manure and organic materials from agricultural fields and refuge sites are inevitable in man's life style. Transportation activities and combustion of fuel in air by which most of the deadly gases matured from, are also required for continuous survival of life.

Continuous measurement and monitoring of these pollutants appears to be the plausible solution to these environmental problems; and has been suggested by many researchers [2-10], health stakeholders and agencies. These stakeholders include the world health institutions like the WHO, United Nations Environment, Green Space, America Lung Association and National Ambient Air Quality. The South African Government is also relentlessly working on the safety of citizens by providing annual reliable data often tagged "STATE OF THE AIR REPORT AND NATIONAL AIR QUALITY INDICATOR" and by publishing Gazettes through the South African Minister of Water and Environmental Affairs under the National Environmental Air Quality Act 2004 (Act No: 39 OF 2004) which emphasizes measurement and monitoring as major solutions. Figure 1.1 is the summary of the critical screening areas and the respective target and interferent compounds.

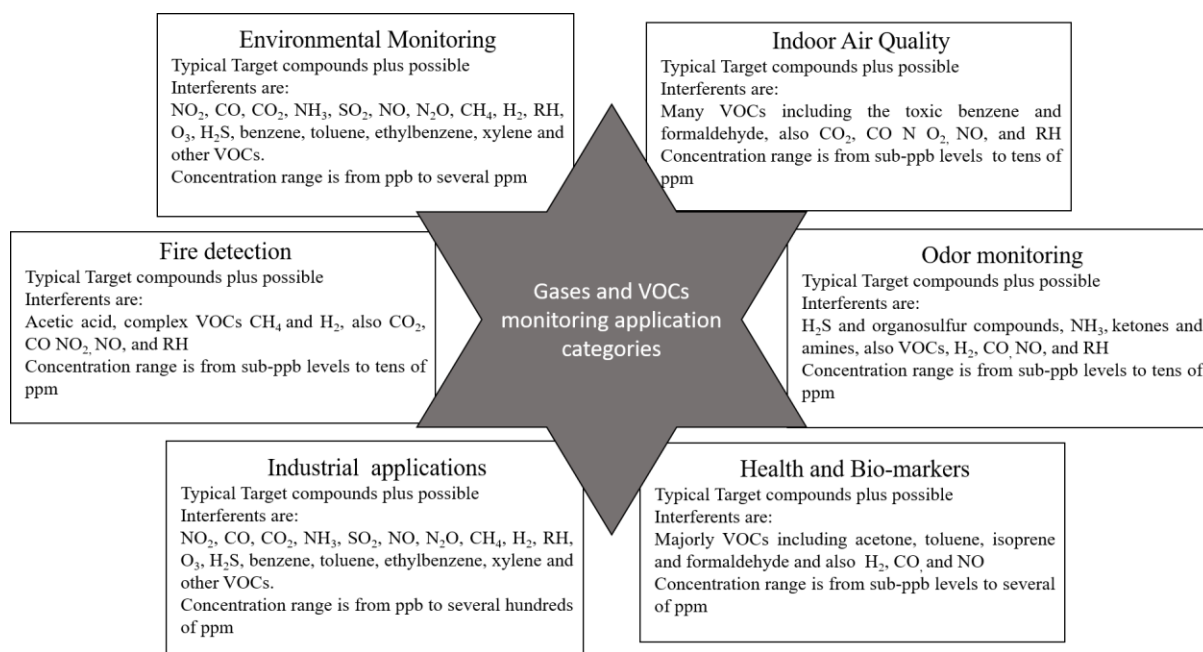


Figure 1.1 Review of the various screening areas and the respective target gases. [This is adopted from [3] but reviewed in this thesis]

Among the many chemical/gas sorption or detection technologies, metal oxides semiconductor (MOS) is the preferred transduction and detection method due to characteristics such as low cost, long life time, fast response time and high sensitivity [2]. This method can be dated back to the 1960s when Seyama *et al.*(1962) discovered the chemoresistive effect as they exposed a zinc oxide (ZnO) surface to chemicals [1]. Since that period, ceramics and high band gap semiconductors like aluminium sesquioxide (Al₂O₃), zinc monoxide (ZnO), thin oxide (SnO₂), titanium dioxide (TiO₂), tungsten trioxide (WO₃), and copper dioxide (CuO₂) etc. have dominated the field [11-15]. Nevertheless, realization of practical sensing devices through these materials has been a major challenge due to limitations such as; (1) poor responses at room temperature - in other words MOSs usually respond at high temperature and thereby placing high demands on electricity, (2) poor recovery - that is, inability of MOSs to completely recover back to their initial electronic state, (3) poor selectivity – that is, inability to detect one species of gas or chemical at a time

[2, 10]. Another challenge of MOSs in chemical and gas sensing technology is that most available devices were not portable; hence there is need for movable or pocket-like devices for easy application in the field.

Recently, the surface properties and low band gaps of vanadium oxide materials (V_2O_5 , VO_2 , etc.) are beginning to draw attention in the field of gas and chemical sensing because of their atomically well-defined geometry, surface chemical reactivity, multiple valence state, adsorption property, magnetic behaviour, optical switching and metal-to-insulator transition properties [16-18]. These properties can be improved significantly when the material's dimensions are reduced from bulk to nano-scale wherein the material loses its gravitational effects (classical) and gain electromagnetic effects (quantum) and consequently yield drastic increase in volume-to-surface ratio properties [19].

Availability of vanadium ore in South African local mining also forms parts of the propelling force driving the objectives of this work. According to the statistics [20-21] South Africa has about 29.4% of vanadium ore commercially available and 40.2% in reserve. The country also hosts some of the world-leading vanadium producing companies including Vanchem vanadium (Pty) Ltd which is located in Witbank, one of the South Africa's industrial cities [22].

This thesis therefore studies the unique properties of vanadium oxides nanostructures with respect to the sensitivity, selectivity, portability and room temperature detection of gases and VOCs by electrical and Raman spectroscopy methods.

1.2 Aims and Objectives

The aims of this research thesis are to synthesise V_2O_5 , V_6O_{13} and VO_2 nanostructures and apply the materials as sensor electrodes for the detection of gases and humidity.

In achieving these aims, the following objectives will be followed:

- To synthesize nanostructures of Vanadium oxides from NH_4VO_3 using temperature programmed CVD and apply them for humidity sensing.
- To study the effect of the structural properties of VO_x on their gas sensing performance.
- To investigate the sensitivity, selectivity and room temperature gas sensing properties of VO_x nanomaterials prepared by microwave irradiation technique.
- To investigate the effects of gate voltage of nano- VO_2 -MOSFET to humidity.
- To study the in-situ Raman spectroscopy of V_2O_5 surface to NH_3 molecules using group theoretical and traditional conductometric approaches. This helps to determine how vibrational modes of V_2O_5 are influenced by NH_3 gas.

References

- [1] T. Seiyama, A. Kato, A new detectors for Gaseous Components Using Semiconductive Thin Films, *Anal Chem.* **34**, 1502-1503 (1962)
- [2] G. Neri, Fifty Years of Chemoresistive Gas Sensors, *Chemosensors* **3**, 1-20 (2015)
- [3] A. Schutze, T. Baur, M. Leidinger, W. Reimringer, R. Jung, T. Conrad, T. Sauerwald, Highly sensitive and selective VOC sensor system based on semiconductor gas sensors: How to? *Environments* **4**, 20, 1-13 (2017)
- [4] S. S. Varghese, S. H. Varghese, S. Swaminathan, K. K. Singh, V. Mittal, Two Dimensional Materials for Sensing: Graphene and Beyond, *Electronics* **4**, 651-687 (2015).
- [5] V. Palmisano, E. Weidner, L. Boon-Brett, C. Bonato, F. Harskamp, P. Moretto, M.B. Post, R. Burgess, C. Rivkin, W.J. Buttner, Selectivity and resistance to poisons of commercial hydrogen sensors. *Int. J. Hyd. Ener.* **40**, 11740-11747 (2015)
- [6] Global Burden of Disease project, BBC Science and Environment <http://www.bbc.com/news/science-environment-35568249>. (13-02-2016)
- [7] Eco Watch <https://www.ecowatch.com> (06-03-2017)
- [8] World Health Organization <http://www.who.int/mediacentre/news/releases/2014/air-pollution/en/> (24-03-2014)
- [9] G. Peng, U. Tisch, O. Adams, M. Hakim, N. Shehada1, Y. Y. Broza, S. Billan, R. Abdah-Bortnyak, A. Kuten, H. Haick, Diagnosing lung cancer in exhaled breath using gold nanoparticles, *Nat. Nano. Lett.* **4**, 669-673, (2009).

- [10] K. Watchakun, T. Samerjai, N. Tamaekong, C. Liewhiran, C. Siritwong, V. Kruefu, A. Wisitsoraat, A. Tuantranont, and S. Phanichphant, Semiconducting metal oxides as sensor for environmentally hazardous gases, *Sen. Act. B.* **160**, 580-591 (2011).
- [11] A.R. Raju, C.N.R. Rao, Gas –sensing characteristics of ZnO and copper-impregnated ZnO, *Sen. Act. B* **3**, 4, 305-310 (1991)
- [12] R. Artzi-Gerlitz, K.D. Benkstein, D.L. Lahr, J.L. Hertz, C.B. Montgomery, J.E. Bonevich, S. Semancik, M.J. Tarlov, Fabrication and gas sensing performance of parallel assemblies of metal oxide nanotubes supported by porous aluminum oxide membranes, *Sen. Act. B.* **136**, 1, 257-264 (2009)
- [13] C. Lu, Z. Chen, High-temperature resistive hydrogen sensor based on thin nanoporous rutile TiO₂ film on anodic aluminum oxide, *Sen. Act. B.* **140**, 1, 109-116 (2009)
- [14] S.T. Jun, G.M. Choi, CO gas-sensing properties of ZnO/CuO contact ceramics, *Sen. Act. B.* **17**, 3, 175 -178 (1994)
- [15] T. Jun, M. Tomoki, M. Norio, Y. Noboru, Copper oxide-promoted tin oxide element for highly sensitive and selective detection of H₂S, International Conference on Solid-State Sen. Act. San Francisco, CA, USA, 150-154 (1991)
- [16] S. Surnev, M. G. Ramsey, F. P. Netzer, Vanadium oxides surface studies, *Prog. Surf. Sc.* **73**, 4, 117-165, (2003).
- [17] S. Laubach, P. C. Schmidt, A. Thiben, F. J. Fernandez-Madrigal, Q. Wu, W. Jaegemann, M. Klemm, S. Horn, Theoretical and Experimental determination of the electronic structure of V₂O₅, reduced V₂O_{5-x} and sodium intercalated NaV₂O₅, *Phys. Chem. Chem. Phys.* **9**, 20, 2564-2576 (2007).

- [18] O. Sipr, A. Simunek, S. Bocharov, Th. Kirchner, G. Drager, Geometric and electronic structure effects in polarized V K-edge absorption near-edge structure space of V₂O₅, *Phy. Rev.* **60**, 20, 14115-14127
- [19] A. A Akande “Vanadium dioxide Nanostructure and Applications in Sensors” MSc Thesis (2014) University of Limpopo Tefloop
- [20] B. Rohrmann, The thermal decomposition of Ammonium Metavanadate (V) in Open and Closed System, *J. S. Afr. Inst. Min. Metal*, **85** 141 -150, (1985)
- [21] <http://www.mbendi.co.za/indy/ming/vand/af/sa/p0005.html> (10-10-2016)
- [22] B W Mwakikunga, Nano-size Effects on Opto-Electronic, Structural and Vibrational Properties of Vanadium and Tungsten Oxides Produced by Laser and Ultrasonic Spray Pyrolysis Techniques, PhD Thesis (2009), University of the Witwatersrand Johannesburg

CHAPTER 2

LITERATURE REVEIW

This chapter provides a theoretical background pertaining to the subject investigated during the study. A general review of nanostructures and nanomaterial is presented and a brief background of group theory and its application to solid materials is included. A review of the three phases of vanadium oxides studied in this work; VO_2 , V_2O_5 and V_6O_{13} in terms of their crystallographic, electronic, phonon structures, metal-insulator mechanisms, and their general applications is included. Surface structures of VO_2 , V_2O_5 and V_6O_{13} oxides and their role in gas sensing application are also covered.

2.1 Properties of nanostructured materials

Nanostructure is the term commonly used to describe the geometrical structure of nanomaterials; given that nanomaterials are a type of material whose dimensions are characterized by the nanometre scale (typically range between 1 – 100 nm) in the field of nanoscience and nanotechnology [1-4]. These are materials with exceptional properties compared to the properties of the bulk, molecule, or single atom [5]. The distinction in the properties of nanostructured materials is a consequence of the proportion of the surface atoms to the atoms in their bulk counterpart [5], an effect which is often referred to as the surface to volume ratio of the material. The whole summary of the expression of surface to volume ratio of typical nanostructured materials which has been observed in nature and grown

experimentally [6-7] were demonstrated by Mwakikunga (2009) [8]. In this expression, an isolated and delocalized surface atom of spherical particles is found to be $(3/r)$, rods or wire-like particles are $(2/a+2/r)$ and cubic particles are $(6/a)$ related to the bulk where r and a are radius and length of the structures respectively [8]. The surface to volume ratio can be very high as the radius and the length of the structure decreases or tends to nanometre regime. This nanostructure and surface property is translated into the physical properties; an example is the case of band gaps and the density of state (DOS) of materials [3]. It is well known that the number of atoms in a material is proportional to the bandwidth of their electronic band, such that each atom in the material contributes with its atomic states to the electronic band. The bandwidth of the electronic band and band gap usually increases as the size of atoms in the material is decreased. Density of states is the number of atoms per energy in a material. The DOS around Fermi level of the material which is very large for bulk matter decreases as its dimensions are confined [2-3]. These are shown below in Figure 2.1, where band gaps, density of states and the numbers of atoms are represented. The Figure demonstrates the evolution of band gap and density of states as a function of the number of atoms as the materials is reduced from the bulk to nano regime. The concept of Kubo's gaps is also added in Figure 2.1 (b), where the highest occupied molecular orbital (HOMO) and the lowest unoccupied molecular orbital (LUMO) states equals thermal energy. The figure shows that the Kubo gap is small for metallic bulk matter and high for insulating nanoclusters - this is an

indication of size induced metal-to-insulator transition usually observed in some metals and transition metals compounds [3, 9].

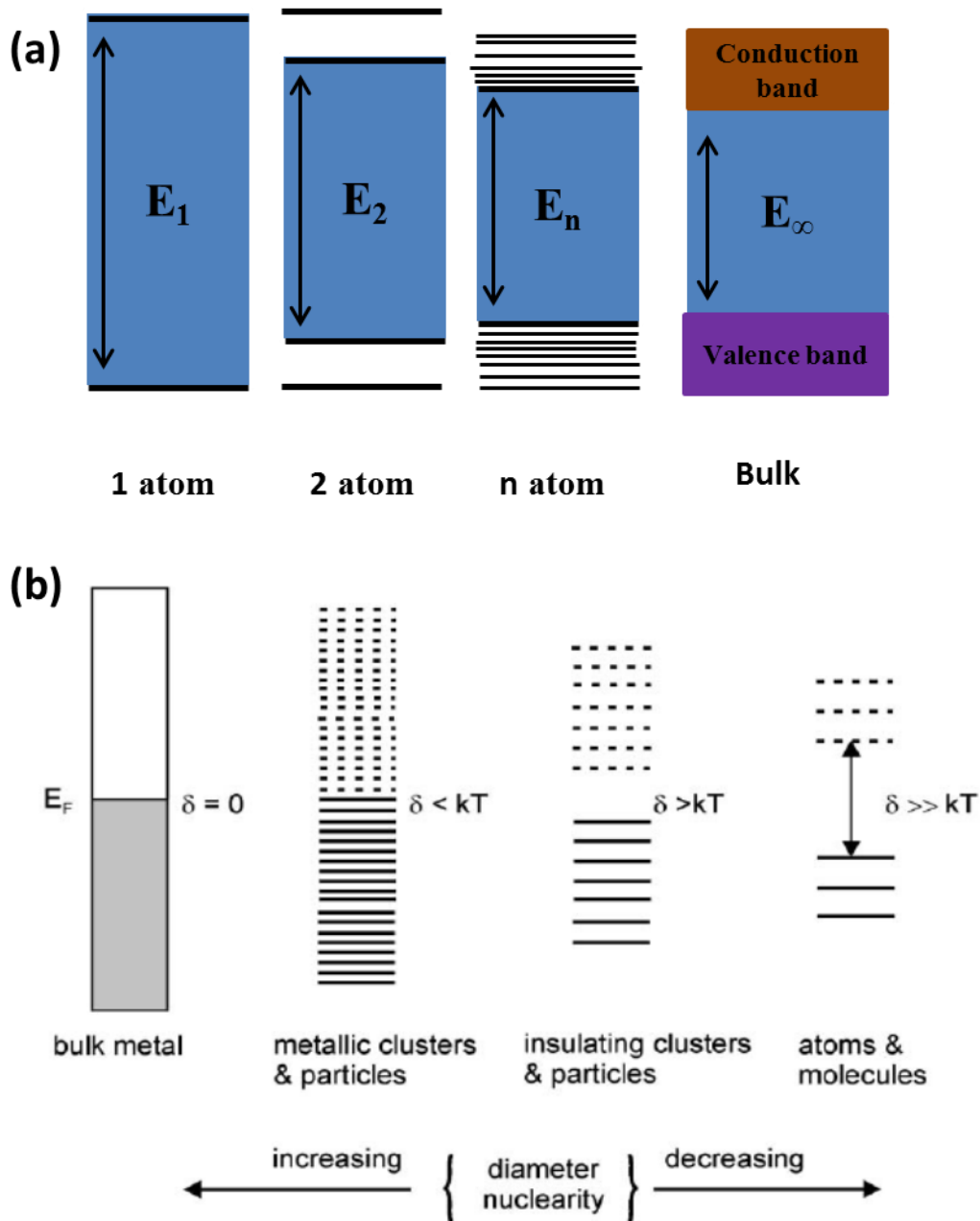


Figure 2.1: Evolution of band gap and density of states as a function of the number of atoms as the materials is reduced from the bulk to nano regime, (a) Band gap scheme from single

atom to bulk, and (b) Kubo's gaps scheme showing effects of the size on metal-to insulator transition. [3]

2.2 Group theory aspect of this work

This work also includes group theory principles to explain the Raman scattering process and other physical properties of VO₂, V₆O₁₃ and V₂O₅ nanostructures. It is well known that the states of quasiparticles such as electrons, holes, phonons, magnons, plasmons etc. in the crystals, molecules or single atoms are classified according to the irreducible representations of space group (crystal) or point group (molecule or single atom) [10-12]. The difference between the space group and point group arises because of the periodicity of the lattice structure exhibited by crystalline solids compared to the structure of molecules [13-15]. While the symmetry and property of crystals or ionic compounds are being generated according to their Bravais unit cell and space groups, point group symmetry and property are derived from the constituent atoms and bonds of the molecules [13]. Because of this, point group of a particular compound is usually contained by its space group [10, 15].

However, due to the periodicity of atoms in the crystal, translation wave vectors k which relate the direct lattice of a crystal to its reciprocal lattices in the Brillouin zone (BZ) [10, 15], and the Bloch function phase effect on the point group symmetry operation. The physical properties of crystals are described by the wave vector selection rule rather than the quantum mechanical rules which are only suitable for single atoms and molecules.

The nanostructure effect discussed in section 2.1 also applies to the phonon property of materials, when the crystal dimension is reduced to the nano-regime, the phonons experience quantum confinement by exhibiting strange vibrational properties compared to the ones observed in a bulk structure [16-20]. This phonon confinement phenomenon has been explained as the consequence of the Heisenberg's uncertainty principle where the change in the nanocrystal diameter ($\Delta d \rightarrow 0$), and change in the ($\Delta q \rightarrow \infty$) resulting in $q \neq 0$, unlike in the case of bulk crystal where ($\Delta d \rightarrow \infty$) and ($\Delta q \rightarrow 0$) resulting in $q = 0$ (allowing the selection rule at $\Gamma = 0$ of the BZ) [16-20]. Physical evidence of phonon confinement is the asymmetric broadening of the Lorentzian-Gaussian peak usually observed in Raman experiments. More details about phonon confinement are presented in chapter three where the sensing mechanism of the in-situ Raman spectroscopy sensing is discussed.

2.3 Correlated Vanadium Oxides Systems

Vanadium oxides are a class of transition metals with several vanadium oxidation states ranging between +2 to +5 in general. These oxidation states usually lead to the formation of a variety of binary oxides of different ionic and valence states which include; VO (V^{2+}), V_2O_3 (V^{3+}), VO_2 (V^{4+}), and V_2O_5 (V^{5+}) [21-22]. They also lead to phases which are other members of the Magneli phase family [6-11] (V_nO_{2n-1}) namely; V_4O_7 , V_5O_9 etc., and phases with the general formula (V_nO_{2n+1}) such as V_3O_7 , V_4O_9 and V_6O_{13} [21-26] have played significant impact on current research in the optical and electronic fields. These oxides are low mobility semiconductors with predominantly n-type conductivity and are classified among the groups

of metal-to-insulator transition (MIT) materials by Adler and Mott (1968) [27], drawing their conclusion from the theoretical distinctions between metal, semimetals, semiconductor and insulator proposed by Bethe (1928), Sommerfeld (1928), Bloch (1929), de Boer (1937) and Peierls (1937) [27]. Figure 2.2 presents the whole series of the vanadium-oxygen system's phase diagram showing different levels of oxygen defects and respective melting temperatures.

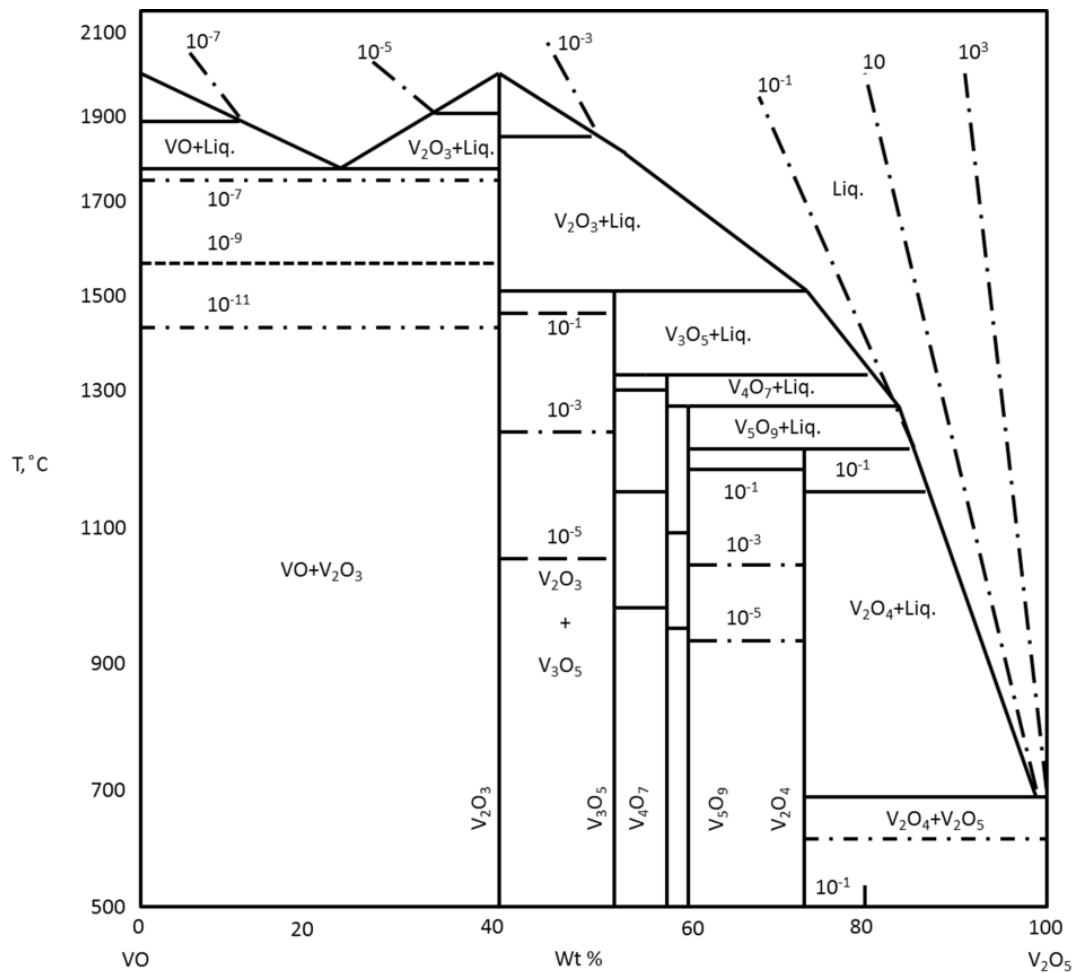


Figure 2.2: Phase diagram of Vanadium oxygen systems [22]

These oxides are fascinating among the class of transition metal oxide materials because of outstanding properties such as atomically well-defined geometry, surface chemical reactivity, oxygen defects, multiple valence state, adsorption properties, magnetic behaviour, optical switching and metal-to-insulator transition properties [21-27]. Numerous novel applications have benefited from the unique properties of vanadium oxides systems, among these, thermo-chromic smart/intelligent windows, electro-chromic windows, gas/chemical sensors, high temperature superconductivity, temperature or bolometer sensors, ultrafast switching devices, electrochemical devices and lithium ion battery applications [28]. This thesis focuses on VO_2 , V_6O_{13} and V_2O_5 which happen to be exceptional materials because of their band gap properties, MIT conductivity and significant impact they are playing on current research and the development of optical and electronic devices.

A summary of band gaps, transition temperatures and Fermi energies versus oxygen to vanadium ratio of semiconductors among the phases of vanadium oxides in Figure 2.2 is presented in Figure 2.3. These oxides are considered for sensing applications in this work because of their low electron mobility, low electron density and band gap compared with the traditional semiconductor materials like carbon and silicon. Among other interesting properties that influence our choice is the surface defect and various valence states that made possible chemical reactivity on their surface

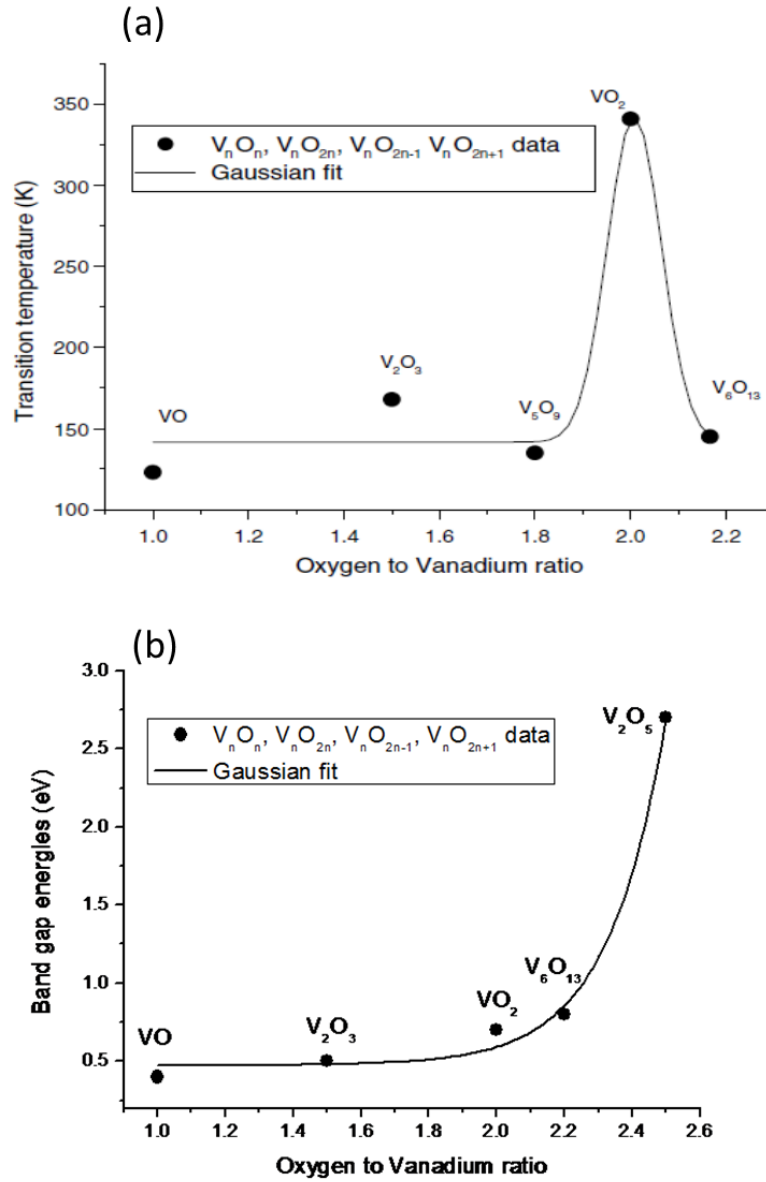


Figure 2.3: (a) Transition temperatures of a selected number of vanadium oxide phases as a function of the oxygen to vanadium ratio. A Gaussian fit shows the exclusivity of VO₂ in comparison with the other phases [29], (b) Band gap energy profiles of VO₂, V₂O₅, V₆O₁₃ and others shows exponential growth relationship with the oxygen to vanadium ratio.

2.4 Vanadium dioxide

Vanadium dioxide (VO₂) is a unique metal oxide inorganic material that exhibits first-order or reversible metal-to-insulator transition (MIT) as a function of temperature (i.e. its properties depend on temperature actuating function). The transition from metal-to-insulator in VO₂ happens around $T_c = \sim 340$ K as a critical temperature, and was first observed by Morin in 1959 [30]. VO₂ is metallic with a tetragonal phase at $T_c \geq 340$ K and an insulator with monoclinic semiconducting phase below the transition temperature T_c (i.e. < 340 K) with thermal hysteresis property of $\Delta T \approx 1$ K for bulk stoichiometric crystal of VO₂ [31-34].

This material has attracted considerable interest because of its unusual change or jumps in electrical conductivity and resistivity, optical transmission and reflections, morphology surface roughness, optical light scattering, Raman phonon intensity and surface plasmon resonance wavelength critically reviewed by Akande *et al* 2015 [23] and presented in Figure 2.4. Other interesting properties of VO₂ which were reported are the magnetic transition of magnetic moments and susceptibility using electron spin resonance (ESR) by Akande *et al* 2015 [23] and Nkosi *et al* 2016 [35].

Many ultrafast concepts like Thermal switch, Thermal sensor, Mott physics, Ultrafast switches for logic, Meta-materials, Chemical sensors, Quantum actuation, Tuneable materials, Spintronics, Solid-oxide fuel cell electrodes and neuromorphic computing have heavily relied on VO₂ properties for many years [28]. Energy technologies have also used

VO₂ properties especially in the smart or switchable window (thermo-chromic and photo-chromic technology) for environmental conditionings and energy savings [36] wherein VO₂ film reflects or blocks near infrared radiation (which is part of solar) in the metallic (tetragonal) phase and transmits or allows it in the semiconducting or insulating phase [36]. Sensor applications in the area of gases/chemicals (gaso-chromic property) [37] and cosmic microwave radiation (bolometer) [38] are also applicable. Electrochemistry technologies such as rechargeable lithium ion batteries and electro-chromic windows where VO₂/V₂O₅ is a hybrid with tungsten oxide to acts as a passive electrode [39]. Thermo-mechanical analysis applications such as thermal actuators and thermo-pneumatic actuators [40], all have benefited immensely from this material.

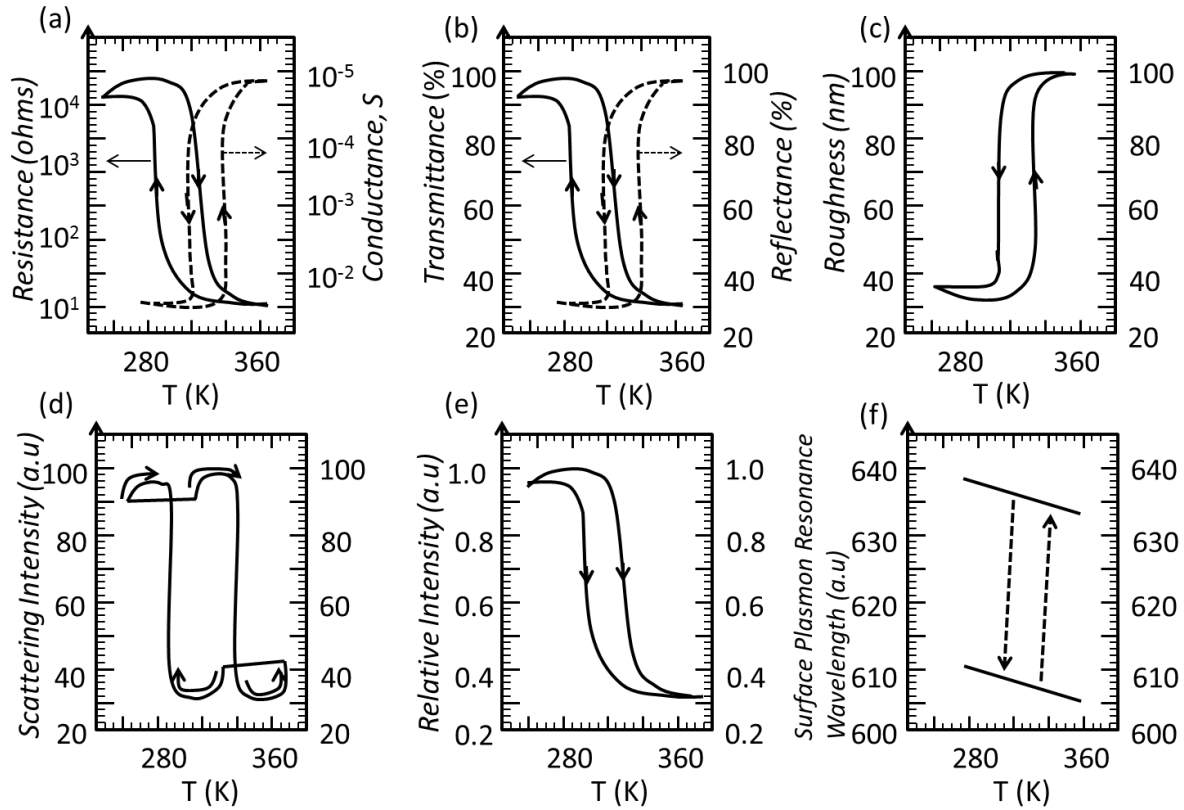


Figure 2.4: Resistance and Conductance, (b) Transmittance and Reflectance, (c) Roughness (d) Scattering, (e) Raman relative intensity of 618 cm^{-1} phonon frequency and (f) Surface Plasmon resonance wavelength [23].

Despite these strong and astonishing properties, motivations and devices obtained from VO_2 , physicist's understanding is still far from complete [41]. Many questions and controversies have risen among physicists as to whether the above hysteretic properties are due to Mott - Hubbard's theory of metal-to-insulator transition (MIT) (electron-to-electron correlations) or Peirerls's explanation of structural phase transition (SPT) (electron-to-phonon interaction) [41-42].

2.5 Transition Mechanism of Vanadium dioxide

2.5.1 Crystal Structure of VO₂

Rutile crystals of VO₂ (especially bulk structure) are isomorphic to TiO₂ crystals above the transition temperature T , with a body centred tetragonal lattice as shown in Figure 2.5 and space group $P4_2/mnm$ (D_{4h}^{14} , No. 136) [42 - 49]. The vanadium atoms (metal or cation V⁴⁺) are embedded in an octahedral of six oxygen atoms (non-metal or anions O²⁻). The octahedra form edge-shared chains along c_R -axis, and with the shortest V-V distance along this direction. The metal atoms V are located at the atomic positions Wyckoff (2a): (0, 0, 0), (½, ½, ½) and the non-metal atoms O occupy Wyckoff positions (4f): $\pm (u, u, 0)$, $\pm (½ + u, ½ - u, ½)$ with u value of 0.3001 for pure (un-doped) structures [40]. Translational symmetry influences the transformation of a body centred tetragonal lattice of VO₂ into a simple tetragonal lattice with parameters $a_R = b_R = 4.5546 \text{ \AA}$ and $c_R = 2.8514$ [41-49].

Below the transition temperature (at $T_c < 340 \text{ K}$), the tetragonal rutile structure Figure 2.5 distorts/tilts (with shear stress and small dilation of 0.044% [50]) and become monoclinic Figure 2.6 which is isomorphic to MoO₂ structure with space group $P2_1/c$ (C_{2h}^5 No. 14) [41, 42 - 49]. This distortion causes V-V pairs to emerge along the c_R -axis and the vanadium atom to the neighbouring vanadium atom separation of 2.872 \AA (which is c_R) to disproportionate into 2.62 \AA within V-V pair and 3.16 \AA between pairs. The axis of each pair is also shifted away from c_R to make a slight separation of V-O bonds. Lattice parameters for the monoclinic structure are $a_{MI} = 5.7434 \text{ \AA}$, $b_{MI} = 4.517 \text{ \AA}$, $c_{MI} = 2.8514$ and $\beta_{MI} = 122.61^\circ$ [41]. The metal atoms V and the two different types of oxygens mentioned above all occupy the same Wyckoff atomic positions as (4e): $\pm (x, y, \text{ and } z)$, $\pm (x, ½ - y, ½ + z)$ with different x , y , and z parameters [41]. Linking the unit cell of T and M_I phases together we can have $a_{MI} \leftrightarrow 2$

c_R , $b_{M1} \leftrightarrow a_R$ and $c_{M1} \leftrightarrow a_R - c_R$ [33, 41 - 47] which implies that the monoclinic crystallographic cell doubles that of tetragonal. There also exist an intermediate phase monoclinic M_2 between T and M_1 phases when VO_2 is doped with chromium, aluminium, titanium or tungsten.

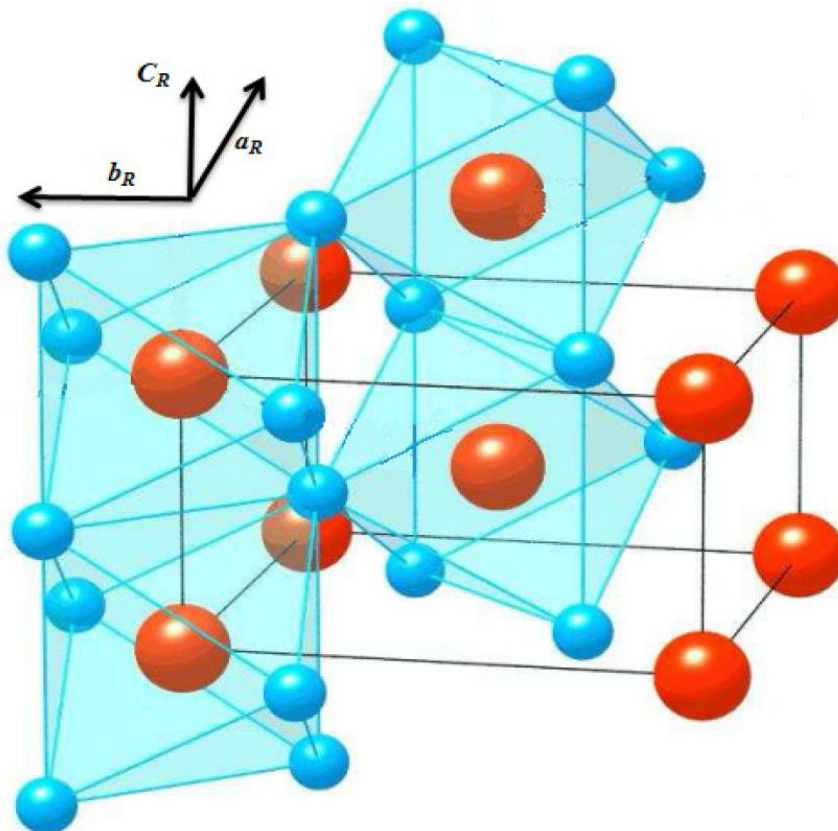


Figure 2.5: VO_2 Tetragonal (T) $P4_2/mnm$ (metallic) above or at 340 K [41]

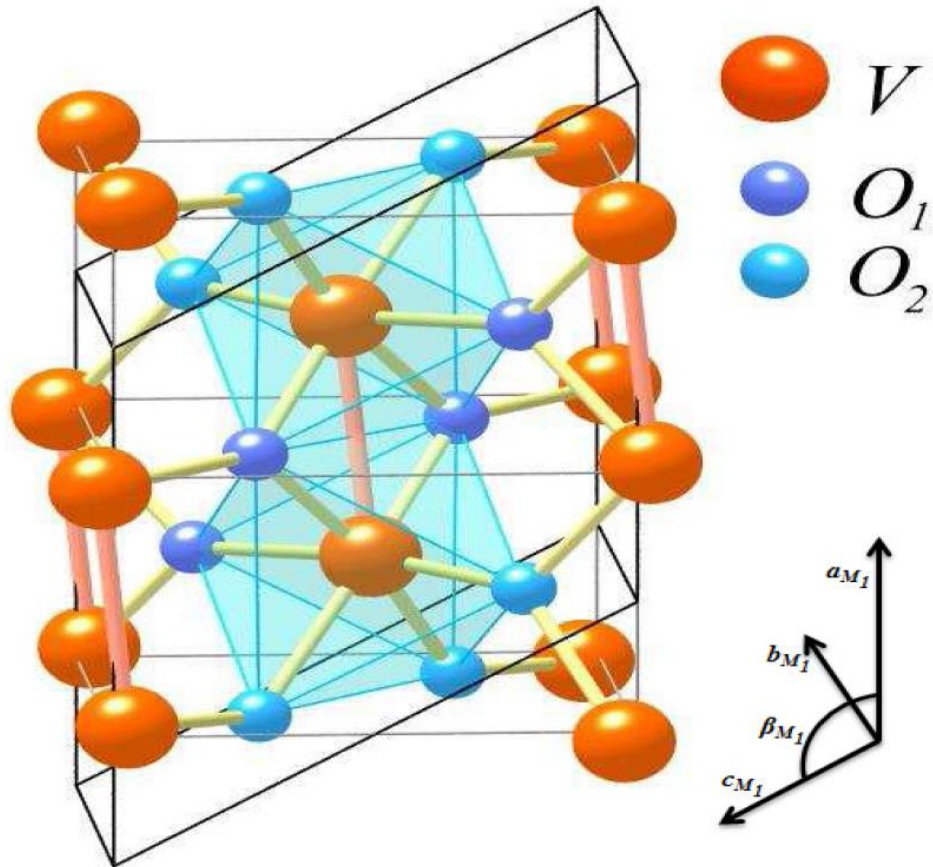


Figure 2.6: VO₂ monoclinic (M₁) $P2_1/c$ (insulator) below 340 K [41]

2.5.2 Electronic Structure of VO₂

Detailed explanation of electronic structure of VO₂ from the molecular picture proposed by Goodenough has been provided in Akande *et al* 2015 [23]. Vanadium dioxide's Fermi energy (E_F) usually falls above the top of the oxygen O²⁻ 2p band and below the vanadium 4s band [27, 33-34,] as illustrated in Figure 2.4. The vanadium atom with 3d orbital and V⁴⁺ valence state in the metallic (tetragonal) phase splits into two levels $d_{||}$ and π^* orbital comprising the electronic states near Fermi level. The $d_{||}$ is nonbonding (anti-bonding), while the π^* orbitals are strongly hybridized with oxygen O 2p π and consequently lie in a higher level than $d_{||}$. The insulating (monoclinic) phase is different in that the pairing of the V⁴⁺ atom along the c_R -axis pushes the 3d-2p hybridization and up-shifts the π^* band away from the Fermi, causing

the bonding and anti-bonding splitting of the $d_{||}$ which is classified as the opening of band of ≈ 0.7 eV band gap [27]. Goodenough and Hong (1971) also made some useful suggestions which are relevant to the explanation of the two phases of VO_2 . These suggestions are based on its molecular orbitals and the band gap diagram. They considered anti-ferroelectric transition as a potential driving force for MIT in VO_2 . It was proposed that $\text{V}^{4+} - \text{V}^{4+}$ pairing in the tetragonal rutile (metallic) phase is energetically stable above the transition temperature upon heating, followed by the rearrangement of the band structure to give the monoclinic (insulating) phase at a lower temperature upon cooling [34, 51]. Their studies revealed that the anti-ferroelectric nature of monoclinic (insulating phase) of VO_2 is the driving force of the crystal distortion, and concluded that the transition temperature T_c is not controlled by thermal excitation of electrons into the anti-bonding bands, but by the entropy of the lattice vibration modes [51].

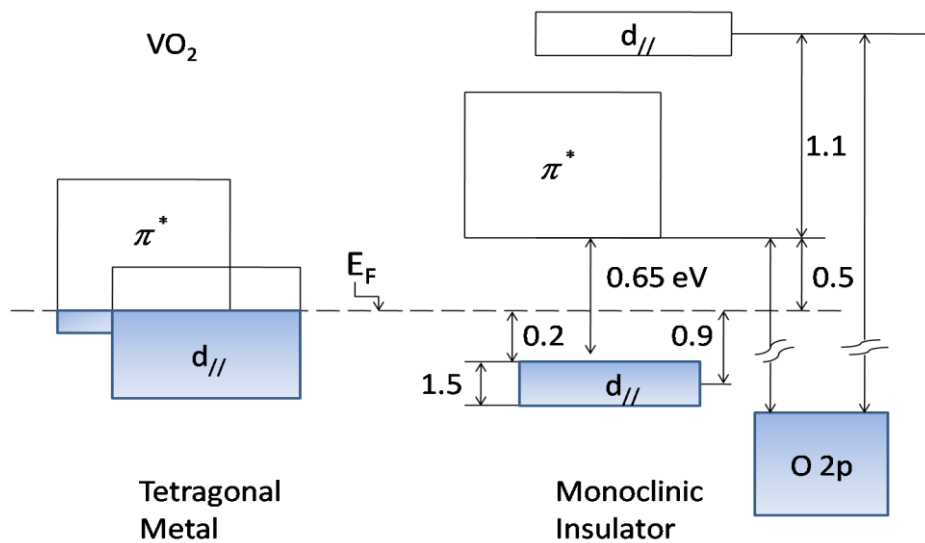


Figure 2.7: VO_2 Tetragonal (T) $P4_2/mnm$ (metallic) above or at 340 K [23, 32]

2.5.3 Phonon band structure of VO₂

The change in the crystallographic structure of VO₂ around the MIT regime makes it exhibit two different Brillouin zone (BZ) and symmetry paths. Figure 2.8 illustrates the first BZ of both stable tetragonal and distorted monoclinic phases. The VO₂ structure contains 3 atoms in 3 degrees of freedom (x, y, and z) occupying 2 atoms per unit cell ($Z = 2$). Group theory predicts 18 total modes, 15 optical zone-centre modes and 3 ground state acoustics modes at wave vector $q = 0$ ($\Gamma = 0$) in the Brillouin zone according to the lattice mode representation and by acting 4 symmetry elements. These 15 optical zone-centre modes are determined by factor group analysis and selection rule for C_{2h} point group for low temperature phase monoclinic, $P2_1/C_{2h}^5$ (No. 14). The symmetry elements are E, $C_2(z)$, I and $\sigma(xy)$, where E is the identity, $C_2(z)$ is 180° rotation in the z axis, I is the inversion and $\sigma(xy)$ is mirror in the horizontal plane. These 15 modes have been reported to compose A_{1g} , B_{1g} , B_{2g} and B_{3g} Raman modes which were distributed in different configurations [52-58]. High temperature phase tetragonal, $P42/mnm$ (D_{4h}^{14} , No. 136) has 4 modes distributed in A_{1g} , B_{1g} , B_{2g} and E_g symmetries [52-55]. Phonon band structures or dispersion curves of the two phases have been calculated showing their phonons energies and assignments of different modes. These phonon energy distributions and temperature dependent Raman spectroscopy experiments have been used to study the MIT mechanism [52-59].

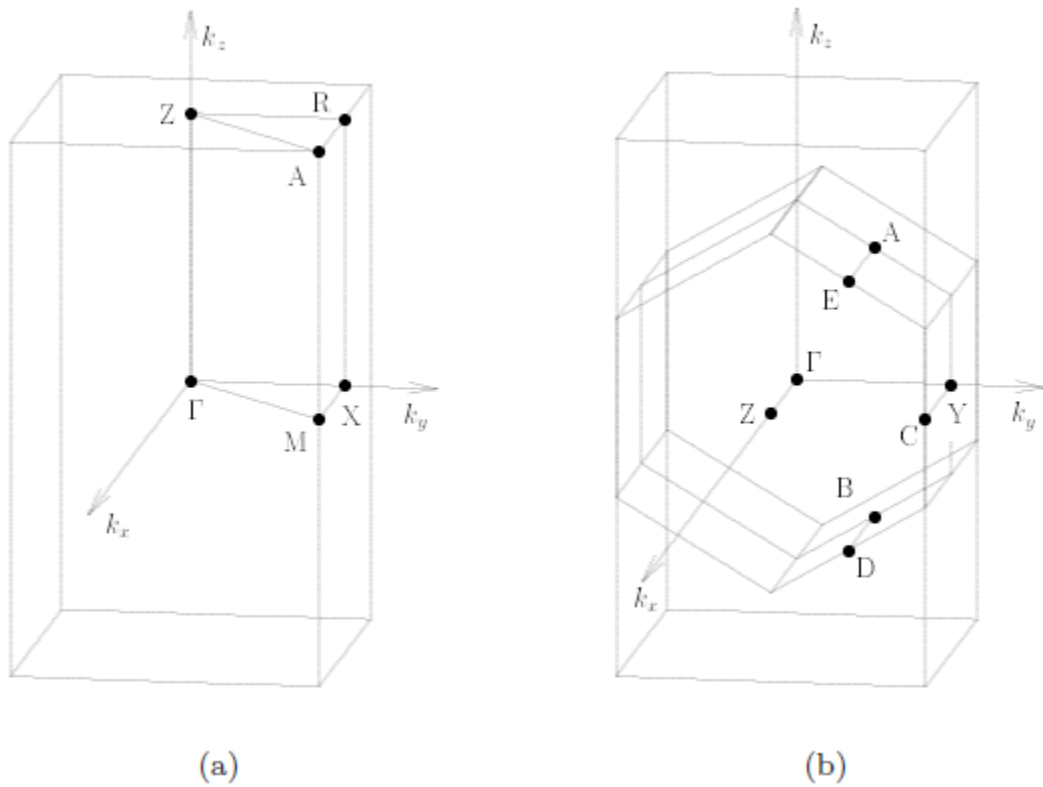


Figure 2.8: First Brillouin zone of (a) tetragonal, and (b) monoclinic structures [41]

2.6 Vanadium pentoxide (V_2O_5)

2.6.1 V_2O_5 Crystallographic, Electronic and Phonon structures

Other oxides of vanadium presented in the Figure 2.2 are also relevant; being members of Magneli (V_nO_{2n-1}) and Wadsley (V_nO_{2n+1}) functional groups. Vanadium sesquioxide or trioxide (V_2O_3), vanadium oxide (V_6O_{13}) and vanadium pentoxide (V_2O_5) are the most relevant phases because of their semiconductor properties (Figure 2.2). The vanadium sesquioxide (V_2O_3 , in V^{3+} ionic state) is close to VO_2 stoichiometry but with some oxygen defects (Figure 2.2), the crystal of V_2O_3 also exhibits first order MIT as the temperature is lower to $T_c \sim 150$ K. The crystallographic transition from α -corundum to monoclinic is usually followed by a change in electrical resistivity and transition from paramagnetic to

antiferromagnetic material [21-28, 60-61]. Electrochemical application of V_2O_3 has also been reported [62].

V_2O_5 macroscopic bulk crystal structure, nanostructure and the one whose radius is comparable with Debye length is thermodynamically favoured as the orthorhombic unit cell at ambient conditions. V_2O_5 has highest oxygen concentration among all other vanadium oxide members; its crystallographic atomic arrangement gives room for corner-sharing and edge-sharing VO_5 octahedral geometry layered structure forming VO_5 pyramids edges sharing networks with opposite orientations to maximize distances between V-V cations as represented in Figure 2.9 [26]. It has space group $Pmmn$ (D_{2h}^{13} No. 59) and lattice parameters $a = 11.510 \text{ \AA}$, $b = 3.563 \text{ \AA}$ and $c = 4.369 \text{ \AA}$ where b and c are frequently interchanged in the orthorhombic system [62-63]. V_2O_5 is also a member of Mott Hubbard's metal-to-insulator transition materials with MIT temperature of $\sim 375 \text{ }^\circ\text{C}$ [24], but with no structural change during MIT behaviour. This oxide has been extensively studied for technological application because of its thermodynamic stability and the fact that it is easy to produce.

One of the major highlights of this thesis which has also been reported to the gases and chemicals sensing communities is the unusual performances of V_2O_5 surfaces to gases, chemicals, VOCs and water vapour [64]. This work explored the sensing properties V_2O_5 , VO_2 and their mixtures V_6O_{13} .

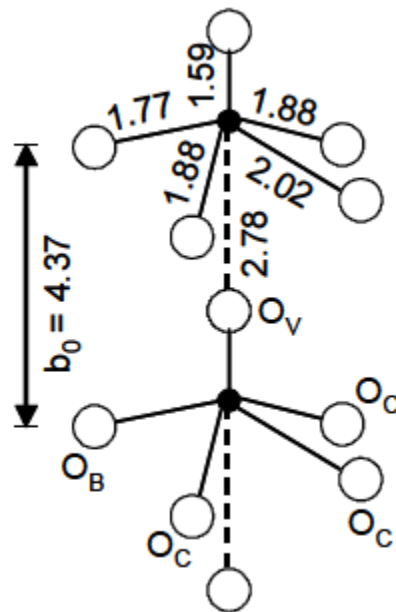


Figure 2.9: Local coordination of vanadium and oxygen atoms in the Pmm (D_{2h}^{13} No. 59) lattice indicating the crystal axes and nearest-neighbour distances. The solid circles in the centre represent a vanadium atom which is surrounded by three different types of oxygen; O_V – vanadyl oxygen, O_B – bridge oxygen and O_C – chain oxygen respectively [65]

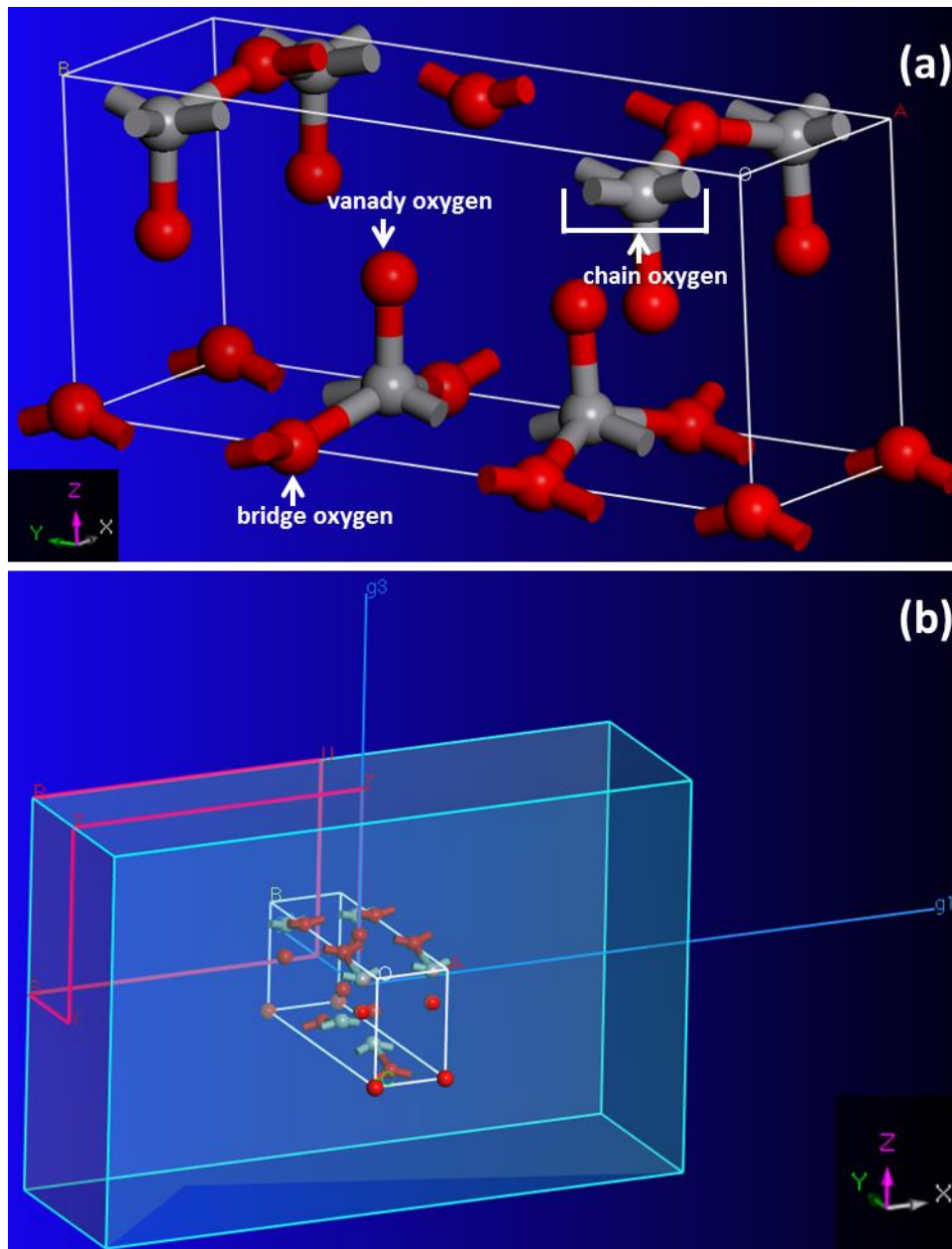


Figure 2.10: (a) Unit cell of Orthorhombic Pmm (D_{2h}^{13} No. 59) lattice. The atoms with the grey colours are the vanadium atoms and the ones with red colours are oxygen atoms. (b) Brillouin Zone of the structure.

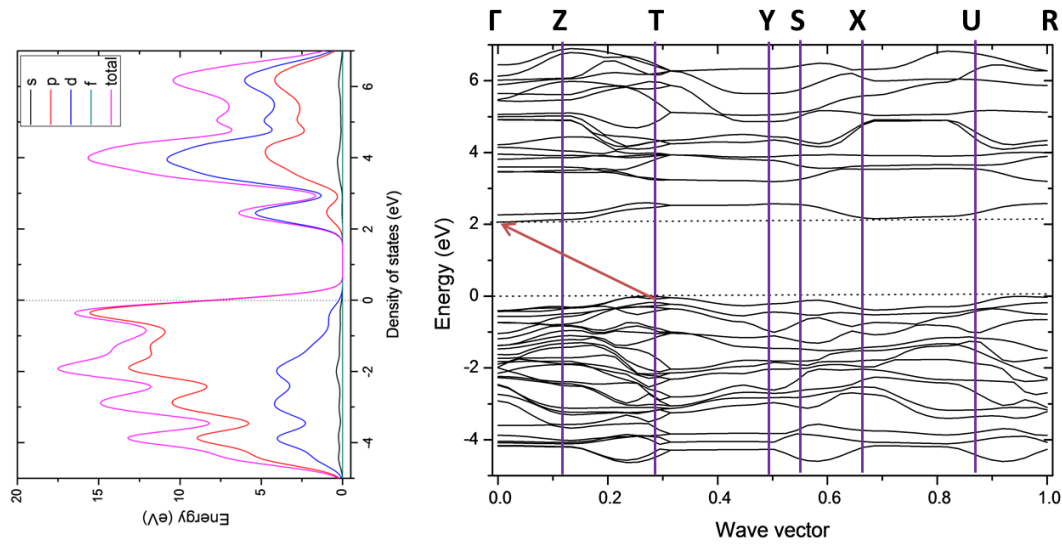


Figure 2.11: Band structure and partial density of states (PDOS) profiles of Figure 2.10. The brown arrow ($T \rightarrow \Gamma$) in the band structure profile indicates where the indirect band gap lies.

According to the international crystallographic tables, coordination of atoms (Figure 2.8) and density functional approximation records [62-63, 65], the stoichiometric orthorhombic V_2O_5 structure should have four types of atoms in terms of their geometry coordination i.e. by their nature of bonding and bond length. One vanadium atom V and three different oxygen atom O (1) O (2) and O (3) are located at different Wyckoff positions. V atom together with O (1) and O (3) occupy $4f$ Wyckoff position with cite symmetry C_s whereas O (2) atom can occupy $2a$ Wyckoff position with cite symmetry of C_{2v} [62-63, 65]. High symmetry orthorhombic lattice of V_2O_5 crystal structure with two formula per unit cell ($Z = 2$) contains a total of 42 optical and acoustic modes. using factor group analysis, selection rules for D_{2h} point group and the following symmetry elements; E , $C_2(z)$, $C_2(y)$, $C_2(x)$, i , $\sigma(xy)$, $\sigma(xz)$ and $\sigma(yz)$ where E is the identity, $C_2(z)$, $C_2(y)$, $C_2(x)$ are 180° rotation in the x , y and z axes respectively, I is the inversion, $\sigma(xy)$ is horizontal mirror and $\sigma(xz)$, $\sigma(yz)$ are vertical mirrors. The 42 modes are reduced to 39 optical-zone centre modes after taking the 3 ground state modes which are acoustic at $\Gamma = 0$ symmetry point of the BZ.

The electronic band structure (EBS) and PDOS of V_2O_5 is presented in Figure 3.11 showing an indirect transition of electrons between HOMO (valence band) and LUMO (conduction band) from $T \rightarrow \Gamma$ symmetries within the BZ. This is clear evidence of the role of phonons in the electronic and optical transitions of V_2O_5 structure. The calculated indirect band gap (E_g) ≈ 2.2 eV, is consistent with the experimental values [66]. These EBS and PDOS results are generated from the simple orthorhombic lattice shown in Figure 2.10 (a) and the corresponding BZ in Figure 2.10 (b).

2.7 Vanadium oxide (V_6O_{13})

2.7.1 Crystallographic, Electronic and Phonon structures of V_6O_{13}

Vanadium oxide (V_6O_{13}) exists as mixed valence/ionic state of VO_2 and V_2O_5 . Its stoichiometry falls between the stable V_2O_5 and VO_2 as shown in Figure 2.3, hence often referred to as metastable phase of vanadium oxide. This oxide maintains monoclinic crystallographic structure at both high temperature (space group - $C2/m$ C_{2h}^3) and low temperature $P2_1/$ (C_{2h}^5) with MIT property at $T_c \sim 130$ K [67-70]. The two monoclinic structures slightly differ in lattice parameters with $a = 11.921$ Å, $b = 3.6811$ Å and $c = 10.147$ Å, $\beta = 100.88^\circ$ for the high temperature phase (room temperature) and $a = 11.963$ Å, $b = 3.707$ Å and $c = 10.064$ Å, $\beta = 100.96^\circ$ for the low temperature phase [67-70].

Figure 2.12 (a) presents the monoclinic $C2/m$ C_{2h}^3 structure of the room temperature phase of V_6O_{13} . This structure shows that V_6O_{13} crystalizes in zig-zag string chain layers as orthorhombic V_2O_5 structure shown in Figure 2.10 (a) but with displacement as a consequence of transformation from orthorhombic to monoclinic system [67-68]. This displacement formed double zig-zag ribbon structures shown in Figure 2.12 (b) as opposed to

the single zig-zag string of the orthorhombic V_2O_5 structure [68]. There are three vanadium and seven oxygen atoms in V_6O_{13} structure each occupying different sites in the unit cell Figure 2.12 (b). According to the group theoretical analysis, V_6O_{13} monoclinic $C2/m C_{2h}^3$ crystal contain 114 atoms which includes 3 atoms in the 3 degree of freedom (x, y, and z) occupying 2 atoms per unit cell ($Z = 2$). The optical modes in the centre of the Brillouin zone can be classified as $\Gamma = 18A_{1g} + 9B_g + 9A_u + 18 B_u$, 27 Raman active modes ($18A_{1g} + 9B_g$), 27 IR active modes ($9A_u + 18B_u$) and 3 ground state acoustic modes [67]. This oxide is well known for electrochemistry applications (lithium ion and sodium ion battery) and catalysis application [39, 67-71]. In this thesis, room temperature phase of V_6O_{13} structure is reported for the first time for sensing applications.

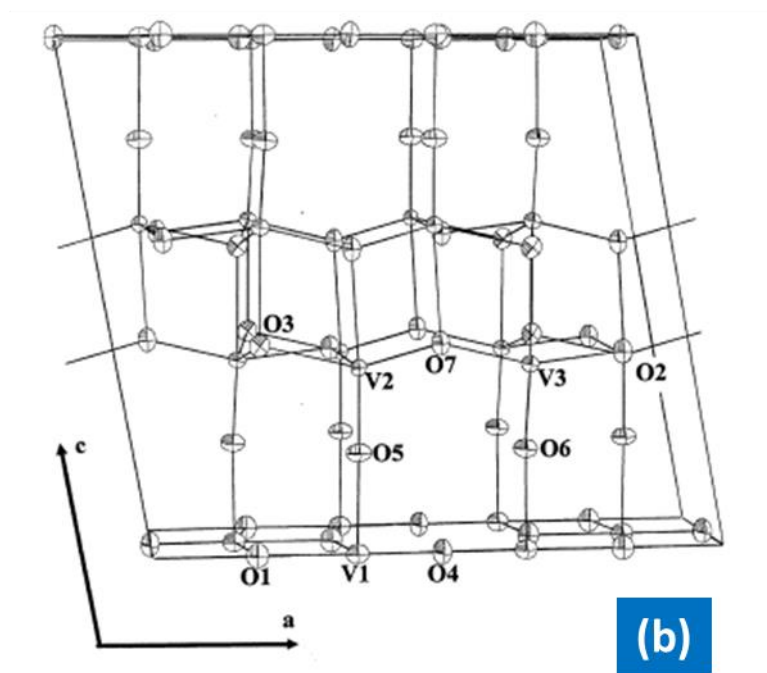
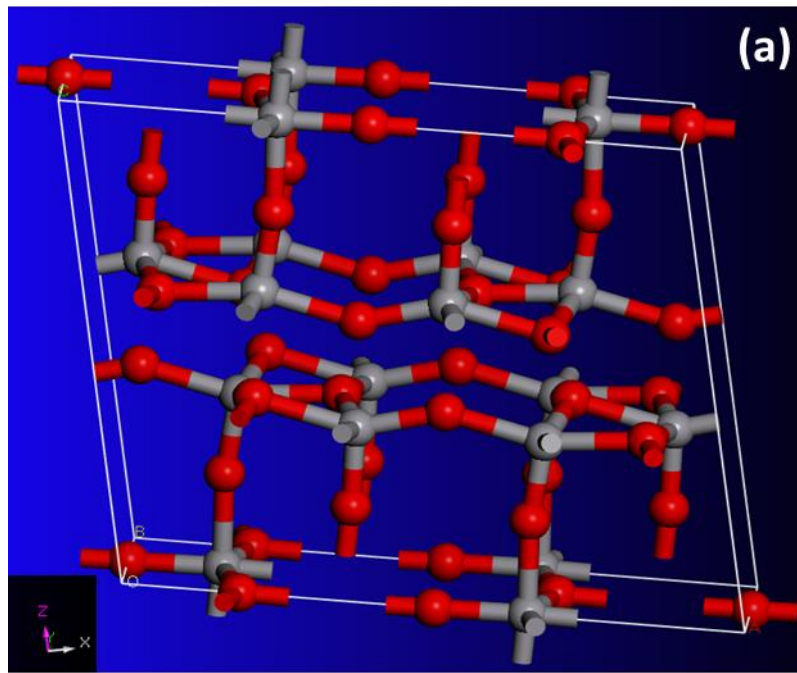


Figure 2.12: (a) Unit cell of monoclinic lattice $C2/m C_{2h}^3$. The atoms with the grey colours are the vanadium atoms and the one with red colours are oxygen atoms. (b) 2D structure in a - c plane showing the local coordination of vanadium and oxygen atoms [68].

2.8 Surface structures of VO₂, V₂O₅ AND V₆O₁₃

Surface properties of vanadium oxides are important when applied as sensing electrodes for detection of chemicals and water vapour. These properties are the layer structures (vanady group configuration), valence states, index cleavage or facet, surface termination, surface relaxation, density of state, surface oxygen emission and hydrogen induced defects [72]. Adsorption studies of the (001) surface of V₂O₅ by high resolution electron energy loss spectroscopy (HREELS) and angle-resolved photoemission spectroscopy (UPS) show hydrogen induced defects and terminations of certain bonds (vibrations) in the surface [73]. This has been reported in catalysis research for hydrocarbon reaction and can also influence the sensing properties of the surface [72-74]. Techniques like low energy electron diffraction, X-ray photoelectron spectroscopy and soft X-ray emission spectroscopy have also been applied to study these properties [72]. This work also applies density functional theory to study the surface adsorption of V₆O₁₃ and V₂O₅ to H₂S, NH₃ and NO₂ molecule.

References

- [1] R.P. Feynman, Plenty of Room at the Bottom, American Physical Society 1959.
- [2] H. Brune, M. Giovannini, K. B. Bromann, K. Kern, Self Organized growth of nanostructures arrays on strain-relief patterns, *Nature* **394**, 451-453, (1998)
- [3] E.I. Roduner, Size matters: why nanomaterials are different, *Chem. Soc. Rev.* **35**, 583-592, (2006)
- [4] H. Kwang , L. Hyungwoo , J. Jikang , L. Dong-Jin , P. Yongju , L. Changhee , L. Byung Yang, H. Seunghun, Bi-Assisted CdTe/CdS Nanostructure Growth for Photoconductive applications, *Nano Scale lett.* **10**, 133, 1-7(2015)
- [5] X. J. Zhao, W.W. Shan, H. He, Xinlian Xue, Z. X. Guoc, S. F. Li, From single atoms to self-embedded single atomic nanowires: noble metal atoms on black phosphorene monolayers, *Phy. Chem. Chem. Phy.* **19**, 11 7864-7870, (2017)
- [6] J. Wu X. Caoc, Growth of bismuth oxyhalide nanoplates on self-standing TiO₂ nanowire film exhibiting enhanced photoelectrochemical performances, *Electrochemical Acta* Vol **249**, 1, 646-656, (2017)
- [7] J. M. Yang, H. Yu, B. Xiao, Z. Li, M. Zhang, MOF derived hollow NiO-ZnO composite micropolyhedra and their application in catalytic thermal decomposition of ammonium perchlorate, *Russia J. Phy. Chem.* **91**, 7, 1214-1220, (2017)
- [8] B. W Mwakikunga, Nano-size Effects on Opto-Electronic, Structural and Vibrational Properties of Vanadium and Tungsten Oxides Produced by Laser and Ultrasonic Spray Pyrolysis Techniques, PhD Thesis (2009), University of the Witwatersrand Johannesburg.

- [9] S. Bose, R. Banerjee, A. Genc, P. Raychaudhuri, H. L. Fraser P. Ayyub, Size induced metal–insulator transition in nanostructured niobium thin films: intra-granular and inter-granular contributions, *J. Phys: Cond. Matt.* **18**, 4553-4566, (2006)
- [10] A. G. J. Machatine, Vibrational and Electronic States of Sapphire and Wurtzite ZnO, PhD Thesis (2010), University of Pretoria.
- [11] H. W. Kunert, M. Govender, A. G. J. Machatine, B. W. Mwakikunga, P. Niyongabo, Optical selection rules and scattering processes in rocksalt wide band gap ZnO, *Phys. Sta. Solidi* **211**, 2, 435-439, (2014)
- [12] A. G.J. Machatine, h.w. Kunert, A. Hoffmann, J. B. Malherbe, J. Barnas, R. Seguin, M.R Wagner, P. Niyongabo, N. Nephale, Phonons and electronic states of ZnO, Al₂O₃ and Ge in the presence of time reversal symmetry, *J. Phys. Conf. Series* **92**, 012071, (2007)
- [13] David Tuschel, Practical Group theory and Raman spectroscopy, Part 11; Application of Polarization, *Spectroscopy* **29** 3, 14-22, (2014)
- [14] Fran Adar, Raman spectra of Metal Oxides, *Spectroscopy* **29**, 10, 16-22, (2014)
- [15] M. S. Dresselhaus, Application of Group Theory to the Physics of Solids, Spring 2002.
- [16] K. W. Adu , H. R. Gutiérrez , U. J. Kim , G. U. Sumanasekera , P. C. Eklund, Confined Phonons in Si Nanowires, *Nano Lett.* **5**. 3. 409 – 414, (2005).
- [17] A. K. Arora, M. Rajalakshmi, T. R. Ravindran, V. Sivasubramanian, Raman spectroscopy of optical phonon confinement in nanostructured materials, *J. Ram. Spec.* **38**, 604-417, (2007).
- [18] P. M. Fauchet, I.H. Campbell, Raman spectroscopy of low dimensional semiconductors, *Critical Review in Solid State Material Science, Solid State. Mat.* **14**, 79-101, (1988)

- [19] B W Mwakikunga, M. Maaza, K.T. Hillie, C.J. Arendse, T. Malwela, E. Sideras-Haddad
From phonon confinement to phonon splitting in flat single nanostructures: A case of
 $\text{VO}_2@V_2O_5$ core-shell nano-ribbons, *J. Vib. Spec.* **02**, 105-111, (2012)
- [20] B. W. Mwakikunga, E. Sideras-Haddad, A. Forbes, C.J. Arendse, Raman spectroscopy
of WO_3 nano-wires and thermos-chromism study of VO_2 belts produced by ultrasonic spray
and laser pyrolysis technique, *Phy. Stat. Sol.* **205**, 1, 150-154 (2008)
- [21] U. Schwingenschlögl, V. Eyert, The vanadium Magnéli phases V_nO_{2n-1} , *Ann. Phys.*
(Leipzig) **13**, 9, 475 (2004).
- [22] C. H Griffith, HK Eastwood, Influence of stoichiometry on metal-semiconductor
transition in vanadium dioxide, *J. Appl. Phys.* **45**, 2201 (1974).
- [23] A.A. Akande , K. E. Rammutla, T. Moyo, N. S.E. Osman, Steven S. Nkosi, C.J. Jafta,
B. W. Mwakikunga, Magnetism variations and susceptibility hysteresis at the metal-insulator
phase transition temperature of VO_2 in a composite film containing vanadium and tungsten
oxides, *J. Magn. Magn. Mater.* **375**, 1-9, (2015).
- [24] A.A. Akande, E.C Linganiso, B.P Dhonge, K.E. Rammutla, A. Machatine, L. Prinsloo,
H. Kunert, B.W. Mwakikunga, Phase Evolution of vanadium oxides obtained through
temperature programmed calcinations of ammonium vanadate in hydrogen atmosphere and
their humidity sensing, *J. Mat. Chem. Phys.* **151**, 206, (2015)
- [25] X. Chen, X. Wang, Z. Wang, J. Wan, and J. Liu, Y. Qian, An ethylene glycol
reduction approach to metastable VO_2 nanowire arrays, *Nanotech.* **15**, 11, 1685-1687,
(2004)
- [26] M.C. Rao, Vanadium Pentoxide Cathode Material for Fabrication of All Solid State Lithium-
Ion Batteries - A Case Study, *Res. J. Recent Sci.*, **2**, 3, 67-73, (2013).

- [27] M. Imada, A. Fujimori, Y. Tokura, Metal-insulator transitions, *Rev. Modern Phys.* **70**, 4, (1998).
- [28] Z. Yang, C. Ko, S. Ramanathan, Oxide Electronics Utilizing Ultrafast Metal-insulator transition, *Ann. Rev. Res.* **41**, (2011)
- [29] B.W. Mwakikunga, E. Sideras-Haddad and M. Maaza, First synthesis of vanadium dioxide by ultrasonic nebula-spray pyrolysis, *Optical Materials* **29**, 481–487, (2007)
- [30] F.J. Morin, Oxides which show a metal-insulator-transition at Neel temperature, *Phys. Rev. Lett.* **3**, 34-36, (1959).
- [31] N.F. Mott, Metal-insulator Transition, *Rev. Modern Phys.* **40**, 4, 677 - 683, (1968).
- [32] D. Adler, Mechanisms for Metal-Nonmetal Transitions in Transitions-Metal Oxides and Sulfides, *Rev. Modern Phys.* **40**, 4, 714 – 736, (1968).
- [33] J.B. Goodenough, The two components of Crystallographic transition in VO₂, *J. Solid State Chem.* **3**, 490 – 500, (1971).
- [34] J.B. Goodenough and H.Y. Hong, Structure and a Two-Band Model for the System V_{1-x}Cr_xO₂, *Phys. Rev. B* **8**, 4, 1323-1331, (1972).
- [35] S.S Nkosi, S. Lafana, B. Masina, O. M. Ndwadwe, The control of magnetism near metal-to-insulator transition of VO₂ nano-belts, *All. Comp.* **689**, 313-317, (2016)
- [36] Y. Gao, H. Luo, Z. Zhang, L. Kang, Z. Chen, J. Du, M. Kanehira and C. Cao, Nanoceramic VO₂ thermochromic smart glass: A review on progress in solution processing, *Nano Energy*, **1**, 221-246(2012).

- [37] E. Strelcov, Y. Lilach and A. Kolmakov, Gas Sensor Based on Metal-Insulator Transition in VO₂ Nanowire Thermistor, *Nano Lett.*, Vol. **9**, No. 6, 2322-23269 (2009)
- [38] N.Sung-Pill, L. Sung-Gap, B. Seon-Gi and L. Young-Hie, Structural and Electrical Properties of Vanadium Tungsten Oxide Thin films Grown on Pt/TiO₂/SiO₂/Si substrates, *J. Cer. Procc. Res.* **10**, 2, 224-226- 76, (2009)
- [39] C.G. Granqvist, Electrochromic tungsten oxide films: Review of progress 1993- 1998, *Solar Energy Mat. Solar Cells* **60**, 201- 262, (2000)
- [40] E. Merced, X. Tan and N. Sepúlveda, Strain energy density of VO₂-based microbolometer, *Sen. Act. A* **196**, 30-37, (2013)
- [41] V Eyert, The metal-insulator transitions of VO₂: A band theoretical approach, *Ann. Phys. (Leipzig)* **11**, 9, 1-61 (2002).
- [42] S. Kumar , J. P. Strachan, M. D. Pickett , A. Bratkovsky , Y. Nishi , R. S. Williams, Sequential Electronic and Structural Transitions in VO₂ Observed Using X-ray Absorption Spectromicroscopy, *Adv. Mat.* **26**, 7504-7509, (2014)
- [43] S. Chen, J. Liu, H. Luo, Y. Gao, Calculation Evidence of Staged Mott and Peierls Transitions in VO₂ Revealed by Mapping Reduced-Dimension Potential Energy Surface, *J. Phy. Chem. Lett.* **6**, 18, 3650-3656, (2015)
- [44] A. D Burton, P. A Cox, A model for electroic structure of VO₂, *Philos. Mag. B* **51**, 2, 255-261, (1985).
- [45] G Andreson, Studies on vanadium oxides. II the crystal structure of vanadium dioxide, *Acta. Chem. Scand.* **10**, 623-628, (1956).
- [46] C. N Berglund, H. J Guggenheim, Electronic properties of VO₂ near the semiconductor-metal transition, *Phys. Rev.***185**, 3, 1022 (1969).

- [47] J. C. Rakotoniaina, R. Mokrani-Tamellin, J. R. Gavarrri, G. Vacquier, A. Casalot, G. Calvarin, The thermochromic vanadium dioxide: I. Role of stresses and substitution on switching properties, *J Solid State Chem.* **103**, 1, 81-94 (1993).
- [48] J. M. Longo, P. Kierkegaard, "A refinement of the structure of VO₂, *Acta Chem. Scand.* **24**, 420-426 (1970).
- [49] J. B. Goodenough, The two components of the crystallographic transition in VO₂, *J. Solid state Chem.* **3**, 4, 490 (1971).
- [50] M. Maaza, K. Bouziane, J. Maritz, D.S. McLachlan, R. Swanepool, J.M. Frigerio, M. Every, Direct production of thermochromic VO₂ thin film coatings by pulsed laser ablation, *Optical Materials*, **15**, 41-45 (2000)
- [51] P. Kiria, G. Hyettb, R. Binions, Solid state thermochromic materials, *Adv. Mat. Lett.* **1**, 2, 86 – 105, (2010).
- [52] R. Srivastava, L. Chase, Raman spectrum of semiconducting and metallic VO₂, *Phys. Rev.* **27**, 11, 727, (1971)
- [53] F. Gervais, Lattice dynamics of oxides with rutile structures and instability at the meta-semiconductor phase transition of NbO₂ and VO₂, *Phys. Rev.* **31**, 8, 4809, (1985)
- [54] J. R. Brews, Symmetry Considerations and the Vanadium Dioxide Phase Transition, *Phys. Rev.* **1**, 6, (1970) 2557
- [55] A. Cavalleri, T. Dekorsy, H. H. W Chong, J. C. Keiffer, R. W. Schoenlein, Evidence for a structurally-driven insulator-to-metal transition in VO₂: A view from the ultrafast timescale", *Phys. Rev. B* **70**, 161102 (2004).

- [56] J. D. Budai, J. Hong¹, M. E. Manley, E. D. Specht, C. W. Li, J. Z. Tischler, D. L. Abernathy, A. H. Said, B. M. Leu, L. A. Boatner, R. J. McQueeney, O. Delaire, Metallization of vanadium dioxide driven by large phonon entropy, *Nature* **515**, 535-539, (2014)
- [57] G.I. Petrov, V.V. Yakovlev, Raman microscopy analysis of phase transformation mechanisms in vanadium dioxide, *App. Phys. Lett.* **81**, 6, 1023-1025, (2002).
- [58] M. Pan, J. Liu, H-M. Zhong, S-W. Wang, Z-F. Li, X-S. Chen and W. Lu, Raman study of the phase transition in VO₂ thin films *J. Cry. Growth* **268**, 178–183, (2004)
- [59] N. Kuroda, H.Y. Fan, Raman scattering and phase transitions of V₂O₃, *Phys. Rev.* **16**, 11, 5003-5006, (1977)
- [60] X.B. Chen, J.H. Shin, H.T. Kim, Y.S. Lim, Raman analyses of co-phasing and hysteresis behaviours in V₂O₃ thin film, *J. Raman Spectrosc.*, **43**, 2025–2028, (2012)
- [61] Y. Zhang, M. Fan, X. Liu, C. Huang, and H. Li, Beltlike V₂O₃@C Core–Shell-Structured Composite: Design, Preparation, Characterization, Phase Transition, and Improvement of Electrochemical Properties of V₂O₃, *Eur. J. Inorganic. Chem.*, **2012**, 10, 1650–1659, (2012)
- [62] S. Laubach, P. C. Schmidt, A. Thiben, F. J. Fenandez-Madrigal, Q. Wu, W. Jaegemann, M. Klemm, S. Horn, Theoretical and Experimental determination of the electronic structure of V₂O₅, reduced V₂O_{5-x} and sodium intercalated NaV₂O₅, *Phys Chem. Chem. Phys* **9**, 2564 (2007)
- [63] B. Zhon, D. He, Raman spectrum of vanadium pentoxide from density-functional perturbation theory, *J Raman Spec.* **29**, 10, 1475-1481, (2008)
- [64] J. Huotari, A.L. Spetz, J. Lappalainen, Gas Sensing Properties of Pulsed Laser Deposited Vanadium Oxide Thin Films, The 14th International Meeting on Chemical Sensors, IMCS (2012).

- [65] O. Sipr, A. Simunek, S. Bocharov, Th. Kirchner, G. Drager, Geometric and electronic structure effects in polarized V K-edge absorption near-edge structure space of V_2O_5 , *Phys. Rev.* **60**, 20, 14115-14127 (1999)
- [66] G. T. Mola, E. A. A. Arbab, B. A. Taleatu, K. Kaviyarasu, I. Ahmad, M. Maaza. Growth and Characterization of V_2O_5 thin film on Conductive electrode, *J. Microscopy*, **265**, 2, 214-221, (2017).
- [67] C. Julien, G.A. Nazri and O. Bergstrom, Raman Scattering Studies of Microcrystalline V_6O_{13} , *Phys. Stat. Solidi B* **201**, 319-326 (1997).
- [68] O. Bergstrom, T. Gustafsson, J. O. Thomas, Electrochemically Lithiated Vanadium Oxides $Li_3V_6O_{13}$, *Sol. Stat. Ionic* **110** 179-186, (1998)
- [69] R. Eguchi, T. Yokoya, T. Kiss, Y. Ueda, S. Shin, Angle-resolved photoemission study of the mixed valence oxide V_6O_{13} : Quasi-one-dimensional electronic structure and its change across the metal-insulator transition, *Phys. Rev. B* **65**, 205124, (2002)
- [70] T. Schmitt, A. Augustsson, J. Nordgren, L.-C. Duda, J. Höwing, T. Gustafsson, U. Schwingenschlögl, V. Eyert, Electronic structure of Li-inserted V_6O_{13} battery cathodes: Rigid band behavior and effects of hybridization, *App. Phys. Let.* **86**, 064101, (2005)
- [71] T. Schmitt, L.-C. Duda, M. Matsubara, M. Mattesini, M. Klemm, A. Augustsson, J.-H. Guo, T. Uozumi, S. Horn, R. Ahuja, A. Kotani, J. Nordgren, Electronic structure studies of V_6O_{13} by soft x-ray emission spectroscopy: Band-like and excitonic vanadium states, *Phys. Rev. B* **69**, 125103, (2004).
- [72] S. Surnev, M. G. Ramsey, F. P. Netzer, Vanadium oxide surface studies, *Prog. Surf. Sc.* **73**, 4-8, (2003) 117-165

[73] B. Tepper, B. Richer, A. C. Dupuis, H. Kuhlenbeck, C. Hucho, P. Schilbe, M. A. Yarmo, H. J. Freund, Adsorption of molecular and atomic hydrogen on vacuum cleaved V_2O_5 (001) Surf. Sci. **496**, (2002), 64-72

[74] S. Zavahir, Q. Xiao, Sarina S. Jian Zhao, S. Bottle, M. Wellard, J. Jia, L. Jing, Y. Huang, J. P. Blinco, H. Wu, H. Y. Zhu, Selective Oxidation of Aliphatic Alcohols using Molecular Oxygen at Ambient Temperature: Mixed-Valence Vanadium Oxide Photocatalysts, ACS Catal., **6**, 3580–3588, (2016)

CHAPTER 3

METHODOLOGY AND SENSING MECHANISMS

3.1 Preparation Methods

Vanadium oxides nanostructures used as sensing electrodes in this work were prepared through thermal calcinations of a vanadium solid precursor, via microwave irradiation of a diluted vanadium source and by pulse laser deposition of a vanadium oxides target.

3.1.1 Chemical Vapour Deposition

Chemical vapour deposition (CVD) is widely used in the semiconductor industry for production, deposition of polycrystalline and amorphous nanoparticles and thin films. Its mechanism is based on the decomposition of the precursor in the presence of inert gas or reacting (oxidative or reducing) gases for nanoparticle production or exposure of one or more volatile precursors which react and decompose in the gas phase on the substrates [1].

Figure 3.1 is the typical thermal CVD system used in this work consisting of a horizontal quartz tube situated in the three zones hot wall furnace. The furnace's temperature could be ramped to about 1100 °C and N₂, H₂, CH₄, O₂ or Argon gas can be allowed to flow through a flow meter into the tube.

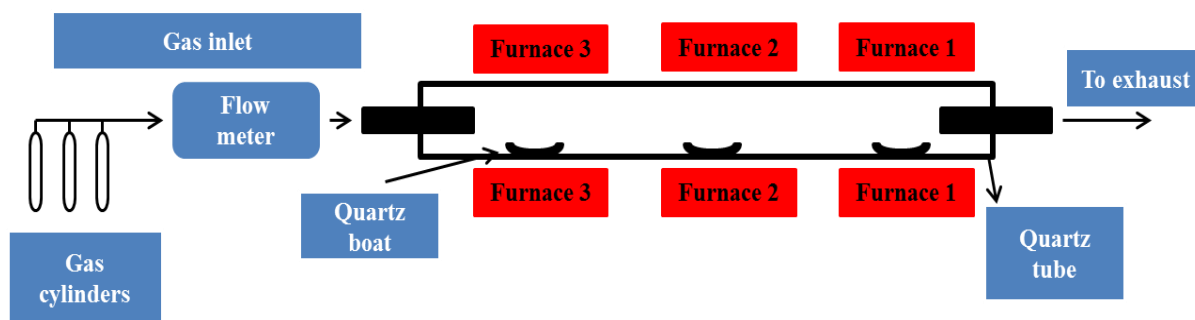


Figure 3.1: Schematic diagram of thermal chemical vapour deposition system

3.1.2 Microwave Assisted Techniques

Microwave chemistry is fast becoming an attractive method to industries for large scale production of nanotechnology applications within a short period of time and at low temperature [2-4]. Microwave synthesis of materials especially in the regime of nanoparticles is more effective than the conventional or traditional way of driving heat into the reacting system. For instance, in the conventional method, the activation of the reactants is slow; the heat flowing into the substance would first pass through the walls of the vessels/tube in order to reach the reacting system and consequently make reaction energy intensive and less efficient. The microwave synthesis process is not limited by the thermal conductivity of the vessel, microwave energy couples directly to the entire molecules of the reacting system, leading to a rapid rise in temperature and efficient use of energy. Many reports containing a higher degree of crystallinity, narrower size distributions and greater control over shape and morphology of nanostructures by microwave synthesis methods have been presented [4]. Figure 3.2 (a) presents the solution form of the precursors for microwave synthesis and (b) illustrates the microwave reactor.

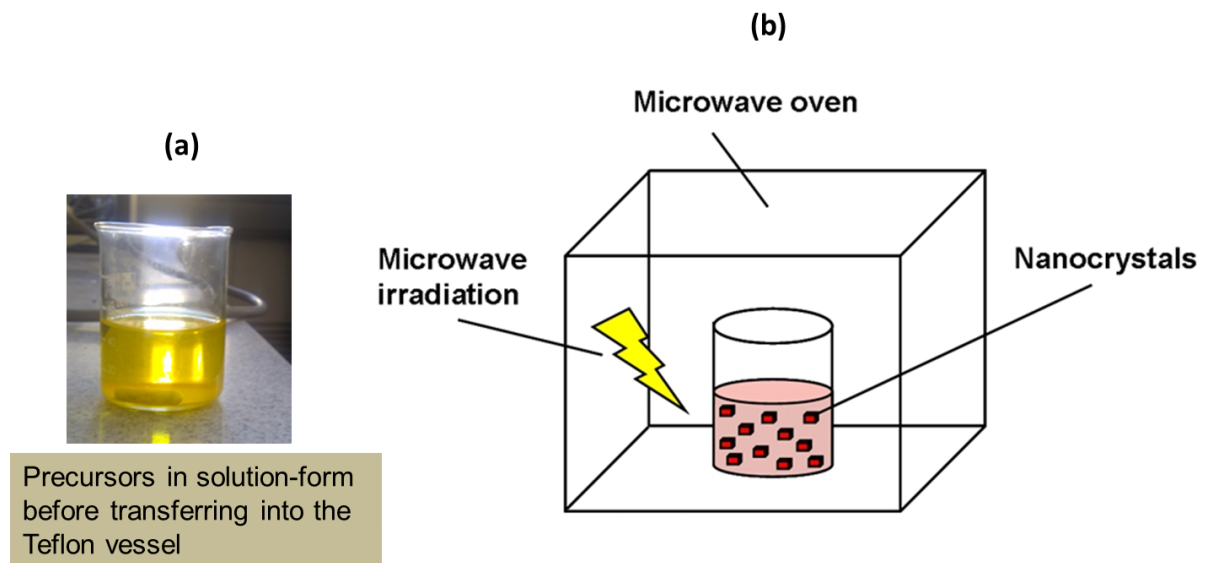


Figure 3.2: (a) Precursors for microwave synthesis (b) Schematic diagram of the microwave reactor [5].

3.1.3 Pulse Laser Deposition

Pulse laser deposition (PLD) which is another form of physical vapour deposition technique was employed in chapter eight of this work. The schematic illustration of this PLD system is presented in Figure 3.3. This system consists of a high power Nd: YAG laser beam (266 nm) which is focused onto a rotating vanadium target in the chamber. The target material vaporizes and deposits as a thin film onto the substrate facing the target. An ultra-vacuum environment and background of oxygen gas is required for deposition of an oxides thin film. Parameters like distance between the target and substrate, deposition time and oxygen concentrations are important for the desirable phase of the thin film [6-7].

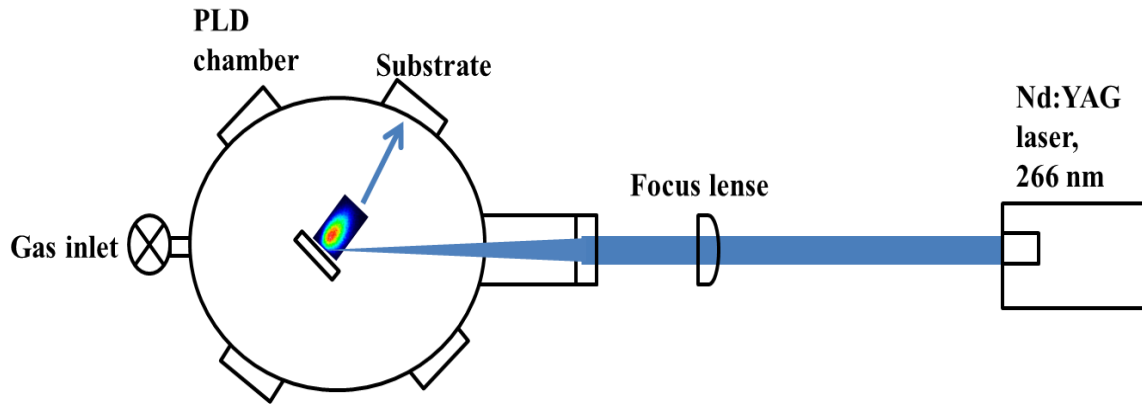
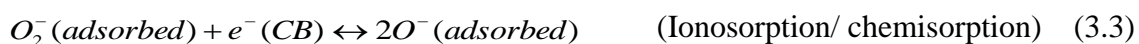
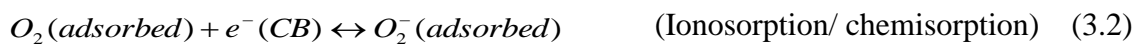


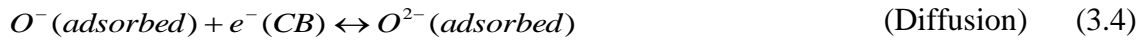
Figure 3.3: Schematic diagram of the pulse laser deposition system

3.2 Sensing Mechanism

3.2.1 Chemoresistors Sensing Mechanism

The sensing mechanism of metal oxide semiconductors (MOS) is generally based on two processes namely; oxygen ionosorption and reduction-reoxidation or oxygen vacancy [8]. For oxygen ionosorption, as we know, when a heated substrate of metal oxides surface is exposed to air, an oxygen adsorption process which would initiate formation of oxygen ionic species will occur. Typical ionic oxygen species during this reaction are; O^- , O_2^- , O^{2-} , and O_2^{2-} . Oxygen ions O^- , O_2^- , and O^{2-} are stable even below 100 – 300 °C while others only achieve stability at high temperatures [8-14]. This adsorption process usually demands an electron from the conduction band (CB) of the metal oxide semiconductors which consequently decreases the electron density of the material. The reaction paths or adsorption kinematics of oxygen adsorption in metal oxides semiconductor can be described as,





The process has been reported to be responsible for the creation of a depletion layer between the interfaces of MOS and the adsorbed oxygen and influences transport properties like; electrical conductivity, electron density and work function of the material [8-17]. Depletion layers (or barrier height) are created in this manner, when electron flow from the CB into the chemisorbed layer of the MOS, a space charge between the MOS interior and the surface as illustrated in Figure 3.4. This barrier height is $(q\Delta V_s)$ where q is the space charge and ΔV_s is the band bending. The space charge induction and the barrier height creation would also lead to a shift in Fermi energy level of the material [8-9, 15-17].

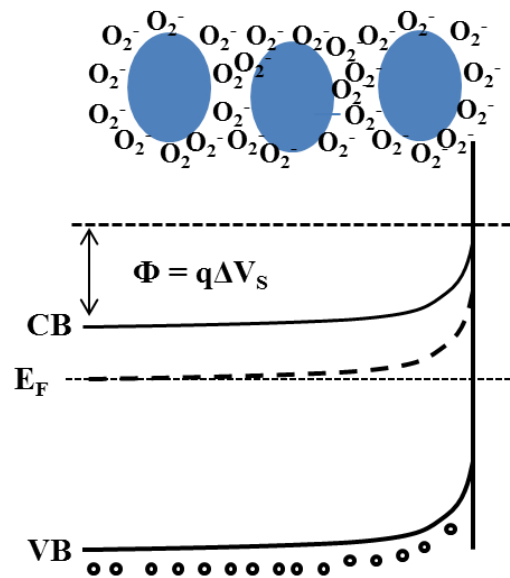


Figure 3.4: Band bending schematic diagram of n-type MOS after ionosorption of oxygen (VB is the valence band and E_F is the Fermi energy level) [8, 16]

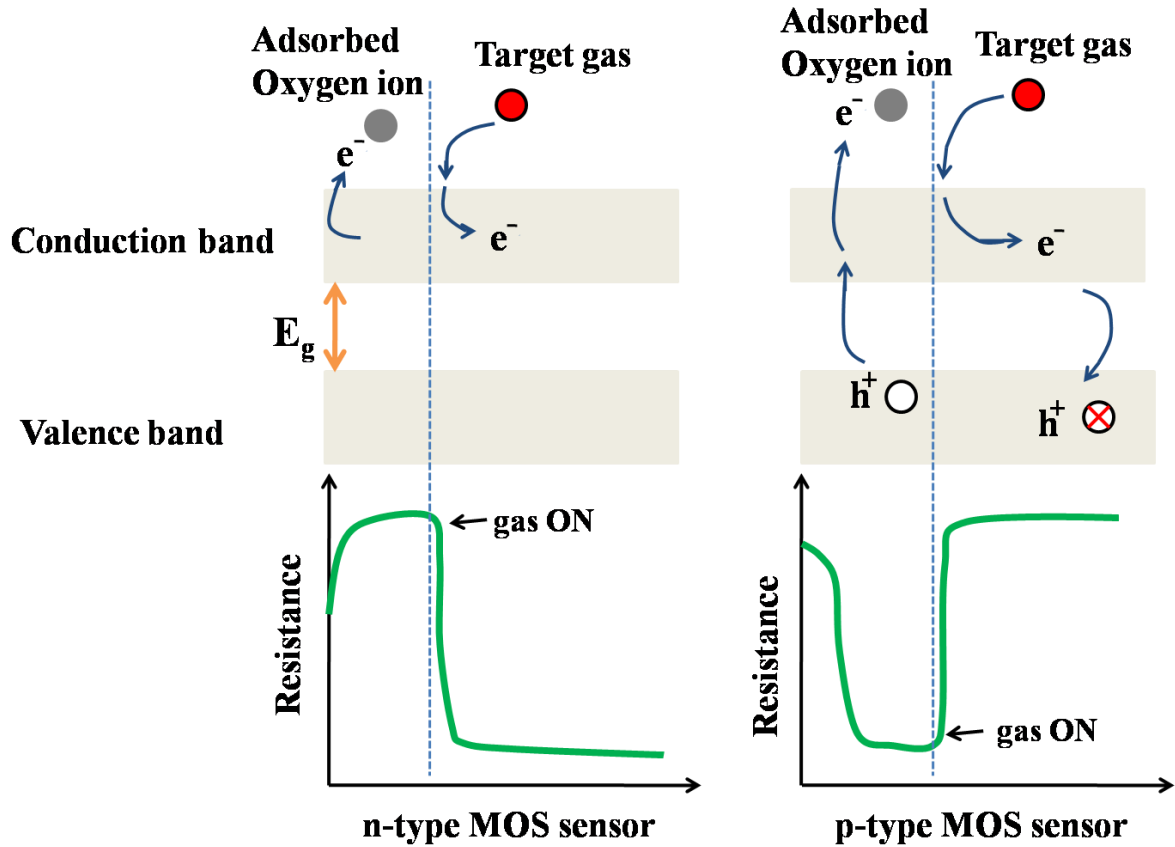


Figure 3.5: Schematic diagram for change of the sensor resistance upon exposure to the target gas (reducing gas) in the cases of n-type and p-type MOS sensors [17]

Now, when the surface of MOS that has undergone the processes in (3.1 – 3.4) is subjected to a reducing gas (e.g NH_3 , CH_4 , H_2S , CO , acetone, ethanol etc.) and provided that the MOS possess n-type property of the semiconductor (that is, electron being the majority charge carriers), the Fermi energy level of such MOS would shift towards the conduction band edge; hence would result in an increase of electron concentration which will lead to a decrease in the resistance (increase in conduction) of the material. When the gas is released and the MOS is disengaged from the exposure, the desorption process, which is the reverse reaction of the above processes (3.1 – 3.4), would occur and consequently lead to decrease in electron

concentration and increase in the resistance (decrease in conduction) of the material as illustrated in the Figure 3.5.

The opposite case is when the MOS surface possesses p-type conductivity (that is, hole being the majority charge carriers) and is exposed to a reducing gas. The holes which were initially created as a result of the formation of ionic oxygen would be occupied by the electrons released from reducing gas, thereby causing a decrease in the holes concentration and consequently result in an increase in the resistance (decrease in conduction) of the material. When this p-type MOS surface is disengaged for the exposure, the desorption process would make MOS gains holes concentration and cause a decrease in resistance (increase in conduction) as illustrated in the Figure 3.5.

The reverse scenario occurs when an oxidizing gas like (e.g. NO₂, CO₂, NO, etc.) is supplied wherein adsorption yield increase in resistance (decrease in conduction) for n-type, decrease in resistance (increase in conduction) for p-type and desorption yield decrease in resistance (increase in conduction) for n-type and increase in resistance (decrease in conduction) for p-type MOS material [8 – 17].



On the other hands, reduction or reoxidation is another mechanism that guides the electrical conductivity of a metal oxide semiconductor. This model suggests that oxygen vacancies at the surface of MOS as the agent responsible for the chemoresistive (chemiresistive)

behaviour of the material. When reducing gases such as CO are introduced to the surface of MOS, the molecules may react with the MOS surface by removing oxygen from its lattice to form CO₂ and to produce oxygen vacancies in the substrate. If this MOS is n-type, the oxygen vacancies may be ionized and induce electrons into the conduction band of the material and consequently increase the conductivity of the material as shown in (3.5 – 3.8). Note that the vacancies sites created as result of the synthesis procedures of the materials may also cause reaction between the material's surface and the molecules and thereby reduce, re-oxidise or influence the formation a new molecule as the derivative of the product [8 – 17].

3.2.2 Mechanism of Gas Sensing using Optical Spectroscopy

Gas sensing using optical techniques especially for selective detection of gases have been demonstrated in the literature [18 - 20]. For instance, Fourier transform infrared (FT-IR) spectroscopy has been applied to trace the variation of free carrier density and to study photoionization of ionized oxygen vacancy at the surface of metal oxides when exposed to different species of gases [18 - 20]. UV-Vis spectroscopy was also previously applied to the surface of metal oxides for the detection of formation of oxygen vacancies and their ionisation in the presence of gases [18]. Raman spectroscopy has also been used to monitor gas adsorption on the surface of metal oxides and to study their selective ability toward certain species of gas [21-23].

Chapter eight of this thesis focuses on an in-situ Raman spectroscopy sensing of gases on the surface of metal oxides nanostructured crystals. Raman spectroscopy is known to be a sensitive and reliable technique for vibrational, rotational and crystal structure study in condensed matter physics and engineering. The Raman set-up used in this work is shown in Figure 3.6 which is a slight modification of the typical commercial Bruker spectrometer to

include a transparent gas chamber and a gas production compartment where gas molecule can flow from.

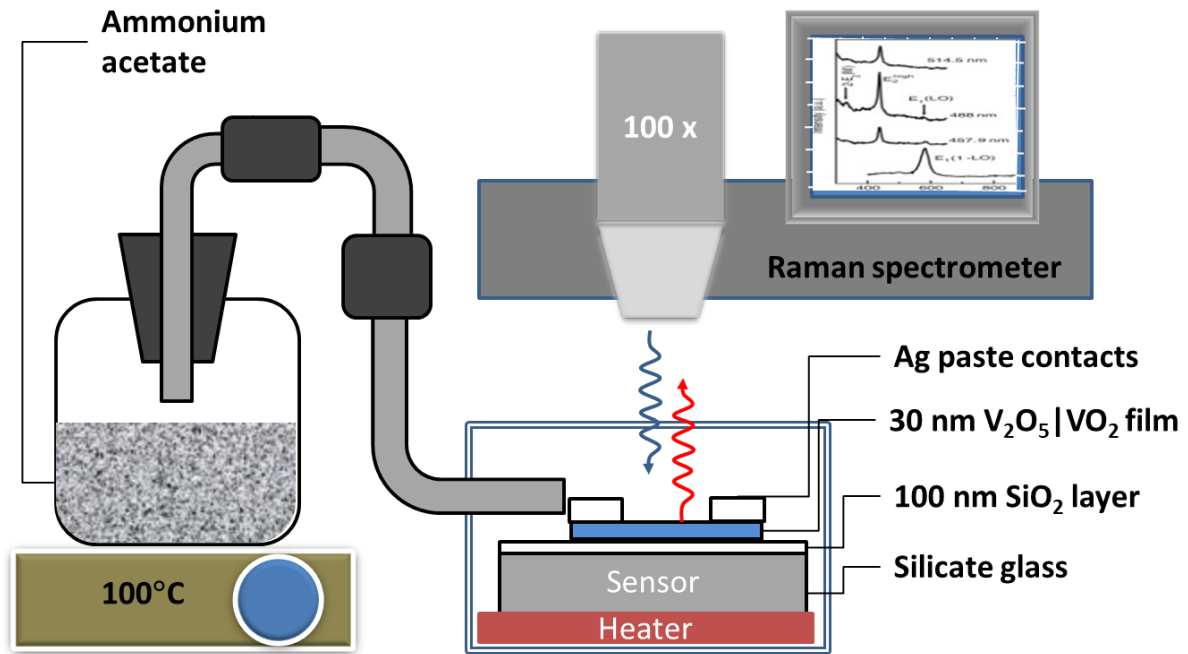


Figure 3.6: Schematic diagram of the in-situ Raman spectroscopy

The rationale for this is similar to that of the surface-enhanced Raman scattering scenario where electromagnetic radiation is suggested to initiate the excitation of the localized surface plasmon, thereby enhancing the Raman scattered signals of the surface through the physisorption process. Surface enhancement of Raman signals also occurs when the molecules are adsorbed on the surface by the chemisorption process to form charge-transfers complex [24 - 26]. In both cases, the scaling factor is used to distinguish the enhanced signals from the original signals. Another Raman principle explored here is the phonon confinement effect where asymmetric broadening of the Lorentzian-Gaussian peak is observed as a consequence of nano effects [27 - 31].

Our in-situ Raman sensing mechanism is based on how the Raman scattered photon population from a typical nanostructured surface is affected by the presence of reducing or oxidising gases. In this regard, one can use a number of basic theories providing the intensity, I , of the Raman scattered photons as a function of surface characteristics. One of the most appropriate theories is the phonon confinement model generally given by [27 - 31]

$$I(\omega, q) = A_0 \int_0^{\infty} \frac{\exp(-\alpha q^2)}{[\omega - \omega(q)]^2 + (\Gamma_0/2)^2} dq \quad (3.9)$$

where q is the wave vector in the Brillouin zone, $\omega(q)$ is the phonon dispersion relation for the material, α is the scaling factor, Γ_0 is the full-width-at-half-maximum broadening of the Raman peak, and A_0 is the proportionality constant. The integral is performed over all ranges of the wave-vector, $q \sim 0$ which is further proportional to $\pi a/\lambda$, where λ is the laser wavelength and a is the lattice parameter of the material. Any change in $I(\omega, q)$ should be due to less or more Raman scattered photons which means less or more phonons in the surface. This is a further signalling indicator of the chemical interactions or reactions that happen in the presence of reducing or oxidising gases. The change in intensity of Raman scattered photons or phonons can be found by differentiating Equation 1 with respect to both variables as follows

$$dI = A_0 \frac{\partial}{\partial \omega} \left(\int_0^{\infty} \frac{\exp(-\alpha q^2)}{[\omega - \omega(q)]^2 + (\Gamma_0/2)^2} dq \right) \Bigg|_q dq + A_0 \frac{\partial}{\partial q} \left(\int_0^{\infty} \frac{\exp(-\alpha q^2)}{[\omega - \omega(q)]^2 + (\Gamma_0/2)^2} dq \right) \Bigg|_{\omega} d\omega \quad (3.10)$$

The first term in Equation (3.10) gives the number of phonons of varying wavenumbers confined in the nano-particle but can only be evaluated numerically. The first part of Equation (3.10) reduces to zero as a differential with respect to ω for the case when ω does not change as will be seen in the experimental section, yields to null. The second term however can be simplified and Equation (3.10) can then be re-written as

$$dI = A_0 \frac{[\exp(-\alpha q^2)]^2}{[\omega - \omega(q)]^2 + (\Gamma_0/2)^2} \left(\frac{2q\alpha[\exp(-\alpha q^2)]^2[\omega - \omega(q)]^2 + (\Gamma_0/2)^2 + [\exp(-\alpha q^2)]^2 2[\omega - \omega(q)] \frac{d\omega}{dq}}{[[\omega - \omega(q)]^2 + (\Gamma_0/2)^2]^2} \right) \quad (3.11)$$

In terms of the response defined from the changes in Raman peak heights and their changes, it is appropriate to rather evaluate the fractional change of intensity than merely change in intensity. The latter suffers from variations from spot to spot. Therefore in this work we define Raman intensity response as a fractional change in intensity referenced to the Raman peak height before the analyte gas is introduced as follows:

$$\frac{dI}{I} = \frac{\frac{[\exp(-\alpha q^2)]^2}{[\omega - \omega(q)]^2 + (\Gamma_0/2)^2}}{\int_0^\infty \frac{\exp(-\alpha q^2)}{[\omega - \omega(q)]^2 + (\Gamma_0/2)^2} dq} \left(\frac{2q\alpha[\exp(-\alpha q^2)]^2[\omega - \omega(q)]^2 + (\Gamma_0/2)^2 + [\exp(-\alpha q^2)]^2 2[\omega - \omega(q)] \frac{d\omega}{dq}}{[[\omega - \omega(q)]^2 + (\Gamma_0/2)^2]^2} \right) \quad (3.12)$$

When Equation (3.12) is further analysed in terms of the actual sensing, one can reduce it to the following shorthand version:

$$\frac{dI}{I} = f(q, \omega(q), \omega, \alpha) \quad (3.13)$$

Since λ is a laser wavelength which is a constant during the Raman spectra acquisition and $q = 2\pi/\lambda$, then q is a constant and $\omega(q)$ is constant. We shall show in the chapter seven that ω is also a constant. Therefore we can re-write it to

$$\frac{dI}{I} = f(\alpha) \quad (3.14)$$

The scaling factor α varies from one materials surface to another and also depends on the polarization effects apart from the number of phonons interacting with the laser photons. The number of phonons is further affected by the presence of gaseous molecules.

It is also very important to discuss the theory of phonon frequency (wavenumber) changes owing to gas interaction with the material surface. There will be blue or red shifts in the vibrational frequencies due to these changes. If one imagines a linear chain model of fundamental frequency $\omega^2 = \kappa/\mu$, where κ and μ are spring constants and reduced mass of the masses on the spring respectively, then the change in vibrational frequency, $d\omega$, should be one that depends on both the change in μ and κ . The change in κ takes place when the number of electrons per bond changes whereas the change in μ happens when active gas elements such as oxygen desorbs or adsorbs. These changes can be, mathematically, represented as follows:

$$\frac{\partial \omega}{\partial \kappa} = \frac{1}{2\sqrt{\kappa/\mu}} \quad (3.15)$$

and

$$\frac{\partial \omega}{\partial \mu} = \left(-\frac{\kappa}{\mu^2}\right) \frac{1}{2\sqrt{\kappa/\mu}} = \left(-\frac{\kappa}{\mu^2}\right) \frac{\partial \omega}{\partial \kappa} \quad (3.16)$$

The total change in frequency can be written as

$$d\omega = \frac{\partial \omega}{\partial \mu} d\mu + \frac{\partial \omega}{\partial \kappa} d\kappa = \frac{1}{2\sqrt{\kappa/\mu}} \left(d\kappa - \frac{\kappa}{\mu^2} d\mu \right) \quad (3.17)$$

So if $d\kappa > d\mu/\mu^2$ one expects a blue shift whereas when $d\kappa < d\mu/\mu^2$ then one should expect a redshift in the Raman spectra. Both change in intensity of the phonon (Equations 3.9 to 3.11)

and their frequencies (Equation 3.12 to 3.14) will be used to explain the in-situ Raman spectra with gas sensing.

References

- [1] D.J. Lockwood, Nanotechnology for Electronic Materials and Devices, 4th edition, Springer 2007.
- [2] B. L. Hayes, Recent Advances in Microwave-Assisted Synthesis, *Aldrichimical Acta*, **37**, 2, 66-77, (2004).
- [3] E. C. Liganiso, Microwave Assisted Techniques for Synthesis of NiS_x and GaN Semiconductor Nanostructures for Application in Sensors, PhD Thesis (2014), University of the Witwatersrand Johannesburg.
- [4] G. A. Kahrilas, L. M. Wally, S. J. Fredrick, M. Hiskey, A. L. Prieto, and J. E. Owens, Microwave-Assisted Green Synthesis of Silver Nanoparticles Using Orange Peel Extract, *ACS Sustainable Chem. Eng.* **2**, 3 367-376, (2013).
- [5] K. Baba, H. Kasai K. Nishida, H. Nakanishi, Functional Organic Nanocrystals, *INTECH* 397 – 414, (2011)
- [6] B. N. Masina, S. Lafane, L. Wu, A. A. Akande, B. Mwakikunga, S. Abedelli-Massaci, T. Kerdja, A. Forbes, Phase-selective vanadium dioxide (VO₂) nanostructured thin films by pulsed laser deposition, *J. Appl. Phys* **118**, 165308 (2015)
- [7] J. Nag, The solid-solid phase transition in vanadium dioxide thin film: synthesis, physics and applications, PhD Thesis (2014), Faculty of Graduate School, Vanderbilt University Nashville Tennessee USA.
- [8] M. A. Carpenter, S. Mathur, A. K. Kolmakov, Metal Oxide Nanomaterials for Chemical Sensors, Springer 2012.
- [9] A. Ponzoni, C. Baratto , N. Cattabiani , M. Falasconi , V. Galstyan, E. Nunez-Carmona, F. Rigoni, V. Sberveglieri, G. Zambotti, D. Zappa, Metal Oxide Gas Sensors, a Survey of Selectivity Issues Addressed at the SENSOR Lab, Brescia (Italy), *Sen.* **17**, 714, 1-27, (2017)

- [10] G. Neri, Fifty Years of Chemoresistive Gas Sensors, *Chemosensors* 3, 1-20, (2015)
- [11] V. Balouria, S. Samanta, A. Singh, A.K. Debnath, A. Mahajanb, R.K. Bedib, D.K. Aswala, S.K. Guptaa Chemiresistive gas sensing properties of nanocrystalline Co_3O_4 thin films, *Sen. Act. B.* 176, 38-45, (2013).
- [12] K. Watchakun, T. Samerjai, N. Tamaekong, C. Liewhiran, C. Siriwong, V. Kruefu, A. Wisitsoraat, A. Tuantranont, and S. Phanichphant, Semiconducting metal oxides as sensor for environmentally hazardous gases, *Sen. Act. B.* **160**, 580-591 (2011).
- [13] A. M. Soleimanpour, A. H. Jayatissa, G. Sumanasekera, Surface and gas sensing properties of nanocrystalline nickel oxide thin film, *Appl. Surf. Sci.* **276**, 291-297, (2013)
- [14] J. L. Johnson, A. Behnam, Y. An, S. J. Parton, A. Ural, experimental study of graphitic nanoribbon films for ammonia sensing, *J. Appl. Phys.* **109**, 124301 (2011)
- [15] N. Jayadev Dayan, S.R. Sainkar, R.N. Karekar, R.C. Aiyer, Formulation and characterization of ZnO:Sb thick-film gas sensors, *Thin Solid Films* 325, 1-2, 254-258, (1998)
- [16] P. Shanker, J. B. B. Rayapan, Gas sensing mechanism of metal oxides: The role of ambient atmosphere, type of semiconductor and gases – A review, *Sci. Lett.* **4**, 126, 1-18, (2015).
- [17] S. Choopun, N. Hongsith, E. Wongrat, Metal-Oxides Nanowires for Gas sensors, *Nano technology and Nanowires*, INTECH (2012)
- [18] A. Chiorin, G. Ghiotti, F. Prinetto, M.C. Carotta, G. Martinelli, M. Merli, Characterization of SnO_2 -based gas sensors. A spectroscopic and electrical study of thick films from commercial and laboratory-prepared samples, *Sen. Act. B.* **44**, 1-3, 474-482, (1997).

- [19] S. Lenaer, M. Honore, G. Huyberegts, J. Roggen, G. Maes, In situ infrared and electrical characterization of tin dioxide gas sensors in nitrogen/oxygen mixtures at temperatures up to 720 K, *Sen. Act. B.* – **19**, 1-3, 498-482, (1994).
- [20] M-I. Baraton, FT-IR surface study of nanosized ceramic materials used as gas sensors, *Sen. Act. B.* **31**, 33-38, (1996).
- [21] T. Pagnier, M. Boulova, A. Galerie, A. Gaskov, G. Lucazeau, Reactivity of SnO₂-CuO nanocrystalline materials with H₂S: a coupled electrical and Raman spectroscopy study, *Sen. Act. B.* **71**, 134-139, (2000)
- [22] M. Boulova, A. Gaskov, Lucazeau, Tungsten oxide reactivity versus CH₄, CO and NO₂ molecules studied by Raman spectroscopy, *Sen. Act. B.* **81**, 1, 99-106, (2001)
- [23] M. Govender, D. E. Motaung, B. W. Mwakikunga, S. Umapathy, S. Sil, A. K. Prasad, A. G. J. Machatine, H. W. Kunert, Operating Temperature Effect in WO₃ Film for Gas Sensing, *IEEE* **978**, 1 (2013)
- [24] A. Champion, P. Kambhampati, Surface-enhanced Raman scattering, *Chem. Soc. Rev.*, **27**, 241-250,(1998)
- [25] X. Lang, L. G. Moura, M. A. Pimenta, J. Zhang, Charge-Transfer Mechanism in Graphene-Enhanced Raman Scattering, *J. Phys. Chem. C* **116**, 47, 25112-25118, (2012)
- [26] K. V. de Oliveira, J. C. Rubim, Surface-enhanced Raman spectroscopy of molecules adsorbed on silver nanoparticles dispersed an agarose gel and their adsorption isotherms, *J. Vib. Spec.* **86**, 290-301, (2016).

- [27] K. W. Adu , H. R. Gutiérrez , U. J. Kim , G. U. Sumanasekera , P. C. Eklund, Confined Phonons in Si Nanowires, *Nano Lett.* **5**, 3, 409-414, (2005).
- [28] A. K. Arora, M. Rajalakshmi, T. R. Ravindran, V. Sivasubramanian, Raman spectroscopy of optical phonon confinement in nanostructured materials, *J. Ram. Spec.* **38**, 6 604-617, 2007.
- [29] P. M. Fauchet, I.H. Campbell, C.R. Raman spectroscopy of low-dimensional semiconductors, *Solid State Mater.* **14**, 1, 79-101, (1988)
- [30] B W Mwakikunga, M. Maaza, K.T. Hillie, C.J. Arendse, T. Malwela, E. Sideras-Haddad From phonon confinement to phonon splitting in flat single nanostructures: A case of VO₂@V₂O₅ core-shell nano-ribbons, *J. Vib. Spec.* **02**, 105-111, (2012)
- [31] B. W. Mwakikunga, E. Sideras-Haddad, A. Forbes, C.J. Arendse, Raman spectroscopy of WO₃ nano-wires and thermochromism study of VO₂ belts produced by ultrasonic spray and *Phys. Stat. Sol.* **205**, 1, 150-154 (2008)

CHAPTER 4

PHASE EVOLUTION OF VO₂, V₂O₅ and V₆O₁₃ NANOSTRUCTURES FROM NH₄VO₃ AND THEIR HUMIDITY SENSING PROPERTIES

A.A. Akande E. C. Linganiso, B. P. Dhonge, K. E. Rammutla, A. Machatine, L. Prinsloo, H. Kunert, B. W. Mwakikunga, *J. Mat. Chem. Phys.* 151, (2015)206-214

In this chapter, the evolution of VO₂, V₆O₁₃ and V₂O₅ from the NH₄VO₃ precursor by thermal annealing using temperature programmed CVD are studied. Thermal characterization (TGA & DSC) of the precursor and the resulting powder across 100 – 350 °C are critically discussed. This is followed by XRD, TEM, Raman Spectroscopy, FTIR, XPS, EDX, VSM, BET and Gas sensing tester characterizations. All these techniques complementarily show the order of appearance of vanadium oxide phases to be VO₂ + V₂O₅ → V₆O₁₃ → V₂O₅ as summarized by the phase diagram provided.

4.1. Introduction

Vanadium oxides among transition metal oxides usually present synthesis difficulties due to their existence in several oxidation states and formation of a variety of binary oxides with the following general formulas for n = 1, 2, 3... (1) V_nO_{2n+1} e.g. V₂O₅, V₃O₇, V₄O₉, V₆O₁₃, (2) V_nO_{2n-1} e.g. VO, V₂O₃, and (3) V_nO_{2n} also with VO₂ and V₂O₄ [1-31]. Among these oxides, V₂O₃, VO₂, V₆O₁₃ and V₂O₅ possess many interesting characteristics which are

employed in various novel applications [1-31]. These characteristics and their mechanisms have been thoroughly reviewed in Chapter Two of this thesis. Here, we study phase evolution of VO_2 , V_2O_5 and V_6O_{13} from the precursor of NH_4VO_3 using various material science characterization techniques and a chemical/humidity sensing tester.

Ammonium meta-vanadate (AMV, NH_4VO_3) has been widely used as a source material for the syntheses of vanadium oxides by various deposition/synthesis techniques, such as chemical precipitation [32, 33], thermal annealing [34], spray pyrolysis [35, 36], and autoclave hydrothermal treatment [37]. In all these synthesis techniques, the phase diagram of V-O system was not followed. As a result, many of such reports indicate either single phase VO_2 or V_2O_5 without validation. In this work, we started by performing thermogravimetry analysis of NH_4VO_3 in a nitrogen environment. Instead of mass loss alone, we also observed mass increase. This prompted further systematic study of phases at various temperatures in a reducing hydrogen atmosphere. This chapter reports the quantitative study of phases of VO_x at various temperatures. This study sheds more light on the existing phase diagrams of VO_x .

4.2. Experimental techniques

4.2.1 Powder Synthesis

Ammonium metavanadate powder (NH_4VO_3 , purity 99.99%, molecular weight of 116.98 a.m.u, density of 2.3 g cm^{-3} and melting (or decomposition) temperature of $200 \text{ }^\circ\text{C}$) was purchased from Sigma-Aldrich Chemical Co. Differential scanning calorimetry (DSC) analysis was performed on the powder using a DSC Q2000 V24.4 Build 116 to measure the amount of heat flow into and out of the sample relative to the reference pan with a linear temperature ramp under nitrogen gas. A series of heat treatments were performed for better understanding of the decomposition and phase change in the material. Firstly, heat treatment of the NH_4VO_3 powder was carried out for 400 and $500 \text{ }^\circ\text{C}$ in a chemical vapour deposition

(CVD) reactor under nitrogen flow (information about the CVD method is already presented in the chapter three). This experiment was followed by the TGA measurement of the resulting powder (5.096 mg) and that of standard NH_4VO_3 (4.726 mg) to study the thermal decomposition process in the materials under a nitrogen atmosphere. The instrument used is a TGA Q500 V20.10 Build 36 by Anton Paar Inc. Furthermore, a comprehensive CVD calcination of NH_4VO_3 powder under 20 mL min^{-1} hydrogen flow was performed in two different sections, firstly at 100, 150, 200 °C and secondly at 250, 300, and 350 °C for 2 hours.

4.2.2 Powder Characterization

The powder was characterized using an X-Ray diffraction instrument (Panalytical X'pert Pro PW 3040/60 XRD equipped with Cu $K\alpha$ ($\lambda=0.154\text{nm}$) monochromatic radiation source). XRD patterns were recorded in the scanning range of 5° - 90°. DSC of these calcined powders was also studied. Raman spectroscopic studies were conducted using a Jobin–Yvon T64000 Raman spectrograph with a 514.5 nm excitation wavelength from an argon ion laser. The power of the laser at the sample was low enough (0.384 mW) in order to minimise localised heating of the sample. The T64000 was operated in a single spectrograph mode, with the 1800 lines/mm grating and a 100x objective on the microscope, and further optical measurements were performed with a standard spectrum 100 PerkinElmer FT-IR spectrometer. The microscopic studies and quantitative elemental composition studies were carried out using a JEOL 2100 Transmission Electron Microscopy (TEM) (from Tokyo Japan) equipped with a LaB6 filament and a Gartan U1000 camera of 2028 X 2028 pixels, and high quality inbuilt Energy dispersive X-ray spectroscopy (EDS).

X-ray photo-electron spectroscopy (XPS) was also performed on a reference sample containing V_2O_5 , VO_2 , V_6O_{13} as well as the domains of WO_3 . EDS taken from VO_x domains (excluding the WO_3 domains) in HRTEM was also performed on the same reference sample. The XPS determinations of the proportion of V^{3+} , V^{4+} and V^{5+} were used to calibrate the EDS spectra and this information was then employed in the determination of the proportions of V^{3+} , V^{4+} and V^{5+} for the current set of samples. X-ray photoelectron spectroscopy analyses were carried using a PHI 5000 Versaprobe- Scanning ESCA Microprobe. The survey scans were recorded with a 100 μm , 25 W, 15 kV beam using monochromatic Al K_{α} radiation ($h\nu = 1486.6$ eV) and for the higher resolution spectra the hemispherical analyzer pass energy was maintained at 514 eV to 520 eV (C 1s, O 1s, V 2p) for 50 cycles. Measurements were performed using either a 1 eV/step and 45 min acquisition time (binding energies ranging from 0 to 1000 eV) for survey scans or a 0.1 eV/step and 20–30 min acquisition times for the high-resolution scans. The pressure during acquisition was typically under 1×10^{-8} Torr. The surfaces were also sputtered clean for 30 s using an Ar ion gun (2 kV energy ions) and measurements were repeated.

The field dependent magnetic characterization was performed using a Lakeshore 735 vibrating sample magnetometer (VSM) at room temperature. It is vital to point out that because this type of sample exhibits small magnetization signals, special care was taken during measurements so as to avoid any trace magnetic contamination. Magnetic measurements performed on the different batches of VO_x powders showed consistent and reproducible results demonstrating paramagnetic behaviour.

BET analyses were carried out using a Micromeritics TriStar II series Surface Area and Porosity instrument and a Micromeritics sample degassing system from the USA.

Gas sensing properties were obtained by placing the VO_x paste dispersed in ethanol onto inter-digitated electrodes and obtaining controlled transient readings of the current in

varying levels of analyte. The measurements were accomplished by employing a KINOSISTEC (Italy) gas sensor test instrument comprising KEITHLEY voltage and current sources as well as source meters.

4.3. Results and Discussions

4.3.1 Thermal Analysis (DSC/TGA)

Figure (4.1 (a)) shows the DSC profile of NH_4VO_3 recorded in the temperature range of $-47\text{ }^\circ\text{C}$ to $350\text{ }^\circ\text{C}$ and an exothermic enthalpy change reaction of about -38.3 mW was observed around $234\text{ }^\circ\text{C}$ which may be due to the decomposition of the material. The other enthalpy change at the $340\text{ }^\circ\text{C}$ is small and may be due to the formation of V_2O_5 phase as it occurred at a temperature close to its phase transition temperature ($375\text{ }^\circ\text{C}$) [38-39]. Figure 4.1 (b) shows TGA/DTA profile of NH_4VO_3 recorded in the temperature range of $26 - 900\text{ }^\circ\text{C}$. This thermogravimetry curve reveals mass loss in three regions during the scan as shown in the figure. The overall mass loss of 22.2% in the material was observed between $155.5\text{ }^\circ\text{C}$ to $309\text{ }^\circ\text{C}$. This value is in agreement with the one previously reported in the literature [40-41].

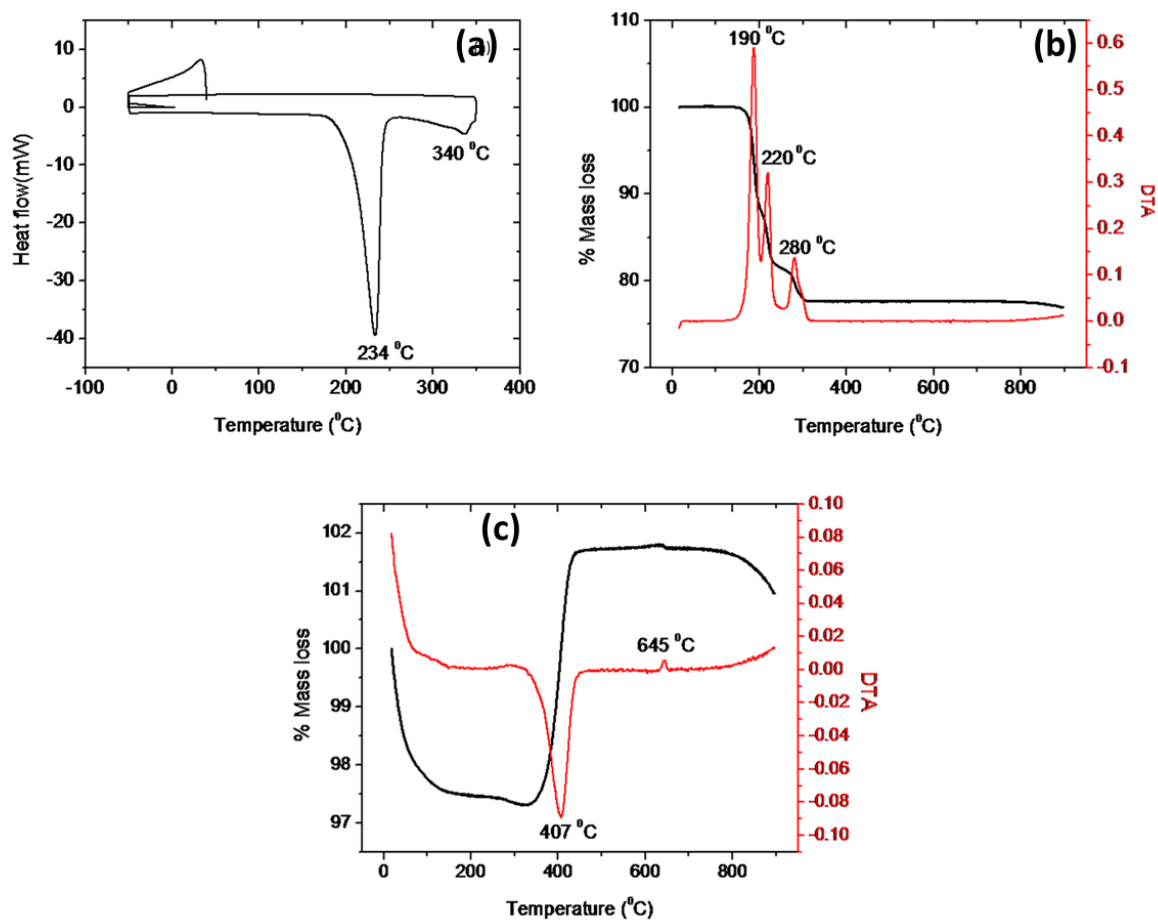


Figure 4.1: (a) DSC thermogram of the starting precursor (NH_4VO_3), (b) TGA/DTA thermogram of the starting precursor (NH_4VO_3) and (c) TGA/DTA thermogram of the sample prepared at 400 °C

However in this work we have thoroughly analysed and accounted for each weight loss. Region one lies in the temperature range of 155.4 – 199 °C, which is accompanied by a mass loss of 11.27%. The mass loss in region two is found to be 6.41% within the temperature range of 199 – 231 °C and in the third region which falls in the temperature range of 231 – 309 °C, the loss was found to be 4.52%. The details of the overall processes, chemical equations followed and reactions occurred during the decomposition of NH_4VO_3 are provided in the attached manuscript.

Figure (4.1(c)) is a TGA/DTA profile of the sample prepared at 400 °C in a synthetic nitrogen environment. The structure at this temperature confirmed with XRD, HRTEM and Raman Spectroscopy is V_6O_{13} . The initial reaction below 100 °C shows some loss in mass of the powder which may be due to the release of moisture absorbed by the powder. Further increase in temperature up to 335 °C reveals a very small change in mass from 5.096 to 4.972 mg, which is 2.53 %. This mass loss is due to the reduction of V_6O_{13} to VO_2 . The possible reduction processes and chemical equations followed are in the attached manuscript.

Above 340 °C, significant mass gain was observed which was followed by the second stability around 440 °C. The increase in mass is due to the oxygenation of VO_2 . The oxygen is contributed from the synthetic nitrogen flow during the TGA experiment. The transformation is ascribed to V_2O_5 since it is known as a very stable oxide among vanadium oxides and usually formed above 340 °C.

Figure (4.2) shows the DSC profiles of the samples prepared by calcination of NH_4VO_3 from 100 - 350 °C in step of 50 °C. The peaks at 185 and 220 °C for the sample calcined at 100 °C show exothermic reactions which may be due to the release of ammonia. Peaks at 78 and 80 °C for the samples calcined at 150 and 200 °C may be due to the formation of VO_2 , since it is close to MIT temperature and the one at 85 °C for samples calcined at 250 and 300 °C may be due to the mixture of VO_2 and metastable phase V_6O_{13} . The formation of various phases with temperature was confirmed with the XRD pattern, discussed in section 4.3.2 and 4.3.4. The development of V_2O_5 phase was observed for the samples calcined at 100, 150, and 200 °C in the temperature region 310 to 340 °C. The actual formation of V_2O_5 occurs at 375 °C. Due to the limitation of the DSC in terms of temperature range, we could not proceed for further higher temperature measurement. Although this peak is absent in the case of the sample calcined at 250 and 300 °C, this may be due to peak shifting to the higher

temperature 375 °C. The sample calcined at 350 °C shows optimum population of phase of V₂O₅.

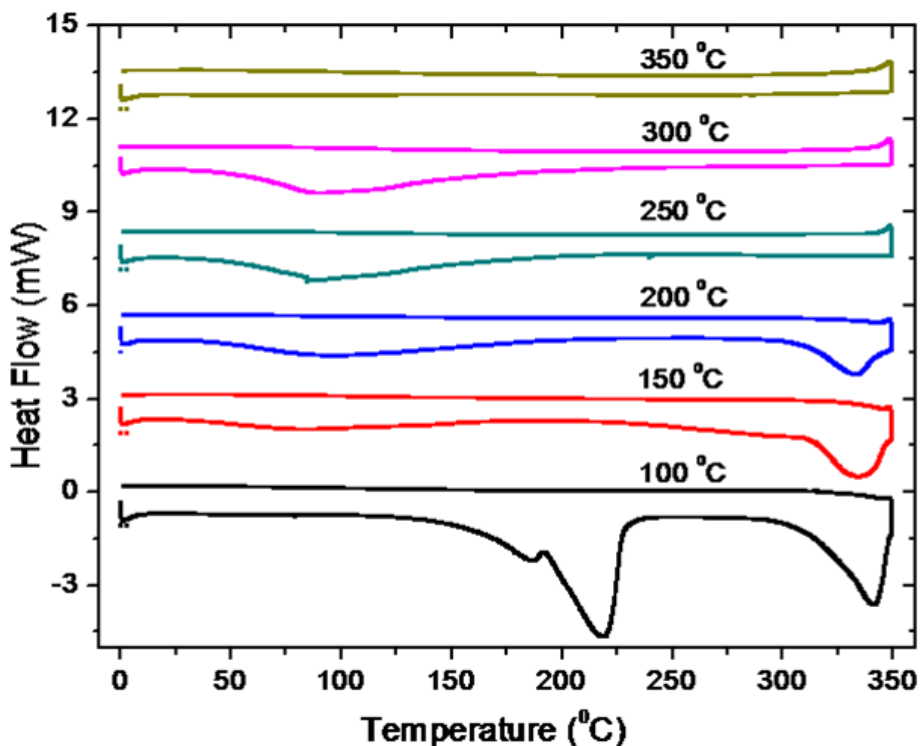


Figure 4.2: DSC thermograms of the samples prepared by thermal annealing of NH₄VO₃ from 100 - 350 °C

4.3.2 X-Ray diffraction Spectra

Figure (4.3 (a)) shows XRD spectra of the standard precursor NH₄VO₃ and samples calcined at temperatures 100 – 350 °C. The XRD patterns were compared with PCDPDFWIN CAS No: 44-0252, 72-1278 and 89-0611 for VO₂, V₆O₁₃ and V₂O₅ respectively. The monoclinic peak of VO₂ at 2θ (diffraction angle) = 27.8 ° corresponding to the plane (011) (PCDPDFWIN CAS No: 44-0252) is found to be dominant among the samples calcined at 100, 150 and 200 °C. Various phases of vanadium oxide were also observed except for those

samples calcined at 250 to 350 °C. The sample prepared at 250 to 350 °C shows the development of single phase of V₂O₅. Predominantly monoclinic metastable V₆O₁₃ was observed for the sample calcined at 250 and 300 °C. The orthorhombic V₂O₅ phase was observed at 350 °C.

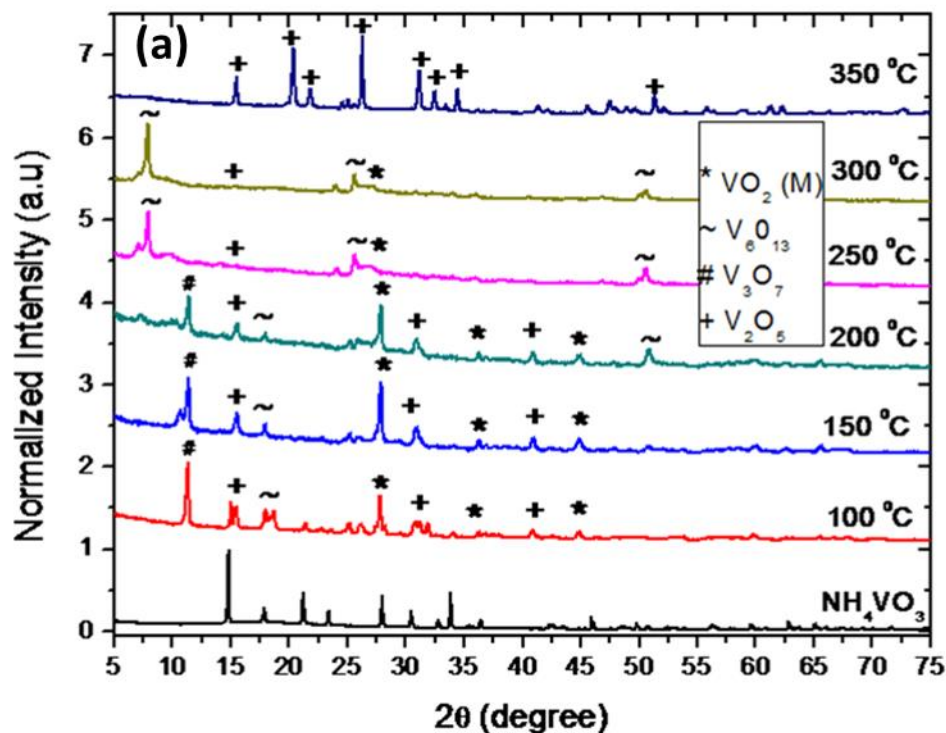


Figure 4.3 (a): XRD spectra of the standard NH₄VO₃ and of the samples prepared by thermal annealing of NH₄VO₃ from 100 - 350 °C.

4.3.3 Transmission Electron Microscope

TEM imaging for the calcined samples at 150 °C, 250 °C and 350 °C were carried out. Figure (4.3 (b)) shows a high resolution TEM image of a sample calcined at 350 °C showing the single plane corresponding to that of (101) of V₂O₅. The upper corner inset shows the SAED pattern and the lower corner shows the corresponding EDS spectrum. The sample calcined at 150 °C reveals sheet and rod like structures with a SAED pattern of non-uniform

diffraction. A single (110) plane of uniform diffraction corresponding to that of V_6O_{13} was observed for the sample at 250 °C. The radius is measured from ImageJ software and the lattice spacing was calculated to be 3.7 Å which is indexed to the monoclinic V_6O_{13} parameters ($b=3.671$ Å). The calculated value of the lattice spacing for the sample calcined at 350 °C is 3.483 Å is corresponding to orthorhombic V_2O_5 phase ($b=3.517$ Å). These TEM images are attached in the Appendix.

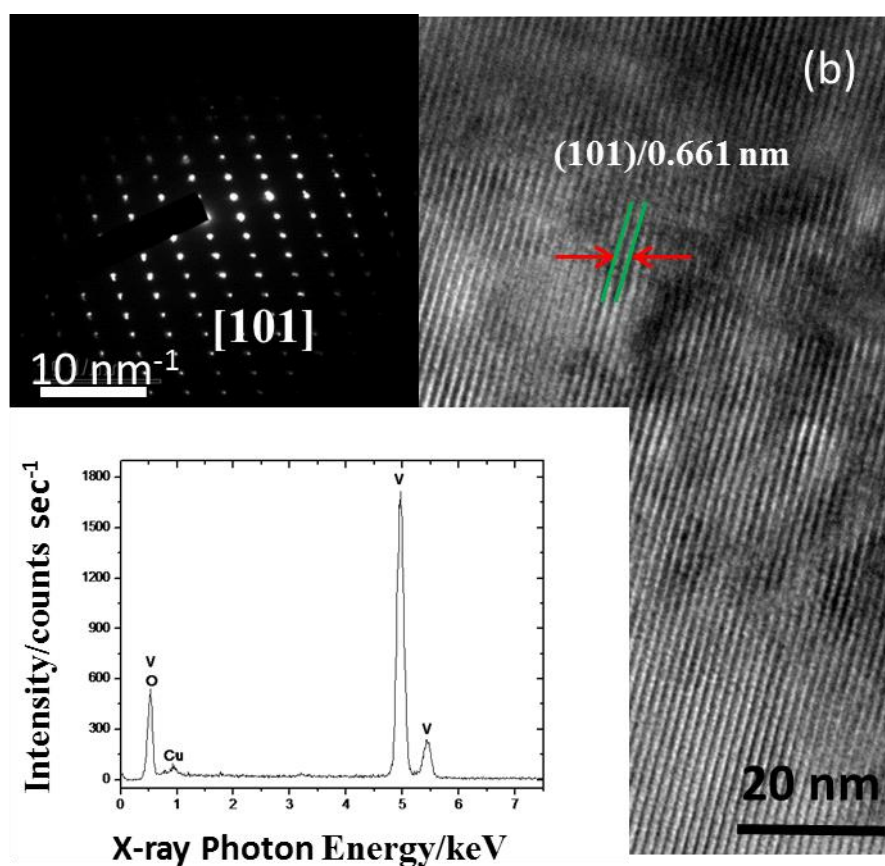


Figure 4.3 (b): High resolution TEM image of sample annealed at 350 °C showing single plane corresponding to that of (101) of V_2O_5 , insert upper corner showing SAED pattern of 101 lattice and insert lower corner showing the corresponding EDS spectrum.

4.3.4 Phase Diagram

Figure 4.4 is the phase evolution diagram showing the distribution of oxides (VO_2 , V_6O_{13} and V_2O_5) with temperature. The XRD pattern of samples calcined at various temperatures has been used to developed a phase diagram. The phase analysis was carried out by calculating the area of Gaussian fitted XRD peaks. The percentage of phase was calculated using Equation. 4.1,

$$\%(VO_x) = \frac{\sum A_x}{\sum A_x + \sum A_y + \dots} \quad (4.1)$$

where A_x, A_y, \dots are the peak areas corresponding to the phases x, y, \dots respectively [42]. It was observed that the formation of VO_2 phase dominates in the temperature range 150 - 200 °C, whereas V_6O_{13} phase is the dominant around 250 – 300 °C. V_2O_5 is found to be present for all temperatures and optimum population at 350 °C.

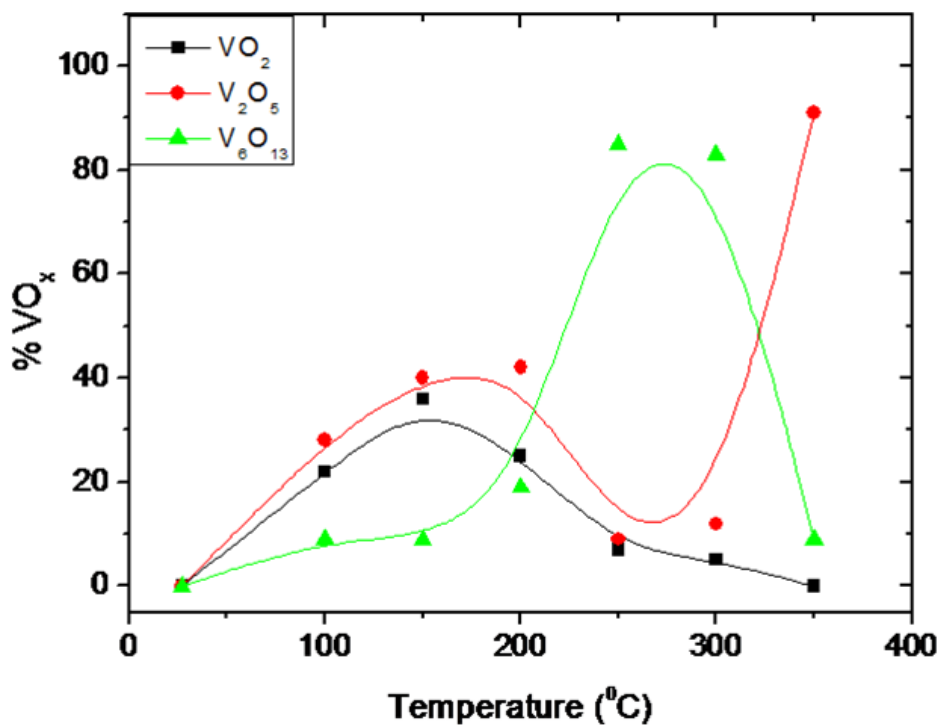


Figure 4.4: Vanadium Oxides (VO_2 , V_6O_{13} and V_2O_5) Phase Evolution diagram.

4. 3.5 Raman Spectroscopy

Figure 4.5 (a) shows Raman spectra of the standard and calcined NH_4VO_3 precursor in the temperature range of 100 - 350 °C. The presence of 194, 223, 265, 385, 600 and 628 cm^{-1} vibration modes in the samples calcined at 100 – 200 °C shows the predominant population of VO_2 in this region [43]. The sample calcined at 250 – 350 °C shows a peak at 137 cm^{-1} , belonging to the V_6O_{13} phase. The peak at 142 and 992 cm^{-1} belong to the V_2O_5 phase [44, 45]. The extra peaks at 265 and 385 cm^{-1} reveals the presence of VO_2 phase at higher temperatures. The peak, due to ammonia vibrations, is observed around 142 cm^{-1} for the precursor NH_4VO_3 [46].

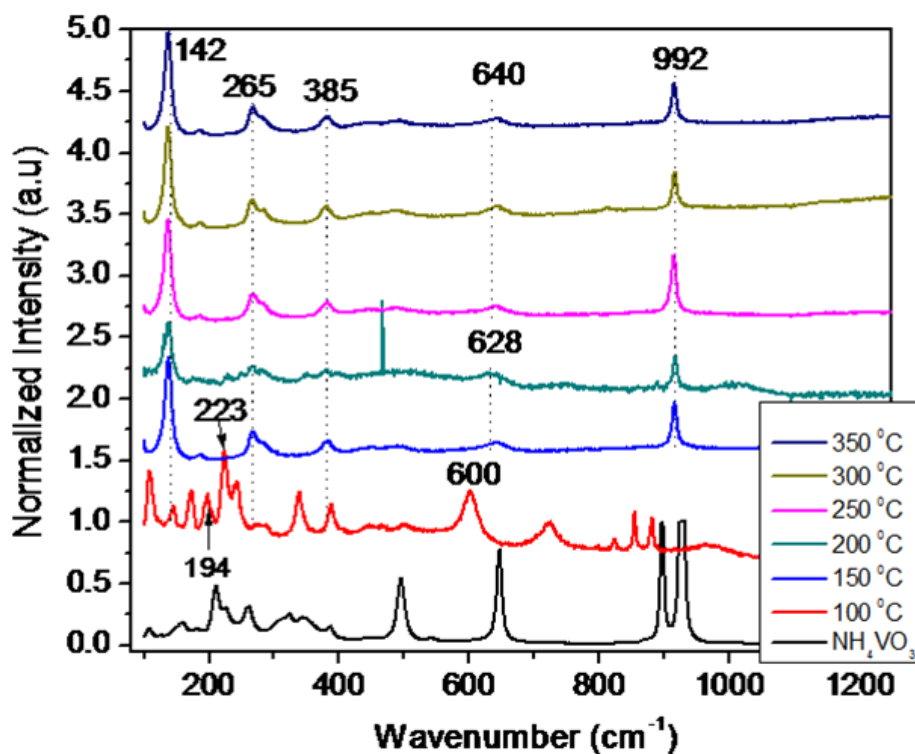


Figure 4.5 (a): Raman spectra of the standard NH_4VO_3 and of the samples prepared by annealing of NH_4VO_3 from 100 - 350 °C.

4.3.6 Fourier Transform Infrared Spectroscopy (FT-IR)

Figure 4.5 (b) shows the FTIR spectra of the standard and calcined NH_4VO_3 precursor in the temperature range of 100 - 350 °C.

The observed absorption shoulder at 715 cm^{-1} and strong peak at 972 cm^{-1} correspond to the VO_2 [47], The shoulder at 715 cm^{-1} was not observed for higher temperatures (250 – 350 °C) and the shift in 972 cm^{-1} peak was observed at 350 °C. The peak shifted to a higher frequency 1009 cm^{-1} at 350 °C corresponding to a single polycrystalline V_2O_5 phase [47]. The presence of both shoulder and strong peaks at lower temperatures (100 – 200 °C) reveals the higher population of VO_2 . The higher population of V_2O_5 at higher temperatures and VO_2 at lower temperatures is also supported by our XRD phase calculation and Raman study.

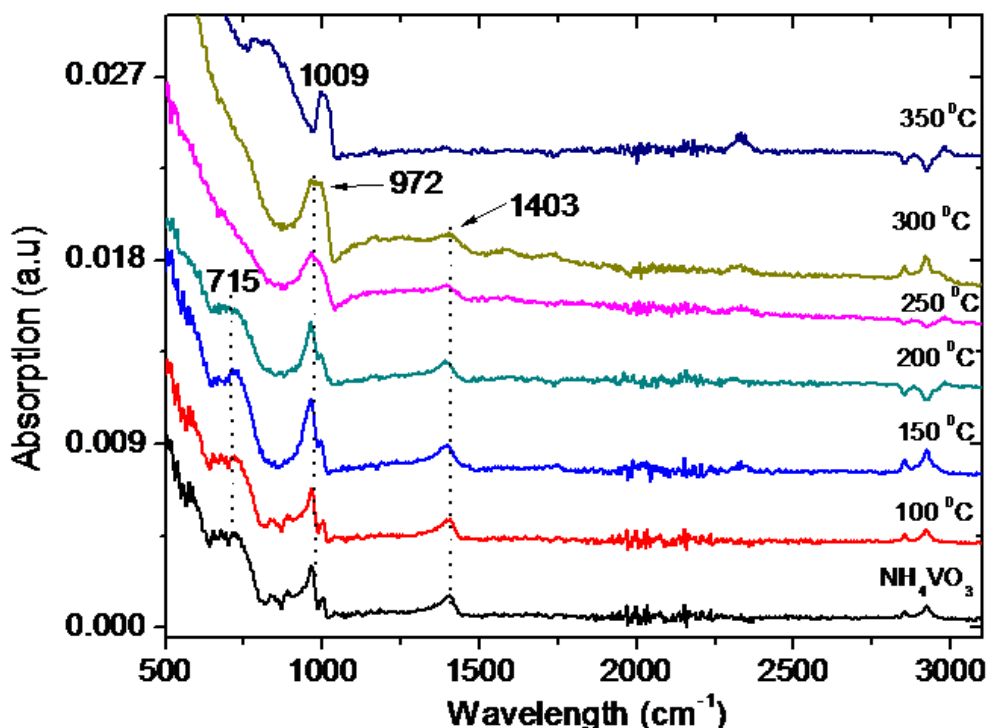


Figure 4.5 (b): FT-IR of the standard NH_4VO_3 and of the samples prepared by annealing of NH_4VO_3 from 100 - 350 °C.

4.3.7 X-ray Photoelectron Spectroscopy and Energy Dispersive Spectroscopy (XPS and EDX)

XPS and EDS on a reference sample containing known mixed V^{3+} , V^{4+} and V^{5+} phases of VO_x were performed, and their full spectra were reported in our paper [48]. This analysis has been used to calibrate all EDS results for our current samples containing V_6O_{13} , VO_2 and V_2O_5 . The analysis results are summarized in Table 1 - first the heights and the widths of the peaks were determined for each peak in XPS and in EDS and areas under such peaks were calculated. The proportions were determined from the ratio of the area under each peak to the total of all peaks considered.

From Table 1 (a) the reference sample has 69% proportion of V_2O_5 or a contribution from mixed (metastable) V_6O_{13} and the rest 31% of the photo-electrons come from VO_2 with a small contribution from V_6O_{13} again. EDS results of the same sample indicate 70% X-ray emission from V_L electronic shell ($2p \rightarrow 3d$ transition). This could be attributed to V_2O_5 and a small contribution from the mixed phase V_6O_{13} as suggested by XPS in Table 1 (a). This shows that the XPS and EDS results are in good agreement and one can use local EDS results with this XPS calibration to determine the local composition of the current VO_x materials.

Table 4.1 (a): XPS analysis for reference or standard sample containing VO₂, V₂O₅, V₆O₁₃ and WO₃.

Orbitals	Height, H (a.u)	H ₀ (a.u.)	Width, W (eV)	A	% V + W	% of V ⁱ⁺
W(4f) _{7/2} , W ⁶⁺	2100	150	3	5850	51.5	
W(4f) _{5/2} , W ⁶⁺	1600	250	3	4050	35.6	
V(2p) _{3/2} , V ⁴⁺	3500	3200	1.5	450	3.9	30.8
V(2p) _{3/2} , V ⁵⁺	3975	3300	1.5	1012.5	8.9	69.2

Table 4.1 (b): EDS analysis for reference or standard sample containing VO₂, V₂O₅, and V₆O₁₃

Electronic shell	Height, H (a.u)	Width, W (eV)	A	% of V ⁱ⁺
V _M	500	0.2	100	15.6
V _L	1500	0.3	450	70.3
V _K	300	0.3	90	14.1

One can conclude that the V_L shell peak in EDS can be used to mark V₂O₅ whereas the V_M and V_K shells are mostly for VO₂ although in both cases V₆O₁₃ has a strong indeterminate influence. One can understand the V₆O₁₃ poses a challenge in ascertaining its exact contribution owing to its meta-stable nature.

Table 4.2: EDS analysis based on the calibrations in Tables 1 (a) and (b) and local composition for the VO_x samples annealed at 150, 200, 250, 300 and 350 °C

Sample	Electronic shell	Height, H (a.u)	Width, W (eV)	A	% of Vi+
EDX 150 °C	V _M	900	0.15	135	10.5
	V _L	5000	0.2	1000	77.8
	V _K	750	0.2	150	11.7
EDX 200 °C	V _M	800	0.1	80	10
	V _L	5500	0.1	550	68.8
	V _K	850	0.2	170	21.2
EDX 250 C°	V _M	530	0.15	79.5	27.5
	V _L	1700	0.1	170	58.7
	V _K	200	0.2	40	13.8
EDX 300 °C	V _M	250	0.15	37.5	22.7
	V _L	720	0.15	108	65.2
	V _K	100	0.2	20	12.1
EDX 350 °C	V _M	990	0.15	148.5	15.7
	V _L	3500	0.2	700	73.8
	V _K	500	0.2	100	10.5

We have summarized the EDS analysis results from the VO_x samples annealed at 150, 200, 250, 300 and 350 °C based on the calibration undertaken in Tables 1 (a) and 1(b). These results are summarized in Table 2. It can be observed that the proportions of the phases change with annealing temperatures. The changes are plotted in Figure 4.6. The V_L – temperature profile shows a decrease from 100 °C to 250 °C and then increases again up to the annealing temperature of 350 °C. This profile agrees very well with the phase diagram shown in Figure 4.4 in the previous section. Similarly, the proportions determined from the

V_M peak at 150 °C is exactly the VO_2 profile in the phase diagram in Figure 4.4, whereas the proportions calculated from V_K shell increase to a maximum value at an annealing temperature of 200 °C which agrees with the V_6O_{13} profile in Figure 4.4. This assures us that the present XPS calibration of the EDS results is correct.

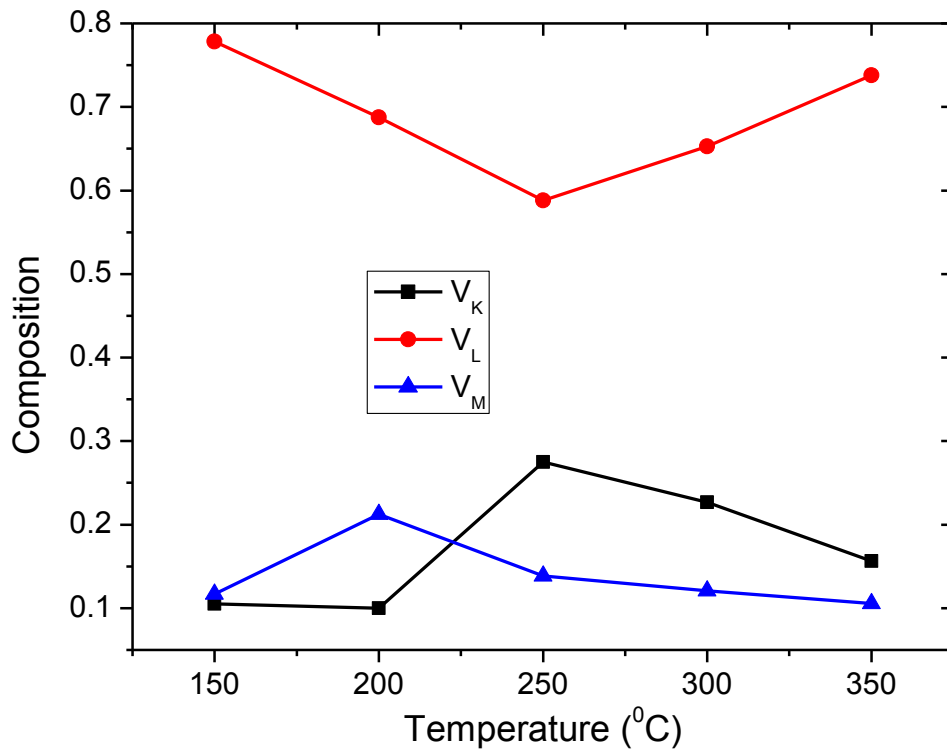


Figure 4.6: Proportions of V_2O_5 , VO_2 , and V_6O_{13} determined by EDS calibrated with XPS as they vary with annealing temperatures.

4. 3.8 Vibrating Sample Magnetometry (VSM)

The traditional definitions of remnant magnetization (M_R^+ and M_R^-), saturation magnetization (M_S^+ and M_S^-) and squareness (SQ) in bulk and nano-scale magnetic materials are schematically illustrated in Figure 4.7 (a and b). It should be noted that nano-materials display a shift of the hysteresis loop due to what is called exchange bias [48-50]. In Figure 4.7 (c) we show the hysteresis loops for all VO_x samples annealed at 100, 150, 200, 250, 300 and 350 °C including the precursor materials of ammonium metavanadate, NH_4VO_3 . One can note that all samples show a degree of shift in the hysteresis loops which reveals that all the powders are nano-scale materials. As to whether these materials are ferro- or ferri- or para-magnetic, the loops show a very small amount of squareness, of the order of 10^{-2} , and a very small opening in the loops [typical values of $H_c^+ - H_c^-$ of the order of 10^{-2}]. This points to the fact that these materials are largely para-magnetic. However, there is a finite coercivity (Figure 4.7 d and e) in samples (from 17 to 300 G) showing there is a degree of ferro-magnetic order in this paramagnetic matrix.

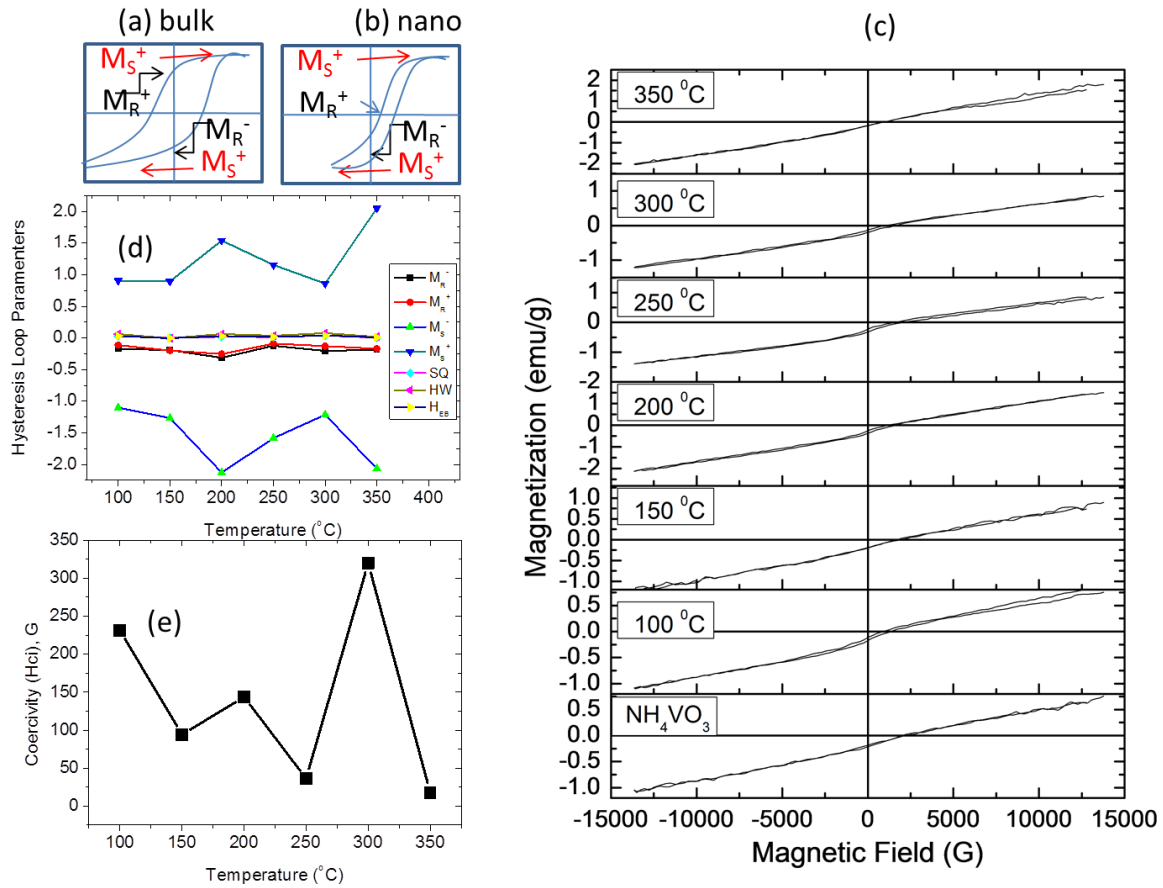


Figure 4.7: Vibrating sample magnetometry (VSM) for VO_x samples annealed at 100, 150, 200, 250, 300 and 350 °C (a) Parameters definition for a hysteresis loop for bulk and nano materials (b) Hysteresis loops for VO_x samples annealed at 100, 150, 200, 250, 300 and 350 °C and (c) A plot of the hysteresis loop parameters against annealing temperatures.

In Table 3 we give a summary of the parameters of remanent magnetization (M_R^+ and M_R^-), saturation magnetization (M_S^+ and M_S^-) and squareness (SQ) as well hysteresis width and exchange bias width obtained from the hysteresis loops given in Figure 4.7 (b). The hysteresis width has been estimated to be proportional to the loop opening in the vertical axis which is the difference between M_R^+ and M_R^- .

$$HW \propto (M_R^+ - M_R^-) = k(M_R^-(high) - M_R^-(low)) \quad (4.2)$$

The exchange bias width has been estimated to be half of this opening as previously done [50].

$$H_{EB} \propto \frac{(M_R^+ - M_R^-)}{2} = \frac{k}{2} (M_R^-(high) - M_R^-(low)) \quad (4.3)$$

A plot of these parameters for all annealed samples is given in Figure 4.7 (d,e) and it is interesting to note that coercivity generally decreases with annealing temperature although it shows a high point at 300 °C, whereas remanent magnetization (M_R^+ and M_R^-), saturation magnetization (M_S^+ and M_S^-) all show the lowest values at 200 °C. At the former temperature, it is interesting to note that this is a transition temperature from V_6O_{13} to V_2O_5 and the latter is a transition temperature from VO_2 to V_6O_{13} . VSM confirms the following order of appearance: $VO_2 \rightarrow V_6O_{13} \rightarrow V_2O_5$ as temperatures of annealing are elevated.

Table 4.3: A summary of the hysteresis loop parameters of remanent magnetization (M_R^+ and M_R^-), saturation magnetization (M_S^+ and M_S^-) and squareness (SQ) as well as hysteresis width and exchange bias width

Annealing	Coercivity	MR	MR	MS	MS	Squareness	Loop opening	Exchange bias
Temp °C	(Hci), G	Negative, emu/g	Positive, emu/g	Negative, emu/g	Positive, emu/g		emu/g	emu/g
100	231.12	-0.17	-0.11	-1.1	0.9	0.03	0.06	0.03
150	94.32	-0.19	-0.2	-1.26	0.89	0	-0.01	0
200	143.64	-0.31	-0.25	-2.13	1.54	0.02	0.06	0.03
250	36.42	-0.12	-0.09	-1.58	1.15	0.01	0.04	0.02
300	320.09	-0.2	-0.13	-1.21	0.86	0.04	0.08	0.04
350	17.9	-0.19	-0.17	-2.06	2.05	0	0.02	0.01

4.3.9 Brunauer-Emmett-Teller (BET)

Brunauer-Emmett-Teller theory relies on the physical adsorption (physisorption) of gas molecules on the surface of solid-state materials. This technique gives information about the specific surface area of a nano-material. This theory is an extension of Langmuir theory which described the amount of adsorbed molecules (adsorbate) on the surface of material (adsorbent) as a function of pressures or concentration [51]. The BET equation is expressed below in Equation. (4.2),

$$\frac{1}{v\left(\frac{p_0}{p}-1\right)} = \frac{c-1}{v_m c} \left(\frac{p}{p_0}\right) + \frac{1}{v_m c} \quad (4.4)$$

where p and p_0 are the equilibrium and saturation pressure of the adsorbate at the temperature of adsorption, v is the adsorbed gas quantity, v_m is the monolayer adsorbed gas quantity and c is the BET constant.

The BET measurements were carried out for standard and calcined NH_4VO_3 at various temperatures 100 to 350⁰C. The change in N_2 adsorption with partial pressure for the sample calcined at 250⁰C is shown in Figure 4.8(a). The monolayer adsorbed gas v_m and BET constant c were measured as the intercept of linear plot of $1/v(p_0/p - 1)$ and p/p_0 , shown in inset image in Figure 4.8(a). The BET surface area ($S_{\text{BET}} = v_m \cdot N_s / Va$, where N_s is Avogadro's number, V is molar volume of adsorbate gas and a is the mass of the adsorbent) of calcined samples were calculated and are shown in Figure 4.8 (b). The surface area is found to increase with the calcination temperatures. It follows the Langmuir isotherms pattern with temperatures.

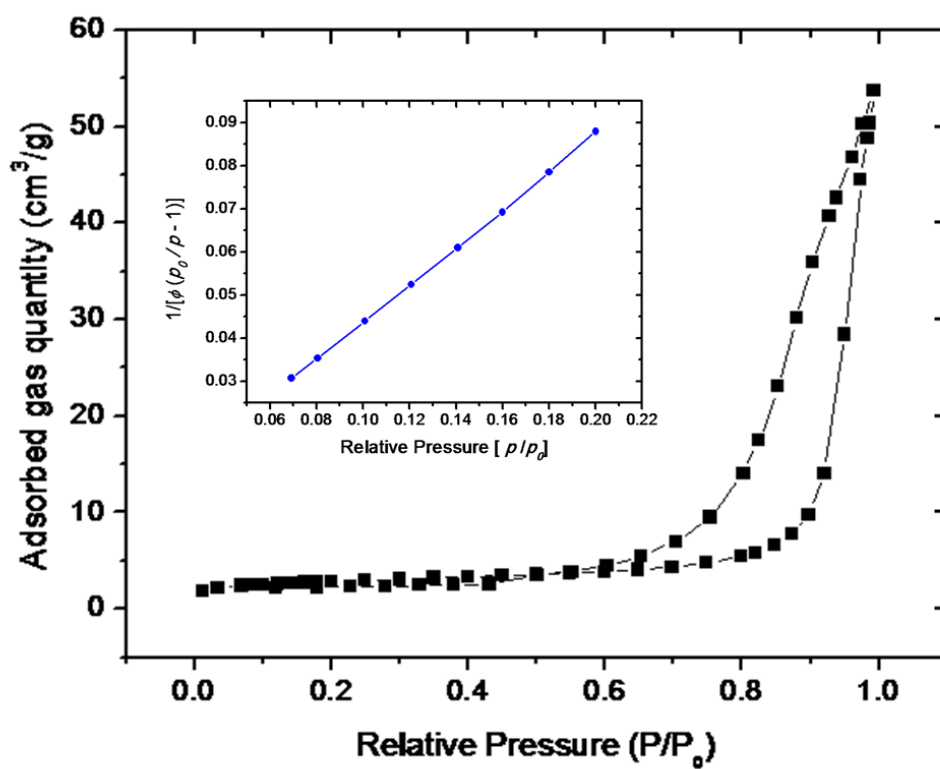


Figure 4.8: (a) N₂ adsorption and desorption isotherms profile of the powder annealed at 250 °C, insert is the BET plot.

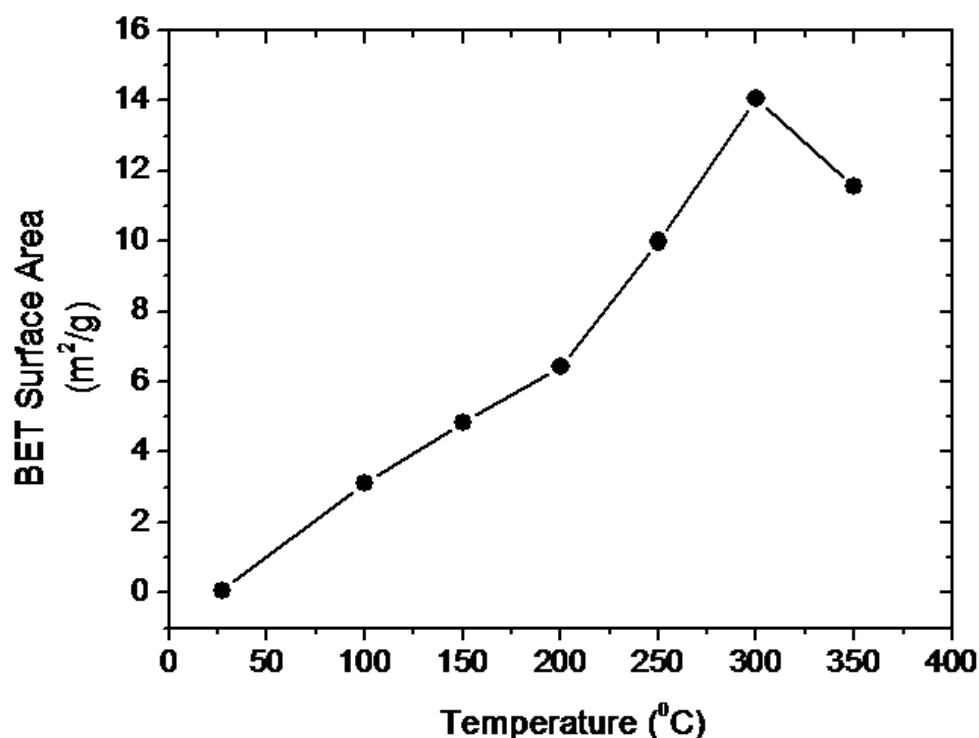


Figure 4.8: (b) BET surface area versus temperature for all the annealed powders and including NH_4VO_3 .

4.3.10 Applications: Humidity Sensing.

The VO_2 phase of VO_x semiconductors has been employed in sensing of hydrogen [52, 53]. In this present work, we have also subjected the VO_x samples annealed at 150 °C (VO_2), 250 °C (V_6O_{13}) and 350 °C (V_2O_5) to the sensing of humidity. The transient profiles of the current through the sample placed on inter-digitated electrodes in the presence or absence of varying humidity levels are shown in Figure 4.9 (a). Each time the humidity level is allowed in the chamber, the current through the samples decreases. This means that all VO_x samples gain resistance upon interaction with water vapour. Since all these VO_x phases are known to show n-type conductivity, we could explain the increase in resistance as an indication of water molecules taking away electrons or O^{2-} species from VO_x surfaces during adsorption but releasing these electrons back on desorption as discussed in the section (3.2.1) in chapter

three. In Figure 4.9 (b) we plot response [defined as $S = (I_{out}-I_{in})/I_{in}$] as a function of humidity level. This plot reveals the Langmuir type of adsorption-desorption isotherms.

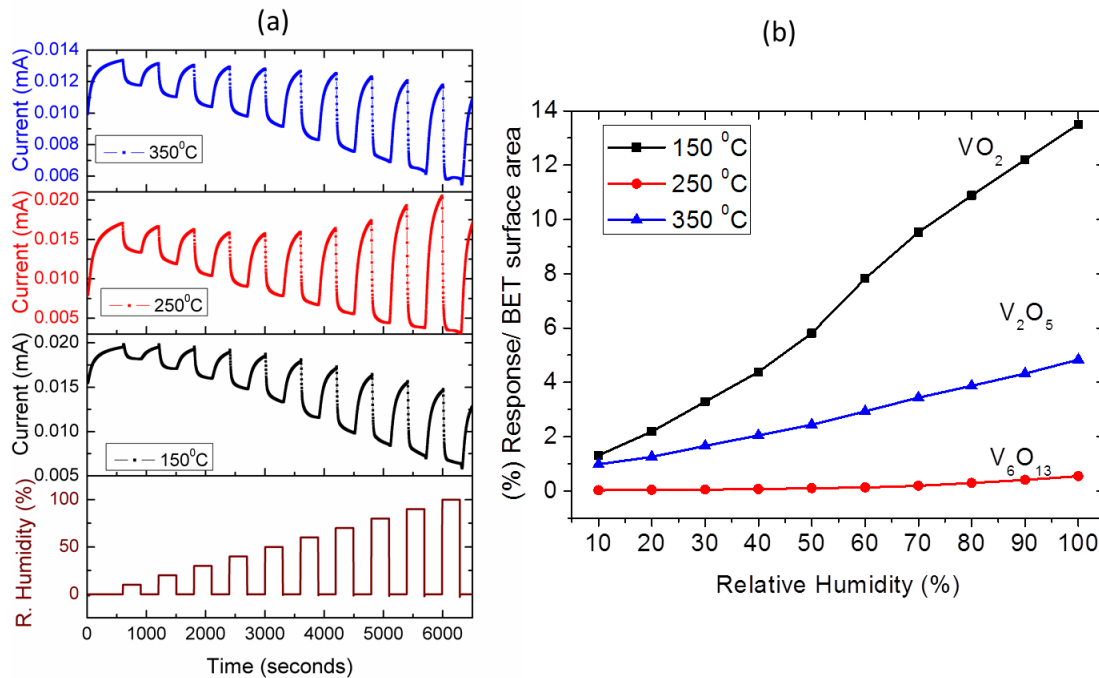


Figure 4.9: (a) Transient profiles of current through the VO_x samples in varying levels of humidity (b) Responses weighted against BET surface area for VO_x samples as a function of humidity level.

4.4 Conclusion

A few milligrams of ammonium metavanadate powders were calcined in pure hydrogen atmosphere at temperatures of 100, 150, 200, 250, 300 and 350 °C. The samples were characterized by TGA/DSC, XRD, TEM, Raman spectroscopy, FTIR, BET, VSM and XPS/EDS. All these characterization methods lead us to conclude that the progression from NH₄VO₃ to V₂O₅ is as follows: NH₄VO₃ → VO₂ + V₂O₅ (150-200°C) → V₆O₁₃ (300°C) → V₂O₅ (above 325°C). At no temperature does one find a single phase; each temperature of

calcinations will have a major and a minor phase or a number minor phases. The total surface area appears to increase with a decreasing rate as the temperature of calcinations is increased. A phase diagram based on XRD and Raman has been constructed for VO_2 , V_6O_{13} and V_2O_5 . XPS/EDS analysis agrees with this phase diagram. It is also found that VSM confirms the order of $\text{VO}_2 \rightarrow \text{V}_6\text{O}_{13} \rightarrow \text{V}_2\text{O}_5$ transitions as temperatures of annealing are elevated.

References

- [1] X. Chen, X. Wang, Z. Wang, J. Wan, J. Liu, Y. Qian, An ethylene glycol reduction approach to metastable VO₂ nanowire arrays, *Nanotech.* **15** 1685-1687, (2004).
- [2] M. Imada, A. Fujimori, Y. Tokura, Metal-insulator transitions, *Rev. of Modern Phys.* **70**, No.4 1039-1263 (1998).
- [3] N.F. Mott, Metal-insulator Transition, *Rev. Modern Phys.* **40**, 4, (1968) 677.
- [4] D. Adler, Mechanisms for Metal-Nonmetal Transitions in Transitions-Metal Oxides and Sulfides, *Rev. Modern Phys.* **40**, 4, 714-736, (1968).
- [5] F.J. Morin, Oxides which show a metal-insulator-transition at Neel temperature, *Phys. Rev. Lett.* **3**, (1959) 34.
- [6] J.B. Goodenough, The two components of Crystallographic transition in VO₂, *J. Solid State Chem.* **3**, 490-500 (1971).
- [7] S. Shin, S. Suga, M. Tanuguchi, M. Fujisawa, H. Kanski, A. Fujimori, H. Damon, Y. Ueda, K. Kosuge, S. Kachi, Vacuum-ultraviolet reflectance and photoemission study of the metal - insulator phase transitions in VO₂, V₆O₁₃, and V₂O₃, *Phys. Rev. B* **41**, 4993-5009 (1990).
- [8] J.M. Reyes, J.R. Marko, M. Sayer, Hysteresis in the Semiconductor-Metal Transition of Cr-doped VO₂, *Solid State Comm.*, **13** 1953-1957 (1973).
- [9] D. Paquet, P. Leroux-Hugon, Electron correlations and electron-lattice interactions in the metal-insulator, ferroelastic transition in VO₂: A thermodynamical study, *Phys. Rev.* **B22**, 5284-5301 (1980).
- [10] N.F. Mott, R. Peierls, Discussion of the paper by de Boer and Verwey *Proc. Phys. Soc. London, Ser. A.* **49**, 72 (1937).

- [11] A. I. Buzdin, L. N. Bulaevskii, P. N. Lebedev, Spin-Peierls transition in quasi-one dimensional crystals, Physics Institute, Academy of Sciences of the USSR, Moscow Usp Fiz Nauk, **131**, 495-510 (1980).
- [12] G.I. Petrov, V.V. Yakovlev, Raman microscopy analysis of phase transformation mechanisms in vanadium dioxide, App. Phys. Lett. **81**, No. 6 (2002).
- [13] S.-Y. Li, G. A. Niklasson, and C. G. Granqvist, Nanothermochromics: Calculations for VO₂ nanoparticles in dielectric hosts show much improved luminous transmittance and solar energy transmittance modulation, J. Appl. Phys. **108**, 063525 (2010).
- [14] R. Lopez, R. F. Haglund, Jr., L. C. Feldman, L. A. Boatner, T. E. Hayness, Optical nonlinearities in VO₂ nanoparticles and thin films, App. Phys. Lett **85**, (2004).
- [15] S. Lysenko, A. Rua, F. Fernandez, H. Liu, Vanadium dioxide based plasmonic modulators, J. Appl. Phys. **105**, 043502 (2009)
- [16] J. Cao, W. Fan, J-Q. Wu, Strain and temperature dependence of the insulating phases of VO₂ near the metal-insulator transition, Phys. Rev. B **85**, 020101(R) (2012)
- [17] Z. Lu, C-G.Lia, Y. Yin, Synthesis and thermochromic properties of vanadium dioxide colloidal Particles, J. Mater. Chem., **21**, 14776-14782 (2011)
- [18] E .U. Donev, J. I. Ziegler, R. F Haglund Jr., L. C. Feldman, Size effects in the structural phase transition of VO₂ nanoparticles studied by surface-enhanced Raman scattering, J. Opt. A: Pure Appl. Opt. **11**, 125002, (2009).
- [19] A. C. Jones, S. Berweger, J. Wei, D. Cobden, M. B. Raschke, Nano-optical investigations of the metal-insulator phase behaviour of individual VO₂ microcrystals, Nano Lett. **10**, 1574–1581, (2010).
- [20] M. Maaza, O. Nemraoui, C. Sella, A. C. Beye, B. Baruch-Barak, Thermal induced tenability of surface plasmon resonance in Au-VO₂ nano-photonics, Optics Comm. **254** 188-195, (2005).

- [21] A. Pergament, G. Stefanovich, O. Berezina, D. Kirienko, Electrical conductivity of tungsten doped vanadium dioxide obtained by the sol-gel technique, *Thin Solid Films*, **531**, 572-576 (2013)
- [22] Y. Gao, H. Luo, Z. Zhang, L. Kang, Z. Chen, J. Du, M. Kanehira, C. Cao, Nanoceramic VO₂ thermochromic smart glass: A review on progress in solution processing, *Nano Energy* **1**, 221-246, (2012).
- [23] W. Burkhardt, T. Christmann, B.K. Meyer, W. Niessner, D. Schalch, A. Scharmann , Wand F-doped VO₂ films studied by photoelectron spectrometry, *Thin Sol. Films.* **345**, 229-235, (1999).
- [24] O. Y. Berezina, A. A. Velichko, L.A. Lugovskaya, A.L. Pergament, G.B. Stefanovich, D.V. Artyukhin, A. N. Strelko, Properties of Tungsten-Doped Vanadium Oxide Films, *Tech. Phys. Lett.* **33**, 7, 552-555, (2007).
- [25] R. Binions, G. Hyett, C. Piccirillo, I. P. Parkin, Doped and Undoped vanadium dioxide thin films prepared by atmospheric pressure chemical vapour deposition from vanadyl acetylacetonate and tungsten hexachloride: the effects of thickness and crystallographic orientation on thermocromic properties, *J. Mat. Chem.* **17**, 4652-4660 (2007)
- [26] E. Strelcov, Y. Lilach, A. Kolmakov, Gas Sensor Based on Metal-Insulator Transition in VO₂ Nanowire Thermistor, *Nano Letters* **9**, No. 6, 2322-23269, (2009)
- [27] C.G. Granqvist, Electrochromic tungsten oxide films: Review of progress 1993- 1998, *Solar Energy Mat. Solar Cells* **60**, 201- 262, (2000).
- [28] J. Livage, D. Ganguli, Sol-gel electrochromic coatings and devices: A review, *Solar Energy Mat. Solar Cells* **68**, 365-381, (2001).
- [29] J. Huotari, A. L. Spetz, J. Lappalainen, Gas Sensing Properties of Pulsed Laser Deposited Vanadium Oxide Thin Films, The 14th International Meeting on Chemical Sensors, IMCS 2012.

- [30] M.C. Rao, Vanadium Pentoxide Cathode Material for Fabrication of All Solid State Lithium-Ion Batteries - A Case Study, *Res. J. Recent Sci.* **2**, 3, 67-73, (2013)
- [31] P. Kiria, G. Hyettb, R. Binions, Solid state thermochromic materials, *Adv. Mat. Lett.* **1**, 2, 86-105, (2010).
- [32] H. Bai, M. Berkahn, M.B. Cortie, 31 Annual Condensed Matter and Materials 2007
- [33] L. Chen, Ch. Huang, G. Xu, L. Miao, J. Shi, J. Zhou, X. Xiao, Synthesis of Thermochromic W-Doped VO₂ (M/R) Nanopowders by a Simple Solution-Based Process, *J. Nanomaterials*, 1-8, (2012).
- [34] M. Taniguchi, T.R. Ingraham, Mechanism of thermal decomposition of Ammonium metavanadate, *Canadian Journal of Chemistry*, **42**, 11, 2467-2473, (1964).
- [35] B.W. Mwakikunga, E. Sidras-Haddad, M. Maaza, First synthesis of vanadium dioxide by ultrasonic nebula-spray pyrolysis, *Optical Materials* **29**, 481-487, (2007).
- [36] B.W. Mwakikunga, M. Maaza, K.T. Hillie, C.J. Arendse, T. Malwela, E. Sideras-Haddad, From phonon confinement to phonon splitting in flat single nanostructures: A case of VO₂@V₂O₅ core-shell nano-ribbons, *Vib.l Spect.*, **02**, 105-111, (2012).
- [37] X. Wua, Y. Taa, L. Donga, Z. Wangb, Z. Hua, Preparation of VO₂ nanowire and their characterization, *Mat. Res. Bullet.* **40**, 315-321, (2005)
- [38] S. Zinzuvadiya, U. S. Joshi, *AIP Conf. Proc.* **1837**, 040053, 1 - 4, (2017).
- [39] M. Kang, S.W. Kim, J.-W.Ryu, High temperature-high pressure, **45**, 5-6, 415-423, (2016)
- [40] U.V. Sacken, J.R. Dahn, TGA/MS Studies of the thermal decomposition of NH₄VO₃, *J. Power Sources*, **26**, 461-465, (1989)
- [41] M.E. Brown, B.V. Stewart, The thermal decomposition of ammonium metavanadate, *J. Thermal Anal.* **2**, 287-299, (1970).

- [42] R. F. Karlak, D. S. Burnett, Quantitative phase analysis by X-ray diffraction, *Analytical Chem.* **38**, 1741-1745, (1966).
- [43] J. Twu, C-F. Shih, T-H, Guo, K-H, Chen, Raman spectroscopic studies of the thermal decomposition mechanism of ammonium metavanadate, *J. Mater. Chem.*, **7**, 11, 2273-2277, (1997)
- [44] C. Julien, G. A. Nazri, and O. Bergstrom, Raman Scattering Studies of Microcrystalline V_6O_{13} , *Phys. Stat. Solidi B* **201**, 319-326 (1997)
- [45] D. Vernardou, M. Apostolopoulou, D. Louloudakis, E. Spanakis, N. Katsarakis, E. Koudoumas, J. MacGrath, M.E Pemble, Electrochemical properties of Opal- V_6O_{13} composites, *J. Alloy Comp.* **582**, 621-626, (2014)
- [46] K. Virkler, I. K. Lednev, Raman spectroscopic signature of semen and its potential application to forensic body fluid identification, *Forensic Science International* **193**, 56–62, (2009)
- [47] I.L. Botto, M.B. Vassallo, E.J. Baran, G. Minelli, IR spectra of VO_2 and V_2O_5 , *Matt. Chem. and Phy.* **50**, 267-270, (1997).
- [48] A.A. Akande , K. E. Rammutla, T. Moyo, N. S.E. Osman, Steven S. Nkosi, C.J. Jafta, Bonex W. Mwakikunga, Magnetism variations and susceptibility hysteresis at the metal-insulator phase transition temperature of VO_2 in a composite film containing vanadium and tungsten oxides, *J. Magn. Magn. Mater.* **375**, 1–9, (2015)
- [49]] J. Nogués, J. Sort, V. Langlais, V. Skumryev, S. Surinack, J.S. Munoz, M.D. Baró, Exchange bias in nanostructures, *Phys. Rep.* **422**, 65–117, (2005)
- [50] K. Mbela, T. Moyo, J.Z. Msomi, M. Ozturk, N. Akdogan, Synthesis and magnetic properties of $Mg_{0.2}Cr_{1.8-x}Fe_xO_3$, *J. Magn. Magn. Mater.* **330**, 159-162, (2013)
- [51] S. Brunauer , P. H. Emmett , E. Teller, Adsorption of Gases in Multimolecular Layers, *J. Am. Chem. Soc.*, **60**, 2, pp 309–319 (1938).

[52] B. W. Mwakikunga, S. Motshekga, L. Sikhwivhilu, Mathew Moodley, M. Scriba, Gerald Malgas, A. Simo, B. Sone, M. Maaza, S. S. Ray, A classification and ranking system on the H₂ gas sensing capabilities of nanomaterials based on proposed coefficients of sensor performance and sensor efficiency equations, *Sensors & Actuators B* **184**, 170–178, (2013)

[53] A. Simo, B. Mwakikunga, B. T. Sone, B. Julies, R. Madjoe, M. Maaza, VO₂ nanostructures based chemiresistors for low power energy consumption hydrogen sensing, *Int. J. of Hydro. Energy* **39**, 8147 – 8157, (2014)

CHAPTER 5

SELECTIVE ADSORPTION OF H₂S GAS TO VANADIUM MIXED VALENCE STATE V₆O₁₃ NANORODS PARTICLE

Following our conclusions from the annealing of NH₄VO₃ in the reducing atmosphere, the stable characteristics of V₂O₅ and its sensing properties in chapter 4 of this thesis, we decided to obtain V₂O₅ nanostructures in an inert atmosphere at different annealing times. V₆O₁₃ and V₂O₅ nanorods were obtained. Preferential adsorption of the V₆O₁₃ particles to H₂S among CH₄, NO₂, H₂, NH₃ and CO gases is discussed. A theoretical investigation of this selective adsorption is studied by *ab initio* molecular dynamics.

5.1 Introduction

Hydrogen Sulphide (H₂S) is among the most toxic, poisonous, flammable and odorant gases which are usually a by-product of crude petroleum, natural and volcanic gases. This gas has been reported to be life-threatening to human health and can cause death in very high concentration and within short time of exposure [1-5]. The American Conference of Government Industrial Hygienists (ACGIH) has established a threshold limit of 10 ppm as a safety standard for H₂S gas [4]. Many other agencies have reported that concentrations higher than 250 ppm cause death of humans and animals within a short time of exposure [5]. Research based on sensor quality assurance has also shown that H₂S molecules are not only harmful to humans but can also pose a threat of poisoning or contamination to chemical sensors [5-7]. Metal oxides nanostructures and carbon based materials such as Cu nanowires, SnO₂, WO₃, TiO₂, MoO₃ Nanowires and NiO porous nanoballs [8-14] have been applied to detect

H₂S gas in the past. However, selectivity and stability of these materials to H₂S gas have posed many challenges towards applying the technologies in the commercial world. In this chapter, we report novel characteristics of V₆O₁₃ nanorods in the sensitivity and selectivity of H₂S gas. This novelty points to the high response of the V₆O₁₃ to H₂S compared with other gases and its remarkable short response and recovery times. Theoretical investigation of the adsorption process and energy between the interface of H₂S and the sensor material also support our observations.

5.2. Experimental and Computational techniques

5.2.1 Powder Synthesis

Decomposition of Ammonium meta-vanadate (NH₄VO₃) and Vanadium oxides phases progression of this precursor was studied in detail in chapter four [15] using differential DSC, TGA, XRD, TEM, EDX, XPS, FTIR and Raman spectroscopy. Based on these analyses, the calcination/annealing temperature of the nanostructures produced in this study has been selected. An amount of NH₄VO₃ was heat-treated during solid-state reaction in a furnace at 500 °C for 2, 12 and 24 hours in nitrogen atmospheric conditions. Nano-powders whose colours progressed from deep tangerine orange to pure orange as a function of the reaction time were obtained.

5.2.2 Powder Characterization

These nano-powders were characterized to extract their crystal structural information using Panalytical XPERT PRO PW3050/50 diffractometer with CuK α radiation (45 kV, 400 mA, $\lambda = 0.1540598$ nm and $5^\circ \leq 2\theta \leq 90^\circ$). Microstructure studies were carried out using JEOL 2100 Transmission Electron Microscopy (TEM) (from Tokyo Japan) equipped with a LaB6 filament and a Gatan U1000 camera of 2028 \times 2028 pixels, and a high quality in-built

Energy dispersive X-ray spectroscopy (EDS) set-up. Surface morphology studies of these nano-powders were achieved through LEO 1525 field emission scanning electron microscope (FE-SEM).

Raman Spectrograph (RS) Jobin–Yvon T64000 with a 514.5 nm excitation wavelength from an argon ion laser was used for vibrational and rotational aspects of the structural information. These samples were excited by 10 kV electron beam for cathode-luminescence (CL) measurements on a FE-SEM Jeol (6330) at room temperature. Magnetic characterization was performed using Lakeshore 735 vibrating sample magnetometer (VSM) at room temperature.

5. 2.3 Gas sensing measurement/test

The gas sensing tests were carried out using KSGA565 KENOSISTEC instrument from Italy. The sensing electrodes were prepared by ultrasonically dispersing the nanoparticles in the organic solvent for 30 minutes and later drop casting the solution onto an Al₂O₃-Pt interdigitated electrode (IDE) with heating terminal at the reverse side. The whole schematic arrangement of the measurement process is illustrated in Figure 5.1.

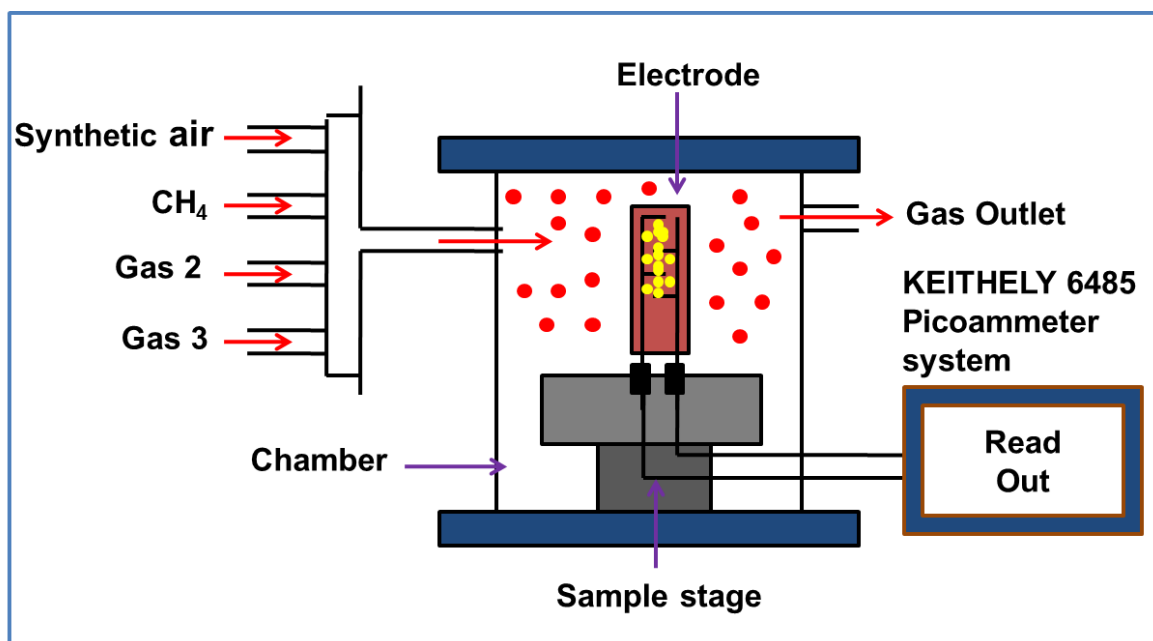


Figure 5.1: Schematic diagram of KSGA565 KENOSISTEC sensing station illustrating how the gas sensing measurement was performed.

5.2.4 Computational procedures

The computational part of this work is carried out by density functional theory of BIOVIA material studio package hosted and controlled at the Centre for High Performance Computing (CHPC) Cape Town, South Africa. The unit cell files were obtained from the Material Project database [16]. These unit cells were optimized for geometric relaxation, electronic self-consistency and convergence by generalized gradient approximation (GGA) using the Perdew-Burke-Ernzerhof (PBE) functional [17-19]. The exchange-correlation convergence tests were performed by setting the k-point set to $1 \times 1 \times 1$ and basis set to 3.5. These approximations were achieved using Dmol3 code. The surface (110) of V_6O_{13} and V_2O_5 primitive unit cells was cleaved and extended by 2×2 along the a- and b- directions. The molecule H_2S , built using sketch atom function, is also optimized by GGA-PBE approximations. For the gas adsorption calculations, adsorption locator code which is part of

the BIOVIA package was employed. A uniform vacuum spacing of 20 nm was maintained in all calculations.

4.3. Results and Discussions

X-ray diffraction spectra of the sample annealed at 500 °C for 2, 12 and 24 hours are shown in Figure 5.2. The spectra showed two close phases of VO_x ; V_6O_{13} (2 hrs) and V_2O_5 (12 and 24 hrs). Both phases are polycrystalline and were indexed using PDF #43-1050 and PDF #41-1426 to identify the planes present in the crystals. The three spectrums in Jade 6 environment showed strong Bragg positions. The V_6O_{13} sample is monoclinic with rod-like microstructures as shown by the TEM results in Figure 5.3 (a) and (b), while V_2O_5 samples are orthorhombic structures of short rods growing from bundles of layered sheets as shown by the Figure 5.3 (c) and (d). Figure 5.3 (c) is the corresponding EDS spectrum of (a) showing the quality of V and O atoms and depicting the purity of the sample. Samples' morphologies by the FE-SEM in Figure 5.4 shows clusters of rod particles. These images show the growth pattern of the particles with Figure 5.4 (a) (sample prepared at 2 hrs) showing longer rods with less agglomeration compared with the Figure 5.4 (b) (sample prepared at 12 hrs) and (c) (sample prepared at 24 hrs) whose rod particles were short. It is also observed that the long-time heating effect on the particles in Figure 5.4 (c) and (d) causes the particles to expand and melt gradually. This is consistent with the TEM observations in Figure 5.3 and the V_2O_5 stability reported in chapter four. Raman spectra in Figure 5.5 show vibrations corresponding to the V_2O_5 modes. Figure 5.5 (a) shows that the spectrum of the sample annealed at 2 hours is similar to the rest; this is common in V_6O_{13} structures since they share a similar layered structure with the V_2O_5 structure. However, the appearance of the peak at 102 cm^{-1} confirms the structure to be V_6O_{13} [15]. The spectrum of the sample annealed at 12 hours is observed to be red shifted to a lower frequency and lower diffraction angle (by XRD analysis), implying larger lattice parameters than the V_2O_5

structure annealed at 24 hrs. The shows that the particles which initially expanded at 12 hours are now relaxing from their thermal strain at 24 hours.

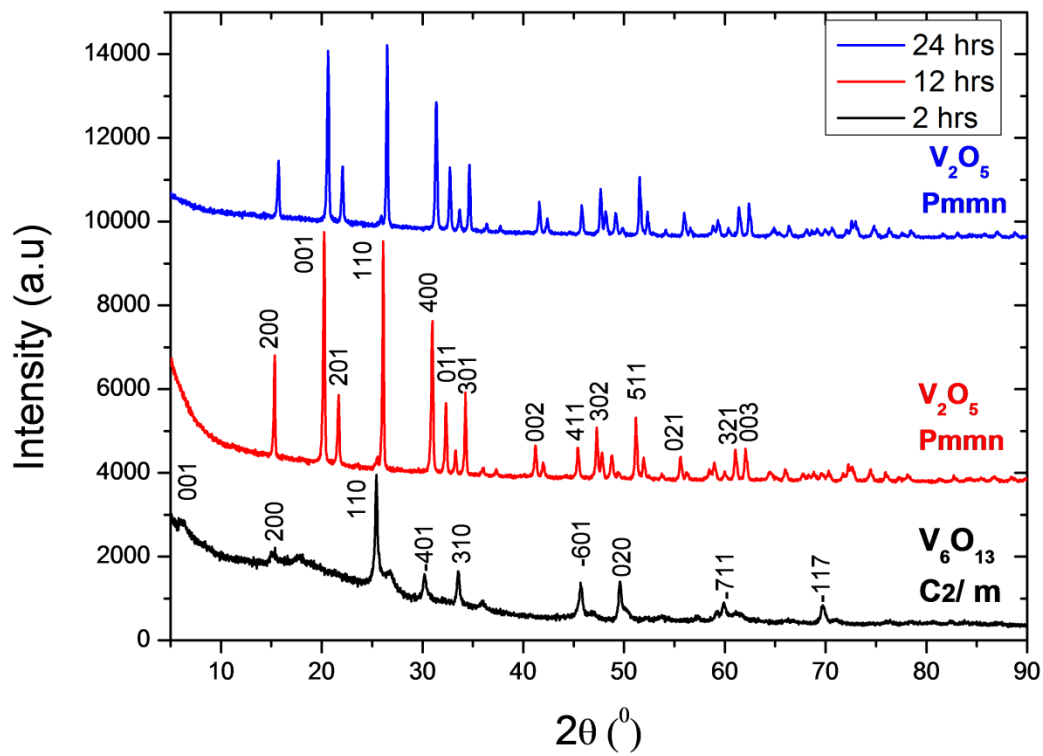


Figure 5.2: XRD spectra of the samples prepared by thermal annealing of NH_4VO_3 500 $^{\circ}C$ at for 2, 12, and 24 hours.

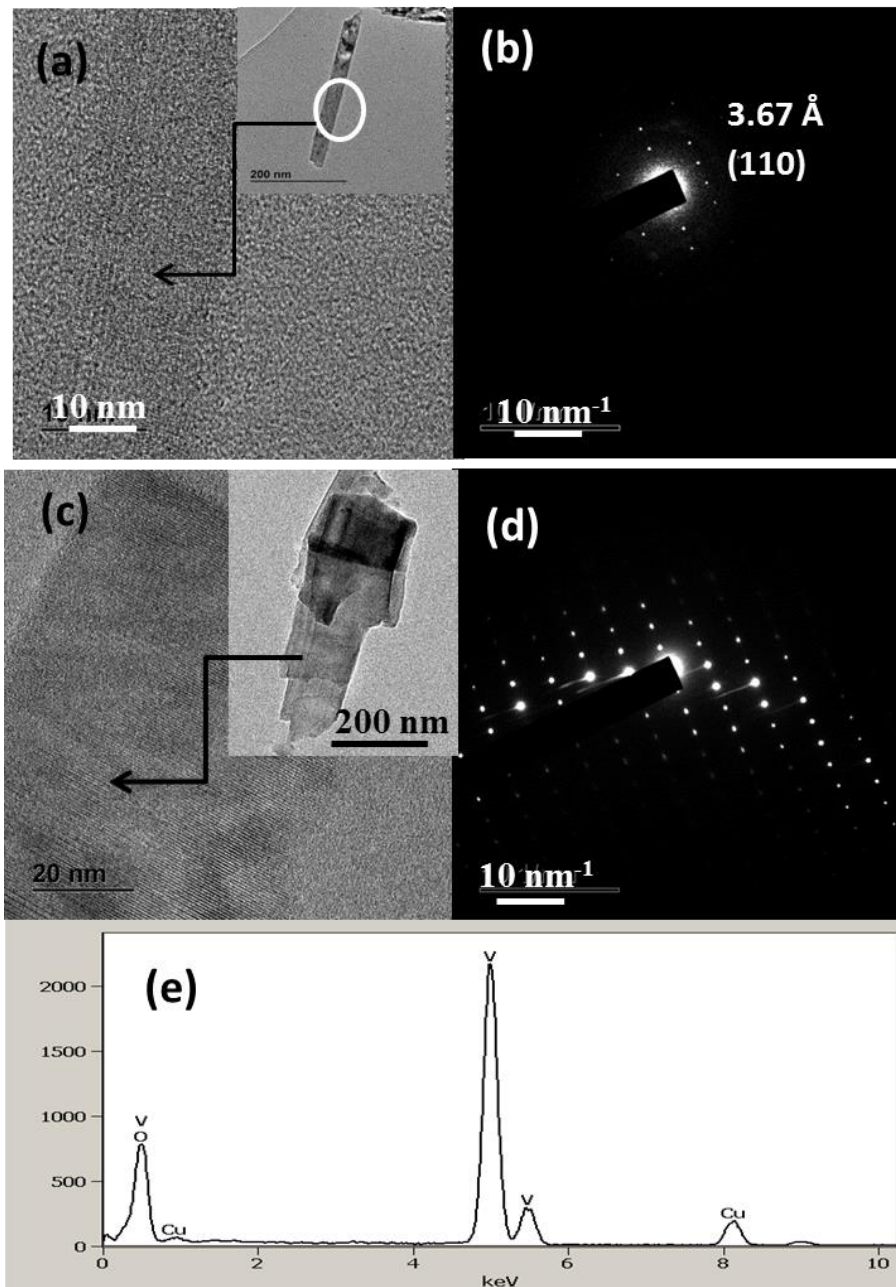


Figure 5.3 (a): Low and HRTEM images of V₆O₁₃, (b) SAED of V₆O₁₃ (110) plane of the structure, (c) Low and HRTEM images of V₂O₅ (prepared for 12 hrs), (c) SAED of V₂O₅ (prepared for 12 hrs), and (e) corresponding EDX spectrum of (a).

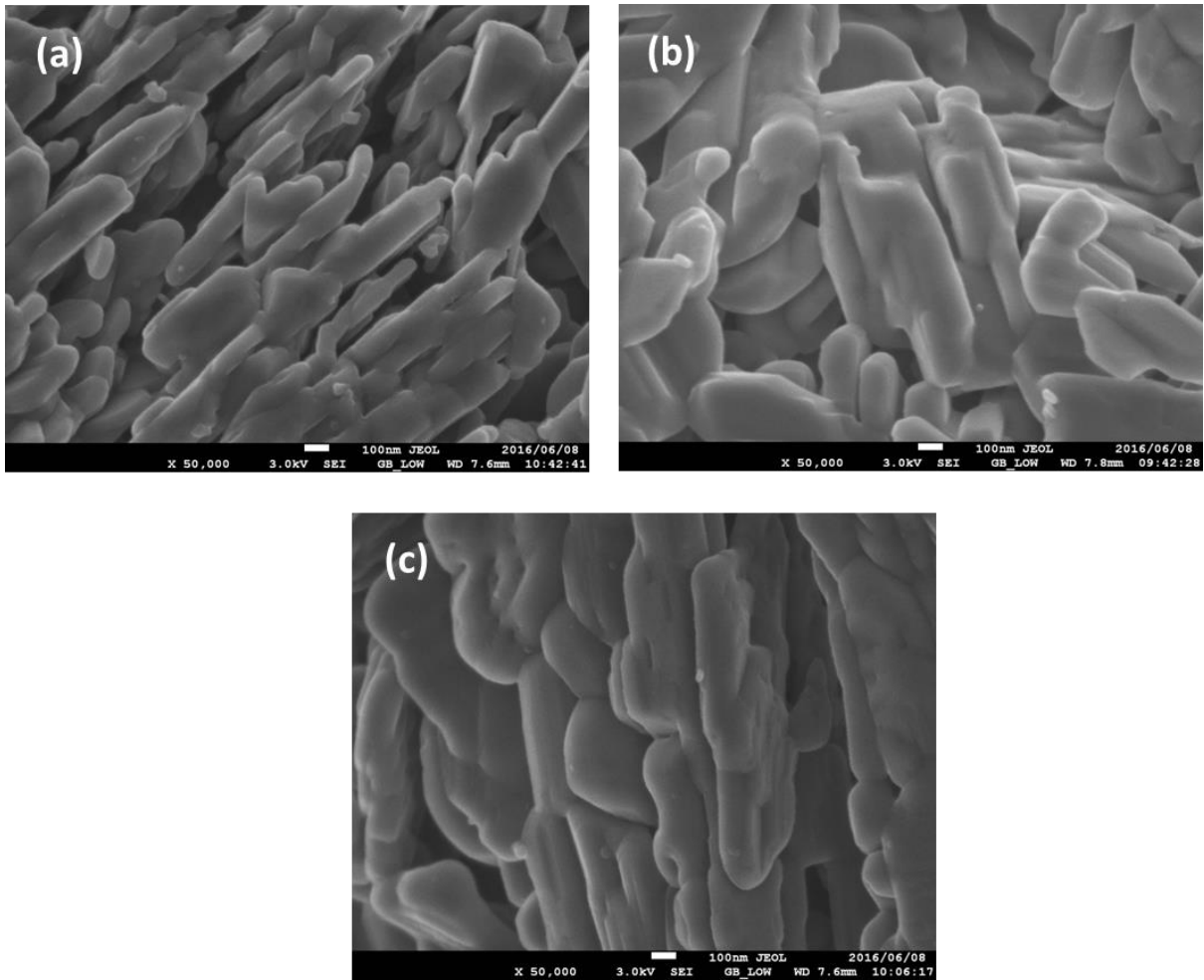


Figure 5.4: FE-SEM images of (a) V_6O_{13} , (b) V_2O_5 (prepared for 12 hrs), (c) V_2O_5 (prepared for 24 hrs),

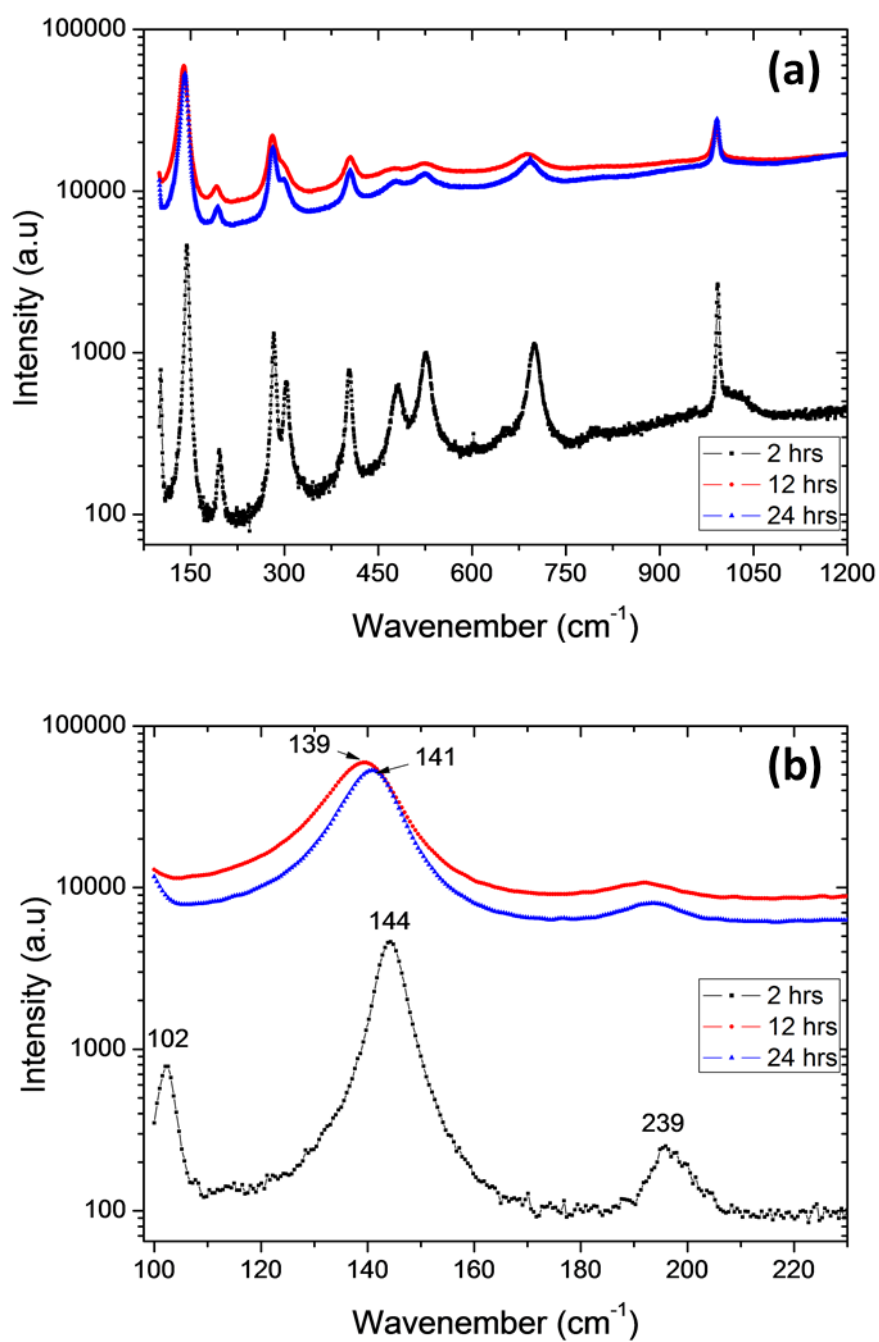


Figure 5.5: (a) Raman spectra of the samples prepared by thermal annealing of NH_4VO_3 at 500 °C for 2, 12, and 24 hours (b) Spectra in (a) between 100 – 250 cm^{-1} range.

Table 5.1: Summary of crystallite size, strain and magnetic properties of the samples prepared by thermal annealing of NH_4VO_3 at 500 °C for 2, 12, and 24 hours.

Samples	Particle Size (nm)	Strain	Magnetic Saturation (emu/g)	Remanence Magnetization (emu/g)	Coercivity, H_{ci} , Oe
2 hrs	83	-	0.524	0.078	174.01
12 hrs	115	$4.60\text{E-}04$	0.407	0.027	83.464
24 hrs	91	$3.96\text{E-}04$	0.604	0.179	295.84

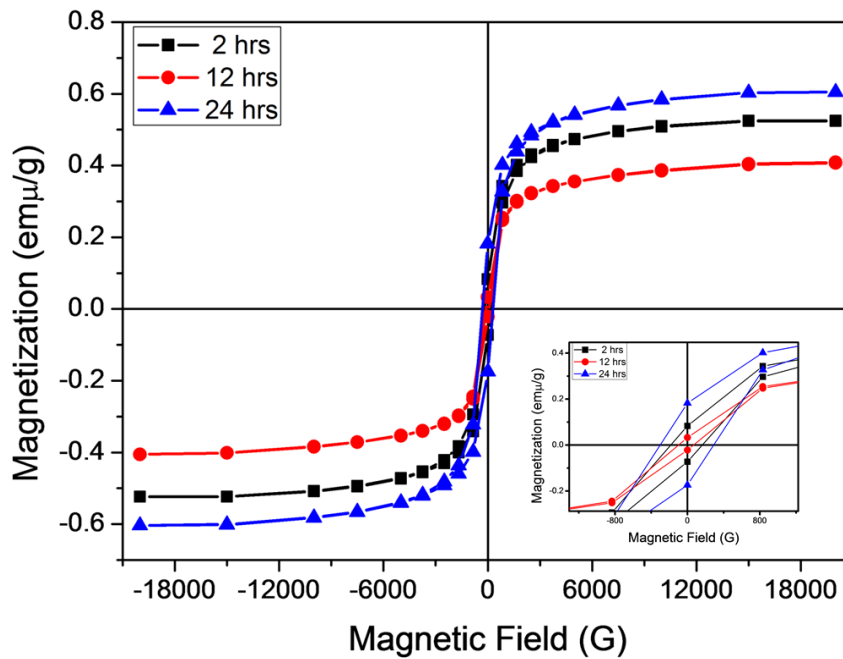


Figure 5.6: VSM profile of the samples prepared by thermal annealing of NH_4VO_3 at 500 °C for 2, 12, and 24 hours.

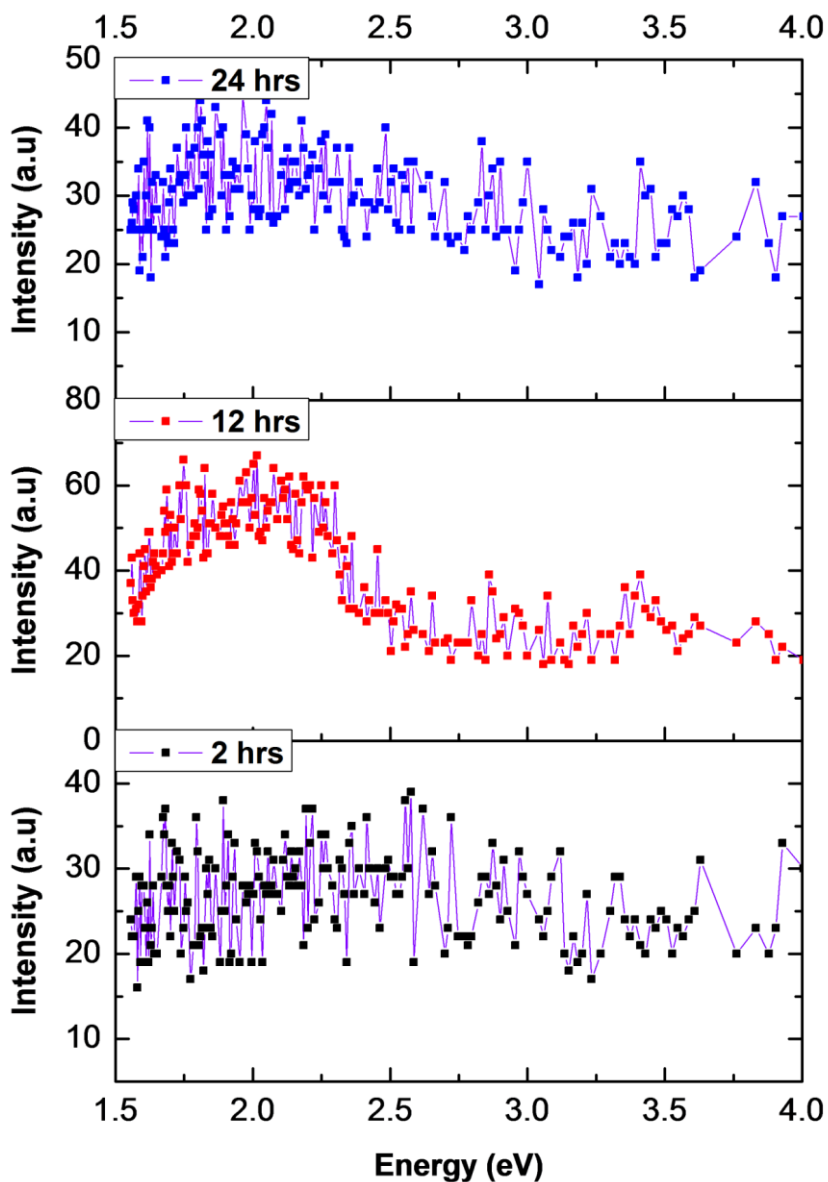


Figure 5.7: VSM profile of the samples prepared by thermal annealing of NH_4VO_3 at $500\text{ }^\circ\text{C}$ for 2, 12, and 24 hours.

Table 5.1, the summary of the characteristics of the three samples shows that the samples prepared at 2 hours is smaller in size with less strain compared with the one at 12 and 24 hours. These size and strain analyses were achieved using the Debye Scherrer and Williamson-Hall methods [20], and are related to the VSM magnetic features in Figure 5.6.

This features shows that the samples prepared at 2 and 24 hours have better magnetic properties (coercivity, remanence and saturation) compared with the one at 12 hours. This large strain may be the consequence of the particle expansion observed in the FE-SEM images of samples prepared at 12 and 24 hours Figure 5.4 (b) and (c)). Surprisingly, the sample prepared at 12 hours shows better CL emission in the Figure 5.7 than the ones at 2 and 24 hours. This emission band falls between 1.6 – 2.5 eV which happened to be the band gap of standard V₂O₅ structure (calculated and shown in chapter two). This further confirms XRD and Raman analysis in the above sections. The sample prepared at 2 and 24 hours also shows some CL emission in the same energy range but with less intensity, one can conclude that the larger strain or particle expansion promotes the CL emission of the sample prepared at 12 hours.

The transient profiles of the currents through the sample prepared at 2 hours to the synthetic air and to different concentrations of H₂S and NH₃ for 25 °C, 250 °C, 300 °C, 350 °C, and 400 °C are shown in Figure (5.8). These profiles show that the sensor is generally poor at room temperature (25 °C) during H₂S sensing Figure 5.8 (a)) and NH₃ sensing Figure 5.8 (b) which is not strange for a metal oxide material. Figure 5.9 (a) is the plot of the sensor response (sensitivity %) to H₂S gas at different concentrations. This profile shows continuous increase or adsorption of H₂S in all operating temperatures with highest and distinctive adsorption at 350 °C. A similar pattern is observed for NH₃ gas in Figure 5.9 (b) but with far less response compared to the H₂S gas. The sensor response (sensitivity) in this work is defined as;

$$S(\%) = \frac{I_{gas} - I_{air}}{I_{air}} \times 100 \quad (5.1)$$

where I_{gas} and I_{air} are the currents flowing through the nanoparticles in the presence of the analyte gas and air respectively [21].

Each time the reducing gas H_2S is introduced into the chamber, the currents through the nanoparticles (sensing electrode) increases with respect to the H_2S concentrations as shown by the $350\text{ }^\circ\text{C}$ conductometric measurement in Figure 5.10 (a). This is an indication that the sample prepared at 2 hours possesses n-type conductivity as discussed in section 3.2.1 of chapter 3. The response and recovery time of Figure 5.10 (a) calculated at 60 ppm of the H_2S gas is shown in Figure 5.10 (b). Response time in this work is defined as the time it takes the nanoparticles current to reach 90% of its maximum after exposed to the gas, while recovery time is the time taken for it to return by 90% to the original value (current value in the air/base-line). The response time is 32 seconds while the recovery time is 129 seconds showing that this sensor is remarkably strong and fast among H_2S sensors.

The same sensor was also tested for NH_3 Figure 5.8 (b) and 5.9 (b) and CH_4 , NO_2 , H_2 and CO gases, but in all gases concentrations and the sensor's operating temperatures, H_2S sensitivity is found to be about 647.2 % higher than the second ranked sensitive NH_3 which showed only 17.6 % response. This shows that V_6O_{13} nanoparticles are more selective to H_2S gas compared with the other gases. This is shown by the plot these gases responses at 60 ppm and $350\text{ }^\circ\text{C}$ in Figure 5.11 (a).

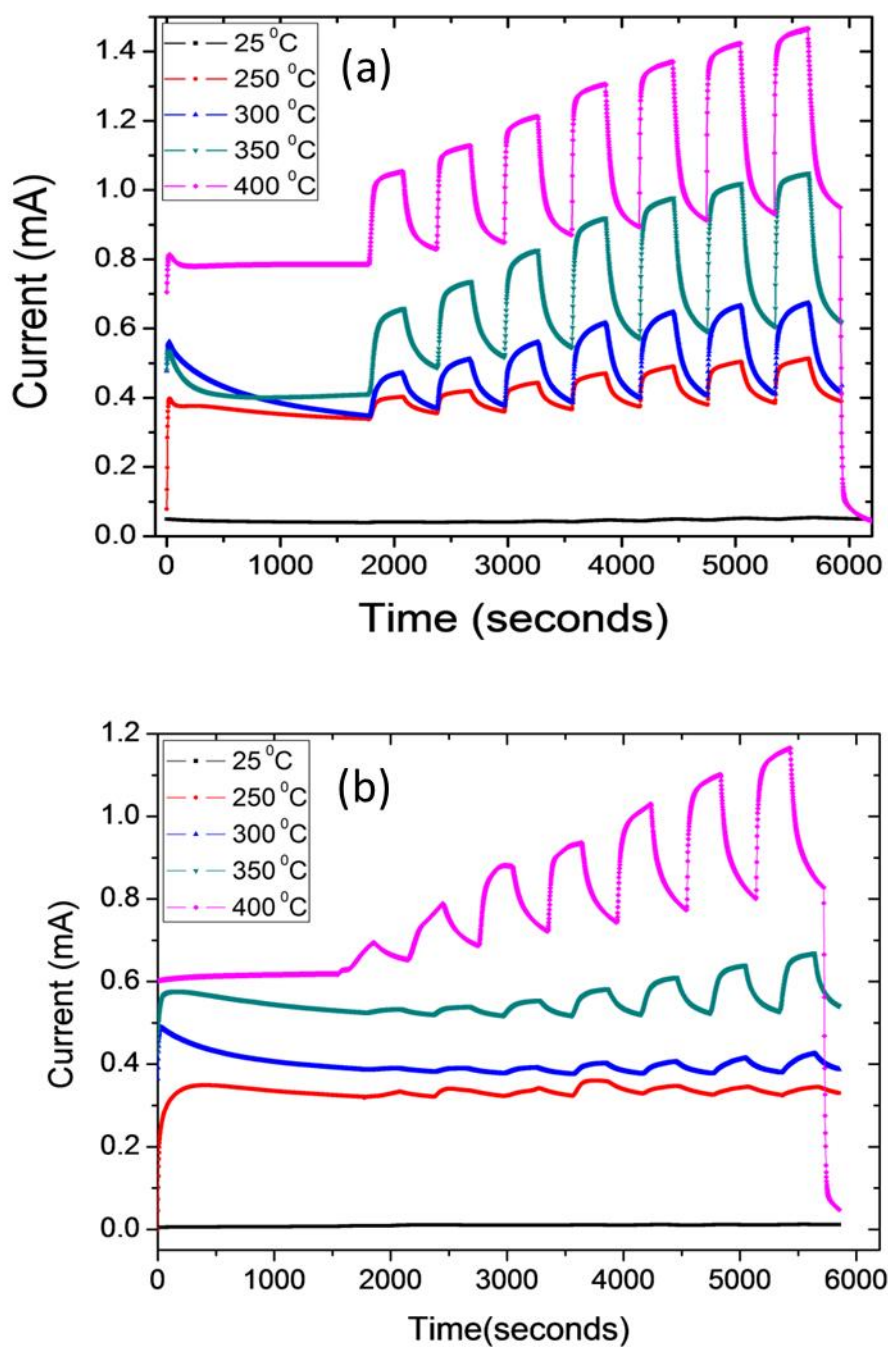


Figure 5.8: Conductometric sensing signal from 25 - 350 °C (a) of H₂S (b) of NH₃.

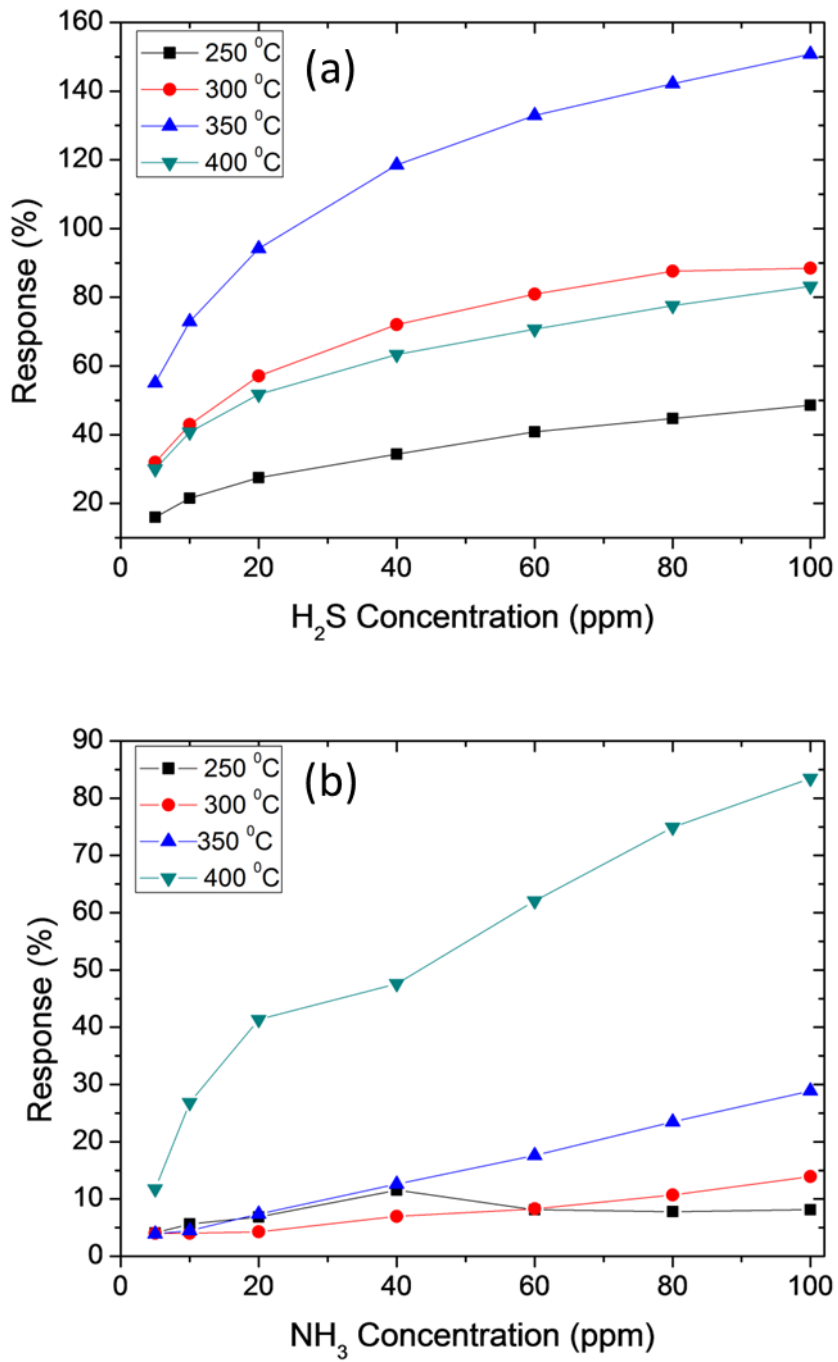


Figure 5.9: Response profiles as a function of different gas concentrations (a) for H₂S, (b) for NH₃

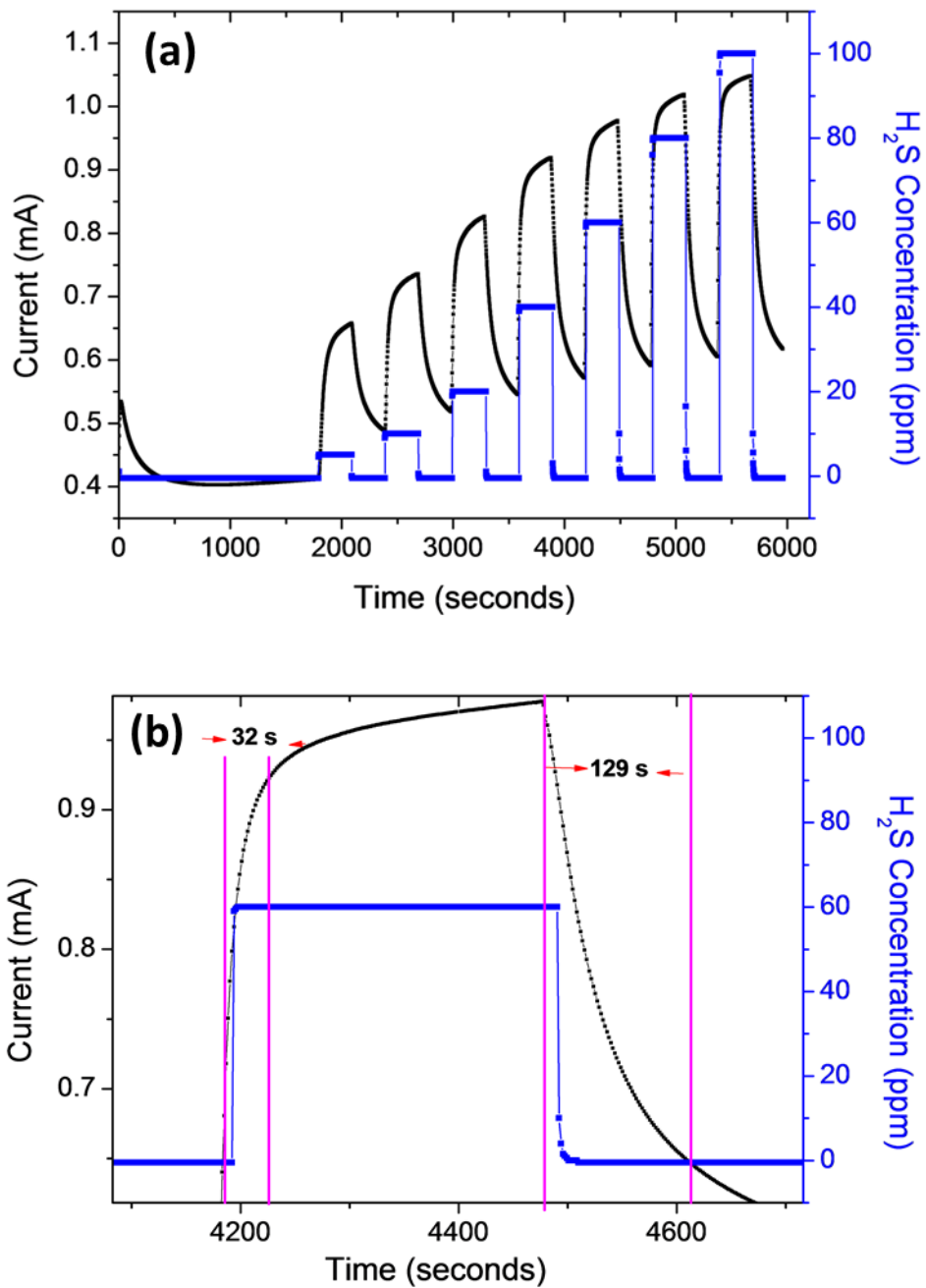


Figure 5.10 (a) Conductometric sensing signal of H₂S at 350 °C (b) Response and recovery time calculations of 60 ppm of the profile in (a)

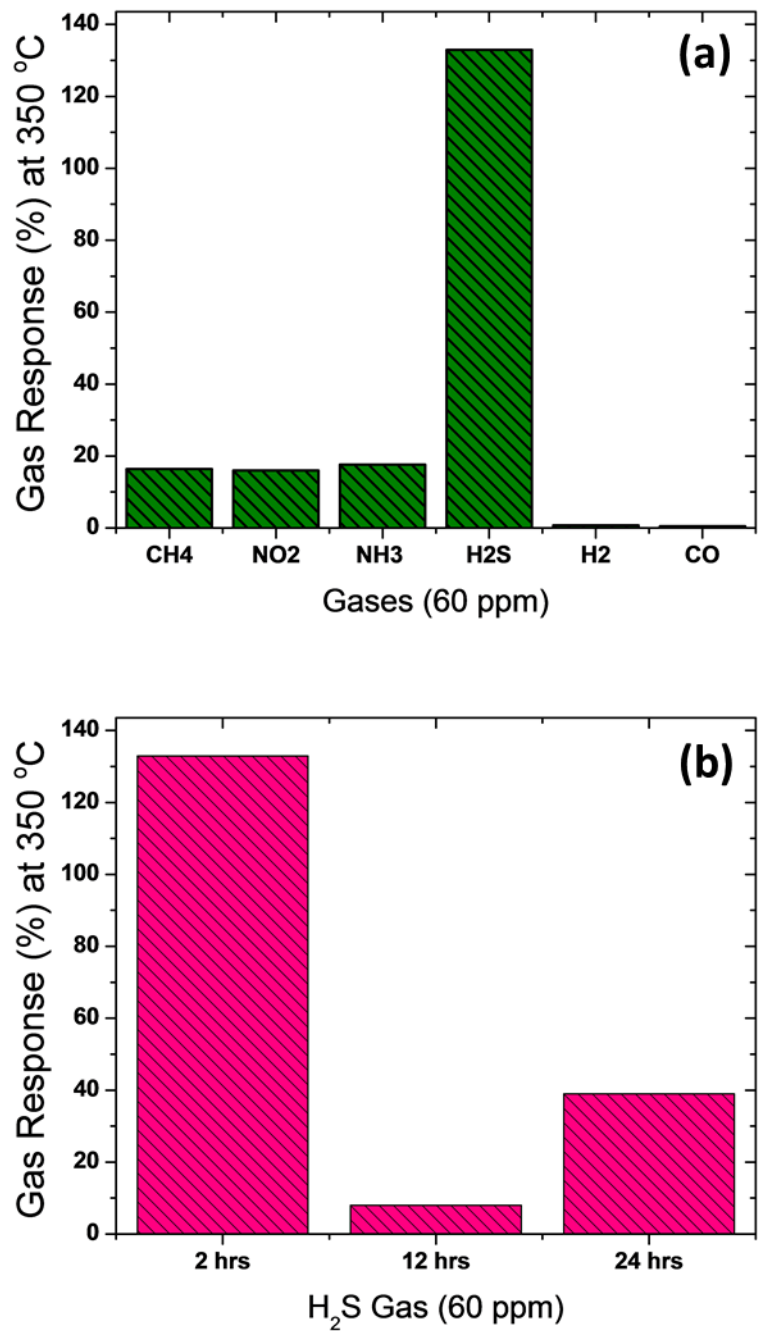


Figure 5.11 Gas response of 60 ppm at 350 °C, (a) Gas responses for the samples prepared at 2 hours (b) H₂S responses for the samples prepared at 2, 12 and 24 hours

Further tests were carried out by applying the two other samples which are V_2O_5 structures (i.e the samples annealed at 500 °C for 12 and 24 hours) for H_2S sensing, still, the results in Figure 5.11 (b) show outstanding adsorption for the sample annealed at 2 hours. This shows that the high sensitivity and selectivity property of these nanoparticles to H_2S may be due to their structural property and surface adsorption energy. Hence, DFT calculations were performed on (110) surfaces of V_6O_{13} and V_2O_5 to obtain the adsorption energy between their interfaces and H_2S gas. Figure 5.12 is the modelled structures of (110) surfaces of V_6O_{13} Figure 5.12 (a) and V_2O_5 Figure 5.12 (b) and 4 H_2S molecules. In this Figure one can observe that the V_6O_{13} (110) surface shows strong affinity to the H_2S molecules and that certain sites are preferred during the adsorption process. A total of 15 calculations and 15 maximum numbers of H_2S molecules were considered.

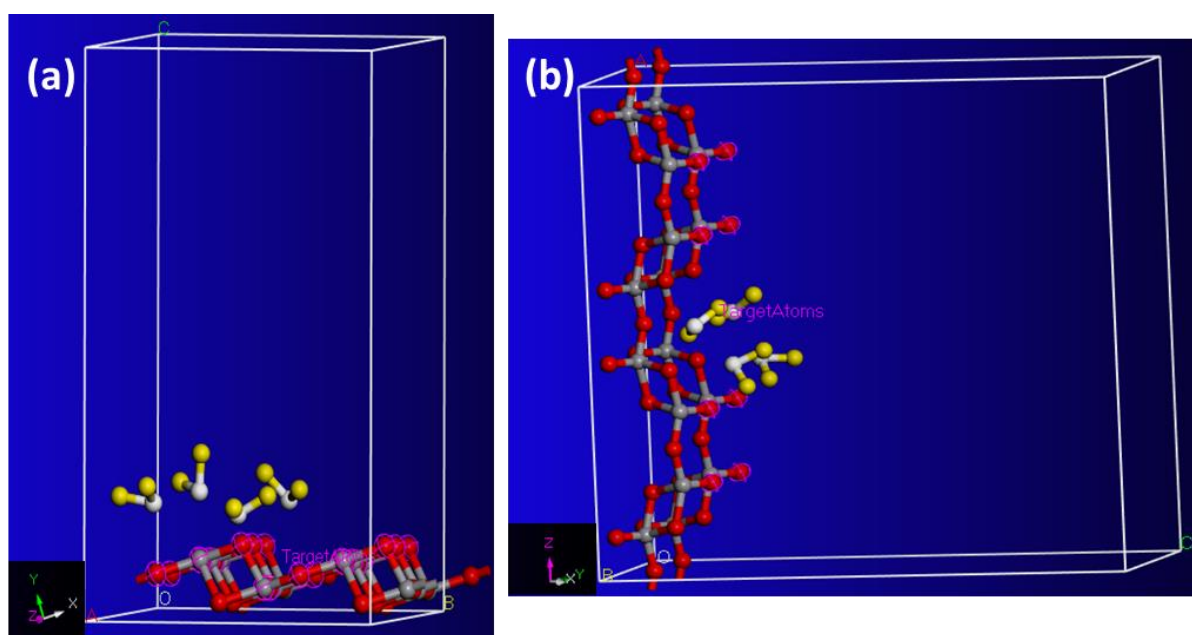


Figure 5.12 (a) V_6O_{13} (110) surface and H_2S molecules, (b) V_2O_5 (110) surface and H_2S molecules.

The plot of the corresponding adsorption energies of each number of molecules in Figure 5.13 (a) shows a linear relationship between them. Adsorption energy in this case is defined as follows,

$$E_a = E_{system} - E_{surface} - E_{adsorbate} \quad (5.2)$$

Here, E_{system} refers to the total energy of the optimized VOx system, $E_{surface}$ is the total energy of the clean VOx surface and $E_{adsorbate}$ is the energy of the H₂S gas. By this definition, $E_a < 0$ which corresponds to an exothermic reaction which is also indicative of an attractive interaction, whereas, if $E_a > 0$, it means that the system is thermodynamically unstable relative to the standalone H₂S gas [17-18]. In our case, $E_a < 0$ is negative in all calculations, which shows that these systems are stable. According to these definitions, negative values of adsorption energies in our results (Figure 5.13 (a)) show that the V₆O₁₃ (110) surface adsorbed H₂S molecules are better than V₂O₅ (110) surface. This observation is consistent with our experimental results. Figure 5.13 (a) is the plot of absolute adsorption energy per H₂S molecules, this profile mimics the Langmuir pattern of response as a function of H₂S gas concentrations in Figure 5.9 (a). Figure 5.13 (a) also shows clear distinction of adsorption between (110) surface V₆O₁₃ and V₂O₅.

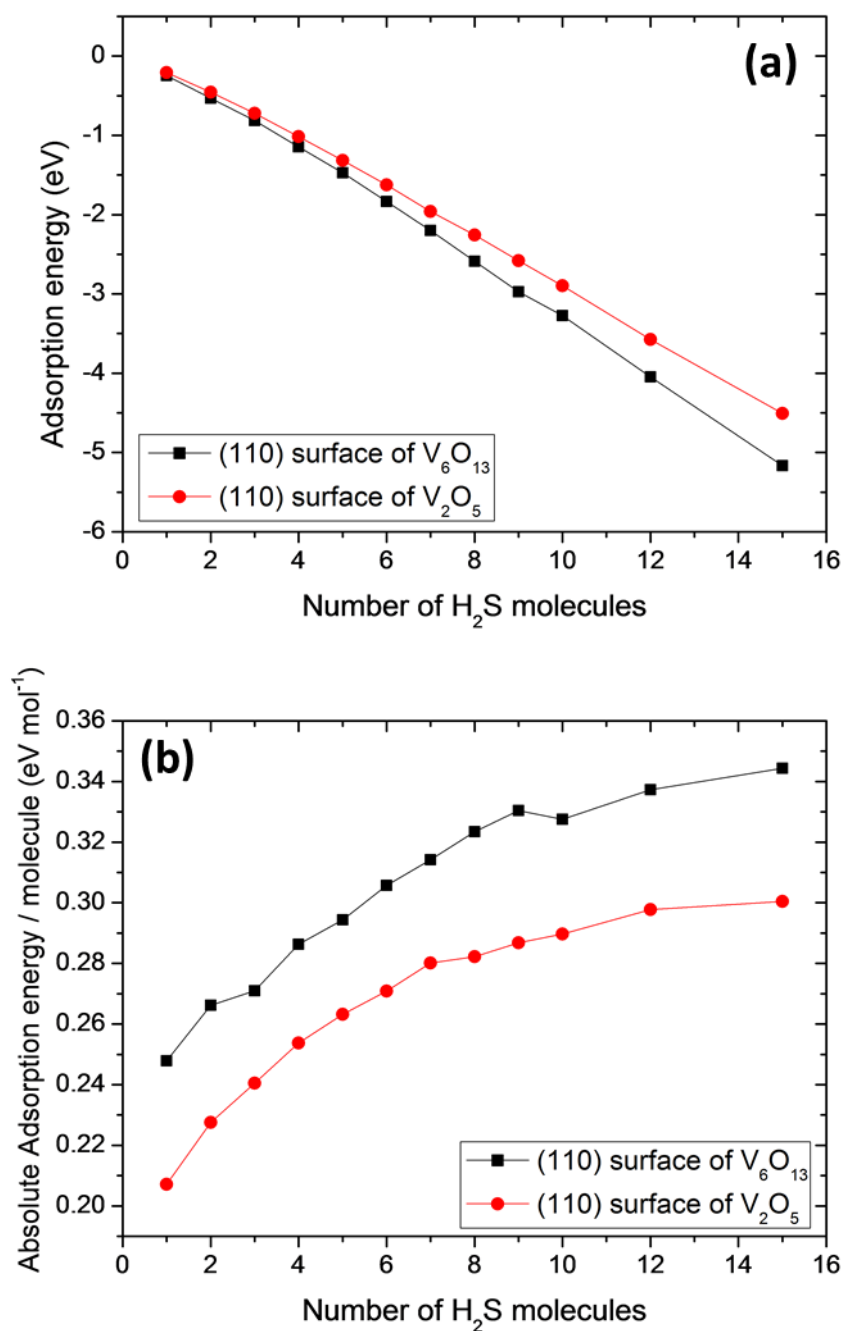


Figure 5.13 (a) Adsorption energies vs number of H₂S molecules of V₆O₁₃ and V₂O₅ (110) surfaces, (b) Absolute Adsorption energies per molecules vs number of H₂S molecules of V₆O₁₃ and V₂O₅ (110) surfaces

5.4 Conclusion

This chapter reports preferential adsorption of V_6O_{13} nano rods structure which happen to be mixed valence state of Vanadium Oxides to H_2S gas. The structure alongside two others (which are V_2O_5) was obtained by a solid-state decomposition reaction of NH_4VO_3 at $500\text{ }^\circ\text{C}$ for 2, 12 and 24 hours in an inert environment. The samples with the least exposure to heat (annealed at 2 hours) crystallized as V_6O_{13} and the ones with longer exposure (annealed at 12 and 24 hours) are V_2O_5 structures. This is based on the XRD, TEM, Raman Spectroscopy and CL studies. Gas sensing tests of the V_6O_{13} sample showed preferential and selective adsorption to H_2S among CH_4 , NO_2 , H_2 , NH_3 and CO gases. The sensitivity of this structure to H_2S surpassed other gases by 647.2 % and the response and recovery time are remarkable. When the other two samples (annealed at 12 and 24 hours) which are V_2O_5 were tested for the same H_2S gas and ranked with the V_6O_{13} structure, V_6O_{13} still stands tall in its performance. This prompted our attentions to a theoretical understanding by DFT calculation of adsorption energy between the interface of the two structures and the H_2S gas. The results for the (110) plane/surfaces showed that the V_6O_{13} poses higher energy than the V_2O_5 structure. Hence, when the adsorption energies data was transformed into adsorption energy per individual molecule of H_2S and related to the number of molecule, the profile followed a typical Langmuir pattern which is a replica of the experimental H_2S response profiles as a function of concentrations. This is the first report of selective adsorption of V_6O_{13} structures to H_2S gas and may be commercialized as a nano-super-sensitive H_2S sensor.

References

- [1] Y. Wang, S.R. Wang, Y.Q. Zhao, B.L. Zhu, F.H. Kong, D. Wang, et al., H₂S sensing characteristics of Pt-doped alpha-Fe₂O₃ thick film sensors, *Sen. Act. B.* **25**, 1, 79-84, (2007).
- [2] Q.Y. Ouyang, L. Li, Q.S. Wang, Y. Zhang, T.S. Wang, F.N. Meng, et al., Facile synthesis and enhanced H₂S sensing performances of Fe-doped alpha-MoO₃ micro-structures, *Sen. Act. B* **169**, 17-25, (2012).
- [3] L.Q. Mai, L. Xu, Q.A. Gao, C.H. Han, B. Hu, Y.Q. Pi, Single β -AgVO₃ Nanowire H₂S Sensor, *Nano Lett.*, **10**, 7, 2604-2608, (2010).
- [4] L. Zhang, Z. Liu, L. Jin, B. Zhang, H. Zhang, M. Zhu, W. Yang, Self-assembly gridding α -MoO₃ nanobelts for highly toxic H₂S gas sensor, *Sen. Act. B* **237**, 350-357, (2016).
- [5] K. Watchakun, T. Samerjai, N. Tamaekong, C.Liewhiran, C. Siriwong, V.Kruefu, A.Wisitsoraat, A.Tuantranont, and S.Phanichphant, Semiconducting metal oxides as sensor for environmentally hazardous gases, *Sen. Act. B* **160**,580-591, (2011).
- [6] V. Palmisano, E. Weidner, L. Boon-Brett, C. Bonato, F. Harskamp, P. Moretto, M.B. Post, R. Burgess, C. Rivkin, W.J. Buttner, Selectivity and resistance to poisons of commercial hydrogen sensors, *Int. J. Hydro. Energy*, **40**, 35, (2015) 11740-11747
- [7] T. Minming, F. Yingbo, Z. Chuang, Proceeding of Int. Cof. Information Aquisition, Jeju Korea July 9-11 (2007) 83-85
- [8] J.J. Chen, K. Wang, L. Hartman, W.L. Zhou, H₂S Detection by Vertically Aligned CuO Nanowire Array Sensors, *J. Phys. Chem. C*, **112**, 16017-16021, (2008).
- [9] M.D. Shirsat, M.A. Bangar, M.A. Deshusses, N.V. Myung, A. Mulchandani, Polyaniline nanowires-gold nanoparticles hybrid network based chemiresistive hydrogen sulfide sensor, *Appl. Phys Lett*, **94**, 083502-083502-3, (2009).

- [10] S. Mubeen, T. Zhang, N. Chartuprayoon, Y. Rheem, A. Mulchandani, N.V. Myung, et al., Sensitive Detection of H₂S Using Gold Nanoparticle Decorated Single-Walled Carbon Nanotubes, *Anal Chem*, **82**, 250-257, (2010).
- [11] L. Liao, H.B. Lu, J.C. Li, H. He, D.F. Wang, D.J. Fu., Size dependence of gas sensitivity of ZnO nanorods, *J. Phys Chem C*, **111**, 1900-1903, (2007).
- [12] Z.S. Hosseini, A.I. Zad, A. Mortezaali, Room temperature H₂S gas sensor based on rather aligned ZnO nanorods with flower-like structures, *Sen. Act. B-Chem*, **207**, 865-871, (2015).
- [13] T.T. Yu, X.L. Cheng, X.F. Zhang, L.L. Sui, Y.M. Xu, S. Gao, Highly sensitive H₂S detection sensors at low temperature based on hierarchically structured NiO porous nanowall arrays, *J. Mater. Chem. A*, **3**, 11991-1199, (2015).
- [14] T.T. Yu, X.F. Zhang, Y.M. Xu, X.L. Cheng, S. Gao, H. Zhao, Low concentration H₂S detection of CdO-decorated hierarchically mesoporous NiO nanofilm with wrinkle structure, *Sen. Act. B*, **230**, (2016) 706-713.
- [15] A.A. Akande, E.C Linganiso, B.P Dhonge, K.E. Rammutla, A. Machatine, L. Prinsloo, H. Kunert, B.W. Mwakikunga, Phase evolution of vanadium oxides obtained through temperature programmed calcinations of ammonium vanadate in hydrogen atmosphere and their humidity, *J of Mat. Chem. Phys.* **151**, 206-214, (2015).
- [16] <https://materialsproject.org>
- [17] M-F. Ng, M. K. Teo, K. H. Lim, L. Zhou, M. B. Sullivan, S-W. Yang, Towards tuning of surface properties by atomic and molecular adsorption on boron-terminated cubic boron nitride (111) surface: A first-principles study, *Diamond & Related Mat.* **17** 2048-2053, (2008).

- [18] V. V. Kulish, M-F. Ng, O. I. Malyi, P. Wu, Z. Chen, Enhanced Li Adsorption and Diffusion in Single-Walled Silicon Nanotube: An ab Initio Study, *Chem. Phys. Chem.* **14**, 6 (2013) 1161-1167
- [19] N. Martsinovich, D. R. Jones, A. Troisi, Electronic Structure of TiO₂ Surfaces and Effect of Molecular Adsorbates Using Different DFT Implementations, *J. Phys. Chem. C*, **114**, 22659-22670, (2010)
- [20] B. R. Rehani, P. B. Joshi, K.N. Lad, A. Pratap, Crystallite size estimation of elemental and composite silver nano-powders using XRD principles, *Indian J. Pure & App. Phy.* **44**, 157 – 161, (2006).
- [21] B. Mwakikunga, S. Motshekga, L. Sikhwivhilu, M. Moodley, G. Malgas, M. Scriba, and S. Sinha-Ray, A classification and ranking system on the H₂ gas sensing capabilities of nanomaterials based on proposed coefficients of sensor performance and sensor efficiency equations, *Sens. Act. B.* **184**, (2013) 170-178

CHAPTER 6

ROOM TEMPERATURE SENSING OF CH₄ AND SELECTIVITY OF NO₂ COMPARED TO NH₃ OF NANOSPHERICAL VO_x PARTICLES

A. A. Akande, P. Dhonge, K. E. Rammutla, A. G. J. Machatine, B. W. Mwakikunga, *Advanced Sci. Lett.* 22, 4, (2016)

A. A. Akande, B. W. Mwakikunga, K. E. Rammutla, A. G. J. Machatine, *Sensors & Transducers* 192, 9, (2015)

The properties of Microwave assisted VO_x nanoparticles are discussed in this chapter. Room temperature sensitivity of VO_x samples to low concentration of CH₄ gas and larger selectivity of V₂O₅ sensitivity to NO₂ compared to NH₃ is discussed as well. Discussions on sensing mechanisms are also presented.

6.1 Introduction

Elevated atmospheric pollution has attracted the attention of scientists in recent years, and has geared their interest towards building effective and inexpensive systems for detection and quantification of environmentally hazardous gases [1]. Methane among others is a highly explosive and flammable gas with higher potential to cause and escalate fire in industries and household kitchens since it is being widely used as a cooking gas. Nitrogen dioxide (NO₂) and its by-products NO, N₂O are very dangerous inorganic gases forming a reddish-brown gas with pungent and irritating odour. Nitrogen oxides usually irritate lungs and eyes and often cause problems in the human respiratory system. These gases have been reported to be

responsible for asthma, lung diseases, kidney impairment and as carcinogenic agents [1-2]. Ammonia (NH_3) gas on the other hand is non-toxic, pungent, colourless gas but also affects the environment through irritation of human eyes and malfunctions or failure of the human liver. NH_3 gas also emanates from the decomposition of animal manures and often cause fishes and livestock's death in the farm land [1-3].

Metal oxide nanoscale materials are suitable for the detection of these gases even at the molecular level due to their inherent small size, high conductance, large surface to volume ratio and band gap properties discussed in chapter two [4]. Nanostructured metal oxides semiconductors such as ZnO , SnO_2 , WO_3 , TiO_2 , CuO , etc [5 - 10] prepared using various physical and chemical methods have been investigated for the detection of CH_4 , NH_3 and NO_x gases [1]. Nevertheless, detection of low concentration at room temperature and selective adsorption or sensing of a particular gas species has been a challenge to the metal oxides gas sensing field [1, 11-12]. Methods such as doping or decoration of metal oxides with noble metals like Ag, Pt, Sb, etc. have been employed to make them sensitive and selective at room temperature [10-15]. These methods are rather expensive and not as easy to synthesise as metal oxides. This chapter reports room temperature CH_4 sensing of V_2O_5 nano-spherical particles at very low concentration and their greater selectivity to NO_2 than NH_3 sensitivity.

6.2 Experimental Details

About 0.5g of NH_4VO_3 powder (purity 99.99%) was ultrasonically dissolved (1) in 10 mL ethanol, and (2) in 10 mL deionized water. A diazene (N_2H_2) reagent of 5 mL was added drop-wise to each specimen. These mixtures were transferred into 100 mL Teflon vessels and placed into the Multiwave 3000 Microwave reactor described in chapter three. The reactor power was set to 600 W and the temperature was maintained at 180 °C for 20 minutes. The

vessels in the reactor were allowed to cool for 25 minutes. Afterwards, the resultant mixtures were collected by filtration and washed repeatedly using isopropanol and acetone in an ultrasonic bath to remove undesired impurities and to minimise particle agglomeration. The final products were dried at 100 °C for 11 hours.

The powders produced were characterized using a Panalytical X'pert Pro PW 3040/60 XRD equipped with Cu K α ($\lambda=0.154nm$) monochromatic radiation source. XRD patterns were recorded at 45.0 kV and 40.0 mA from $2\theta = 5 - 90^\circ$. Raman spectroscopic studies were conducted using a Jobin–Yvon T64000 Raman spectrograph with a 514.5 nm excitation wavelength from an argon ion laser. The power of the laser at the sample was low enough (0.384 mW) in order to minimise localised heating of the sample. The T64000 was operated in a single spectrograph mode, with the 1800 lines/mm grating and a 100x objective on the microscope. Morphology studies were carried out using a LEO 1525 field emission scanning electron microscope (FESEM) and JEOL 2100 Transmission Electron Microscopy (TEM) (from Tokyo Japan) for high resolution imaging.

BET analyses were carried out using Micromeritics TriStar II series Surface Area and Porosity instrument and a Micromeritics sample degassing system from USA.

Gas testing measurements were achieved using KSGA565 KENOSISTEC from Italy. The illustration in chapter five Figure 5.1 shows the schematic of the gas sensing station. The set-up consists of a test chamber, sensor holder, interdigitated electrode (for contacting the nano-powder) and source meters. To carry out the measurements, VO_x powder was dispersed in ethanol and formed a thick paste on the interdigitated electrode.

6.3 Results and Discussion

The XRD pattern of VO_x nanoparticles (NPs) produced when the precursor NH₄VO₃ is dissolved with ethanol in Figure 6.1 (a) shows the diffraction peaks belonging to the

monoclinic phase of VO_2 and orthorhombic V_2O_5 . Diffractions at $2\theta = 27.8^\circ$ (011), 42.3° (211) and 65.2° (031) are characteristics of monoclinic VO_2 which was identified using PCDFWIN CAS No: 44-0252 and the broad diffraction at $2\theta = 17.4^\circ$ (200) is associated with V_2O_5 orthorhombic using PCDFWIN CAS No: 89-0611. This XRD profile showed broad diffraction peaks denoting that the nanostructures are composed of an amorphous network and crystalline region. The crystallites size of about 6 nm was calculated using Debye Scherer's model. This sample will be referred to as VO_x throughout the discussions in this chapter. SEM micrograph of VO_x NPS in Figure 6.1 (b) shows formation of "sphere-like" particles (spheres consist of tiny particles) with an average diameter of ≤ 100 nm. Analysis of this SEM image reveals that the material particles' are predominantly in the range of nanometres. Figure 6.1 (c) is the HRTEM of VO_x NPs showing diffraction planes corresponding to (200) of V_2O_5 , and Fig 6.1 (d) is the selected area electron diffraction (SAED) pattern showing that the particles composed mixed crystalline and amorphous grains. The plane with high crystallinity (first ring) among the four rings in the SAED is attributed to the plane (200) of V_2O_5 as suggested by the XRD profile. The lattices spacings were determined from Image J and matched and corresponded to the V_2O_5 orthorhombic phase.

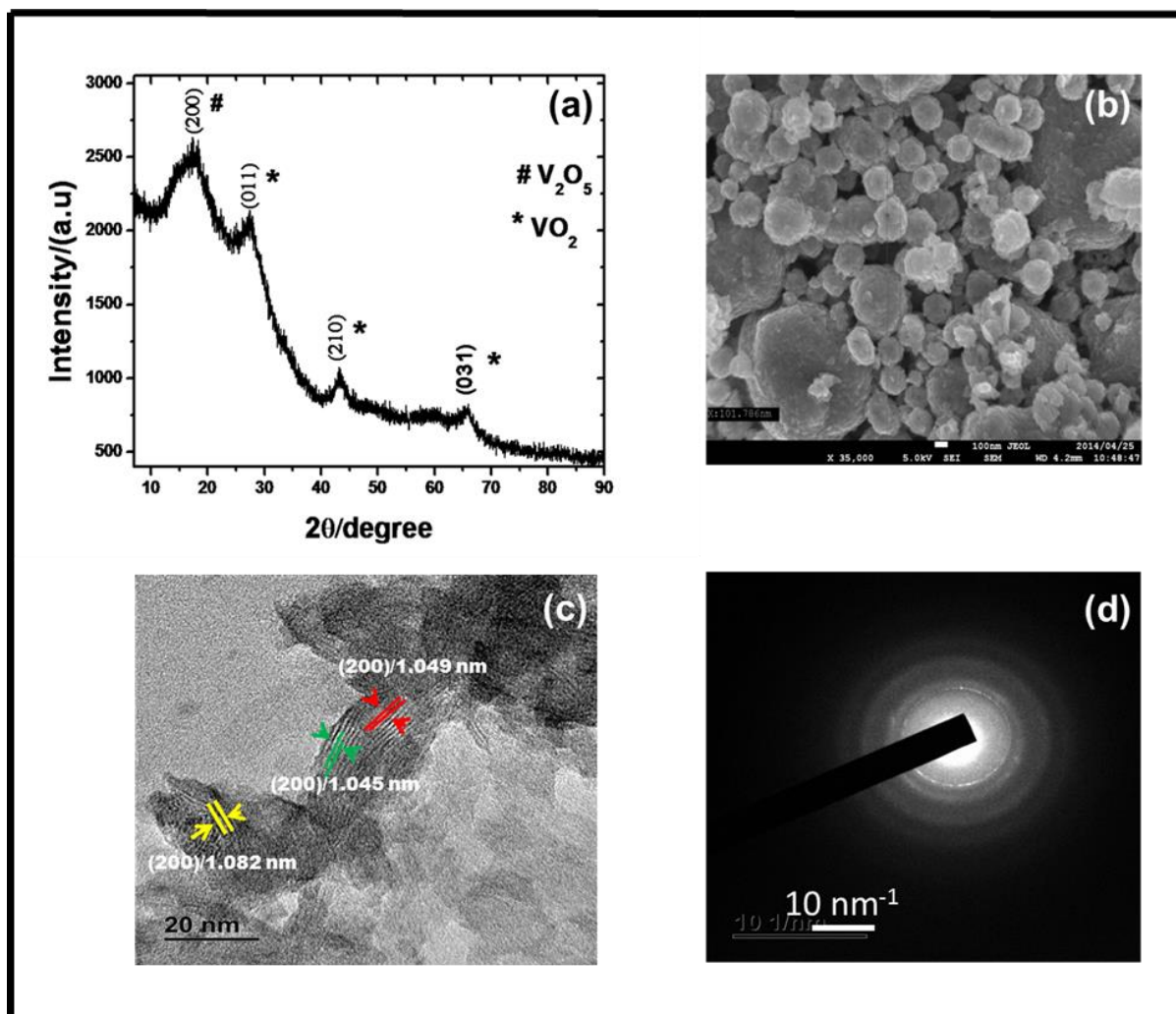


Figure 6.1 (a) XRD pattern of VO_x nanoparticles, (b) SEM micrograph of VO_x nanoparticles, (c) HRTEM of VO_x NPs, (d) SAED pattern of VO_x NPs.

Raman spectrum of VO_x nanoparticles in Figure 6.2 (a) shows Raman active modes of V_2O_5 and VO_2 . A strong peak at lower frequency band 141 cm^{-1} corresponding to the B_g symmetry while the high frequency vibration at 992 cm^{-1} corresponds to stretching of O-V-O atoms. Vibration modes at 282 , 402 and 525 cm^{-1} are resulting from the bending mode of V-O band while the stretching mode at 692 cm^{-1} corresponds to the motion parallel and perpendicular to ab-plane [16 - 17]. These vibrations are characteristics of V_2O_5 . The development of the VO_2 vibration mode is observed at 194 cm^{-1} and the frequency band of

142 cm^{-1} was assigned to VO_2 by Petrov *et.al* [18]. This profile showed that V_2O_5 dominates the surface of VO_x .

The specific surface area S_{BET} and pore size/diameter (d_{por}) of $67 \text{ m}^2\text{g}^{-1}$ and d_{por} of 16 nm, respectively, were determined by physisorption of nitrogen according to BET theory as shown in Figure 6.2 (b). This surface area and nano porous properties revealed the potential of the material in gas and chemical sensor applications. BET surface area of $67 \text{ m}^2\text{g}^{-1}$ and average pore diameter of 16 nm obtained are large compared to that of VO_2 (B) nanoneedles previously reported by Sediri *et al.* [19].

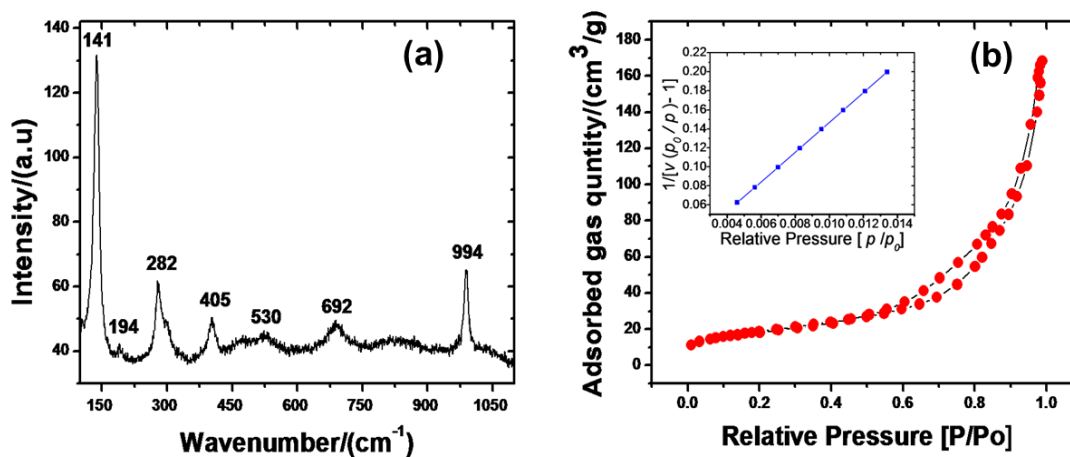


Figure 6.2. (a) Raman spectrum of VO_x nanoparticles, (b) N_2 adsorption/desorption isotherms. profile of VO_x nanoparticles, insert is the BET plot.

Electrical and gas sensing properties of VO_x NPs were measured as described in Figure 5.1. The sensor test was performed by measuring the resistance of the sensor when exposed to CH_4 gas. Figure 6.3 (a) shows variations of the current flowing through VO_x NPs for different concentrations of CH_4 gas (at room temperature). The underlying sensing mechanism between VO_x and CH_4 gas is as follows, when VO_x which is an n -type

semiconductor is exposed to air at either at changed or ambient conditions, the chemisorbed oxygen at the surface of the material will acquire an electron from its conduction band to form ionic species [1, 20]. An acquisition of an electron from the conduction band of an *n*-type semiconduction would lead to a decrease in electron concentration and increase in the resistance (decrease in conduction) of the material. Introducing VO_x to a reducing species such as CH₄ gas [1, 20] could decrease the resistance (increase the conduction) of the sensor. The full details of the conductometric sensing mechanism is provided in section 3.2 of chapter 3.

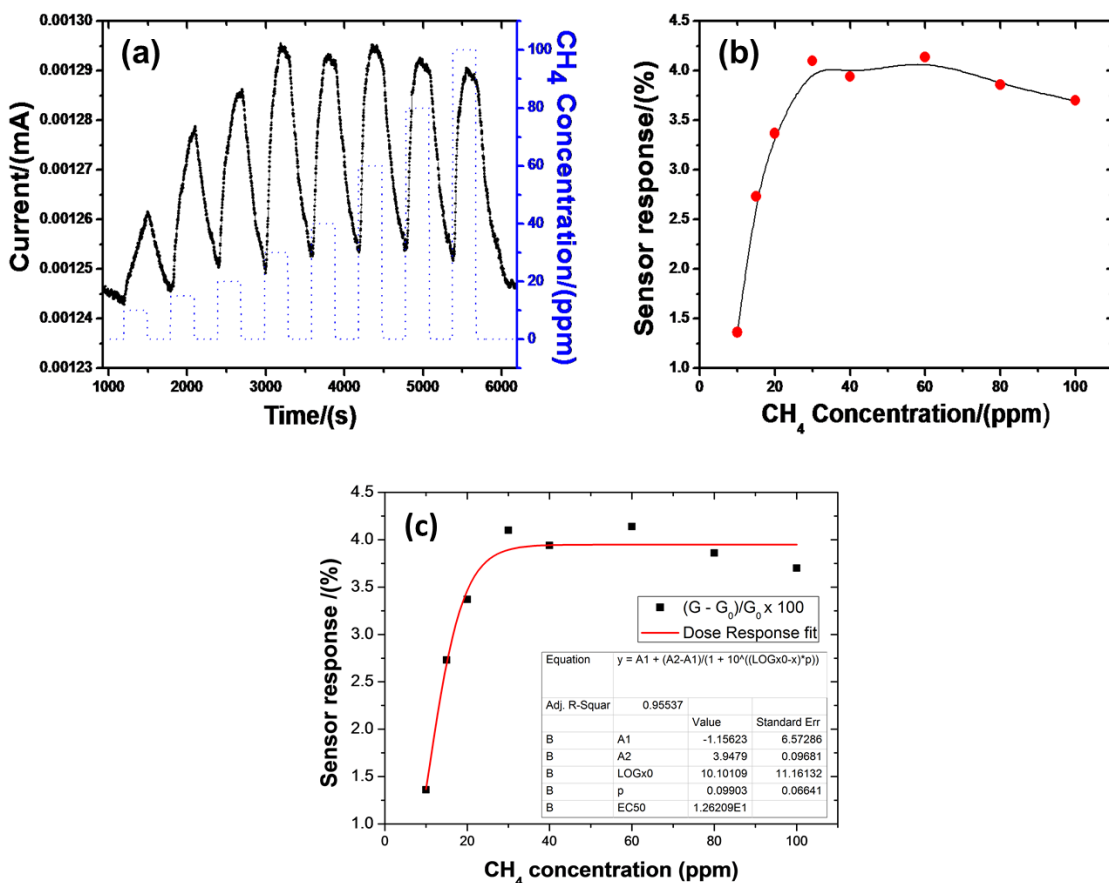


Figure 6.3 (a) Variation of the current flowing through VO_x nanoparticles recorded for different concentrations of CH₄ gas, (b) Sensor response as a function of different CH₄ gas

concentrations (c) Profile of Dose response curve with variable Hill slope of the VO_x responses vs CH₄ gas concentrations.

Figure 6.3 (b) represents the VO_x sensor response as a function of different CH₄ gas concentrations.

The sensor response is defined as

$$S(\%) = \frac{G_{gas} - G_{air}}{G_{air}} \times 100 \quad (6.1)$$

where G_{gas} and G_{air} are the conductance of VO_x in the presence of CH₄ (analyte gas) and air respectively. The sensor response follows the Langmuir isotherm profile in that the response increases with gas concentrations before the saturation effect at 40 ppm of CH₄ concentration. The chemical reaction between CH₄ and the oxygen atom in the VO_x is assumed to be responsible for the saturation effect at a high concentration of CH₄. The product of this reaction could be CO and H₂O, the sensor response shows a damping trend at a higher concentration which implies that the VO_x could not detect the product of CH₄ degradation. The narrow band gap property and low MIT temperature of VO₂ compared to other transition metal-oxides may be the reason why VO_x NPs were able to detect CH₄ with high responsiveness and at room temperature.

Also using non-linear regression which is symptomatic of S- shaped curves, one can speculate that the other part of the S- shaped curve exists at much lower concentration of Figure 6.3 (c) which is our dose-response characteristic curve with a variable Hill slope. The dose response curve is defined in (6.2), where where A_1 and A_2 are the bottom and top sensor responses, $\log(CH_4 -_{bottom})$ is the logarithm of the CH₄ concentration at 50% response, whereas EC50 is the antilogarithm of $\log(CH_4 -_{bottom})$ dose at which 50% response is achieved by the sensor and p is the Hill factor.

This equation fits perfectly with the response vs concentration data as shown in Figure 6.3 (c). From the fitting, EC50 value is 1.262×10^{10} p = 0.099 whereas $\log(\text{CH}_4\text{-bottom})$ is 10.101, A_1 and A_2 are respectively -1.156 and 3.947 with a correlation coefficient, R^2 , of 0.955. This statistic shows that the VO_x sensor response mimics nature, and that the EC50 value is huge which is an indication that the sensor is strong and sensitive.

$$G_{res} = \frac{G_{top} - G_{bottom}}{G_{bottom}} = A_1 + \frac{A_2 - A_1}{1 + 10^{(\log \text{CH}_{4\text{bottom}} - \text{CH}_{4\text{top}})p}} \quad (6.2)$$

Figure 6.4 shows the XRD pattern of V_2O_5 NPs produced when the precursor NH_4VO_3 is dissolved with deionized water. The spectrum shows diffractions belonging to the orthorhombic phase of V_2O_5 . The broad diffractions at $2\theta = 17^\circ$ are the characteristics of the orthorhombic V_2O_5 (200) reflection [PCDPDFWIN CAS No. 890611].

However, the development of the VO_2 monoclinic phase was also observed at $2\theta = 27.6^\circ$ [PCDPDFWIN CAS No. 710042] corresponding to the spectrum in Figure 6.1 (a). It is important to note that the amorphous background is wide and that the VO_2 peak is shallow when deionized water is used as a solvent. This shows that the enhanced crystallization and reduction from $\text{V}_2\text{O}_5 \rightarrow \text{VO}_2$ of the VO_x sample may be due to the addition of ethanol. The crystallite size of V_2O_5 NPs was also calculated and found to be 5 nm. The SEM micrograph of V_2O_5 NPs in Fig. 6.4 (b) shows the formation of amorphous sphere-like colloidal particles which agrees with the XRD spectrum in Figure 6.4 (a).

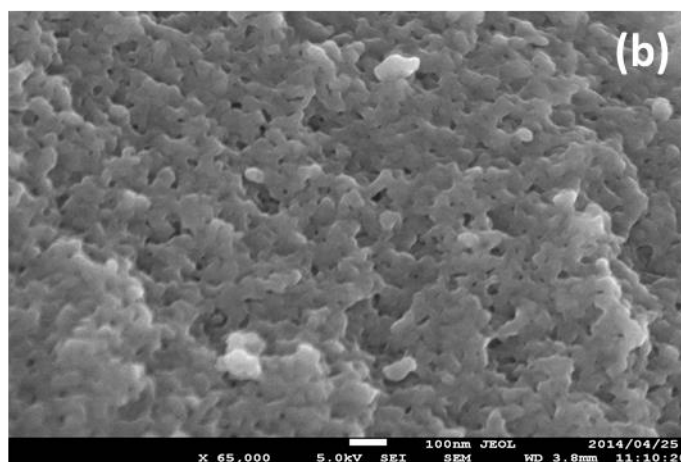
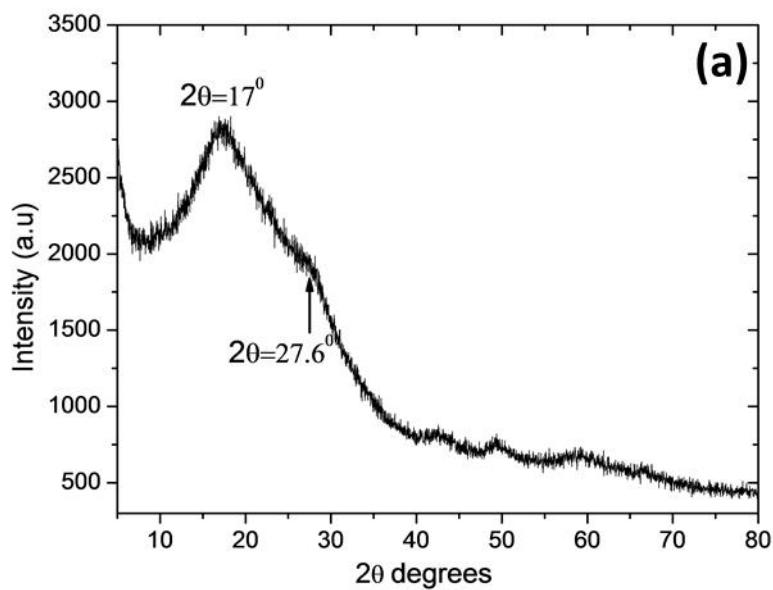


Figure 6.4 (a) XRD spectrum of V_2O_5 nanoparticles, (b) SEM micrograph of V_2O_5 nanoparticles.

Raman analysis of V_2O_5 NPs (not included) revealed similar vibrations with the one in Figure 6.2 (a), which also showed the development of 194 cm^{-1} belonging to the VO_2 monoclinic mode.

The specific surface area S_{BET} and pore size/diameter (d_{por}) of $92.7\text{ m}^2\text{g}^{-1}$ and d_{por} of 12 nm shown in Figure 6.5 is larger than the one obtained in the case of the VO_x sample. This may be due to the smaller crystallite size and better nano-porous properties of these particles.

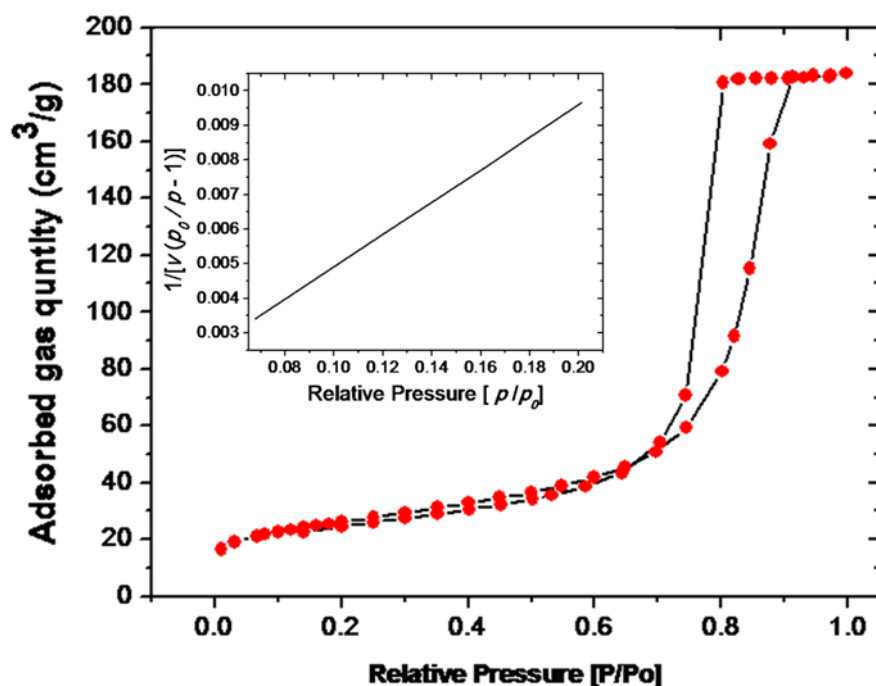


Figure 6.5 N₂ adsorption/desorption isotherms profile of V₂O₅ NPs, insert is the BET plot.

The measured electrical response for different NH₃ concentrations is presented in Figure 6.6 (a), with the operating or substrate temperature kept at 28 °C. The material showed good response to NH₃. Figure 6.6 (b) shows a linear profile for the NH₃ sensitivity plot, where R_{gas} and R_{air} are the resistance of V₂O₅ NPs in the presence of the analyte gas and air respectively [1, 20]. The measured electrical response for different NO₂ concentrations is presented in Figure 6.7 (a) with the operating temperature kept at 28°C. The material showed a good response for all concentrations. An increase in the electrical resistance of the V₂O₅ NPs sensor upon injection of the oxidising gas NO₂ shows p-type semiconductor behaviour. Figure 6.7 (b) is the NO₂ sensitivity profile.

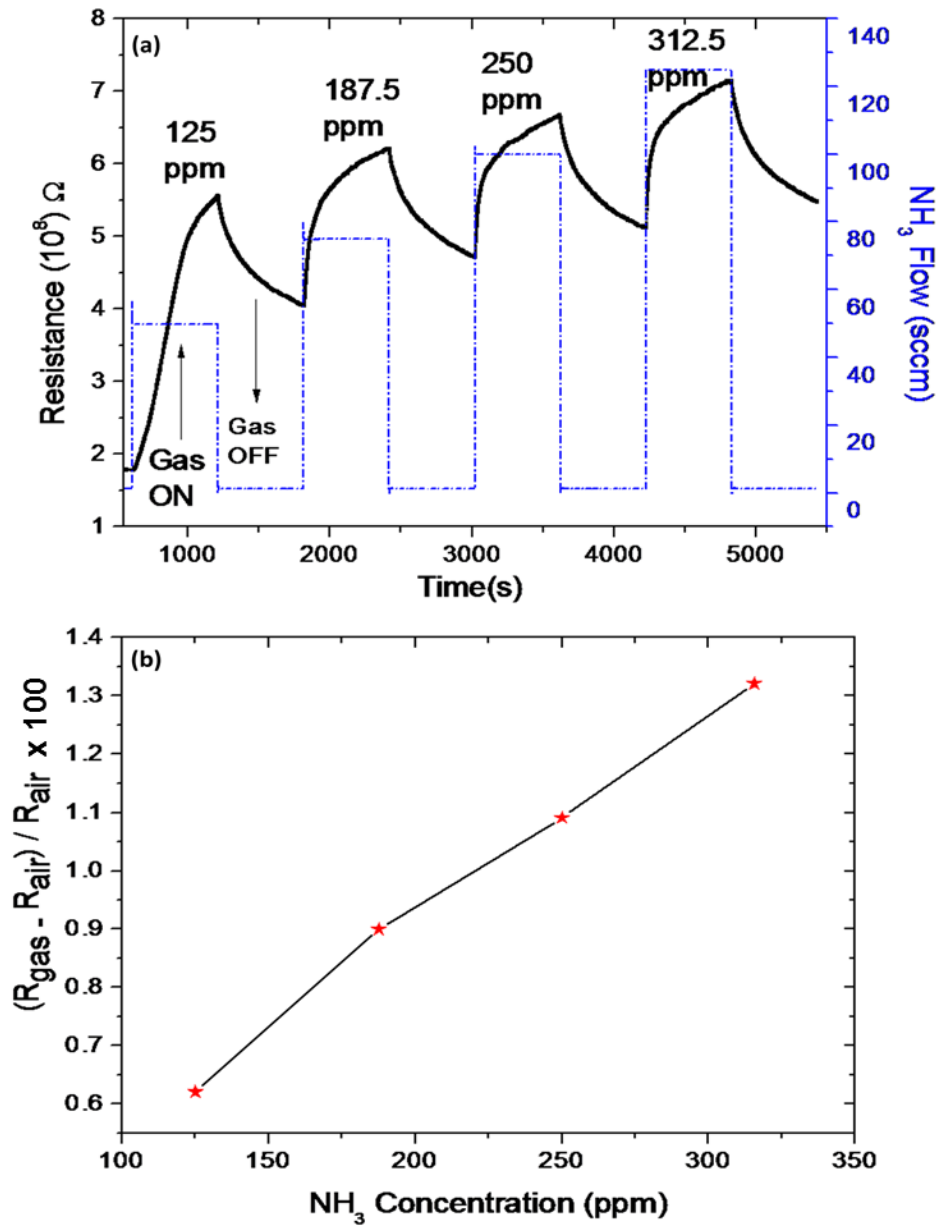


Figure 6.6 (a) The electrical response of V₂O₅ NPs for different concentrations of NH₃, (b) Sensor response as a function of different NH₃ gas concentrations.

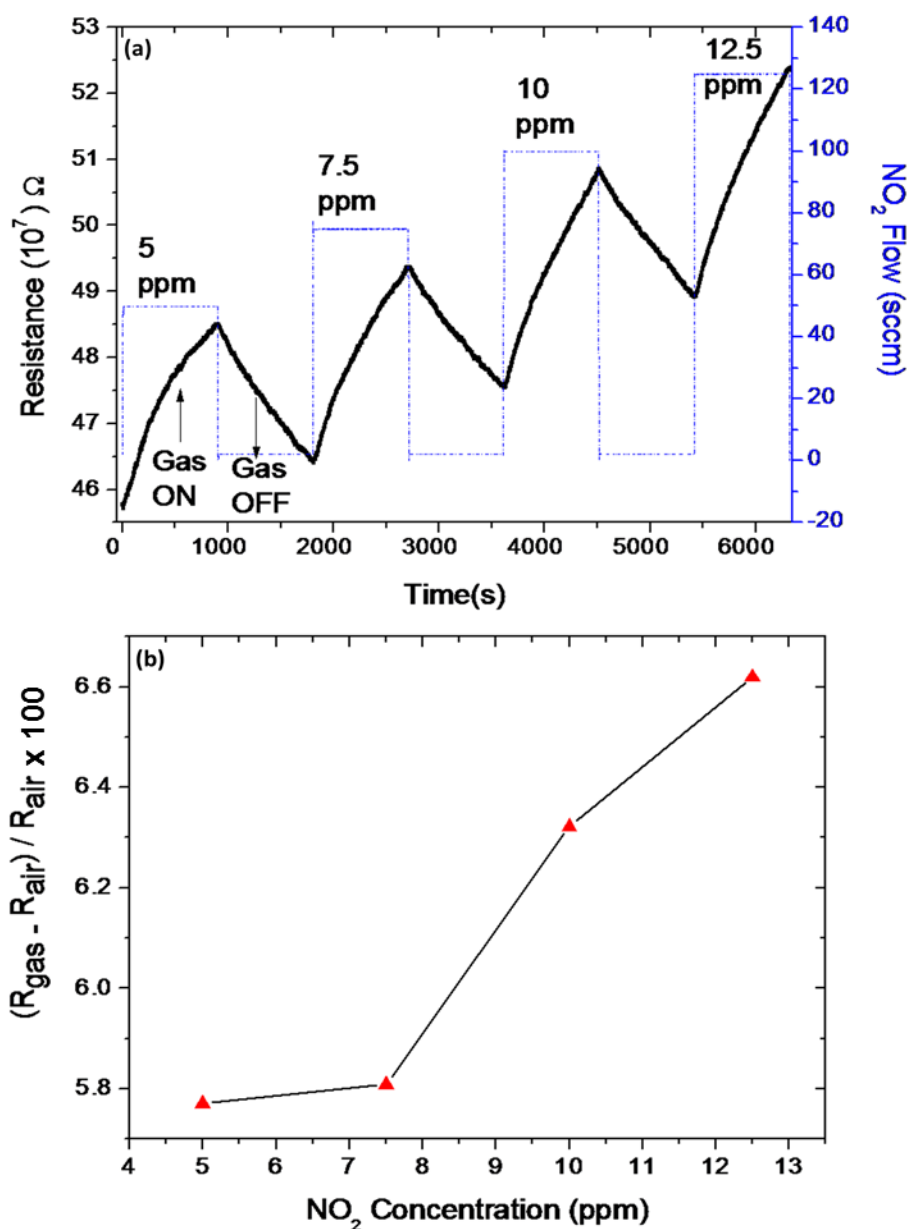


Figure 6.7 (a) The electrical response of V₂O₅ NPs for different concentrations of NO₂, (b) Sensor response as a function of different NO₂ gas concentrations.

The proposed mechanism is based on the fact that V₂O₅ is known to exhibit both p-type and n-type conductivities [21-22]. The results show that NH₃ prefers to interact with the n-type phases of V₂O₅. In this case the NH₃ molecule captures the adsorbed O₂⁻ ions from the V₂O₅ surface and oxidize to NO₂ and H₂ as depicted in Figure 6.8. This process robs the n-type phase of V₂O₅ of its electrons leading to less electron population in the conduction band

(CB) and hence an increase in resistance as shown in Fig. 6.6 (a).

As for the proposed sensing scheme for NO₂, the results show an increase in resistance regardless of the fact that NO₂ is an oxidising gas [1]. This is clear evidence that NO₂ prefers to interact with the p-type phase of V₂O₅. In this case NO₂ interacts with holes or vacancies in the adsorbed O₂⁻. When such a hole interacts with NO₂, the NO₂ is broken into N₂ and adsorbed O₂⁻. Only N₂ is released in the process leaving behind the O₂ as adsorbed at the V₂O₅ surface as O₂⁻. In the process the p-type phase will have gained an electron in the CB or lost a hole in the VB. The loss of holes in the VB of a p-type V₂O₅ leads to an increase in resistance as shown in Fig.6. 7 (a).

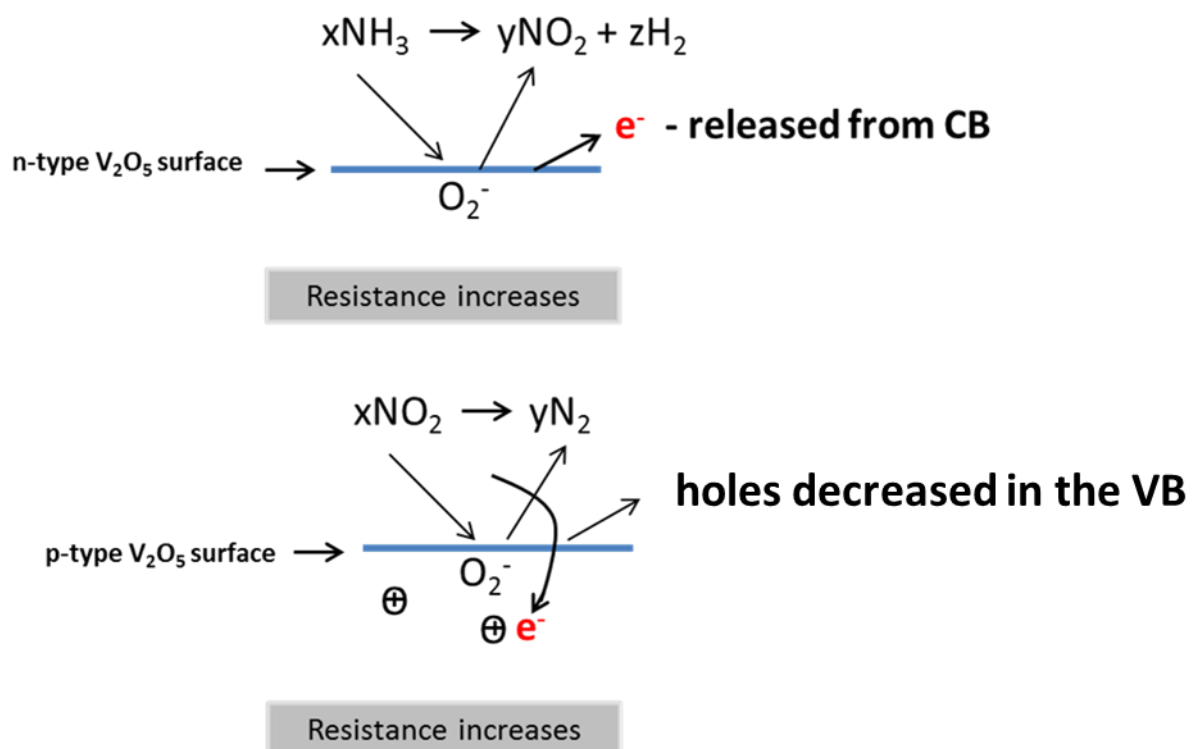


Figure 6.8 Sensing mechanism of V₂O₅ NPs (Chemisorption effect is also observed rather than only Iono-sorption – refer to the Section 3.2 of chapter 3)

It is worth noting that the magnitude of responses of V_2O_5 sensor to both NH_3 and NO_2 are many magnitude different. The sensitivity of the n-type phase to NH_3 is calculated as the slope of the response vs concentration curve in Figure 6. 6 (b). This works out to be $3.47 \times 10^{-3} \text{ ppm}^{-1}$. When the same sensitivity calculation is done for the p-type phase to NO_2 from Figure 6.7 (b) one finds the value of 0.11. The response of the p-type phase to NO_2 is therefore 32 times greater than the sensitivity of the n-type phase to NH_3 . Therefore, this V_2O_5 sensor is 32 times more selective to NO_2 than to NH_3 . This further suggests that the V_2O_5 nanoparticles are predominantly p-type. Tables 6.1 summarized the surface properties of ethanol and water microwave synthesized VO_x in terms of the gas sensing responses sensitivity at 10 ppm. One can infer that the water synthesized sample is more responsive with ~ 6.4 response magnitude to NO_2 .

Table 6.1: Summary of surface properties versus gas sensing responses (%) of ethanol and water synthesized VO_x

Sample	Specific Surface area (m ² /g)	Particle size (nm)	Pore size (nm)	Response at 10 ppm CH ₄ (%)	Response at 10 ppm NO ₂ (%)	Response at 10 ppm NH ₃ (%)
Ethanol synthesized VO_x (m-VO₂+o-V₂O₅)	67	6	16	1.5		
Water synthesized VO_x (m-VO₂+o-V₂O₅)	92.7	5	12		6.4	<0.2

6.4 Conclusions

Room temperature sensing of CH₄ gas was performed by VO_x (V₂O₅ + VO₂) NPs and selectivity of NO₂ compared to NH₃ of V₂O₅ NPs synthesized using the microwave assisted hydrothermal method have been demonstrated. Both VO_x and V₂O₅ particles composed of sphere-like mixed crystalline and amorphous grains with high surface area and porosity. VO_x showed higher crystallinity and high diffraction for VO₂ than V₂O₅ NPs sample. In room temperature (25 °C) sensing, a low concentration detection and high sensitivity of CH₄ gas was achieved in the case of VO_x NPs. Underlying sensing mechanism between VO_x and CH₄ gas followed the iono-sorption process and showed that the VO_x semiconductor is of n-type conductivity. The VO_x sensor response showed a Langmuir isotherm profile and non-linear regression. Dose response statistics showed that the sensor is relatively strong and sensitive.

A V_2O_5 NP sensor on the other hand is predominantly a *p*-type semiconductor with a ratio of *p*-type- to- *n*-type of 32:1 of NO_2 to NH_3 . This suggests that for every one electron in V_2O_5 NPs there are 32 holes. This show a chemisorption reaction between the V_2O_5 NPs surface and the two gases. Hence, we conclude from the results that V_2O_5 NPs is 32 times more selective to NO_2 than to NH_3 .

References

- [1] K. Watchakun, T. Samerjai, N. Tamaekong, C. Liewhiran, C. Siri Wong, V. Kruefu, A. Wisitsoraat, A. Tuantranont, S. Phanichphant, Semiconducting metal oxides as sensor for environmentally hazardous gases, *Sens. Act. B* **160**, 580-591 (2011).
- [2] G. Peng, U. Tisch, O. Adams, M. Hakim, N. Shehada1, Y. Y. Broza, S. Billan, R. Abdah-Bortnyak, A. Kuten, H. Haick, Diagnosing lung cancer in exhaled breath using gold nanoparticles, *Nat. Nano. Lett.* **4**, 669-673, (2009).
- [3] G. Neri, Fifty Years of Chemosensitive Gas Sensors, *Chemosensors* **3**, 1-20, (2015)
- [4] B. Vishah, S. Samanta, A. Singh, A. K. Debnath, A. Mahajan, R. K. Bedi, D. K Aswal, S. K. Gupta, Chemiresistive gas sensing properties of nanocrystalline Co_3O_4 thin films, *Sens. Act. B.*, **176**, 38-45, (2013).
- [5] A. Friedberger, P. Kreisl, E. Rose, G. Muller, G.K. Uhner, J. Wollenstein, H. Bottner, Micromechanical fabrication of robust low-power metal oxide gas sensors, *Sens. Act. B.* **93**, 345-349, (2003).
- [6] N.J. Dayan, S.R. Sainkar, R.N. Karekar, R.C. Aiyer, Formulation and characterization of ZnO:Sb thick-film gas sensors, *Thin Sol. Fil.* **325**, 254-258, (1998).
- [7] W.H. Zhang, W.D. Zhang, Fabrication of SnO_2 -ZnO nanocomposite sensor for selective sensing of trimethylamine and the freshness of fishes, *Sens. Act. B.* **134**, 403-408, (2008).
- [8] G. Sberveglieri, L. Depero, S. Gropelli, P. Nelli, WO_3 sputtered thin films for NO_x monitoring, *Sens. Act. B.* **26**, 89-92, (1995)
- [9] M. Sauvan, C. Pijolat, Selectivity improvement of SnO_2 films by superficial metallic films, *Sens. Act. B.* **58**, 295-301, (1999).
- [10] M. Kasalizadeh, A. A. Khodadadi, Y. Mortazavi, Coupled Metal Oxides-Doped Pt/ SnO_2 Semiconductor and Yttria-Stabilized Zirconia Electrochemical Sensors for Detection of VOCs, *J. Elec. Soc* **1160**, 11, 218-224, (2013)

- [11] V. Kruefu, A. Wisitsoraat, A. Tuantranont, S. Phanichphant, Gas sensing properties of conducting polymer /Au-loaded ZnO nanoparticles composite materials at room temperature, *Nano Res Lett.* **9**, 467 (2014)
- [12] J. Wu, K. Tao, J. Miao, L.K. Norford, Improved Sensitivity and Selectivity of Gas Sensing Using a 3D Reduced Graphene Oxide Hydrogel with an Integrated Microheater, *ACS Mater Interface* **7**, 27502 -27510, (2015)
- [13] W. Zeng, T. Liu, Z. Wang, S. Tsukimoto, M. Saito, Y. Ikuhara, Selective Detection of Formaldehyde Gas Using a Cd-Doped TiO₂-SnO₂ Sensor, *Sens* **9**, 9029, (2009)
- [14] S. Mathur, S. Barth, Molecular-Based Chemical Vapour Growth of Alligned SnO₂ nanowires and Branched SnO₂/V₂O₅ Heterostructures, *Small* **3**, 2070, (2007)
- [15] C. S. Dandeneau, Y. H. Jeon, C. T. Shelton, T. K. Plant, D. P. Cann, B. J. Gibbon, Thin Film Chemical Sensors Based on p-CuO/n-ZnO Heterocontacts, *Thin Solid Films*, **517**, 4448 (2009)
- [16] B.W. Mwakikunga, E. Sidras-Haddad, and M. Maaza, First synthesis of vanadium dioxide by ultrasonic nebula-spray pyrolysis, *Optical Mat.* **29**, 5, 481-487, (2007)
- [17] Se-Hee Lee, H. M. Cheong, M. J. Seong, P. Liu, C. E. Tracy, A. Mascarenhas, J. R. Pittsa, S. K. Deb, Improving the durability of ion insertion materials in a liquid electrolyte, *Sol. St. Ionics* **165**, 81-87, (2003).
- [18] G.I. Petrov, V.V. and Yakovlev, Raman microscopy analysis of phase transformation mechanisms in vanadium dioxide, *App. Phys. Lett.* **81**, 6, 1023, (2002)
- [19] F. Sediri, N. Gharbi, From crystalline V₂O₅ to nanostructured vanadium oxides using aromatic amines as templates, *J. Phy. Chem. Sol.* **68**, 10, 1821-1829, (2007).

- [20] Yu M., Liub X., Wang Y., Zheng Y., Zhang J., M. Li, Lan W., Q. Su, Gas sensing properties of p-type semiconducting vanadium oxide nanotubes, *Appl. Surf. Sc.* Vol. 258, 9554-9558, (2012)
- [21] A. A. Akande, E. C. Linganiso, B. P. Dhonge, K. E. Rammutla, A. Machatine, L. Prinsloo, H. Kunert, B. W. Mwakikunga, Phase evolution of vanadium oxides obtained through temperature programmed calcinations of ammonium vanadate in hydrogen atmosphere and their humidity, *J. Mat. Chem. Phy.*, **151**, 206-214 (2015)
- [22] M. C. Rao Vanadium Pentoxide Cathode Material for Fabrication of all Solid State Lithium Ion Batteries - a Case Study, *Research Journal of Recent Sciences*, **2**, 3, 67-73 (2013).

CHAPTER 7

GATE VOLTAGE CONTROLLED HUMIDITY SENSING USING MOSFET OF VO₂ NANOFLOWERS

A. A. Akande, B. P Dhonge, B. W. Mwakikunga, A. J. G. Machatine, Int. J. Chem. Molecular Nuclear Materials and Metallurgical Engineering Vol 11, No. 1, (2017)

This chapter reports gate controlled humidity sensing of VO₂ (B) nanoflower particles. An optimum sensitivity of 5 V was observed which could be used for selective humidity detection. Faster response and recovery times were obtained compared with the non-gate humidity sensor reported in this work.

7.1 Introduction

Owing to VO₂'s strong electron to electron correlation and metal to insulator transition characteristics; it has been used for developments and designs in various novel ultrafast devices [1]. These devices are the optical modulators or gating, quantum actuators, ultrafast switches for logic, spintronics, thermal switches which use external perturbation in the form of thermal, electrical, optical, or magnetic fields to trigger phase transition from a high-resistance OFF state to a low resistance ON state [1-4]. Rutile (*T*) and monoclinic (*M*₁) structures of VO₂ have been critically reviewed in chapter two, but apart from these phases, meta-stable phases; VO₂ (B), VO₂ (A), VO₂ (A_H) [4-5] and *M*₂, the intermediate phase between the *M*₁ and R phase have been reported. These phases have also been useful in the above technologies [1, 5]. Table 7.1 summarizes these VO₂ phases alongside their properties. Recently humidity

sensing of vanadium oxides particles seated on Al₂O₃-Pt an interdigitated electrode configuration has been demonstrated [6]. This chapter investigates the effect of gate voltage to the humidity response of mixed amorphous-crystalline VO₂ (B) in MOSFET configuration with the aim that the gating of sensor electrodes could help in controlling their sensitivity and selectivity.

Table 7.1: List of known VO₂ polymorphs alongside their major properties

Phases	Density (g/cm ³)	Band gap (eV)	Formation energy (eV)	Transition temp (°C)	Ref
VO ₂ (R)	4.67	Metal	-6.93	-	[7]
VO ₂ (M)	4.67	0.84	-7.18	70	[8]
VO ₂ (B)	4.031	0.65	-6.66	150	[4], [5]
VO ₂ (A)	4.035	0.21	-7.14	120	[5], [9], [10]
VO ₂ (A _H)	4.035	Metal	-6.97	-	[5],

7.2 Experimental details

7.2.1 Material preparation and characterization

The synthesis of VO₂ powders was achieved through microwave irradiation. The precursor NH₄VO₃ (purity 99.99%) and oxalic reagent were thoroughly dissolved in deionized water. The solution was transferred into 100 mL Teflon vessel and placed into the Multiwave 3000 microwave reactor. The reactor power, temperature and the reaction time were maintained at 600 W, 180°C and 20 minutes, respectively. The synthesised sample was allowed to cool for 30 minutes and washed repeatedly with organic solvents in an ultrasonic bath to remove impurities and to minimize agglomeration. Finally, the sample was dried at 100°C for 12 h.

The characterization techniques used to analyse this material were: Panalytical X'pert Pro PW 3040/60 (XRD) with Cu K_{α} ($\lambda=0.154nm$) monochromatic radiation and Jobin-Yvon T64000 Raman spectrograph (RS) with argon ion laser (power 0.384 mW) operated in 514.5 nm excitation wavelength for structural analyses and JEOL 2100 transmission electron microscopy (TEM) for the morphological studies. Adsorption and desorption isotherm to N_2 molecule was carried out using Brunauer-Emmett-Teller (BET) Micromeritics TriStar II series Surface Area, Porosity instrument and degassing system from the USA.

7.2.2 VO₂ MOSFET fabrication and humidity sensing measurements

The VO₂ MOSFET was fabricated by ultrasonically dispersing the VO₂ particles in an organic solvent for 30 minutes and drop-casted onto drain-gate-source electrodes. The MOSFET used in this work is that of lateral-gate MOSFET configuration designed and patented by B. W. Mwakikunga [11]. The pictorial and micrograph images of this MOSFET are shown in Figure 7.1.

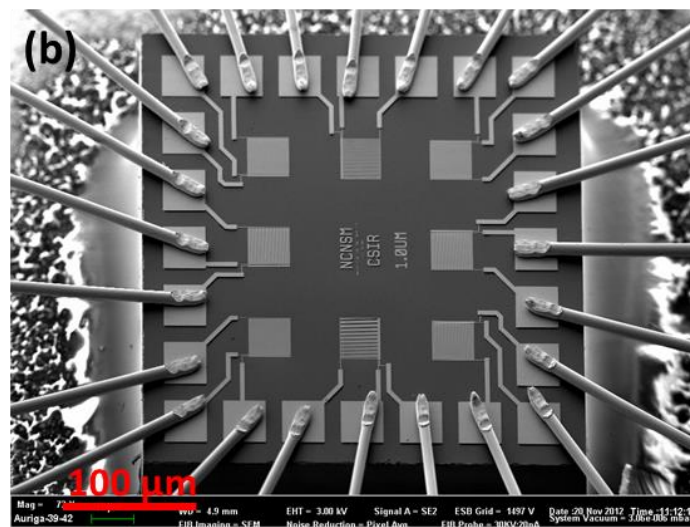
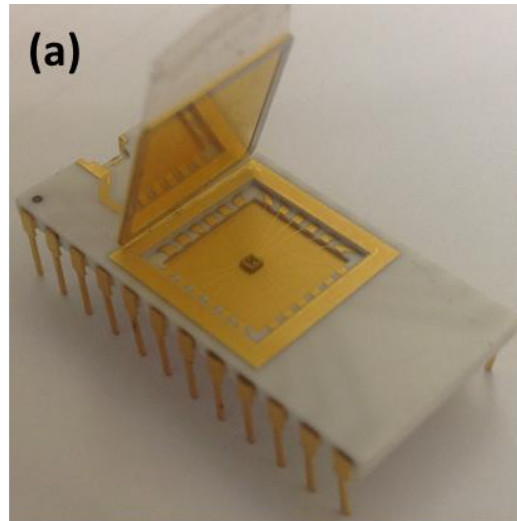


Figure 7.1 (a) Pictorial image of the lateral-gate MOSFET (b) SEM micrograph of the lateral-gate MOSFET.

Humidity sensing measurements were conducted using a KSGA565 KENOSISTEC instrument from Italy. VO₂ MOSFET was situated in the chamber and connected to the KEITHLEY source-metre incorporated in the system. The instrument set-up and sample preparation details are reported elsewhere [12]. Humidity measurements were performed for relative humidity ranging from 15 to 85 % at different gate voltages.

7.3 Results and discussions

The crystal structure of the VO₂ particles is shown by the XRD spectrum in Figure 7.2 (a). The spectrum clearly shows that the phase produced herein is VO₂ (B) with a trace presence of V₂O₅ and the amorphous phase of both V₂O₅ and VO₂ (B). The low angle peak at 15° (2θ) is the characteristic peak of V₂O₅ (PCDPDFWIN CAS No: 89-0611).

This evidence shows that the precursor NH₄VO₃ has undergone a reduction process in the following order: NH₄VO₃ → V₂O₅ → VO₂. This order of formation is validated by the fact that NH₄VO₃ has the vanadium ion in the V⁵⁺ state similar to that of V₂O₅. Reduction from V⁵⁺ of V₂O₅ to V⁴⁺ in VO₂ requires extra energy which is provided from calcination. This observation is consistent with the XPS spectrum in Figure 7.2 (c) which showed a huge peak at 516.7 eV binding energy for VO₂ with a shoulder at 518.1 eV corresponding to the V₂O₅ binding energy. Moreover, the phase VO₂ (B) has been widely reported in the literature as the preferred phase in microwave synthesis and other hydrothermal techniques [4-5]. Many phases VO₂ (B) were identified and indexed, the broad and intense peak at angle 27.8 (2θ) with (002) reflection, the peak at 43.5 (2θ) with (003) reflection and others according to the JCPDS 81 - 2392. The insert TEM diffraction pattern in Figure 7.2 (a) shows that the particles are composed of mixed crystalline grains in the amorphous phase. The first ring of the selected area electron diffraction (SAED) pattern, after the central undiffracted diffuse electron beam can be indexed to (002) Miller plane of the VO₂ (B) crystal structure. The second ring could be attributed to the second intense peak in XRD which also belongs to VO₂ (B). This TEM analysis agrees with XRD that VO₂ (B) is the dominant phase. Figure 7.2 (b), the SEM of the nanoparticles showed that these particles formed flower-like structures.

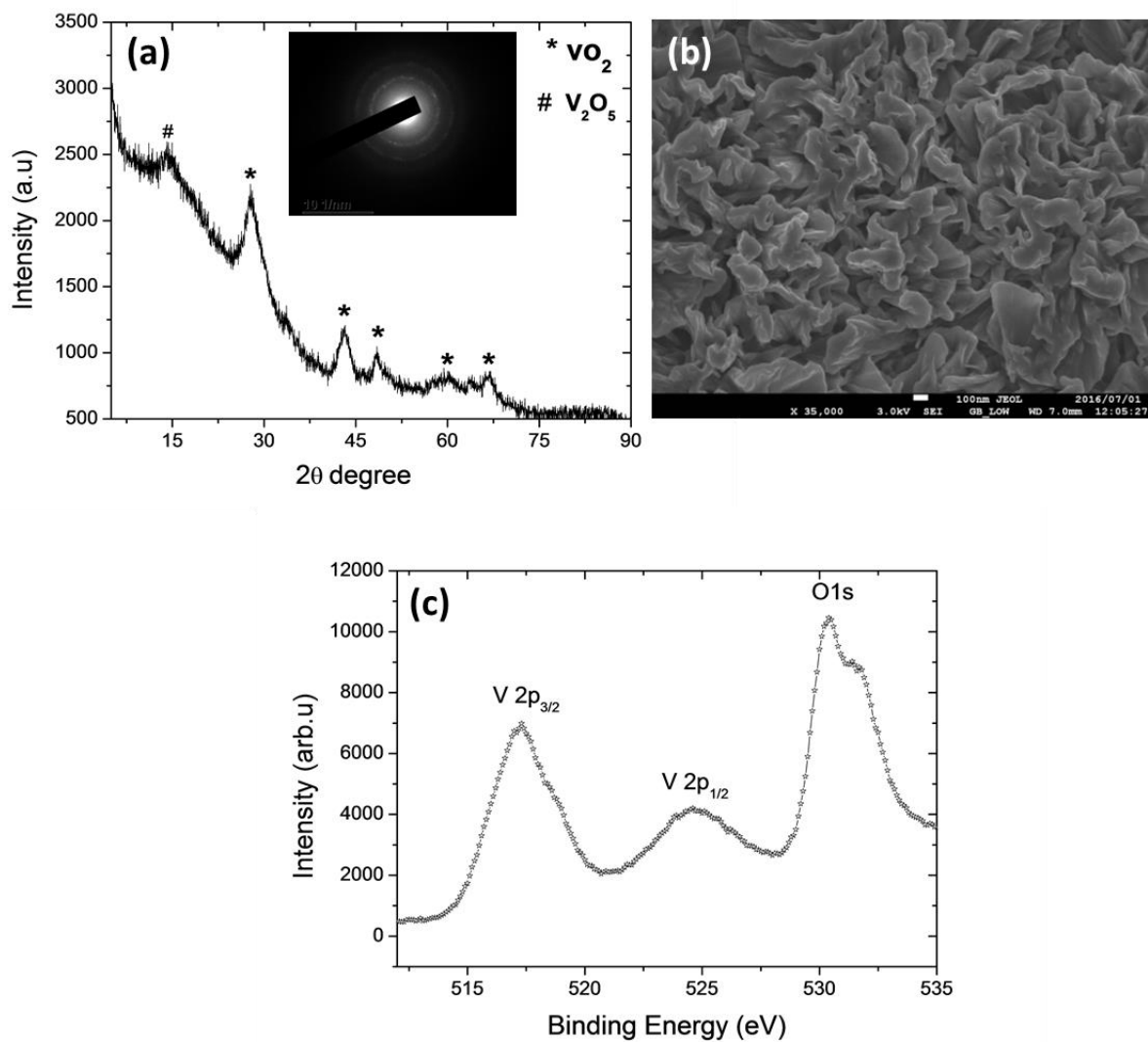


Figure 7.2 (a) XRD pattern (b) SEM image, and (c) core level XPS spectrum of VO_2 nanoflower particles

The Raman spectrum shown in Figure 7.3 (a), reveals the peaks corresponding to VO_2 and V_2O_5 vibrational modes. The peaks belonging to V_2O_5 phase seem to dominate in the spectrum because it is very stable compared to the VO_2 phase of vanadium oxides. This means that the V_2O_5 might be formed at the surface of the core crystalline VO_2 , hence Raman spectroscopy which is surface analysis technique, captured more surface phonons than the core [13-14].

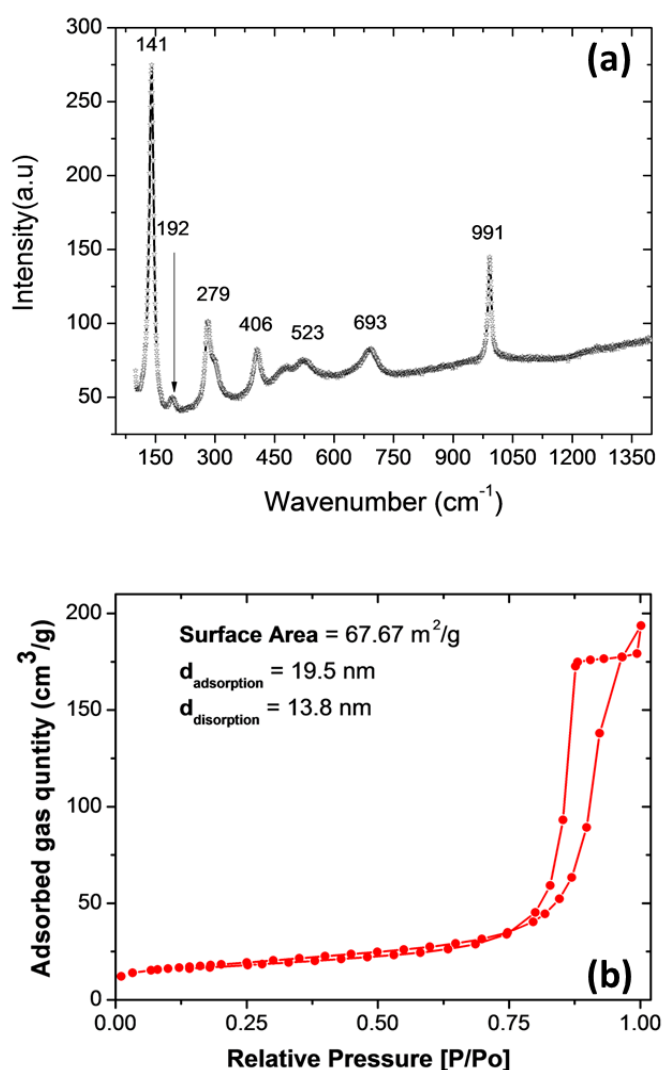


Figure 7.3 (a) Raman spectrum (b) BET - N₂ molecule adsorption and desorption isotherms of VO₂ nanoflower particles.

The BET surface area and physisorption adsorption/desorption isotherm shown in Figure 7.3 (b) shows the high detection capability of the VO₂ particles to N₂ molecules. The quantities in the figure showed improved physisorption effects compared with the one observed in the CVD synthesis of VO₂ [6]. The present surface area is found to be 67.67 m²/g compared to the maximum surface area value of about 16 m²/g in the previous finding [6].

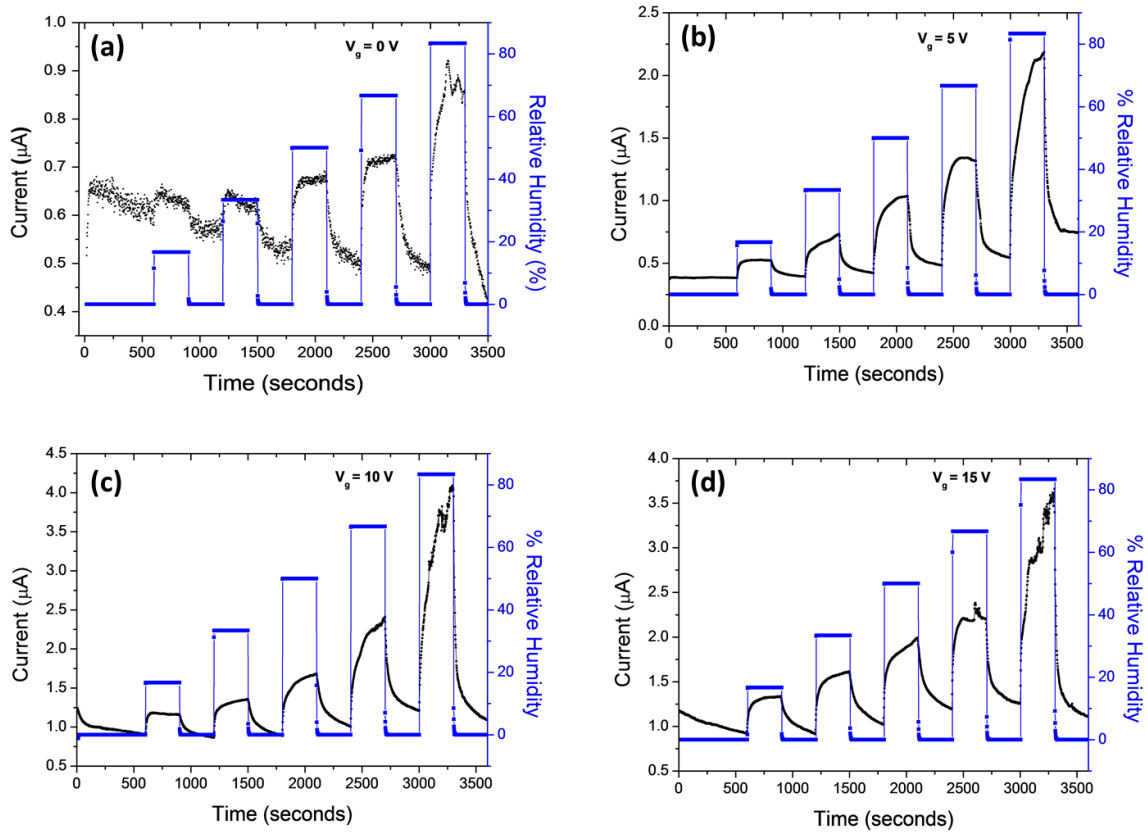


Figure 7.4 Current-time curves for the sensor response to varying levels of relative humidity concentrations (a) 0 V gate bias (b) 5 V gate bias (c) 10 V gate bias (d) 15 V gate bias.

The humidity sensing measurement was carried out at $-V$ of the drain to source voltage. The gate voltages (V_g) were varied from 0 to 15V. The change in the source to drain current versus time with various percentages of humidity for $V_g = 0, 5, 10$ and 15 V are shown in Figure 7.4.

The sensing device response profiles to various humidity levels for different gate voltages is shown in Figure 7.5 with (a) being the response curve against different levels of relative humidity for all gate voltages and (b), the response curve versus gate voltages. The optimum gate voltage was found to be 5 V with a response time of typically 60s and a recovery time of about 70s. This is a very quick response and recovery when compared to the non-gated

VO₂(B) sensor reported in chapter four which showed response and recovery times of the order of 5 minutes [6]. The reason for the 5 V optimum response can be attributed to an effect similar to response-temperature curves in traditional thermally-activated sensors. In such thermally activated sensors, there exists an optimum temperature at which one gets the maximum response. At lower than this critical temperature, it is known that one gets adsorption increasing with temperature. At higher than this critical temperature, the semiconductor properties, where resistance decreases with rising temperature, dominate the adsorption effect. The analogy here is that the heater under the traditional sensor is replaced with a gate or bias voltage. At lower than the critical gate voltage, the adsorption of water vapor molecule effect dominates any other mechanisms available. At higher than this voltage the transistor is driven by its pinch-off state where reduced current leads to a drastic reduction in response of the adsorbing water vapor molecules. The pinch-off state is synonymous to either the Gunn effect or the Josephson's junction effect where negative resistance has been reported for this configuration of transistors in the patent [11].

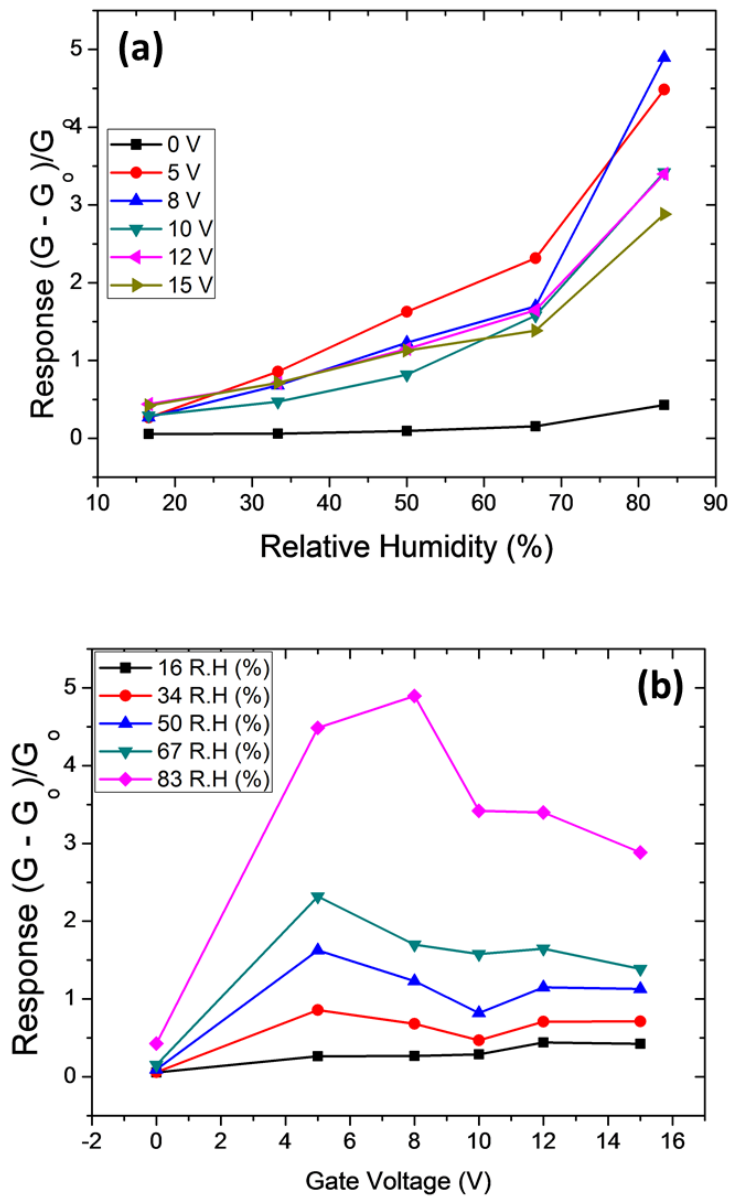


Figure 7.5 (a) Response of the VO₂ nanoflower sensor versus levels of relative humidity (b) Response of the VO₂ nanoflower sensor to relative humidity versus the respective gate voltages.

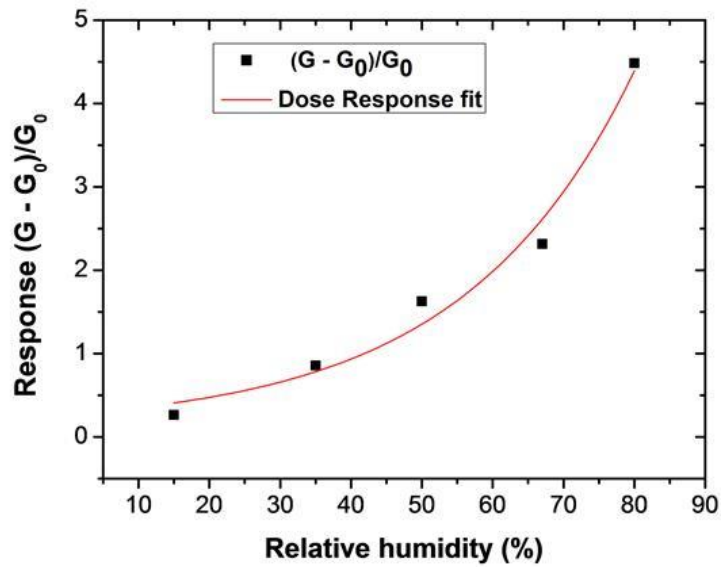


Figure 7.6 Non-linear profile of the response to humidity as a function of the level of the relative humidity for 5V gate bias

When one considers the response to humidity as a function of the level of the relative humidity (at $V_g = 5 \text{ V}$) as shown in Figure 7.6, one observes a non-linear profile which is symptomatic of S-shaped curves in dose-response characteristic equations such as that of Hill or Boltzman S-curve equation or the dose-response equation. When the three equations were tried for fitting, the does-response equation is given by

$$G_{res} = \frac{G - G_0}{G_0} = A_1 + \frac{A_2 - A_1}{1 + 10^{(\log RH_0 - RH)p}} \quad (7.1)$$

where A_1 and A_2 are the lowest and highest sensor responses, $\log(RH_0)$ is the logarithm of the relative humidity at 50% response whereas EC_{50} is the antilogarithm of $\log(RH_0)$ dose at which 50% response is achieved by the sensor and p is the Hill factor. From the fitting, EC_{50} value is 272%, $p = 1.26 \times 10272$ whereas $\log(RH_0)$ is 272.1, A_1 and A_2 are respectively 0.118 and 12096 with a correlation coefficient, R^2 , of 0.925. These results suggest that the VO_2

sensor is very resilient to humidity such that it does not saturate even when humidity approaches 100%. This sensor can then withstand rainy conditions.

7.4 Conclusions

VO₂ (B) nanoflower particles were successfully synthesised and used for the humidity sensing measurements in the MOSFET configuration. The gate voltage was optimized to $V_g = 5V$. The high intensity peak of V₂O₅ vibration modes observed in the Raman spectra reveals the formation of core-shell structures. The presence of V₂O₅ phase with amorphous background was also observed in XRD and TEM measurements. The BET surface area was found to be 67.67 m²/g. The response and recovery times of the gated sensor are remarkably greater (of the order of 60-70 s) than the non-gated VO₂ sensor (which showed time of more than 300 s). The response-humidity data are non-linear and follow the typical S-curve profile. The response-dose equation fits the response-humidity data better than the Hill or Boltzmann S-curve equations and it found that the sensor is very resilient to humidity by showing a humidity level of more than 100% where the response of the sensor could be reduced to 50%. The humidity response versus respective gate voltages profile showed the optimum response for 5 V. This gate voltage (5 V) could be used to calibrate the sensor for humidity detection.

References

- [1] Z. Yang, C. Ko, S. Ramanathan, Oxide Electronics Utilizing Ultrafast Metal to Insulator Transitions, *Annu. Rev. Mater. Res.* **41** (2001) 337-367
- [2] Maksim A. Belyaev, Vadim V. Putrolaynen, Andrey A. Velichko, Genrikh B. Stefanovich, and Alexander L. Pergamen, Field-effect modulation of resistance in VO₂ thin film at lower temperature, *Japanese J. Appl. Phys.* **53**, 111102 (2014)
- [3] Yong Wook Lee, Eung-Soo Kim, Bo-Sung Shin and Sang-Mae Lee, High-Performance Optical Gating in Junction Device based on Vanadium Dioxide Thin Film Grown by Sol-Gel Method, *J. Elect. Eng. Tech.*, **7**, 5, 784-788, (2012)
- [4] E. Strelcov, Y. Lilach, A. Kolmakov, Gas sensor based on metal to insulator transition in VO₂ nanowire thermistor, *Nano Lett.* **9**, 2322-2322, (2009)
- [5] C. Wang, X. Liu, W. Xiong, Y. Zheng, PEG-Assisted hydrothermal synthesis of VO₂ (A) nanowire with remarkable optical switching properties, *Interenational Conference on Mechanics and structural Engineering (ICMMSE 2016)*
- [6] A. A. Akande, E. C. Liganiso, B. P. Dhonge, K. E. Rammutla, A. Machatine, L. Prinsloo, H. Kunert, B. W. Mwakikunga, Phase evolution of vanadium oxides obtained through temperature programmed calcinations of ammonium vanadate in hydrogen atmosphere and their humidity, *J. Mat. Chem. Phys.* **151**, 206-214, (2015).
- [7] J. M. Baik, M. H. Kim, C. Larson, C.T. Yavuz, G.D. Stucky, A.M. Wodtke, M. Moskovits, Pd-Sensitized Single Vanadium Oxide Nanowires: Highly Responsive Hydrogen Sensing Based on the Metal–Insulator Transition, *Nano Lett.* **9**, 3980-3984, (2009).
- [8] D. Manno, A Serra, M Di Giulio, G. Micocci, A. Taurino, A. Tepore, D. Berti, Structural and electrical properties of sputtered vanadium oxide thin films for applications as gas sensing material, *J. Appl. Phys.* **81**, 2709-2714, (1997)

- [9] H. Yin, K. Yu, Z. Zhang, M. Zeng, L. Lou, Z. Zhu, *Electroanal* **23** (2011) 1752-1758
- [10] Y. Oka, S. Sato, T. Yao, N. Yamamoto, Hydrothermal synthesis of W and Mo co-doped VO₂ (B) nanobelts, *J. Sol. St. Chem.* **141** 594-598, (1998)
- [11] B. W. Mwakikunga, A field effect transistor and a gas detector including a plurality of field effect transistors, PA158013/P No. WO2014191892 A1 PCT/IB2014/061713 also published as China (CN105474006A) Germany (DE112014002575T5) and USA (US20160116434)
- [12] A.A. Akande, B.W. Mwakikunga, K.E. Rammutla, A. Machatine, L., “Lager selectivity of the V₂O₅ nano-particles sensitivity to NO₂ than NH₃” *J of Sensor and Trasducers* **151**, 206, (2015)
- [13] B W Mwakikunga, M. Maaza, K.T. Hillie, C.J. Arendse, T. Malwela, E. Sideras-Haddad From phonon confinement to phonon splitting in flat single nanostructures: A case of VO₂@V₂O₅ core-shell nano-ribbons, *J. Vib. Spec.* **02**, 105-111, (2012)
- [14] A.A. Akande, Vanadium dioxide Nanostructure Production and Applications in Sensors, MSc Thesis, University of Limpopo (2014).

CHAPTER 8

BLUE- AND RED- SHIFTS OF V₂O₅ PHONONS IN NH₃ ENVIRONMENT BY IN SITU RAMAN SPECTROSCOPY

A. A Akande, A. G. J. Machatine, B. Masina, G. Chimowa, B. Matsoso, K. Roro, M-M Duvenhage, H. Swart, S.S. Ray, B.W. Mwakikunga, *J. Physics D: Applied Physics* (2017)
<https://doi.org/10.1088/1361-6463/aa98fe>.

In this chapter, in-situ Raman spectroscopy sensing of NH₃ gas at the surface of V₂O₅ thin film is demonstrated. Reversible blue and red shift of phonons in the presence and absence of NH₃ is observed for the first time in the in-situ Raman spectroscopy sensing field. The electron transfer mechanism between the NH₃ and V₂O₅ film interface is discussed. Comparisons between the in-situ Raman spectroscopy sensing and chemoresistive technique data are reported.

8.1 Introduction

Raman spectroscopy is a reliable, sensitive and non-destructive method used in characterizing metal oxides and other nanomaterials [1-2]. The Raman technique has been applied to study adsorption of molecules on the surface of metal oxides and to monitor their selective ability toward certain species of gas [3-5]. Among these studies, A_{1g} mode of SnO₂ was observed to show a huge enhancement when H₂S gas reacted with Cu doped SnO₂ nanomaterial [3]. This enhancement is observed to be absent when the material is exposed to air. The effect is reported to be reversible and the band is attributed to Cu₂S vibration, thus showing reactivity of Cu doped SnO₂ with H₂S. Nanocrystalline WO₃ powder has also been

found to react with the reducing gases CH₄ and CO resulting in the growth of two broad band peaks at 1300 cm⁻¹ and 1600 cm⁻¹ which were observed to be absent in the Raman spectrum of pure WO₃ [4-5]. Whereas, these peaks disappeared in the presence of an oxidizing gas NO₂ and thereby are attributed to the graphitic carbon peak usually present in many carbon materials [1]. This also showed reactivity of CH₄ and CO with the WO₃ surface. Vanadium oxide materials are very sensitive to Raman spectroscopy [2, 6-7] and are often characterized by it to explore their structural, metal-insulator and nanostructured properties [2]. The reason for this sensitivity is nothing less than the vanadium oxides' variation in its oxidation state and crystallographic structures which usually cause atomic or lattice displacement (distortion) causing active vibration [2, 6-12]. Crystallographic, electronic and phonon structures of VO₂, V₂O₅ and V₆O₁₃ systems have been reviewed in detail in chapter two of this thesis.

The first order Raman active modes of V₂O₅ structures can be obtained from the symmetrized square of the vector representation (x,y,z) as the second rank polarizability tensor in the space group D_{2h}^{13} with 8 symmetry elements namely; E, C₂ (z), C₂ (y), C₂ (x), *i*, σ (xy), σ (xz) and σ (yz) and by factor group analysis and selection rule for D_{2h}^1 point group. The infrared modes transform as (x,y,z) representation, since they are related to the electric dipole moment. Zhon et al [13] reported that 21 Raman active modes composed of A_g, B_{1g}, B_{2g} and B_{3g} modes may be presented in the V₂O₅ crystal while the remaining 18 modes may be due to infrared absorption (i.e infrared active). On the other hand, the low temperature phase of VO₂ structures has space group P2₁/ (C_{2h}⁵ No. 14) and two atoms per unit cell in the monoclinic crystal system. Group theory predicts 18 total modes and 15 optical zone-centre modes at wave vector q=0 in the Brillouin zone (at Γ – point) from lattice mode representation by acting 4 symmetry elements E, C₂ (z), *i* and σ (xy). These modes composed of A_{1g}, B_{1g}, B_{2g} and B_{3g} which were distributed in different configurations with respect to the crystal structure of the precursor compound. In this Chapter, we identify these vibrational

modes in in-situ Raman spectra of the V_2O_5 surface as it interacts with the NH_3 molecule as predicted from group theory. The study combined Raman spectroscopy methods, group theoretical approaches and electrophysical techniques to show the reactivity of vanadium oxide surface to NH_3 molecules at ambient temperatures and at 100 °C by oxygen ionosorption and lattice vibration mode assignment. The set-up could be miniaturized to find its usefulness in portable sensitive and selective chemical sensors or applied as a stationary industrial gas detector.

8.2 Experimental

A pulse laser deposition (PLD) technique was employed in this study to grow VO_x thin film on Corning glass substrates. The glass substrates were rigorously cleaned and rinsed several times in (ethanol and deionized water) with an ultrasonic bath in order to remove impurities and ensure quality. Vanadium oxide (VO_2 nanoparticles (NPs) powder with 99.9 % purity) from Sigma Aldrich was converted to pellets using ENERPAC P142 hydraulic cold press system made in the USA. About 5 grams of VO_2 (NPs) powder was slightly dampened with methanol and transferred into a 20 mm hollow die after which a load of 100 tons was mounted on the specimen, and the resulting pellet was annealed at 500° C for ~24 hrs. The set-up and plasma plume dynamics of the PLD system used for this work is similar to the one reported in [14]. Nd:YAG laser beam ($\lambda = 266$ nm, $\tau = 8$ ns) was directed to the chamber by the aid of several mirrors and later focused onto the VO_2 pellet target at an incident angle of 45° using two cylindrical lenses. The minimum pulse energy was applied at 45 mJ with laser fluence of 2 J cm^{-1} and the substrate to target distance of 5 cm was maintained during deposition. Oxygen partial pressure was set to 0.05 mbar (37 mTorr) after evacuating the chamber to the base pressure of 3.1×10^{-5} mbar, and the film was deposited for 30 minutes. The x-ray diffraction patterns of the film were measured at room temperature using the Panalytical XPERT PRO PW3050/50 diffractometer with $CuK\alpha$ radiation (45 kV, 400 mA, λ

= 0.1540598 nm and $5^\circ \leq 2\theta \leq 90^\circ$). The Auriga ZEISS Scanning electron microscope (SEM) was employed to study the morphology of the film and to estimate the thickness of oxide layers that are present. High resolution x-ray photoelectron spectroscopy (XPS) was obtained with a PHI 5000 Versaprobe system. A low energy Ar^+ ion gun and low energy neutralizer electron gun were used to minimize charging on the surface. A 100 μm diameter monochromatic Al $K\alpha$ x-ray beam ($h\nu = 1486.6$ eV) generated by a 25 W, 15 kV electron beam was used to analyze the different binding energy peaks. The pass energy was set to 11 eV giving an analyzer resolution ≤ 0.5 eV. Multipack version 8.2 software was utilized to analyze the spectra to identify the chemical compounds and their electronic states using Gaussian–Lorentz fits.

Time of flight secondary ion mass spectroscopy (TOF-SIMS) analyses were performed using an IONTOF TOF SIMS⁵ instrument with bismuth 1+ as the primary ion source (30 kV, 1 pA pulsed at 10 kHz). These analyses were carried out in negative secondary ion mode and under ultra-high vacuum (base pressure) of $\sim 10^{-9}$ mbar. A Cesium (1 kV, 75 nA) sputter gun was used. The analysis area was 100 x 100 μm^2 and the sputter area was 300 x 300 μm^2 at a resolution of 512 x 512 pixels with a binning of 4 pixels.

Raman structural properties of the film and in-situ-sensing measurements of NH_3 effluent produced from ammonium acetate at 100 °C was carried out using a Bruker spectrometer. A Bruker Raman Senterra spectrometer equipped with 50x optical objective and a 532 nm excitation laser, at a laser power of 0,2 mW, was used for accumulating the films' spectra. The typical experimental set-up of the in-situ Raman sensing measurement is presented in Figure 3.6 wherein a 532 nm Neon lamp laser was directed to the film glued onto an Al_2O_3 -Pt interdigitated electrode set. The heating terminals of the interdigitated electrode are connected to a DC power supply and the whole specimen is enclosed in a transparent chamber where NH_3 effluent from the thermal decomposition of ammonium acetate was

allowed flow through. Conductometric sensing measurements were conducted using KSGA565 KENOSISTEC sensing station set-up in Figure 5.1. The film surface was wire bonded by silver paste in two terminals configurations to allow connection with the KSGA565-KEITHLEY source meter, after which the currents across the film were measured for different concentrations of NH_3 gas.

8.3 Results and discussion

Figure 8.1 (a) shows the XRD pattern of the film, the pattern shows that the film is largely composed of V_2O_5 according to the Institute for Crystallographic and Diffraction Database (ICDD) with a powder diffraction number of (PDF 41-1426) but with trace phases of VO_2 and V_6O_{13} according to (PDF 76-0676) and (PDF 27-1318) respectively. This X-ray spectrum has been matched with the Rietveld structure refinement method with the Bragg positions showing strong correlation with the V_2O_5 structure. The average crystallite size L and lattice micro/nano strain ε of the film were calculated using the well-known Scherrer's and Williamson-Hall formula [15-16-] and were found to be ~ 70 nm and $0.000651 \pm 1.32 \times 10^{-4}$ respectively. Figure 8.1 (b) is the plot of the Williamson-Hall assumption for lattice strain determination. The film morphology are presented in Figure 8.2 with (a) showing the in-plane formation of clusters of particles with pores at the surface and (b) the cross section at the edge of the film showing that the film is ~ 30 nm in thickness.

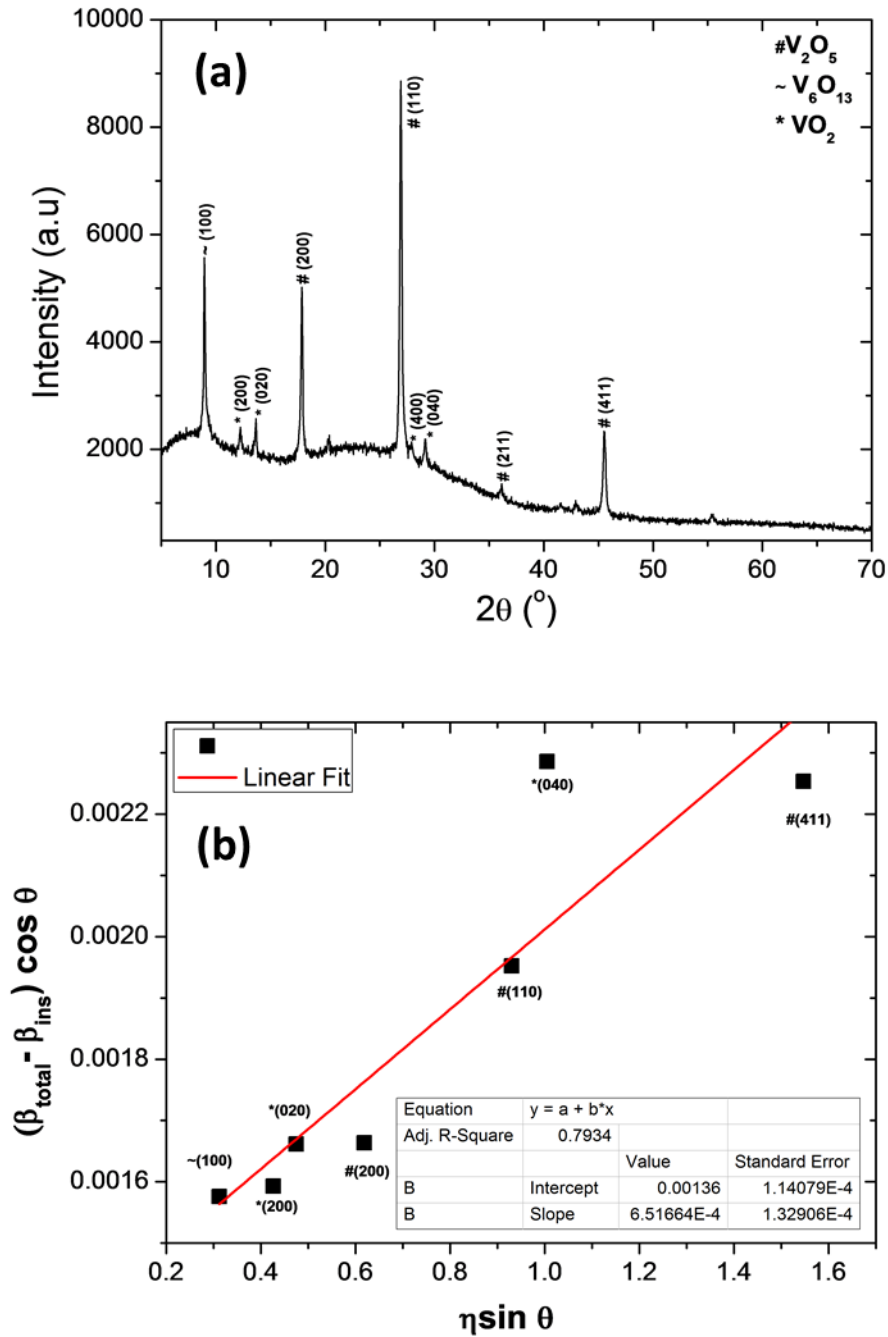


Figure 8.1. (a) XRD pattern of V_2O_5 film, (b) Williamson-Hull plot for the grains stain determination.

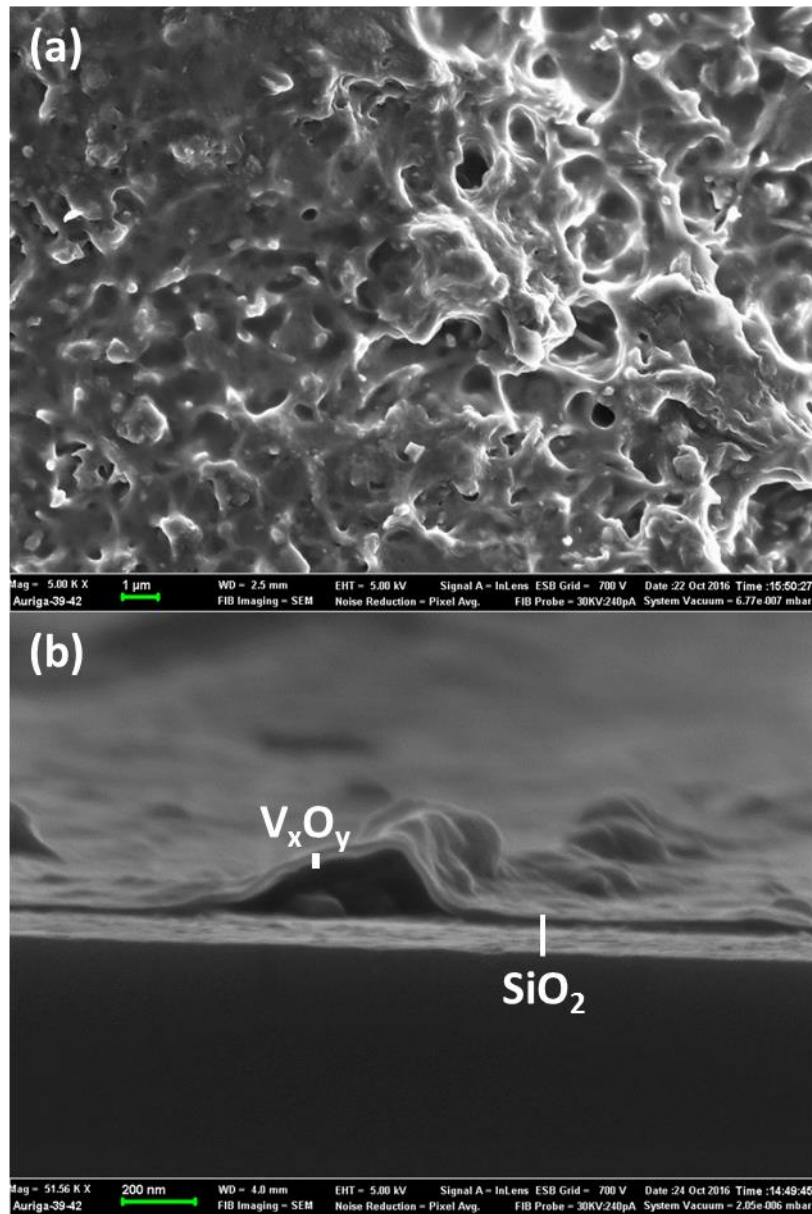


Figure 8.2. SEM images of V_2O_5 film, (a) in-plane surface image (b) cross-section image at the edge of the film showing three distinct layers.

XPS spectrum of the surface of the V_2O_5 film is represented in Figure 8.3 with (a) displaying the overall core level XPS survey spectrum and (b) showing Lorentzian- Gaussian deconvoluted core level spectrum of V-2p and O-1s for the V_2O_5 film. The $\frac{1}{2}$ spin-orbit doublet component of the V-2p photoelectron was found to be 524.1 eV while the $\frac{3}{2}$ spin-orbit component after further Lorentzian- Gaussian dividing peak analysis gives 517.25 and 516.2 eV for V^{5+} and V^{4+} respectively [17-18]. The TOF SIMS measurement has been used

to unveil the chemical elements that are present in V_2O_5 film as a function of sputter-depth, the results are presented in Figure 8.4 where (a) shows depth profile of the negative ions of V, VO, Si and SiO species, (b) is the magnified spectrum of SiO-, V- and VO₃H- species and (c) and (d) are the overlay images of all the compounds present in the film. The spectra of ions with depth in Figure 8.4 (a) and their image overlays in Figure 8.4 (c) shows that vanadium oxides species dominate the film surface to ~ 500 seconds sputter time. This analysis is in good agreement with the above XPS results in that VO₂ (V⁴⁺) and V₂O₅ (V⁵⁺) were seen to be more at the surface. This is also true for XRD analysis that shows diffraction peaks for VO₂ (V⁴⁺), V₂O₅ (V⁵⁺) and V₆O₁₃ which happen to be V⁴⁺ and V⁵⁺ mixed oxide. The TOF-SIMS spectrum in Figure 8.4 (a) and overlay images in Figure 8.4 (c) also made it possible to understand the V₂O₅ film layers in the SEM cross-section image in Figure 8.2 (b) and estimate the film thickness. It was found that in ~ 500 seconds sputter time ~ 30 nm vanadium oxides layer was sputtered completely and thereafter the gun penetrated into the interface region in ~ 700 seconds sputter time which is found to be rich in SiO₂. This SiO₂ layer has been estimated to be ~100 nm from the cross-section SEM image.

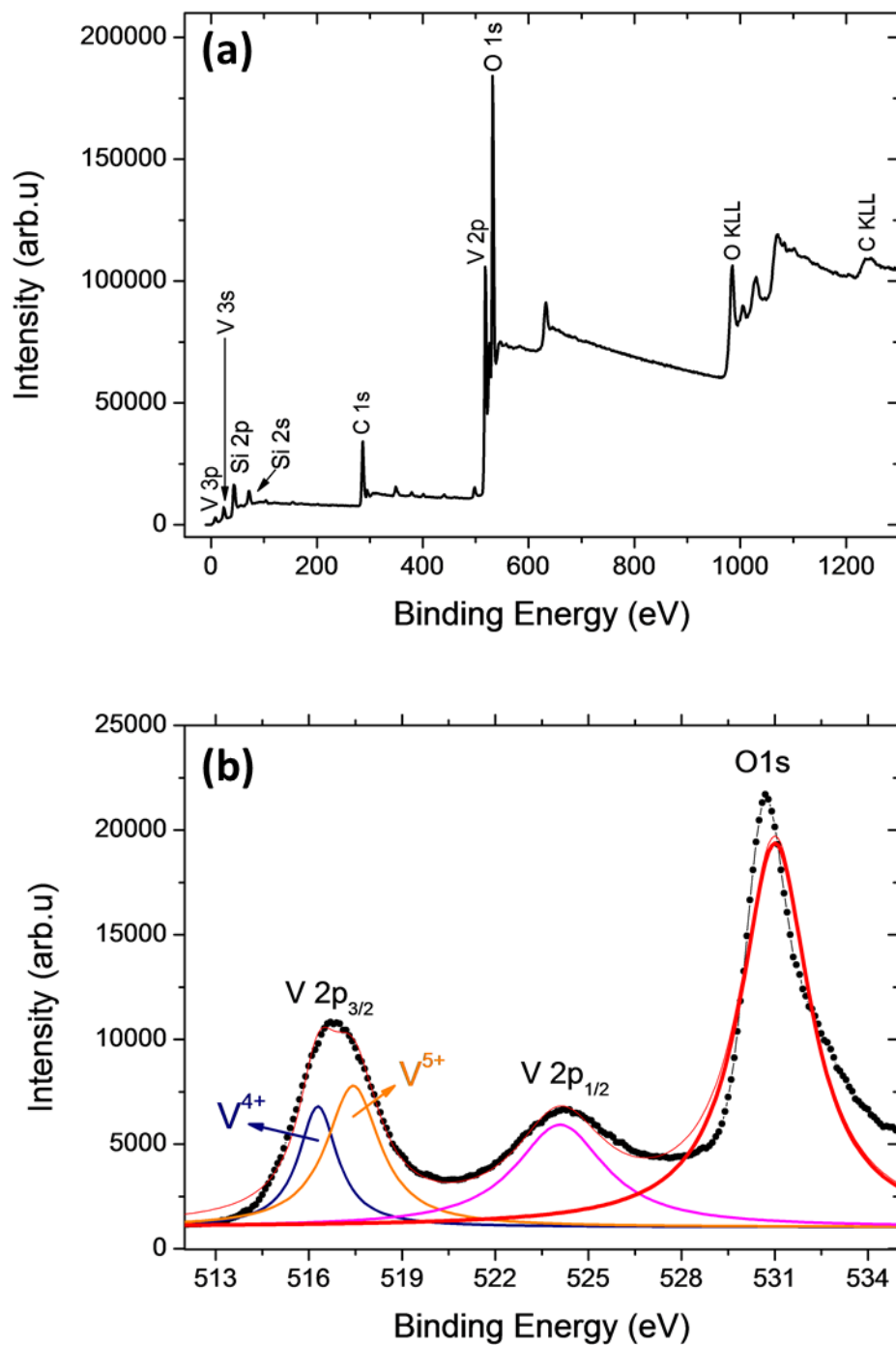


Figure 8.3. XPS spectra of the V_2O_5 film, (a) Broad survey scan spectrum (b) Higher resolution deconvoluted core level spectrum of V-2p and O-1s for the V_2O_5 film.

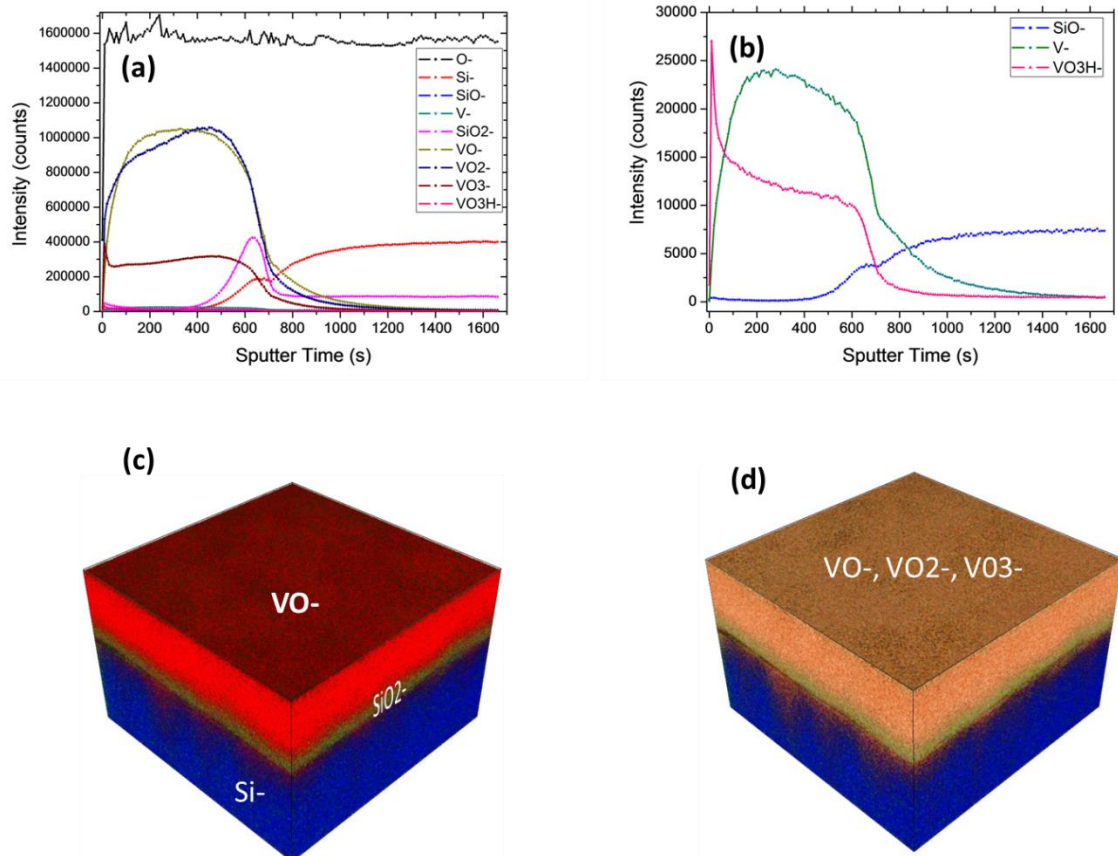


Figure 8.4. (a) TOF-SIMS depth profile of the negative ions of V, VO, Si and SiO species available in the film (b) is the TOF-SIMS depth profile spectrum showing the low counts SiO-, V- and VO3H- species in (a) , (c) 3D overlay image of the ions of the film consisting of Si-, SiO2- and VO- (d) 3D overlay image of the entire film displaying VO-, VO2- and VO3- as the surface ions.

8.3.1 In-situ Raman spectroscopy with gas sensing at 25 °C

Figure 8.5 shows the effect of atmosphere changes in the surface of V_2O_5 film when subjected to the effluent of NH_3 from the compound of ammonium acetate. Figure 8.5 (a) illustrates the change in Raman spectra of the film when exposed to the molecule at different times (with intervals of 6 minutes) and to air (as a control spectrum) at 25 °C while Figure 8.5 (b) represents the change in the Raman spectrum of the film when recovering from NH_3 . In these profiles, the authors observed that the modes at a low-frequency

Raman line region of V_2O_5 , earlier classified as rigid-layer modes [7] with bending vibration characteristics, were mostly unaltered in wavenumber when the film was subjected to the NH_3 effluent. Interestingly, the one at 194 cm^{-1} which shows a shift to low-frequency Raman line was observed to redshift. On the other hand, at the higher-frequency side of the Raman spectra, the 996 cm^{-1} stretching mode displayed significant shift towards high frequency of the Raman line (blueshift) in all spectra (shown in Figure 8.6 (a)). The reverse effect was observed when recovering the film from effluent of NH_3 in Figure 8.5 (b) and 8.6 (b), where both blueshifted 996 cm^{-1} and redshifted 194 cm^{-1} modes showed some recovery potential.

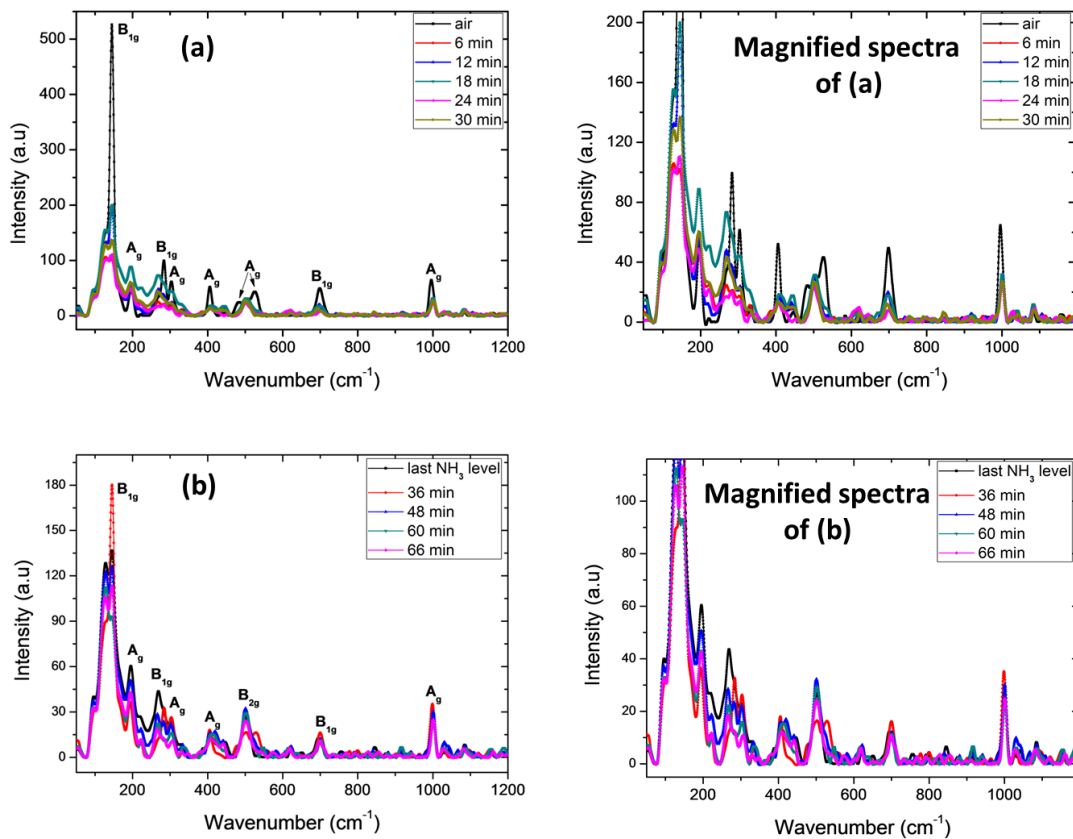


Figure 8.5. (a) Raman spectra at $25\text{ }^\circ\text{C}$ of V_2O_5 film in air, and covered with NH_3 molecules recorded at 6 minutes intervals, (b) Raman spectra at $25\text{ }^\circ\text{C}$ of V_2O_5 film recovering from NH_3 molecules recorded at 6 and 12 minutes intervals.

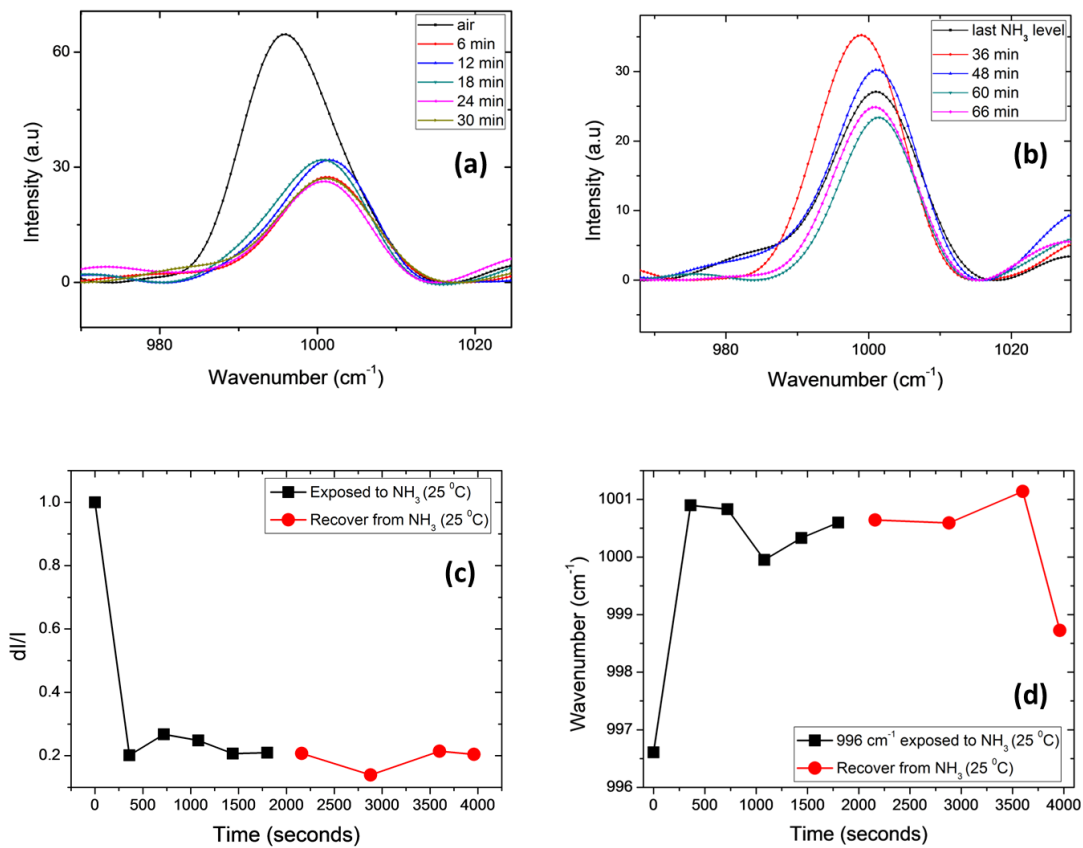


Figure 8.6. (a) Magnified images of 996 cm⁻¹ Raman lines when the film is exposed to NH₃ at 25° C (b) Magnified images of 996 cm⁻¹ Raman lines when the film is recovering from NH₃ at 25° C (c) Gaussian fitted data of the heights of low-frequencies 143 cm⁻¹ Raman lines when the film is exposed to and recovering from NH₃ at 25°, (d) Gaussian fitted data of peak-positions of high-frequencies 996 cm⁻¹ Raman lines when the film is exposed to and recovering from NH₃ at 25 °C.

In accordance with Equation 3.15 where the change in Raman line position $d\omega$, as a function of both elastic constant of the bonds, κ , and reduced mass of the atoms around these bonds, μ , is given by $d\omega \propto d\kappa - (\kappa/\mu^2)d\mu$. In the present system case: $1/\mu = (1/m_O) + (1/m_V)$ or $\mu = m_O m_V / (m_O + m_V)$. The increase in κ could be ascribed to acceptance of an electron by the V₂O₅ surface from the NH₃ effluent and vice versa, whereas an increase in μ could be

ascribed to the acceptance of atoms from the gas by the V_2O_5 surface. Changes in κ should be prevalent at 25°C where adsorption is more likely to happen, while an increase in μ is likely to happen at high temperatures where chemisorption due to breakage of NH_3 bonds is preferred.

Since the 996 cm^{-1} phonon is being blue-shifted [i.e. $d\omega > 0$] when exposed to NH_3 , one expects that $d\kappa > d\mu/\mu^2$. This means that the change in elastic κ is larger than the change in μ . This suggests that V=O bond gains electrons from NH_3 . On the other hand, the observation that the 194 cm^{-1} phonon is being red-shifted when NH_3 is introduced means that $d\kappa < d\mu/\mu^2$. This could indicate that the V-O-V or O-V-O bonds prevalent in the VO_2 system are losing electrons to the NH_3 at 25°C. This surprising result leads to the conclusion that bonds that have many electrons tend to gain more electrons whereas those bonds that have less electrons tend to lose even the few electrons that they have. This phenomenon is similar to an observation made during the halogenation of organic alkanes with HCl or HF or HBr in 1890s by a scientist known as Markovnikov who observed that the H atom preferred to attach itself to carbons with the highest number of H atoms [19-20].

A decrease in intensities of 145 cm^{-1} low-frequency Raman line of V_2O_5 were also observed as a function of NH_3 effluent exposure (Figure 8.5 (a)) [21] but a reverse effect is observed when recovering the surface from NH_3 exposure in that the intensities increased slowly and saturate (Figure 8.5 (b)) with less potential when recovering from the NH_3 effluent. The profiles in Figure 8.6 (c) and (d) are representative of the change in intensity (dI/I) of the 145 cm^{-1} Raman lines and wavelength (ω) peak-positions of 996 cm^{-1} Raman line at 25 °C. These line profiles show that the intensities of 145 cm^{-1} phonon decrease and saturate with time during exposure, and experience difficulty in recovery due to the lack of vents in the home made gas sensing cell. This decrease in Raman scattered intensities in the

presence of molecules may also be due to the absorption of laser light of free electrons created as a result of the interaction between V_2O_5 and NH_3 [4]. The Raman fingerprint position of 996 cm^{-1} phonon recorded more significant blueshift (4 cm^{-1}) before saturation when exposed to the NH_3 molecule with relatively high potential of recovery than the redshift of the 194 cm^{-1} (2 cm^{-1}) as shown in Figure 8.6(d).

8.3.2 In-situ Raman spectroscopy with gas sensing at 100 °C

In the same manner, Figure 8.7 (a) displays the Raman spectra of the film when exposed to the effluent of the NH_3 molecule at different times (with interval of 6 minutes) and to air (as control spectrum) at 100 °C, while Figure 8.7 (b) shows the change in Raman spectra of the film when recovering from the molecule. The fact that the phonons are thermally mediated coupled with the possibility of less scattering of light at the less-dense environment may be responsible for the change observed at 100 °C relative to the effects observed in the case of room temperature measurements (25 °C). It is true that the way and manner in which the NH_3 molecule sits on the V_2O_5 will greatly influence the charge distribution between them [21-22]. In addition to the V_2O_5 crystal, geometrical structure and space group discussed in chapter two, V_2O_5 is a layered structure having distorted square pyramids of VO_6 which share edges and corners with the apex of the V-O configuration having a much shorter bond length compared to other bonds. This short bond length corresponds to a double bond attachment [11, 22]. One may propose that hydrogen atoms in an NH_3 molecule in a trigonal pyramid structure preferred to attach themselves to the vanadyl oxygen (i.e the one with double bond and shorter length). If so, that may cause the molecule to give away some of their charges to the V=O layer and consequently increase the spring constant which leads to a blueshift in the Raman spectrum. Thus, the remnant of the NH_3 dissociation that are lying in the chamber may regroup and attach themselves to the bonded hydrogen atom and revert back to the NH_3 molecule when recovering V_2O_5 film from the coverage.

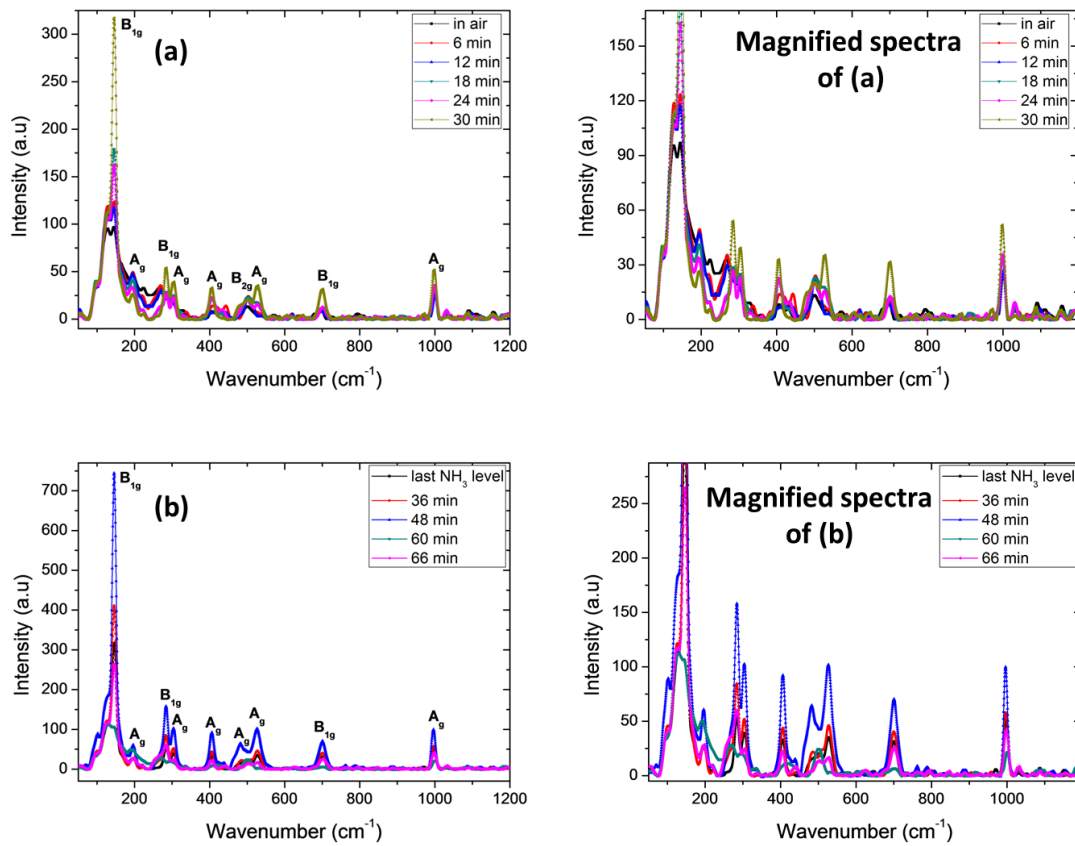


Figure 8.7. (a) Raman spectra at 100 °C of V_2O_5 film in air, and covered with NH_3 molecule recorded at 6 minutes intervals, (b) Raman spectra at 100 °C of V_2O_5 film recovering from NH_3 molecule recorded at 6 and 12 minutes intervals.

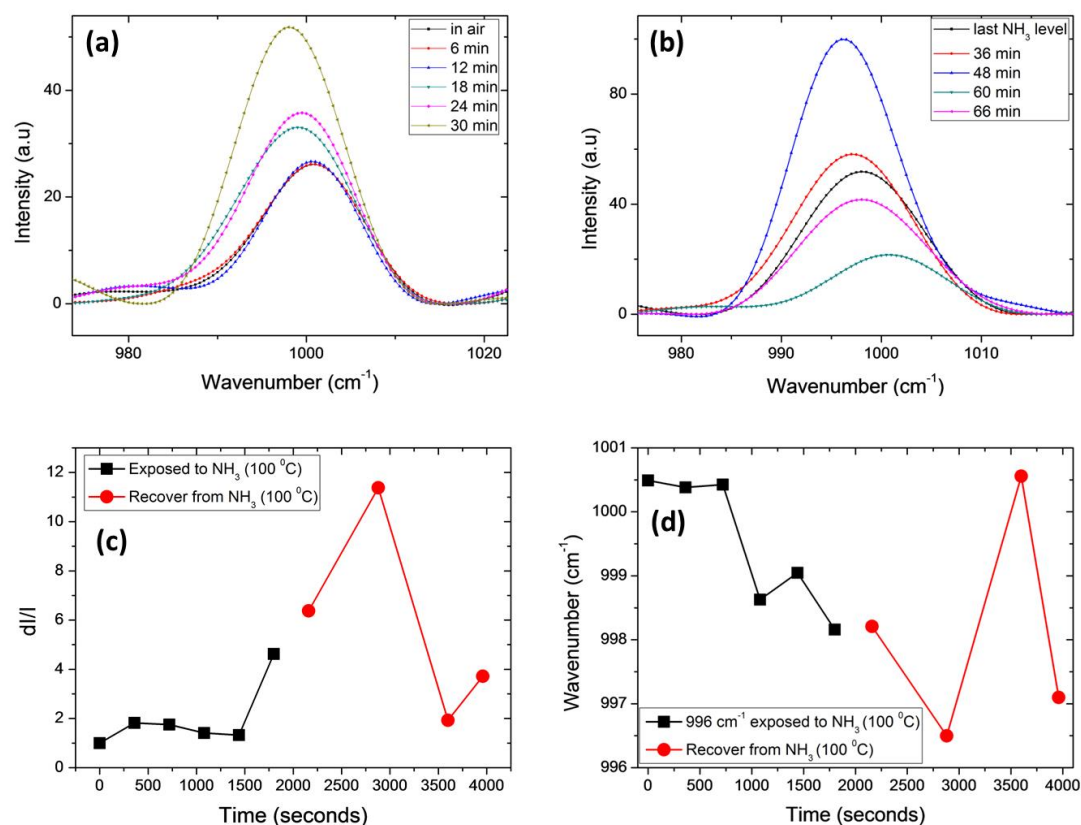


Figure 8.8. (a) Magnified images of 996 cm^{-1} Raman lines when the film is exposed to NH_3 at $100^\circ C$ (b) Magnified images of 996 cm^{-1} Raman lines when the film is recovering from NH_3 at $100^\circ C$ (c) Gaussian fitted data of the heights of low-frequencies 143 cm^{-1} Raman lines when the film is exposed to and recovering from NH_3 at $100^\circ C$, (d) Gaussian fitted data of peak-positions of high-frequencies 996 cm^{-1} Raman lines when the film is exposed to and recovering from NH_3 at $100^\circ C$.

Other Raman frequency modes of V_2O_5 observed were $225, 270, 283, 305, 335, 406, 503, 614$ and 700 cm^{-1} at $25^\circ C$ and $100^\circ C$, and they all belong to the vibration modes of V_2O_5 except the modes at 194 cm^{-1} and 614 cm^{-1} which are Raman fingerprint positions for the VO_2 structure [7, 13, 15, 23-24]; this shows that VO_2 crystallites are not participating in the reactivity of the NH_3 effluent molecule.

8.3.3 Comparison of in-situ Raman spectroscopy-gas-sensor tester and the traditional chemoresistive gas-sensor testing station

Figure 8.9 shows electrical measurements of the V₂O₅ film in the presence and absence of NH₃ gas via the set-up described in the experimental section and previously reported [8, 25]. Figure 8.9 (a) is the transient time-conductometric signals of the film when exposed to NH₃ gas at room (25 °C) and Figure 8.9 (b) is the signals at 100 °C. The profile shows a decrease in conduction of the film in the presence of NH₃ gas at 25 °C and 100 °C for every concentration. The sensor response and response time constant calculations for different concentrations of NH₃ gas are given as follows:

$$\frac{i}{i_0} = \exp\frac{t}{\tau_1} \quad 0 \leq t \leq t_1 \quad (8.1)$$

$$\frac{i}{i_0} = \exp\frac{t}{\tau_1} \times \exp\frac{t-t_1}{\tau_2} \quad t_1 < t \leq t_2 \quad (8.2)$$

where i_0 is the initial current of the sensor in synthetic air (flowing through the chamber), t_1 is the time for i_0 value, i is either the current when the target gas is turned on or off, t_2 is the time at which the sensor recovers to its original value. The quantity τ_1 and τ_2 are the time constants for response and recovery steps, these parameters were calculated by fitting the first order exponential function in Equation (8.1) and (8.2). Figure 8.10 (a) shows a response profile which was calculated from Equation (8.1). The pattern shows better adsorption for all concentrations of the NH₃ gas at 25 °C compared to the one at 100 °C. A response time constant plot was extracted from the same Equation (8.1) as shown in Figure 8.10 (b). The response time constant in this work is defined as the time it takes the sensor to reach 63% i.e. $1-e^{-1}$ of its maximum after exposed to the gas [9, 26-27]. This result also showed that the responses at 25 °C are faster than that of 100 °C but responses at 100 °C showed stability

compared with ones at 25 °C. There is a cross-over in the response time at 20 ppm where the response time is found to be 50 seconds.

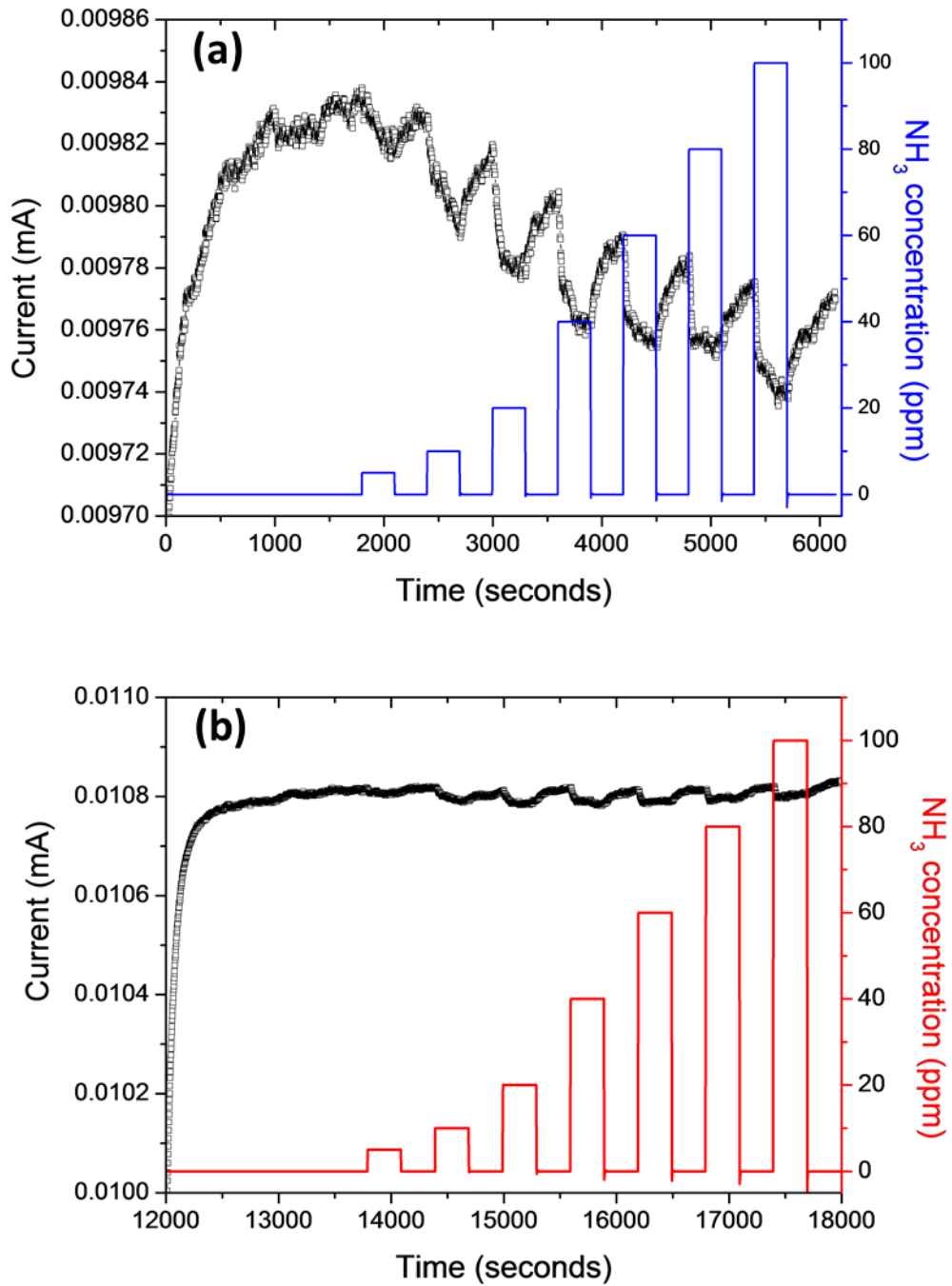


Figure 8.9. Conductometric sensing signal for NH₃ (a) at room temperature (b) at 100 °C.

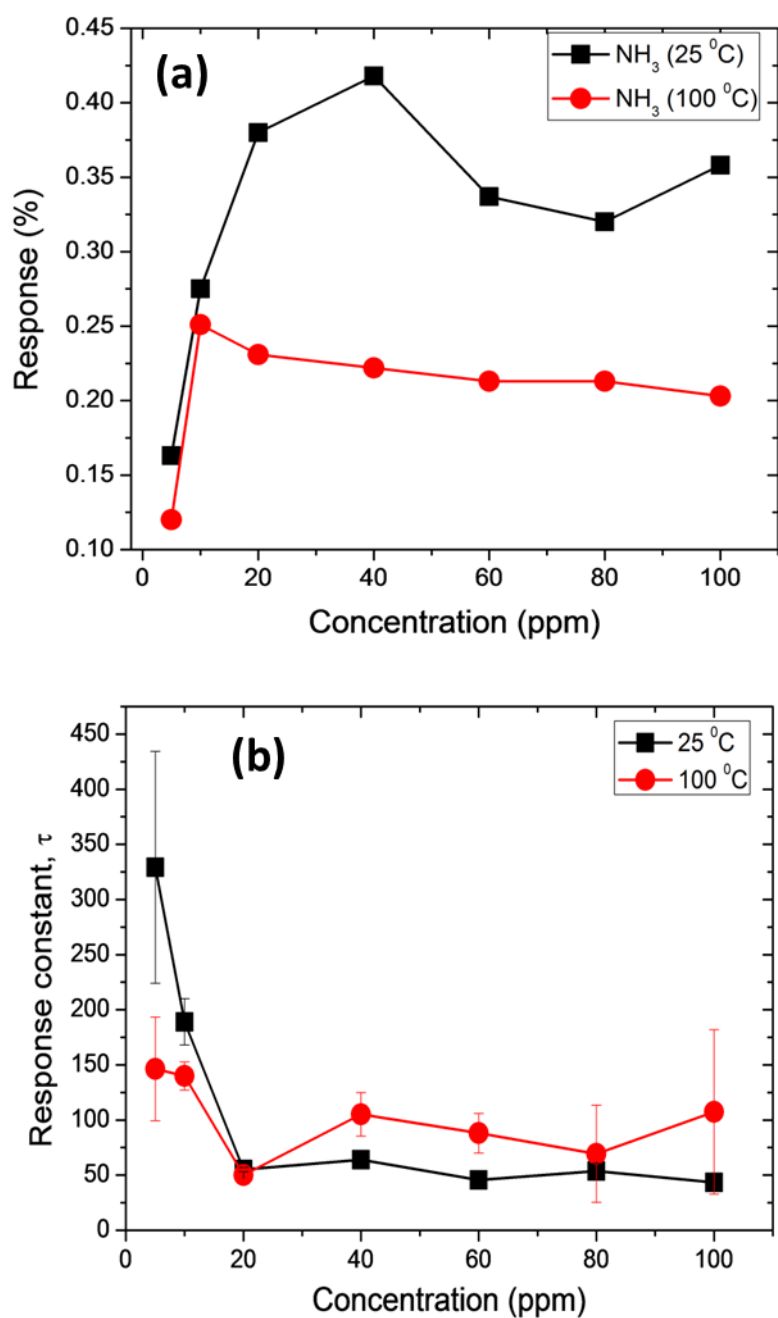


Figure 8.10. (a) Response curve as a function of different NH₃ gas concentrations, (b) Plot of the response time constant for different concentration of NH₃ gas.

When one compares both the in-situ Raman spectroscopy gas sensor tester and the traditional conductometric sensing as summarized in the Table 8.1 below, firstly one can

infer that at 25 °C the change in the wavenumber of 996 cm^{-1} (with + shift or blue shift of 4 cm^{-1}) is bigger than at 100 °C (with – shift or red shift of 3.2 cm^{-1}) and that the two temperatures showed significant and comparable recovery. On the other hand, the response according to the fractional change in intensity at 25 °C is great (with downward turn or – 0.799) compared with the 0.419 of the chemoresistive test and the one at 100 °C (with upward turn or + 3.6) is large compared with the 0.222 of the chemoresistive test. This showed that the in-situ Raman spectroscopy gas-sensor tester is more responsive than the chemoresistive sensor especially when considering the fact that the NH_3 effluent concentration in the chamber may be less or even far less than 40 ppm. Also when one compares the two response time constants, the chemoresistive sensor showed faster response compared with the in-situ Raman spectroscopy gas sensor-tester. Again a low concentration of the effluent NH_3 in the in-situ Raman gas sensing chamber may be the cause. This study shows that apart from using the response due to the fractional change in Raman intensity and chemoresistive signal, Raman wavenumber (frequency) shift can be employed to selectively monitor gases leakages in the environment or to monitor decomposition of gases in industry during gas processing.

Table 8.1: Summary of Raman signatures versus chemoresistive sensing of NH₃ molecules at the V₂O₅ surface.

Sensing properties due to Raman signatures			Change in frequency ($\Delta\omega$) of 996 cm ⁻¹
Temp °C	Derivative (dI/I) of 143 cm ⁻¹		
	<i>response</i>	<i>response</i> τ (s)	<i>response</i>
25	-0.799	300	4
100	3.6	1400	-3.2
Sensing properties due to Chemoresistive test			
Temp °C	Chemoresistive at 40 ppm		
	<i>response</i>	<i>response</i> τ (s)	
25	0.419	59	
100	0.222	105	

8.4 Conclusions

In summary, in-situ Raman spectroscopy has been employed to monitor the reactivity of NH₃ effluence produced from ammonium acetate salt decomposed at 100 °C at the surface of 30 nm layers of V₂O₅ film deposited by PLD techniques. The results showed recoverable red shift in the 194 cm⁻¹ phonons and blue shift in the 996 cm⁻¹ phonons upon the interaction of the molecule at ambient temperature (25 °C) and 100 °C. Adsorption effects (increase in intensity) of 145 cm⁻¹ phonons were also observed at these two temperatures. The Raman scattered adsorption effect has been explained using phonon confinement models by taking fractional change in intensity into account while the blue or red shift in the wavenumber (frequency) is related to the change in elastic constant and the reduced mass of the sensing surface in-situ with NH₃ ambience. The adsorption effect is related to more and/or less Raman scattered photons while frequency shift is explained as a decrease in the elastic

constant (acceptance of charges from the molecule) when blue shifted and a decrease in the elastic constant (donation of charges) or increase in reduced mass (chemisorption) when red shifted. Acceptance of charges by the V_2O_5 surface from the molecule is observed to be prevalent at the ambient temperature while an increase in the reduced mass is observed at 100 °C. This is considered to be true since the breaking of chemical bonds or decomposition of NH_3 could only take place at a temperature higher than that of the ambient temperature.

Comparison and rankings of in-situ Raman spectroscopy gas-sensor tester with the traditional chemoresistive sensor tester showed that the in-situ Raman spectroscopy sensor tester is excellent. Additionally, the significant recoverable blue shift and red shift observed when NH_3 interacts with the surface may be considered an outstanding feature of in-situ Raman spectroscopy on selective monitoring of gas leakage in the environment or to monitor decomposition in industry during gas processing. Hopefully the technique will be helpful in advancing or upgrading the design of chemical sensors for environmental or industrial pollution monitoring.

References

- [1] P. K. Chu, L. Li, Characterization of amorphous and nanocrystalline carbon films, *J of Mat. Chem. Phys.* **96**, 253-277, (2015)
- [2] A. A. Akande, E.C Linganiso, B.P Dhonge, K.E. Rammutla, A. Machatine, L. Prinsloo, H. Kunert, B.W. Mwakikunga, Phase Evolution of vanadium oxides obtained through temperature programmed calcinations of ammonium vanadate in hydrogen atmosphere and their humidity sensing, *J of Mat. Chem. Phys.* **151**, 206, (2015).
- [3] T. Pagnier, M. Boulova, A. Galerie, A. Gaskov, G. Lucazeau, Reactivity of SnO₂-CuO nanocrystalline materials with H₂S: a coupled electrical and Raman spectroscopy study, *Sen. Act. B.* **71**, 134 (2000)
- [4] M. Boulova, A. Gaskov, Lucazeau, Tungsten oxide reactivity versus CH₄, CO and NO₂ molecules studied by Raman spectroscopy, *Sen. Act. B.* **81**, 99 (2001)
- [5] M. Govender, D. E. Motaung, B. W. Mwakikunga, S. Umapathy, S. Sil, A. K. Prasad, A. G. J. Machatine, H. W. Kunert, Operating Temperature Effect in WO₃ Film for Gas Sensing, *IEEE* **978**, 1 (2013)
- [6] S-H Lee, H.M. Cheong, M.J. Seong, P. Liu, C.E. Tracy, A. Mascarenhas, J. R. Pittsa and S. K. Deb, Raman spectroscopic studies of amorphous vanadium oxide thin films, *Solid State Ionics* **165**, 111 – 116, (2003).
- [7] C. Julien, G. A. Nazari, O. Bergstrom, Raman Scattering Studies of Microcrystalline V₆O₁₃ *Phys. State Sol. B* **201**, 319-325 (1997)

- [8] A. A. Akande, K. E. Rammutla, B. P. Dhonge, A. G. J. Machatine, and B. W. Mwakikunga, Room temperature Methane (CH_4) sensing by vanadium oxide (VO_x) nanoparticles, *Adv. Sci. Lett.* **22**, 901-904 (2016)
- [9] B. Mwakikunga, S. Motshekga, L. Sikhwivhilu, M. Moodley, G. Malgas, M. Scriba, and S. Sinha-Ray, A classification and ranking system on the H_2 gas sensing capabilities of nanomaterials based on proposed coefficients of sensor performance and sensor efficiency equations, *Sen. Act. B.* **170**-178 (2013)
- [10] A. Simo, B. Mwakikunga B. T. Sone, B. Julies, R. Madjoe, and M. Maaza, VO_2 nanostructures based chmiresistors for low power consumption hydrogen sensing, *Int. J. Hydro. Ener.*, **39**, 15, (2014).
- [11] M.C. Rao, Vanadium Pentoxide Cathode Material for Fabrication of All Solid State Lithium-Ion Batteries - A Case Study, *Res. J. Recent Sci.*, **2**, 3, 67-73, (2013).
- [12] S. Laubach, P. C. Schmidt, A. Thiben, F. J. Fenandez-Madrigal, Q. Wu, W. Jaegemann, M. Klemm, S. Horn, Theoretical and Experimental determination of the electronic structure of V_2O_5 , reduced V_2O_{5-x} and sodium intercalated NaV_2O_5 , *Phys. Chem. Chem. Phys.* **9**, 2564 (2007)
- [13] B. Zhon, D. He, Raman spectrum of vanadium pentoxide from density-functional perturbation theory, *J. Raman Spec.* **29**, 10, (2008)
- [14] B. N. Masina, S. Lafane, L. Wu, A. A. Akande, B. Mwakikunga, S. Abedelli-Massaci, T. Kerdja, A. Forbes, Phase-selective vanadium dioxide (VO_2) nanostructured thin films by pulsed laser deposition, *J. Appl. Phys.* **118**, 165308 (2015)
- [15] A. A Akande “Vanadium dioxide Nanostructure and Applications in Sensors” MSc Thesis 2014 University of Limpopo

- [16] K. Sajilal, M. E. Raj, Effect of thickness on physi-chemical properties of p-NiO (bunsenite) thin films prepared by chemical spray pyrolysis (CSP) techniques *Int. J. Light Elec. Opt.* **127**, 3, 1442-1449 (2016)
- [17] Q. Yu, W. Li, J. Liang, Z. Duan, Z. Hu, J. Liu, H. Chen, J. Chu, Oxygen pressure manipulations on the metal-insulator transition characteristics of highly (011)-oriented vanadium dioxide films grown by magnetron sputtering, *J. Phys D* **46**, 055310 (2013)
- [18] P. Zang, T. Huang, Q. You, J. Zang, W. Li, J. Wu, Z. Hu, J. Chu, Effects of crystal orientation on electronic band structure and anomalous shift of higher critical point in VO₂ thin films during the phase transition process, *J. Phys D* **48**, 055310 (2015)
- [19] R. Kerber, *Foundation of Chemistry* 4, 61-72, 2002
- [20] X. Cai-Xia Ma, Cun-Hua, X. Fu-Rong, C. Hong-Wei, D. Bin, Catalyst-free hydrochlorination protocol for terminal arylalkynes with hydrogen chloride, *Chinese Chem. Lett.* **27**, 1683-1685 (2016)
- [21] B. Tepper, B. Richer, A. C. Dupuis, H. Kuhlenbeck, C. Hucho, P. Schilbe, M. A, Yarmo, H. J. Freund, Adsorption of molecular and atomic hydrogen on vacuum cleaved V₂O₅ (001) *Surf. Sci.* **496**, 64 (2002)
- [22] O. Sipr, A. Simunek, S. Bocharov, Th. Kirchner, G. Drager, Geometric and electronic structure effects in polarized V K-edge absorption near-edge structure space of V₂O₅, *Phys. Rev.* **60**, 20, 14115
- [23] G.I. Petrov and V.V. Yakovlev, Raman microscopy analysis of phase transformation mechanisms in vanadium dioxide, *App. Phys. Lett.* **81**, 6, 1023, (2002).
- [24] M. Pan, J. Liu, H-M. Zhong, S-W. Wang, Z-F. Li, X-S. Chen and W. Lu, Raman study of phase transition in VO₂ thin film, *J. of Cry. Growth* 268, 178–183, (2004).

- [25] A. A. Akande, B. W. Mwakikunga K. E. Rammutla, A. Machatine, Larger Selectivity of the V₂O₅ Nano-particles Sensitivity to NO₂ than NH₃, *Sens & Tran* **192**, 9, (2015)
- [26] A. M. Soleimanpour, A. H. Jayatissa, G. Sumanasekera, Surface and gas sensing properties of nanocrystalline nickel oxide thin film, *Appl Surf. Sci.* **276**, 291-297, (2013)
- [27] J. L. Johnson, A. Behnam, Y. An, S. J. Parton, A. Ural, Experimental study of graphitic nanoribbon films for ammonia sensing, *J. Appl. Phys.* **109**, 124301 (2011)

CHAPTER 9

CONCLUDING REMARKS AND RECOMMENDATIONS

9.1 SUMMARY

In this study, the gas sensing properties of nanostructured correlated vanadium oxides; VO₂, V₂O₅, V₆O₁₃ have been investigated using chemoresistive and Raman spectroscopy methods. Primarily, critical studies of the phase evolution of vanadium oxides with temperatures from the precursor NH₄VO₃ were carried out by various analytical techniques. Thermal analysis by TGA and DSC provided information about the decomposition and phase transitions of these oxides. TGA and DSC data also validated the theoretical mass loss from the stoichiometry calculations thus confirming the mechanisms of formation of various VO_x phases.

Further investigation by X-ray diffraction method (XRD and TEM), elemental analysis (EDS and XPS), magnetic analysis (VSM) and optical methods (FTIR and Raman spectroscopy) showed VO_x phases orders as follows; NH₄VO₃ → VO₂ + V₂O₅ (150 – 200 °C) → V₆O₁₃ (300 °C) → V₂O₅ (above 350 °C). This has been summarized as the VO_x phase evolution diagram. Adsorption tests of these VO_x phases showed a profile of BET surface areas which increased with the annealing temperature until 300 °C after which the transition occurred. This transition is probably due to the enlargement of the particles at that temperature. Their sensing applications with different levels of relative humidity showed high response to the V₆O₁₃ (300 °C) and V₂O₅ (above 325 °C) phases. However, the Langmuir isotherm plot in

the form of the response (%) per BET surface area with respect to different levels of relative humidity showed a high response for the VO₂ (150 °C) phase. This observation depicted the Langmuir's hypothetical relationship between adsorption, desorption, pressure, surface area and number of sites.

Another study involves selective or preferential adsorption of H₂S gas to monoclinic V₆O₁₃ nano rod structures. This V₆O₁₃ structure and other two α -orthorhombic V₂O₅ were obtained by solid-state decomposition reaction of NH₄VO₃ at 500 °C for 2, 12, and 24 hours respectively in nitrogen atmosphere. The crystal structures of these samples were confirmed with X-ray diffraction, HRTEM from the selected area electron diffraction pattern (SAED), Raman spectroscopy and cathode-luminescence technique. All these characterization techniques with SEM and VSM also showed that the crystal structures at 12 and 24 hours annealing time are α -orthorhombic V₂O₅ with varying degrees of thermal strain which resulted into expansion of the particles at 12 hours and their relaxation thereof at 24 hours.

Gas sensing applications of these structures revealed that the H₂S gas is selective in adsorption to the V₆O₁₃ phase with % response 132 at 350 °C and 60 ppm considering that the internationally accepted threshold limit value of H₂S gas is 50 ppm. This % response value is calculated to be 647.2 % higher than that of NH₃, CH₄, NO₂, H₂ and CO gases with the response and recovery time of 32 and 129 seconds respectively. H₂S sensing tests on the V₆O₁₃ and the two V₂O₅ at 350 °C and 60 ppm also showed that V₆O₁₃ is 238.5 % higher.

In the DFT computational studies of (110) facet of monoclinic V₆O₁₃ and α -orthorhombic V₂O₅ by *ab initio* molecular dynamics, each H₂S molecule minimizes its energy on the surface of V₆O₁₃ greatly compared with the V₂O₅ surface. This is further translated to V₆O₁₃ gaining higher adsorption energies for different loadings of H₂S molecules. The profile of the

absolute adsorption energies per H₂S molecules against number of H₂S molecules showed the same trend with the experimental response (%) per different H₂S concentrations.

Microwave assisted synthesis of VO_x nanostructures from NH₄VO₃, N₂H₂ and an oxalic reagent presented very small and homogeneous core crystallites with shells of amorphous networks suggested by the X-ray diffraction and SAED of the HRTEM analysis. These nanostructures were observed to demonstrate higher BET surface area and pore diameters compared to the data from thermal CVD method when subjected to the N₂ adsorption and desorption isotherm test. SEM analysis of these structures also revealed their high surface property.

In one case ethanol was used to dilute the NH₄VO₃ and N₂H₂ and in another case deionized water was applied, both reactions yielded VO_x with major VO₂ and minor V₂O₅ phases and vice versa by XRD, HRTEM and Raman spectroscopy. Room temperature sensing of CH₄ by ethanol-VO_x particles and of NH₃ and NO₂ by the water-VO_x particles were demonstrated. The surface properties of the structured are assumed to promote room temperature sensing. A summary of the response (%) of all the three gases at 10 ppm showed that the water-VO_x particle is more sensitive and selective to NO₂ gas.

VO₂ (B) nanoflower particles were obtained from NH₄VO₃ and oxalic acid by the microwave technique. This structure was applied for humidity sensing in lateral gate MOSEF configurations. The humidity test was carried out for gate voltages of 0, 5, 8, 10, 12 and 15 V and an optimum response (%) was observed at 5 V. The response and recovery times in this configuration were in the order of 60 – 70 s which is remarkably shorter than the non-gated VO₂ sensor reported in chapter 4, which are more than 300 s. Statistical analysis via the non-linear S-curve Hill Dose rate showed that the VO₂ (B) sensor is very resilient to relative

humidity by showing the humidity level of more than 100% where the response of the sensor could be reduced to 50%.

In-situ Raman spectroscopy sensing of NH_3 gas at the surface of PLD deposited V_2O_5 thin films was demonstrated. The V_2O_5 thin film structure was confirmed with XRD, Rietveld refinement, and XPS. Surface compound (VO) species, the substrate compositions and thickness were analysed by TOF-SIMS and SEM. The results of the in-situ Raman spectroscopy of the V_2O_5 surface showed a recoverable red shift of 194 cm^{-1} and a blue shift of 996 cm^{-1} phonons upon the interaction with the NH_3 gas at 25 and 100 °C. A decrease in the Raman scattered photons of the 145 cm^{-1} phonon was also observed for different levels of NH_3 exposure. The response of 145 cm^{-1} in terms of the fractional change in intensity and the response of the blue shifted of 996 cm^{-1} phonons were 0.799, 4 cm^{-1} (25 °C) and 3.6, 3.2 cm^{-1} (100 °C). This data compared with the chemoresistive sensing of the film at 40 ppm showed that the in-situ Raman spectroscopy techniques are only more sensitive but also showed a possibility for selective gas detection via blue and red shift of phonon frequencies.

9.2 FUTURE RESEARCH WORK AND RECOMMENDATIONS

Despite the outstanding and remarkable sensing characteristics of VO_x nanostructures observed in this thesis, it has been discovered that types of contacts adopted by the sensing devices will influence its performance. Nanomaterials on the other hand have high surface to volume ratio, this makes it difficult to isolate individual particles in order to contact single nanostructures for gas sensing device fabrication. Establishing nano-contacts to individual nanostructures and characterizing them for gas sensing devices would be exciting research in this field. Preliminary results on nano-contact to single nanostructure achieved in this work using the electron beam (e-beam) lithography approach is shown in Figure 9.1.

Gate voltage controlled sensing as a means of tuning the sensitivity and selectivity of nanostructures to gases was also demonstrated in this thesis. However, the e-beam contacting approach (like the one in Figure 9.1) is required rather than the drop cast of dispersed particles in an isopropanol solution. Testing of many gases for selectivity studies is also important.

In-situ Raman spectroscopy sensing experiment demonstrated in this thesis can provide more information regarding the selectivity of V_2O_5 surface to gas. Hence, testing of many gases and critical surface group theoretical analysis of both the V_2O_5 surface and gas molecule is required.

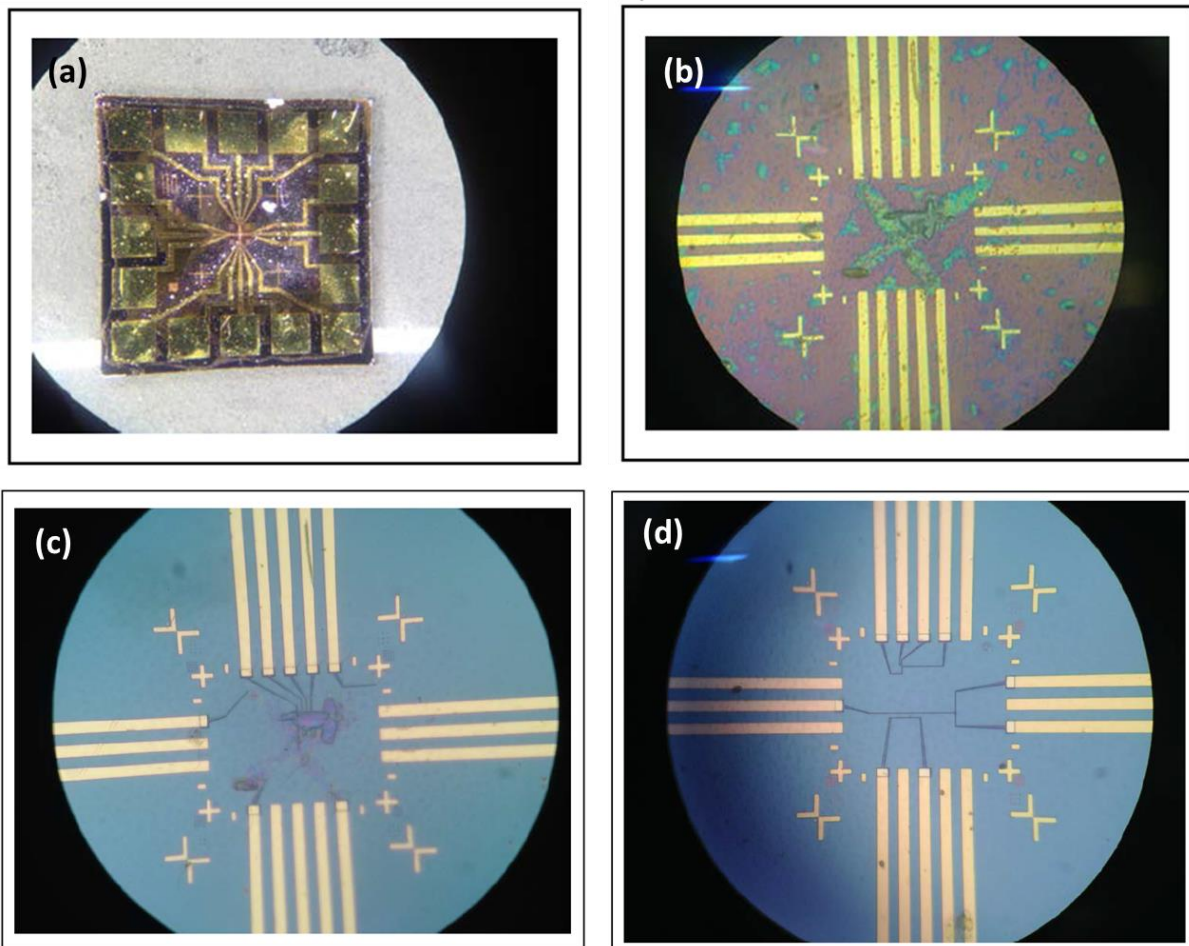


Figure 9.1. (a) Optical microscope of the clean micro-nano transistors array, (b) Magnified image of (a) with VO₂ nanofibers deposited before resist deposition (c) Magnified image of the e-beam developed device after lifting (etching) the resist, and (d) Magnified image of clean transistor showing the device configurations (drain, source and gate pattern).

APPENDIX A

Figure A1 and A2 are the TEM analysis of the sample annealed at 150 °C and 250 °C discussed in chapter four.

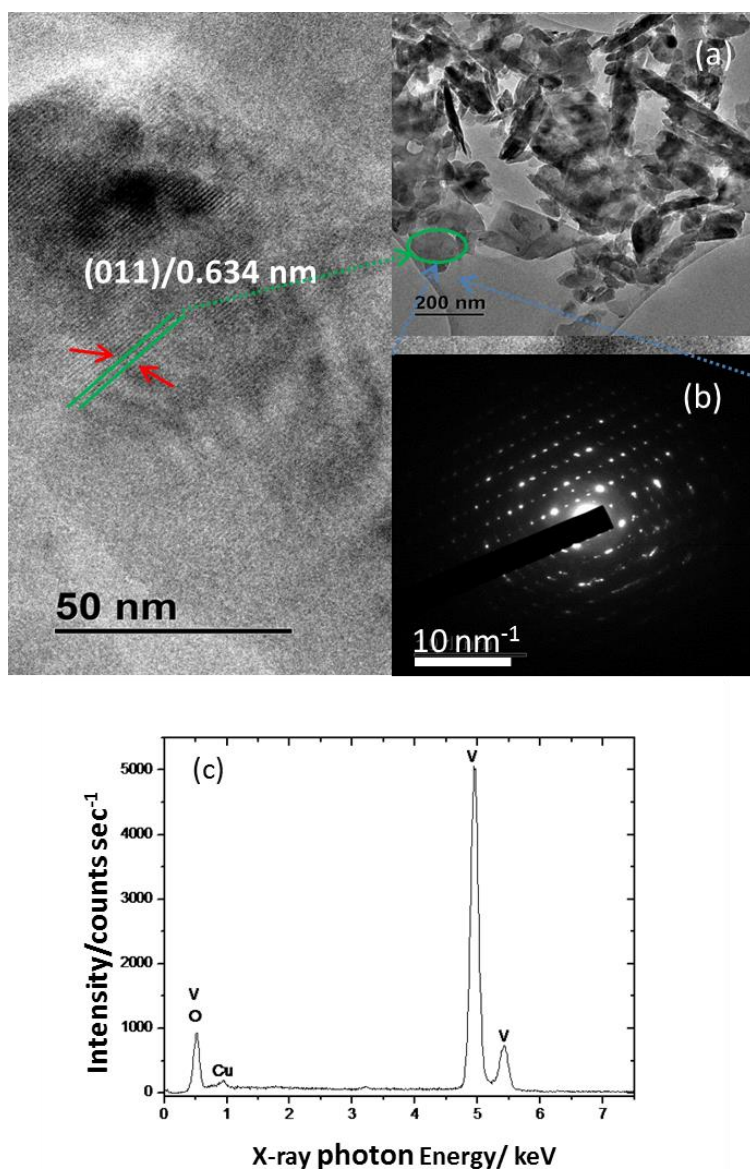


Figure A1: TEM images of sample annealed at 150 °C, with high resolution image (background image) showing a single plane 011 of VO₂ (a) Low resolution image and (b) SAED pattern (c) EDS spectrum of the examined spot.

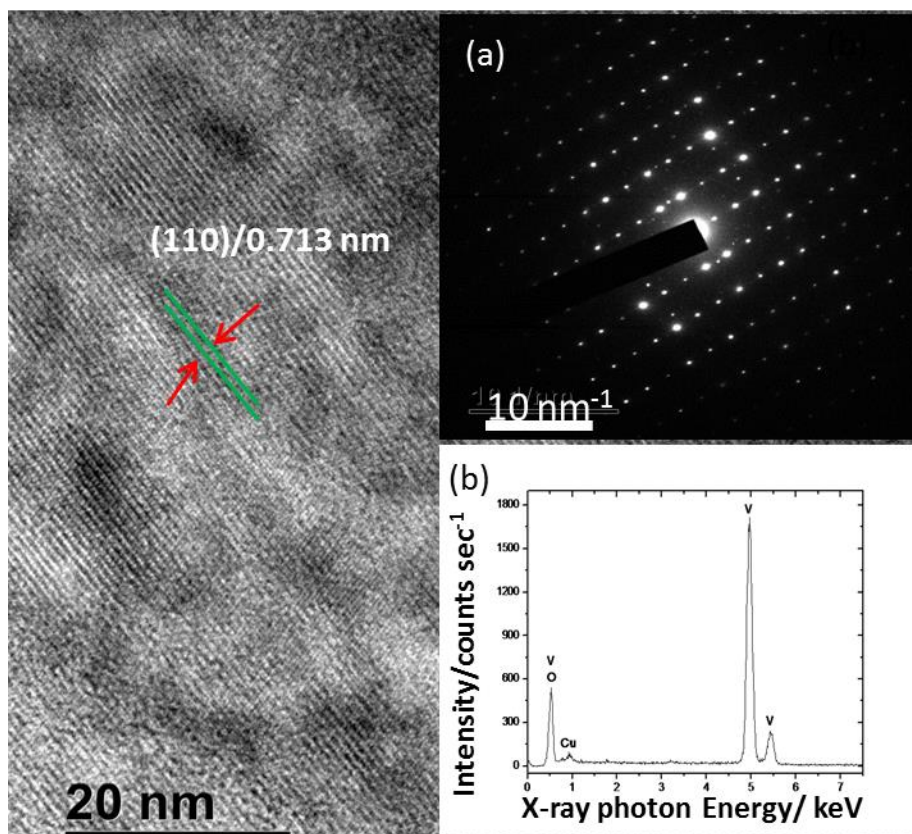
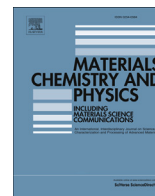


Figure A2: High resolution TEM image of sample annealed at 250 °C, (a) SAED pattern and (b) corresponding EDS spectrum.



Phase evolution of vanadium oxides obtained through temperature programmed calcinations of ammonium vanadate in hydrogen atmosphere and their humidity sensing properties



A.A. Akande ^{a, b}, E.C. Liganiso ^a, B.P. Dhonge ^a, K.E. Rammutla ^b, A. Machatine ^c,
L. Prinsloo ^c, H. Kunert ^c, B.W. Mwakikunga ^{a, *}

^a DST/CSIR National Centre for Nano-Structured Materials, P O Box 395, Pretoria, 0001, South Africa

^b University of Limpopo, Department of Physics, P/Bag X1106, Sovenga, 0727, South Africa

^c School of Physics, University of Pretoria, Pretoria, 0002, South Africa

HIGHLIGHTS

- Validated the theoretical mass losses at each temperature of NH_4VO_3 with TGA.
- Confirmed mechanisms of formation of various stoichiometries of VO_x from NH_4VO_3 .
- Determined the evolution of VO_2 , V_6O_{13} and V_2O_5 with temperature.
- Phase diagram of VO_2 , V_6O_{13} and V_2O_5 by VSM, XPS/EDS, XRD and Raman spectra.
- Comparative response of VO_2 , V_6O_{13} and V_2O_5 to humidity.

ARTICLE INFO

Article history:

Received 19 March 2014

Received in revised form

20 October 2014

Accepted 22 November 2014

Available online 27 November 2014

Keywords:

Annealing

Oxidation

Phase transition

Thermogravimetric analysis

X-ray diffraction

Topology

Adsorption

Desorption

Differential scanning calorimetry

VSM

XPS

ABSTRACT

The possibility of obtaining vanadium dioxide (VO_2) [wherein the vanadium ionic state is 4^+] from a precursor of ammonium metavanadate (NH_4VO_3) bearing the ion V^{5+} is investigated. The reduction is carried out by calcining the NH_4VO_3 powders in similar concentrations of H_2 flow at varying temperatures. The resulting powders have been studied by several techniques including XRD, Raman spectroscopy, FTIR, TEM, BET and DSC. It is found that remnants of bright yellow V^{5+} still exist up to calcination temperatures of 100°C after which the sky-blue VO_2 dominates at calcination temperatures of 150°C – 250°C . There is a population surge of metastable dark-blue V_6O_{13} (where V is in between V^{4+} and V^{5+} ionic states) between 250°C and 300°C . However above 350°C the material reverts to the stable V^{5+} in the yellow–orange V_2O_5 . XPS/EDS and VSM confirm the order of appearance to be $\text{VO}_2(150^\circ\text{C}) \rightarrow \text{V}_6\text{O}_{13}(200^\circ\text{C}) \rightarrow \text{V}_2\text{O}_5(350^\circ\text{C})$.

© 2014 Elsevier B.V. All rights reserved.

1. Introduction

An oxidation state is influenced by ionization energy while ionization energy depends on the shielding effect between the

orbital electron and the nucleus of an atom. In transition metal elements, the electrons enter an inner-shell electron orbital as opposed to other groups where electrons enter the outer-shell electron orbital [1]. The substitution of electrons in the inner-shell in case of transition metals consequently increases the shielding effect, decreases the effective nuclear charge and thereby weakening the ionization energy. All transition metals (Ti, W, Mn, V, Cr, Pd, Pt, Co, Zn, Fe, Cd, Cu, etc.) have low ionization energy, and

* Corresponding author.

E-mail address: bmwakikunga@csir.co.za (B.W. Mwakikunga).

this makes it less costly to remove more than one electron from their orbitals than it is from compounds with completely filled 3s or 3d orbitals such as alkali metals and alkali earth metal elements. Vanadium is one of these transition metals, it usually presents synthesis difficulties due to its existence in several oxidation states by forming a variety of binary oxides with the following general formulas for $n = 1, 2, 3 \dots$ (1) V_nO_{2n+1} e.g. V_2O_5 , V_3O_7 , V_4O_9 , V_6O_{13} , (2) V_nO_{2n-1} e.g. VO , V_2O_3 , and (3) V_nO_{2n} also with VO_2 and V_2O_4 [2]. Among these oxides, V_2O_3 , VO_2 , V_6O_{13} and V_2O_5 possess many interesting characteristics that can be used in various applications because of their tendency to undergo metal to insulator phase transition commonly known as MIT transition [3–12].

Vanadium dioxide (VO_2) is unique among these oxides because of the abrupt changes in its crystal structure that usually follow the phase transition around 68 °C. The transition temperature is considerably low and close to room temperature. This MIT property was first observed by F.J. Morin 1959 and later widely studied by Magneli, Mott Hubbard, Peierls, Goodenough, Adlar, Paquet and Fujimori [3–12]. VO_2 has 4⁺ oxidation state oxide of vanadium with a monoclinic (insulating/semiconducting) before transition temperature and tetragonal (metallic) above the transition temperature. Changes in crystal structure explained by Peierls as electron–phonon interaction or coupling, or band structure shift explained by Mott as electron–electron correlation is usually accompanied by a number of physical properties [13]. Such properties are changes in electrical resistance or conductance, optical transmittance or reflectance, phonon frequencies from Raman spectroscopy and FTIR, surface plasmon resonance from absorption spectra and light scattering studies [14,17–21]. The optical property of VO_2 is also found to be dependent on the surface roughness by AFM studies [15,16]. All these properties make VO_2 feasible for practical application purposes and have been applied in various technological devices. Such devices include smart or switchable window glass panes (thermo-chromic and photo-chromic property) [22–26] as well as gas chemical sensing (gasochromic property) [22,27]. Uses of VO_2 in the fabrication of electrochemical devices (electro-chromic property) have also been recorded [28].

Other oxides such as V_6O_{13} and vanadium pentoxide (V_2O_5) are also relevant as they are close to VO_2 in stoichiometry. V_2O_5 is a V⁵⁺ oxidation state oxide and is the most stable oxide of vanadium. Its orthorhombic crystal structure usually undergoes metal to insulator phase transition at 375 °C. V_2O_5 is used as a passive electrode with WO_3 as an active electrode in electro-chromic glass application [28,29]. It has been reported for gas chemical sensing capabilities [30] and also found applications in the lithium ion batteries [31]. V_6O_{13} is known as a mixed valence oxide as it exists between the V⁴⁺ and V⁵⁺ oxidation states [32]. It is monoclinic in crystal structure at both high and low temperature with a characteristic zigzag chain running along the b-axis with mono V⁴⁺ and mixed V⁴⁺ and V⁵⁺ [32]. Its transition temperature is –143 °C and finds application in lithium ion batteries.

Ammonium meta-vanadate (AMV, NH_4VO_3) has been widely used as a source material for the syntheses of vanadium oxides by various deposition/synthesis techniques, such as chemical precipitation [33,34], thermal annealing [35], spray pyrolysis [36,37], and autoclave hydrothermal treatment [38].

In all these synthesis techniques, the phase diagram of V–O system was not followed. As a result, many such reports indicated either single phase VO_2 or V_2O_5 without validation. In this work, we started by thermogravimetry of NH_4VO_3 in nitrogen. Instead of mass loss alone, we also observed mass increase. This prompted further systematic study of phases at various temperatures in hydrogen atmosphere. This paper reports the quantitative study of phases of VO_x at various temperatures. This study sheds more light on the existing phase diagrams of VO_x .

2. Experimental techniques

Ammonium metavanadate powder (NH_4VO_3 , purity 99.99%, molecular weight of 116.98 a.m.u, density of 2.3 g cm⁻³ and melting (or decomposition) temperature of 200 °C) was purchased from Sigma–Aldrich Chemical Co. Differential scanning calorimetry (DSC) analysis was performed on the powder using DSC Q2000 V24.4 Build 116 to measure the amount of heat flow into and out of the sample relative to the reference pan with a linear temperature ramp under nitrogen gas. A series of heat treatments were performed for better understanding of the decomposition and phase change in the material. Firstly, heat treatment of the NH_4VO_3 powder was carried out for 400 and 500 °C in chemical vapour deposition (CVD) reactor under nitrogen flow. This experiment was followed by the TGA measurement of the resulting powder (5.096 mg) and that of standard NH_4VO_3 (4.726 mg) to study the thermal decomposition process in the materials under nitrogen atmosphere. The instrument used is TGA Q500 V20.10 Build 36 by Anton Paar Inc. Further a comprehensive CVD calcinations of NH_4VO_3 powder under 20 mL min⁻¹ hydrogen flow was performed in two different sections, firstly at 100, 150, 200 and secondly at 250, 300, and 350 °C for 2 h.

The powder was characterized using an X-Ray diffraction (Panalytical X'pert Pro PW 3040/60 XRD equipped with Cu K α ($\lambda = 0.154$ nm) monochromatic radiation source). XRD patterns were recorded in the scanning range of 5°–90°. DSC of these calcined powders was also studied. Raman spectroscopic studies were conducted using a Jobin–Yvon T64000 Raman spectrograph with a 514.5 nm excitation wavelength from an argon ion laser. The power of the laser at the sample was low enough (0.384 mW) in order to minimise localised heating of the sample. The T64000 was operated in a single spectrograph mode, with the 1800 lines/mm grating and a 100 \times objective on the microscope, and further optical measurements were performed with standard spectrum 100 PerkinElmer FT-IR spectrometer. The microscopic studies and quantitative elemental composition studies were carried out using JEOL 2100 Transmission Electron Microscopy (TEM) (from Tokyo Japan) equipped with LaB6 filament and a Gatan U1000 camera of 2028 \times 2028 pixels, and high quality inbuilt Energy dispersive X-ray spectroscopy (EDS).

X-ray photo-electron spectroscopy (XPS) was also performed on a reference sample containing V_2O_5 , VO_2 , V_6O_{13} as well domains of WO_3 . EDS taken from VO_x domains (excluding the WO_3 domains) in HRTEM was also performed on the same reference sample. The XPS determinations of the proportion of V³⁺, V⁴⁺ and V⁵⁺ were used to calibrate the EDS spectra and this information was then employed in the determination of the proportions of V³⁺, V⁴⁺ and V⁵⁺ for the current set of samples. X-ray photoelectron spectroscopy analyses were carried using a PHI 5000 Versaprobe–Scanning ESCA Microprobe. The survey scans were recorded with a 100 μ m, 25 W, 15 kV beam using monochromatic Al K α radiation ($h\nu = 1486.6$ eV) and for the higher resolution spectra the hemispherical analyzer pass energy was maintained at 514 eV–520 eV (C 1s, O 1s, V 2p) for 50 cycles. Measurements were performed using either a 1 eV/step and 45 min acquisition time (binding energies ranging from 0 to 1000 eV) for survey scans or a 0.1 eV/step and 20–30 min acquisition times for the high-resolution scans. The pressure during acquisition was typically under 1×10^{-8} Torr. The surfaces were also sputtered clean for 30 s using an Ar ion gun (2 kV energy ions) and measurements were repeated.

The field dependent magnetic characterization was performed using Lakeshore 735 vibrating sample magnetometer (VSM) at room temperature. It is vital to point out that because this type of sample exhibits small magnetization signals, special care was taken during measurements as to avoid any trace magnetic

contamination. Magnetic measurements performed on the different batches of VO_x powders showed consistent and reproducible results demonstrating paramagnetic behaviour.

Gas sensing properties were obtained by placing the VO_x paste dispersed in ethanol onto inter-digitated electrodes and obtaining controlled transient readings of current in varying levels of analyte. The measurements were accomplished by employing a Kinosistec (Italy) gas sensor test instrument comprising Keithley voltage and current sources as well as source meters.

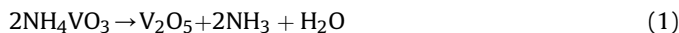
3. Results and discussions

3.1. Thermal analysis (DSC/TGA)

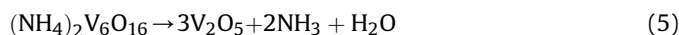
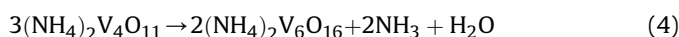
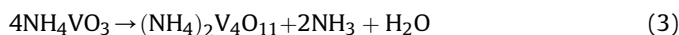
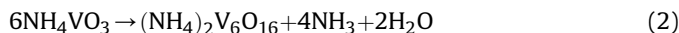
Fig. 1a shows the DSC profile of NH_4VO_3 recorded in the temperature range of $-47\text{ }^\circ\text{C}$ – $350\text{ }^\circ\text{C}$ and exothermic enthalpy change reaction of about -38.3 mW was observed around $234\text{ }^\circ\text{C}$ which may be due to the decomposition of the material. The other enthalpy change at the $340\text{ }^\circ\text{C}$ is small and may be due to the formation of V_2O_5 phase as it occurred at a temperature close to its phase transition temperature ($375\text{ }^\circ\text{C}$). Fig. 1b shows TGA/DTA profile of NH_4VO_3 recorded in the temperature range of 26 – $900\text{ }^\circ\text{C}$. The thermogravimetry curve reveals mass loss in three regions during the scan as shown in the figure. The overall mass loss of 22.2% in the material was observed between $155.5\text{ }^\circ\text{C}$ and $309\text{ }^\circ\text{C}$; this value is in agreement with the one previously reported in the literatures [39,40].

However in this paper we have thoroughly analysed and accounted for each weight loss. Region one lies in the temperature range of 155.4 – $199\text{ }^\circ\text{C}$, which is accompanied by a mass loss of 11.27%. The mass loss in region two is found to be 6.41% within the temperature range of 199 – $231\text{ }^\circ\text{C}$ and in the third region which falls in the temperature range of 231 – $309\text{ }^\circ\text{C}$, the loss was found to be 4.52%.

The overall reaction occurs during the decomposition of NH_4VO_3 is shown in Eq. (1), the net mass loss of 22.2% was observed [40]. The major mass loss occurs due to the evaporation of HN_3 and H_2O .



It is believed that the decomposition involve various reaction stages as shown in Eqs. (2)–(5) [40,41]. In general, decomposition of NH_4VO_3 initiated according to Eq. (2) or 3.



The net mass loss in Eqs. (2)–(5) are calculated as 22.2, 11.11, 4.3 and 8.7% respectively. Representative calculation of mass loss in Eq. (3) is given in the Supplementary material SM1 and the same was followed for Eqs. (2), (4) and (5). However, the mass loss observed in region one (11.27%) suggests decomposition of NH_4VO_3 initiated according to Eq. (3). Thus the further decomposition of out product of Eq. (3) must follow the Eqs. (4) and (5). The mass loss in region two (6.41%) which is higher than the calculated value (Eq. (4)). This may due to the simultaneous reactions according to Eqs. (4) and (5). This simultaneous reaction is also suggested by the lower observed mass loss (4.52%) in region three than the calculated (8.7%) from Eq. (5).

Fig. 1c is a TGA/DTA profile of the sample prepared at $400\text{ }^\circ\text{C}$ in synthetic nitrogen environment. The scan was performed over the temperature range of 26 – $900\text{ }^\circ\text{C}$. The XRD profile (attached in SM3)

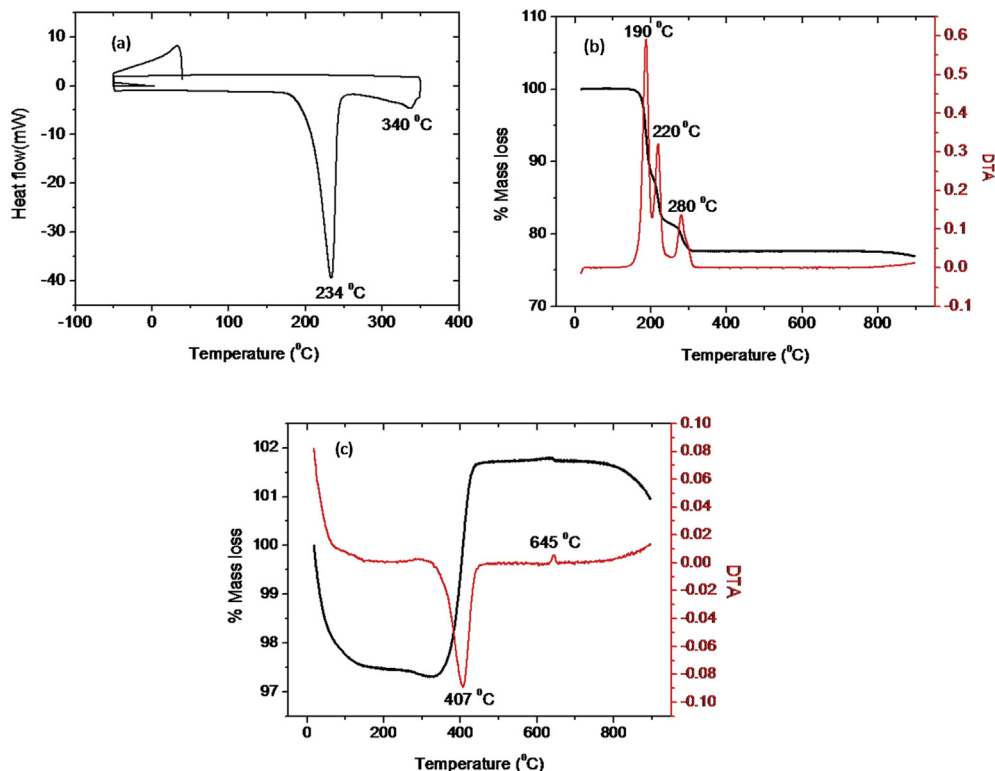


Fig. 1. (a): DSC thermogram of the starting precursor (NH_4VO_3) (b): TGA/DTA thermogram of the starting precursor (NH_4VO_3) (c): TGA/DTA thermogram of the sample prepared at $400\text{ }^\circ\text{C}$.

of the powder before TAG measurement reveal the presence of V_6O_{13} . The initial reaction below 100°C shows some loss in mass of the powder which may be due to the release of moisture absorbed by the powder. Further increase in temperature up to 335°C reveals very small change in mass from 5.096 to 4.972 mg, which is 2.53%. This is due to the reduction of V_6O_{13} . The possible reduction of V_6O_{13} is shown in Eq. (6). Since the calculated mass loss in Eq. (6) is 3.09% (attached in SM2) which is very close to observed value.



Above 340°C , significant mass gain was observed which was followed by the second stability around 440°C . The increase in mass is due to the oxygenation of VO_2 . The oxygen is contributed from the synthetic nitrogen flow during TGA experiment. The transformation is ascribed to V_2O_5 since it is known as a most stable oxide among vanadium oxides and usually formed above 340°C .

Fig. 2 shows the DSC profiles of the samples prepared by calcination of NH_4VO_3 from 100 to 350°C in step of 50°C . The peaks at 185 and 220°C for the sample calcined at 100°C show exothermic reaction which may be due to the release of ammonia. Peaks at 78 and 80°C for the samples calcined at 150 and 200°C may be due to the formation of VO_2 , since it is close to MIT temperature and the one at 85°C for samples calcined at 250 and 300°C may be due to the mixture of metastable phases of VO_2 and V_6O_{13} . The formation of various phase with temperature was confirm with XRD pattern, discussed in Sections 3.2 and 3.4. The development of V_2O_5 phase was observed for the samples calcined at 100 , 150 , and 200°C in temperature region 310 – 340°C . The actual formation of V_2O_5 occurs at 375°C . Due to the limitation of DSC in terms of temperature range, we could not proceed for further higher temperature. Although this peak is absent in the case of sample calcined at 250 and 300 , this may due to peak shifting to the higher temperature 375°C . The sample calcined at 350°C show optimum population of phase of V_2O_5 .

3.2. X-ray diffraction spectra

XRD spectrum of the sample prepared at 400°C depicts the monoclinic system of V_6O_{13} by PCPDFWIN CAS No: 72-1278 with (110) plane as the dominant peak. The peaks were rather sharp,

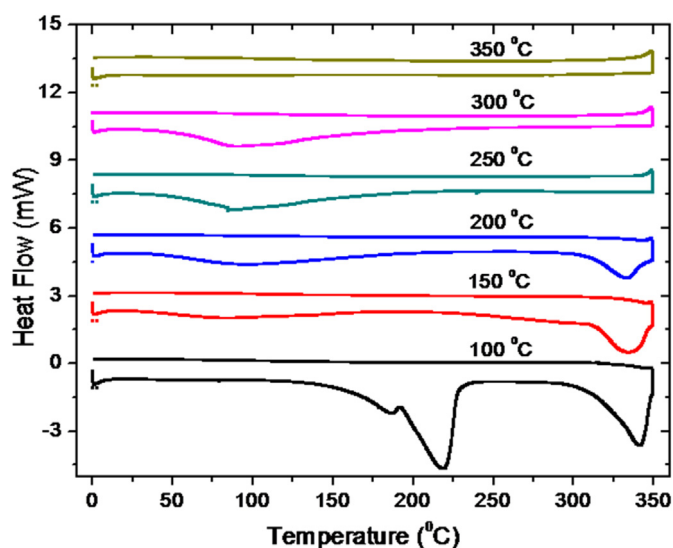


Fig. 2. DSC thermograms of the samples prepared by calcination of NH_4VO_3 from 100 to 350°C .

which indicate relatively high crystallinity of the particles. The average particle size was determined with Debye-Scherrer's model and found to be around 24 nm . And X-ray diffraction pattern of the sample prepared at 500°C also depicts orthorhombic system of V_2O_5 by PCPDFWIN CAS No: 89-0611 with dominant (101) planes and with presence of plane like (200), (310), (111), (411), (005). The average particle size of 26 nm was observed.

Fig. 3a shows XRD spectra of the standard precursor NH_4VO_3 and samples calcined at temperatures 100 – 350°C . The XRD patterns were compared with PCPDFWIN CAS No: 44-0252, 72-1278 and 89-0611 for VO_2 , V_6O_{13} and V_2O_5 respectively. Monoclinic peak of VO_2 at 2θ (diffraction angle) = 27.8° corresponding to the plane (011) (PCPDFWIN CAS No: 44-0252) is found to be dominant among the samples calcined at 100 , 150 and 200°C . Various phases of vanadium oxide were also observed except for those samples calcined at 250 – 350°C . The sample prepared at 250 – 350°C show the development of single phase of V_2O_5 . Predominantly monoclinic metastable V_6O_{13} was observed for the sample calcined at 250 and 300°C . Orthorhombic V_2O_5 was observed at 350°C .

3.3. Transmission electron microscope

TEM images for the calcined samples at 150°C , 250°C and 350°C were carried out. Fig. 3b shows high resolution TEM image of sample calcined at 350°C showing single plane corresponding to that of (101) of V_2O_5 . Inset upper corner showing SAED pattern and lower corner showing the corresponding EDS spectrum. Sample calcined at 150°C reveals sheet and rod like structure with SAED pattern of non-uniform diffraction. Single (110) plane of uniform diffraction corresponding to that of V_6O_{13} was observed for the sample at 250°C . The radius is measured from ImageJ software and the lattice spacing was calculated to be 3.7 \AA which is indexed to the monoclinic V_6O_{13} parameters ($b = 3.671\text{ \AA}$). The calculated value of the lattice spacing for sample calcined at 350°C is 3.483 \AA which is corresponding to orthorhombic V_2O_5 phase ($b = 3.517\text{ \AA}$).

3.4. Phase diagram

Fig. 4 is the phase evolution diagram showing the distribution of oxides (VO_2 , V_6O_{13} and V_2O_5) with temperature. XRD pattern of sample calcined at various temperatures has been used to developed phase diagram. The phase analysis was carried out by calculating the area of Gaussian fitted XRD peaks. The percentage of phase was calculated using Eq. (7).

$$\% (VO_x) = \frac{\sum A_x}{\sum A_x + \sum A_y + \dots} \quad (7)$$

where A_x, A_y, \dots are the peak area corresponding to the phases x, y, \dots respectively [47]. It was observed that formation of VO_2 phase dominates in temperature range 150 – 200°C , whereas V_6O_{13} phase is the dominant around 250 – 300°C . V_2O_5 is found to be present for all temperatures and optimum population at 350°C .

3.5. Raman spectroscopy

Raman spectroscopy is known to be a sensitive and reliable technique for crystal structure study in material science and engineering. This technique is based on the inelastic scattering of monochromatic light irradiated on the sample. The frequency of the scattered light usually collected and compared to that of the incident light. Raman spectrum of the sample prepared at 400°C reveals all Raman active modes of V_6O_{13} [42]. A strong intense peak at lower frequency band 137 cm^{-1} correspond B_g symmetry and the high frequency vibration at 990 cm^{-1} corresponding to stretching

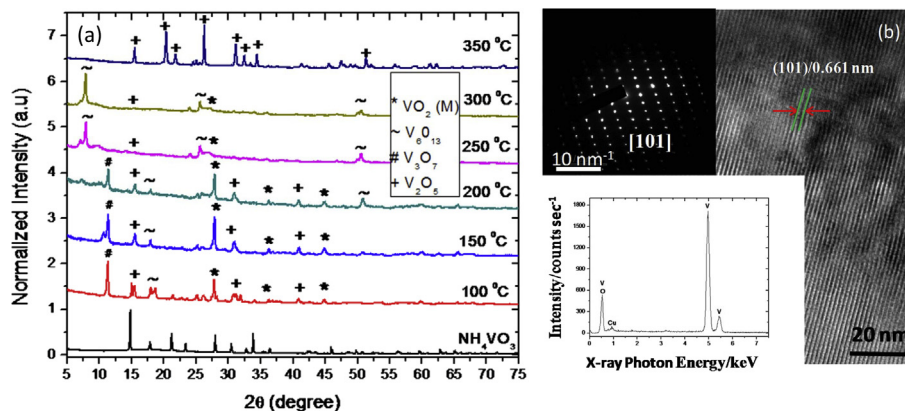


Fig. 3. (a): XRD spectra of the standard NH_4VO_3 and of the samples prepared by calcination of NH_4VO_3 from 100 to 350 °C, (b): High resolution TEM image of sample calcined at 350 °C showing single plane corresponding to that of 101 of V_2O_5 , insert upper corner showing SAED pattern of 101 lattices and insert lower corner showing the corresponding EDS spectrum.

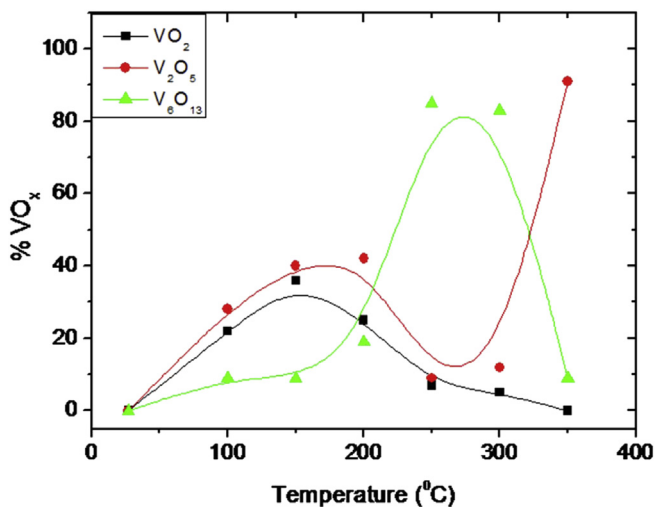


Fig. 4. Vanadium oxides (VO_2 , V_6O_{13} and V_2O_5) phase evolution diagram.

of O–V–O atoms was observed. Vibration modes such as 277, 402 and 523 cm^{-1} are resulting from the bending mode of V–O band and 686 cm^{-1} stretching mode corresponds to the motion parallel and perpendicular to ab-plane [43]. Raman vibrations of the sample prepared at 500 °C show frequencies 993, 693, 527, 407, 284, 192, 140 cm^{-1} vibrations corresponds modes of V_2O_5 [42,43].

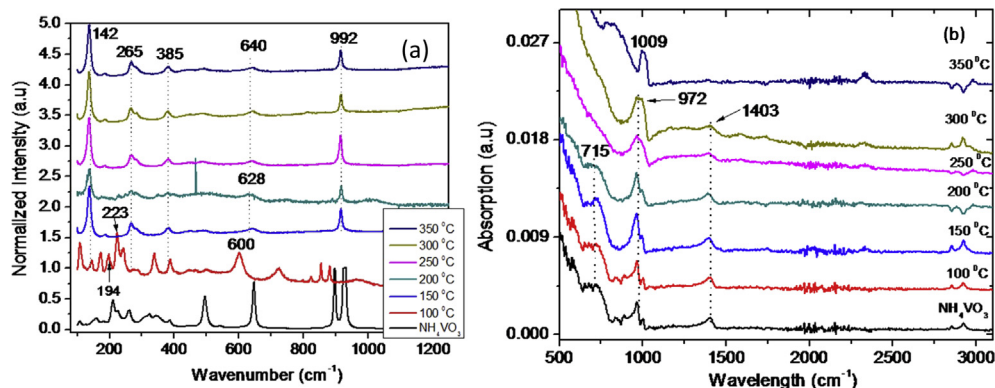


Fig. 5. (a): Raman spectra of the standard NH_4VO_3 and of the samples prepared by calcination of NH_4VO_3 from 100 to 350 °C (b): FT-IR of the standard NH_4VO_3 and of the samples prepared by calcination of NH_4VO_3 from 100 to 350 °C.

Fig. 5a shows Raman spectra of the standard and calcined NH_4VO_3 precursor in the temperature range of 100–350 °C. The presence of 194, 223, 265, 385, 600 and 628 cm^{-1} vibration modes in the samples calcined at 100–200 °C shows the predominant population of VO_2 in this region [42]. The sample calcined at 250–350 °C shows peak at 137, belong to V_6O_{13} phase. The peak at 142 and 992 cm^{-1} belong to V_2O_5 phase [42,43]. The peaks extra at 265 and 385 cm^{-1} reveals the presence of VO_2 phase at higher temperatures. The peak due to ammonia vibrations is observed around 1420 cm^{-1} for precursor NH_4VO_3 [44].

3.6. Fourier Transform Infrared spectroscopy (FT-IR)

FT-IR is a rotational vibrational spectroscopic technique that is based on the absorption of photon by the molecules constituting a material. Molecule absorbs the incident photon and promote to higher energy state (excited state). The changes in energy of incident photon due to the absorption were detected. **Fig. 5b** shows the FTIR spectra of the standard and calcined NH_4VO_3 precursor in the temperature range of 100–350 °C.

The observed absorption shoulder at 715 cm^{-1} and strong peak at 972 cm^{-1} are correspond to the VO_2 [45]. The shoulder at 715 cm^{-1} was not observe for higher temperature (250–350 °C) and the shift in 972 cm^{-1} peak was observed at 350 °C. The peak shifted to higher frequency 1009 cm^{-1} at 350 °C corresponding to single polycrystalline V_2O_5 phase [45]. The presence of both shoulder and strong peak at lower temperature (100–200 °C)

reveals the higher population of VO₂. The higher population of V₂O₅ at higher temperature and VO₂ at lower temperature is also supported by our XRD phase calculation and Raman study.

3.7. Brunauer–Emmett–Teller (BET)

Brunauer–Emmett–Teller theory relies on the physical adsorption (physisorption) of gas molecules on the surface of solid-state materials. This technique gives information about the specific surface area of a nano-material. This theory is an extension of Langmuir theory which described the amount of adsorbed molecules (adsorbate) on the surface of material (adsorbent) as a function of pressures or concentration [46]. BET equation is expressed below in Eq. (8).

$$\frac{1}{v \left(\frac{p_0}{p} - 1 \right)} = \frac{c - 1}{v_m c} \left(\frac{p}{p_0} \right) + \frac{1}{v_m c} \quad (8)$$

where p and p_0 are the equilibrium and saturation pressure of adsorbate at the temperature of adsorption, v is the adsorbed gas quantity, v_m is the monolayer adsorbed gas quantity and c is the BET constant.

The BET measurements were carried out for standard and calcined NH₄VO₃ at various temperatures 100–350 °C. The change in N₂ adsorption with partial pressure for the sample calcined at 250 °C is shown in Fig. 6a. The monolayer adsorbed gas v_m and BET constant c were measured as the intercept of linear plot of $1/v(p_0/p - 1)$ and p/p_0 , shown in inset image Fig. 6a. The BET surface area ($S_{\text{BET}} = v_m \cdot N_A / Va$, where N_s is Avogadro's number, V is molar volume of adsorbate gas and a is the mass of the adsorbent) of calcined samples were calculated and are shown in Fig. 6b. The surface area is found to increase with the calcination temperatures. It follows the Langmuir isotherms pattern with temperatures.

3.8. XPS and EDS

We have performed XPS on a reference sample containing known mixed V³⁺, V⁴⁺ and V⁵⁺ phases of VO_x as well EDS of the same reference sample. The full XPS and EDS spectra of this reference sample were reported in our recent paper [48]. This analysis has been used to calibrate all EDS results for our current samples containing V₆O₁₃, VO₂ and V₂O₅. The analysis results are summarized in Table 1. First the heights and widths of the peaks were determined for each peak in XPS and in EDS and areas under such peaks were calculated. The proportions were determined from the

Table 1

(a): XPS analysis for reference or standard sample containing VO₂, V₂O₅, V₆O₁₃ and WO₃, (b): EDS analysis for reference or standard sample containing VO₂, V₂O₅, V₆O₁₃ and WO₃.

(a)					
Orbitals	Height, H (a.u)	H0 (a.u.)	Width, W (eV)	A	% V + W % of V ⁴⁺
W(4f) _{7/2} , W ⁶⁺	2100	150	3	5850	51.5
W(4f) _{5/2} , W ⁶⁺	1600	250	3	4050	35.6
V(2p) _{3/2} , V ⁴⁺	3500	3200	1.5	450	3.9
V(2p) _{3/2} , V ⁵⁺	3975	3300	1.5	1012.5	8.9
(b)					
Electronic shell	Height, H (a.u)	Width, W (eV)	A	% of V ⁴⁺	
V _M	500	0.2	100	15.6	
V _L	1500	0.3	450	70.3	
V _K	300	0.3	90	14.1	

Table 2

EDS analysis based on the calibrations in Table 1(a) and (b) and local composition for the VO_x samples annealed at 150, 200, 250, 300 and 350 °C.

Sample	Electronic shell	Height, H (a.u)	Width, W (eV)	A	% of V ⁴⁺
EDX 150	V _M	900	0.15	135	10.5
	V _L	5000	0.2	1000	77.8
	V _K	750	0.2	150	11.7
EDX 200	V _M	800	0.1	80	10.0
	V _L	5500	0.1	550	68.8
	V _K	850	0.2	170	21.2
EDX 250	V _M	530	0.15	79.5	27.5
	V _L	1700	0.1	170	58.7
	V _K	200	0.2	40	13.8
EDX 300	V _M	250	0.15	37.5	22.7
	V _L	720	0.15	108	65.2
	V _K	100	0.2	20	12.1
EDX 350	V _M	990	0.15	148.5	15.7
	V _L	3500	0.2	700	73.8
	V _K	500	0.2	100	10.5

ratio of the area under each peak to the total of all peaks considered [47].

From Table 1a the reference sample has 69% proportion of V₂O₅ or a contribution from mixed (metastable) V₆O₁₃ and the rest 31% of the photo-electrons come from VO₂ with a small contribution from V₆O₁₃ again. EDS results of the same sample indicate 70% X-ray emission from V_L electronic shell. This could be attributed to V₂O₅ and a small contribution from the mixed phase V₆O₁₃ as suggested by XPS in Table 1a. EDS This shows that XPS and EDS results are in good agreement and one can use local EDS results with this XPS

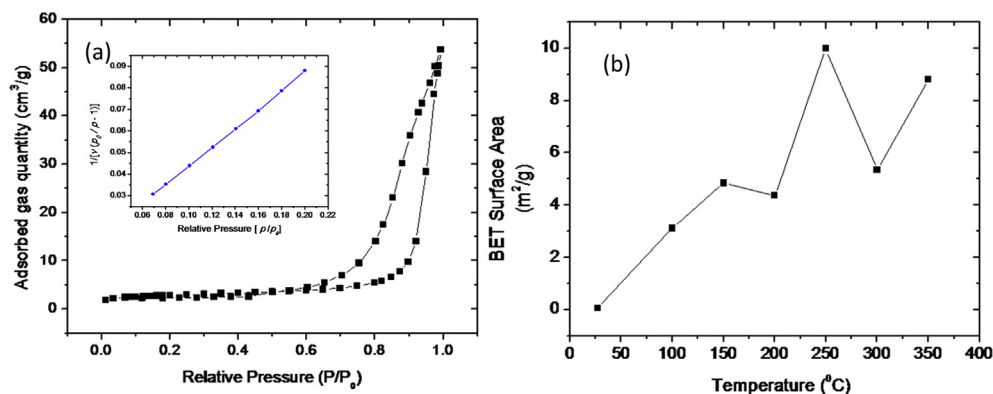


Fig. 6. (a): N₂ adsorption and desorption isotherms profile of the powder calcined at 250 °C, inset is the BET plot, (b): BET surface area versus temperature for all the calcined powders and including NH₄VO₃.

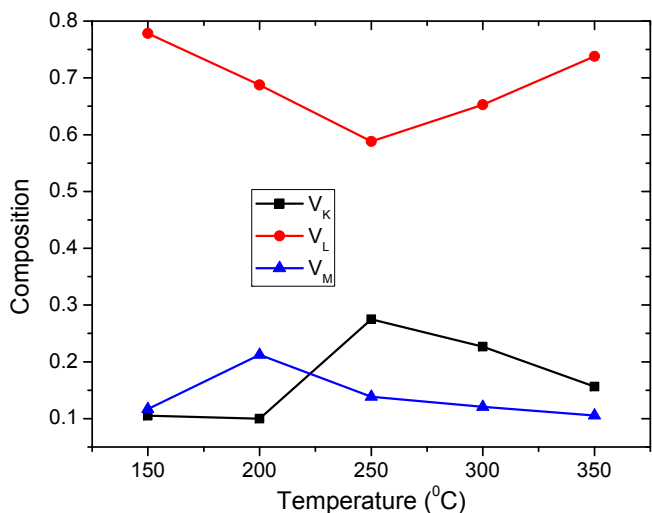


Fig. 7. Proportions of V_2O_5 , VO_2 and V_6O_{13} determined by EDS calibrated with XPS as they vary with annealing temperature.

calibration to determine the local composition of the current VO_x materials.

One can conclude the V_L shell peak in EDS can be used to mark V_2O_5 whereas the V_M and V_K shells are mostly for VO_2 although in both cases V_6O_{13} has a strong indeterminate influence. One can understand the V_6O_{13} poses a challenge in ascertaining its exact contribution owing to its meta-stable nature.

We have summarized the EDS analysis results from the VO_x samples annealed at 150, 200, 250, 300 and 350 °C based on the calibration undertaken in Table 1a and b. These results are summarized in Table 2. It can be observed that the proportions of the phases change with annealing temperature. The changes are plotted in Fig. 7. The V_L –temperature profile shows a decrease from 100 °C to 250 °C and then increases again up to the annealing temperature of 350 °C. This profile agrees very well with the phase diagram shown in Fig. 4 in the previous section. Similarly, the proportions determined from V_M peak at 150 °C which is exactly the VO_2 profile in the phase diagram in Fig. 4 whereas the proportions calculated from V_K shell increase to a maximum value at an annealing temperature of 200 °C which agrees with the V_6O_{13} profile in Fig. 4. This assures us that the present XPS calibration of the EDS results is correct.

3.9. Vibrating sample magnetometry (VSM)

The traditional definitions of remanent magnetization (M_R^+ and M_R^-), saturation magnetization (M_S^+ and M_S^-) and squareness (SQ) in bulk and nano-scale magnetic materials are schematically illustrated in Fig. 8a and b. It should be noted that nano-materials display a shift of the hysteresis loop due to what is called exchange bias [48,49]. In Fig. 8c we show that hysteresis loops for all VO_x samples annealed at 100, 150, 200, 250, 300 and 350 °C including the precursor materials of ammonium metavanadate, NH_4VO_3 . One can note that all samples show a degree of shift in the hysteresis loops which reveals that all the powders are nano-scale materials. As to whether these materials are ferro- or ferri- or paramagnetic, the loops show very small amount of squareness, of the order of 10^{-2} , and a very small opening in the loops [typical values

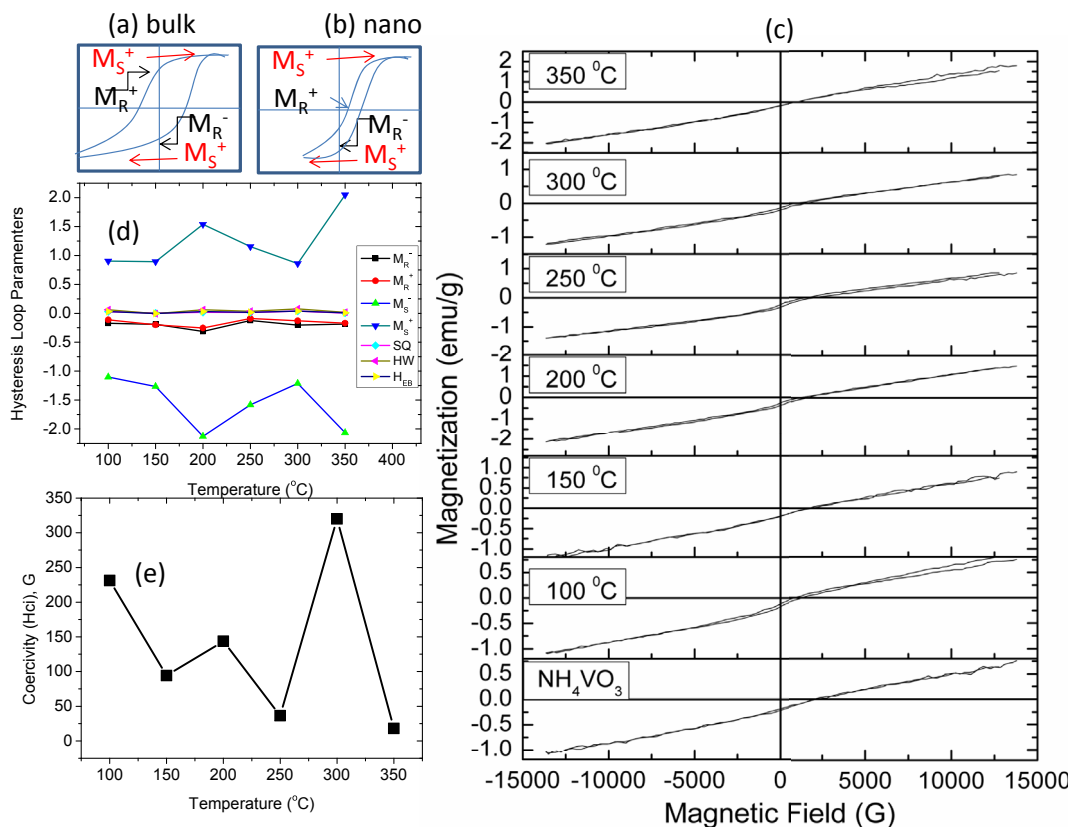


Fig. 8. Vibrating sample magnetometry (VSM) for the VO_x samples annealed at 100, 150, 200, 250, 300 and 350 °C (a) Parameters definition for a hysteresis loop for bulk and nano materials (b) Hysteresis loops for VO_x samples annealed at 100, 150, 200, 250, 300 and 350 °C and (c) A plot of the hysteresis loop parameters against annealing temperatures.

Table 3

A summary of the hysteresis loop parameters of remanent magnetization (M_R^+ and M_R^-), saturation magnetization (M_S^+ and M_S^-) and squareness (SQ) as well hysteresis width and exchange bias width.

Annealing temp °C	Coercivity (Hci) G	MR negative, emu/g	MR Positive, emu/g	MS negative, emu/g	MS positive, emu/g	Squareness	Loop opening emu/g	Exchange bias emu/g
100	231.12	-0.17	-0.11	-1.10	0.90	0.03	0.06	0.03
150	94.32	-0.19	-0.20	-1.26	0.89	0.00	-0.01	0.00
200	143.64	-0.31	-0.25	-2.13	1.54	0.02	0.06	0.03
250	36.42	-0.12	-0.09	-1.58	1.15	0.01	0.04	0.02
300	320.09	-0.20	-0.13	-1.21	0.86	0.04	0.08	0.04
350	17.90	-0.19	-0.17	-2.06	2.05	0.00	0.02	0.01

of $H_C^+-H_C^-$ of the order of 10^{-2} . This points to the fact that these materials are largely para-magnetic. However, there is a finite coercivity (Fig. 8d and e) in samples (from 17 to 300 G) showing there is a degree of ferro-magnetic order in this paramagnetic matrix.

In Table 3 we give a summary of the parameters of remanent magnetization (M_R^+ and M_R^-), saturation magnetization (M_S^+ and M_S^-) and squareness (SQ) as well hysteresis width and exchange bias width obtained from the hysteresis loops given in Fig. 8b. The hysteresis width has been estimated to be proportional to the loop opening in the vertical axis which is the difference between M_R^+ and M_R^- .

$$HW \propto (M_R^+ - M_R^-) = k(M_R^-(\text{high}) - M_R^-(\text{low})) \quad (9)$$

The exchange bias width has been estimated to be half of this opening as previous done [50].

$$H_{EB} \propto \frac{(M_R^+ - M_R^-)}{2} = \frac{k}{2}(M_R^-(\text{high}) - M_R^-(\text{low})) \quad (10)$$

A plot of these parameters for all annealed samples is given in Fig. 8d and e and it is interesting to note that coercivity generally decreases with annealing temperature although it shows a high point at 300 °C whereas remanent magnetization (M_R^+ and M_R^-), saturation magnetization (M_S^+ and M_S^-) all show the lowest values at 200 °C. At the former temperature, it is interesting to note that this is a transition temperature from V_6O_{13} to V_2O_5 and the latter is a transition temperature from VO_2 to V_6O_{13} . VSM confirms the

following order of appearance: $VO_2 \rightarrow V_6O_{13} \rightarrow V_2O_5$ as temperatures of annealing are elevated.

3.10. Applications: humidity sensing

We have shown before how VO_2 has been employed in sensing of hydrogen [51,52]. In this present report, we have also subjected the VO_x samples annealed at 150 °C (VO_2), 250 °C (V_6O_{13}) and 350 °C to sensing of humidity. The transient profiles of the current through the sample placed on inter-digitated electrodes in the presence or absence of varying humidity levels are shown in Fig. 9a. Each time the humidity level is allowed in the chamber, the current through the samples decreases. This means that all VO_x samples gain resistance upon interaction with water vapour. Since all these VO_x phases are known to show n-type conductivity, we could explain the increase in resistance as an indication of water molecules taking away electrons or O_2^- species from VO_x surfaces during adsorption but releasing these electrons back on desorption. In Fig. 9b we plot response [defined as $S = (I_{out} - I_{in})/I_{in}$] as a function of humidity level. This plot reveals the Langmuir type of adsorption-desorption isotherms.

4. Conclusion

A few milligrams of ammonium metavanadate powders were calcined in pure hydrogen atmosphere at temperature of 100, 150, 200, 250, 300 and 350 °C. The samples were characterized by TGA/DSC, XRD, TEM, Raman spectroscopy, FTIR, BET, VSM and XPS/EDS. All these characterization methods lead us to conclude that the progression from NH_4VO_3 to V_2O_5 is as follows:

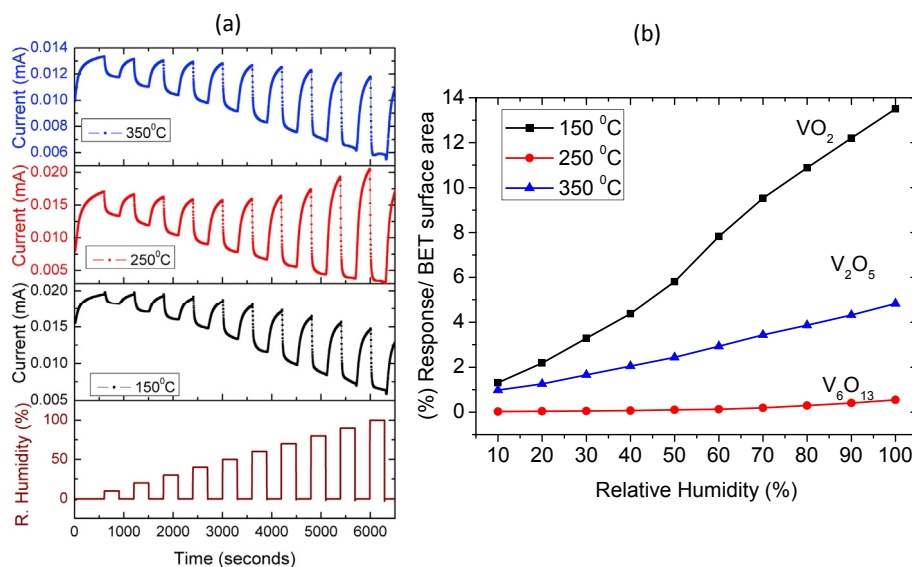


Fig. 9. (a) Transient profiles of current through the VO_x samples in varying levels of humidity (b) Responses weighted against BET surface area for VO_x samples as function of humidity level.

$\text{NH}_4\text{VO}_3 \rightarrow \text{VO}_2 + \text{V}_2\text{O}_5$ (150–200 °C) $\rightarrow \text{V}_6\text{O}_{13}$ (300 °C) $\rightarrow \text{V}_2\text{O}_5$ (above 325 °C). At no temperature does one find a single phase; each temperature of calcinations will have a major and a minor phase or a number minor phases. The total surface area appears to increase with a decreasing rate as the temperature of calcinations is increased. A phase diagram based on XRD and Raman has been constructed for VO_2 , V_6O_{13} and V_2O_5 . XPS/EDS analysis agrees with this phase diagram. It is also found that VSM confirms the order of $\text{VO}_2 \rightarrow \text{V}_6\text{O}_{13} \rightarrow \text{V}_2\text{O}_5$ transitions as temperatures of annealing are elevated.

Acknowledgements

Support from the India-Brazil-South Africa trilateral cooperation under the National Research Foundation (NRF) grant number HGER24X is acknowledged.

Appendix A. Supplementary data

Supplementary data related to this article can be found at <http://dx.doi.org/10.1016/j.matchemphys.2014.11.055>.

References

- [1] P.S. Matsumoto, Trends in ionization energy of transition-metal elements, *J. Chem. Educ.* 82 (11) (2005).
- [2] X. Chen, X. Wang, Z. Wang, J. Wan, J. Liu, Y. Qian, An ethylene glycol reduction approach to metastable VO_2 nanowire arrays, *Nanotechnology* 15 (2004) 1685–1687.
- [3] M. Imada, A. Fujimori, Y. Tokura, Metal-insulator transitions, *Rev. Mod. Phys.* 70 (4) (1998) 1039–1263.
- [4] N.F. Mott, Metal-insulator transition, *Rev. Mod. Phys.* 40 (4) (1968) 677.
- [5] D. Adler, Mechanisms for metal-nonmetal transitions in transition-metal oxides and sulfides, *Rev. Mod. Phys.* 40 (4) (1968) 714–736.
- [6] F.J. Morin, Oxides which show a metal-insulator-transition at neel temperature, *Phys. Rev. Lett.* 3 (1959) 34.
- [7] J.B. Goodenough, The two components of crystallographic transition in VO_2 , *J. Solid State Chem.* 3 (1971) 490–500.
- [8] S. Shin, S. Suga, M. Taniguchi, M. Fujisawa, H. Kanski, A. Fujimori, H. Damon, Y. Ueda, K. Kosuge, S. Kachi, Vacuum-ultraviolet reflectance and photoemission study of the metal – insulator phase transitions in VO_2 , V_6O_{13} , and V_2O_5 , *Phys. Rev. B* 41 (1990) 4993–5009.
- [9] J.M. Reyes, J.R. Marko, M. Sayer, Hysteresis in the semiconductor-metal transition of Cr-doped VO_2 , *Solid State Commun.* 13 (1973) 1953–1957.
- [10] D. Paquet, P. Leroux-Hugon, Electron correlations and electron-lattice interactions in the metal-insulator, ferroelastic transition in VO_2 : a thermodynamic study, *Phys. Rev. B* 22 (1980) 5284–5301.
- [11] N.F. Mott, R. Peierls, Discussion of the paper by de Boer and Verwey, *Proc. Phys. Soc. Lond. Ser. A* 49 (1937) 72.
- [12] A.I. Buzdin, L.N. Bulaeviskii, P.N. Lebedev, Spin-Peierls transition in quasi-one dimensional crystals, in: *Moscow Usp Fiz Nauk*, vol. 131, Physics Institute, Academy of Sciences of the USSR, July 1980, pp. 495–510.
- [13] G.I. Petrov, V.V. Yakovlev, Raman microscopy analysis of phase transformation mechanisms in vanadium dioxide, *Appl. Phys. Lett.* 81 (6) (2002).
- [14] S.-Y. Li, G.A. Niklasson, C.G. Granqvist, Nanothermochromics: calculations for VO_2 nanoparticles in dielectric hosts show much improved luminous transmittance and solar energy transmittance modulation, *J. Appl. Phys.* 108 (2010), 063525.
- [15] R. Lopez, R.F. Haglund Jr., L.C. Feldman, L.A. Boatner, T.E. Haynes, Optical nonlinearities in VO_2 nanoparticles and thin films, *Appl. Phys. Lett.* 85 (2004).
- [16] S. Lysenko, A. Rua, F. Fernandez, H. Liu, Vanadium dioxide based plasmonic modulators, *J. Appl. Phys.* 105 (2009), 043502.
- [17] J. Cao, W. Fan, J.-Q. Wu, Strain and temperature dependence of the insulating phases of VO_2 near the metal-insulator transition, *Phys. Rev. B* 85 (2012), 020101(R).
- [18] Z. Lu, C.-G. Lia, Y. Yin, Synthesis and thermochromic properties of vanadium dioxide colloidal Particles, *J. Mater. Chem.* 21 (2011) 14776–14782.
- [19] E.U. Donev, J.I. Ziegler, R.F. Haglund Jr., L.C. Feldman, Size effects in the structural phase transition of VO_2 nanoparticles studied by surface-enhanced Raman scattering, *J. Opt. A Pure Appl. Opt.* 11 (2009) 8, 125002.
- [20] A.C. Jones, S. Berweger, J. Wei, D. Cobden, M.B. Raschke, Nano-optical investigations of the metal-insulator phase behaviour of individual VO_2 microcrystals, *Nano Lett.* 10 (2010) 1574–1581.
- [21] M. Maaza, O. Nemraoui, C. Sella, A.C. Beye, B. Baruch-Barak, Thermal induced tenability of surface plasmon resonance in Au- VO_2 nano-photonics, *Opt. Commun.* 254 (2005) 188–195.
- [22] A. Pergament, G. Stefanovich, O. Berezina, D. Kirienko, Electrical conductivity of tungsten doped vanadium dioxide obtained by the sol-gel technique, *Thin Solid Films* (2013) 572–576.
- [23] Y. Gao, H. Luo, Z. Zhang, L. Kang, Z. Chen, J. Du, M. Kanehira, C. Cao, Nanoceramic VO_2 thermochromic smart glass: a review on progress in solution processing, *Nano Energy* 1 (2012) 221–246.
- [24] W. Burkhardt, T. Christmann, B.K. Meyer, W. Niessner, D. Schalch, A. Scharmann, Wand F-doped VO_2 films studied by photoelectron spectrometry, *Thin Solid Films* 345 (1999) 229–235.
- [25] O.Y. Berezina, A.A. Velichko, L.A. Lugovskaya, A.L. Pergament, G.B. Stefanovich, D.V. Artyukhin, A.N. Strelko, Properties of tungsten-doped vanadium oxide films, *Tech. Phys. Lett.* 33 (7) (2007) 552–555.
- [26] R. Binions, G. Hyett, C. Piccirillo, I.P. Parkin, Doped and undoped vanadium dioxide thin films prepared by atmospheric pressure chemical vapour deposition from vanadyl acetylacetonate and tungsten hexachloride: the effects of thickness and crystallographic orientation on thermochromic properties, *J. Mater. Chem.* 17 (2007) 4652–4660.
- [27] E. Strelcov, Y. Lilach, A. Kolmakov, Gas sensor based on metal-insulator transition in VO_2 nanowire thermistor, *Nano Lett.* 9 (6) (2009) 2322–23269.
- [28] C.G. Granqvist, Electrochromic tungsten oxide films: review of progress 1993–1998, *Sol. Energy Mater. Sol. Cells* 60 (2000) 201–262.
- [29] J. Livage, D. Ganguli, Sol-gel electrochromic coatings and devices: a review, *Sol. Energy Mater. Sol. Cells* 68 (2001) 365–381.
- [30] J. Huotari, A.L. Spetz, J. Lappalainen, Gas sensing properties of Pulsed laser deposited vanadium oxide thin films, in: *The 14th International Meeting on Chemical Sensors, IMCS*, 2012.
- [31] M.C. Rao, Vanadium pentoxide cathode material for fabrication of all solid state lithium-ion batteries – a case study, *Res. J. Recent Sci.* 2 (3) (March 2013) 67–73.
- [32] P. Kiria, G. Hyett, R. Binions, Solid state thermochromic materials, *Adv. Mat. Lett.* 1 (2) (2010) 86–105.
- [33] H. Bai, M. Berkahn, M.B. Cortie, 31 Annual Condensed Matter and Materials, 2007.
- [34] L. Chen, Ch Huang, G. Xu, L. Miao, J. Shi, J. Zhou, X. Xiao, Synthesis of thermochromic W-doped VO_2 (M/R) nanopowders by a simple solution-based process, *J. Nanomater.* (2012) 1–8, <http://dx.doi.org/10.1155/2012/491051>.
- [35] M. Taniguchi, T.R. Ingraham, Mechanism of thermal decomposition of ammonium metavanadate, *Can. J. Chem.* 42 (11) (1964) 2467–2473.
- [36] B.W. Mwakikunga, E. Sidras-Haddad, M. Maaza, First synthesis of vanadium dioxide by ultrasonic nebula-spray pyrolysis, *Opt. Mater.* 29 (2007) 481–487.
- [37] B.W. Mwakikunga, M. Maaza, K.T. Hillie, C.J. Arendse, T. Malwela, E. Sideras-Haddad, From phonon confinement to phonon splitting in flat single nanostructures: a case of $\text{VO}_2@V_2O_5$ core-shell nano-ribbons, *Vib. Spectrosc.* 2025 (2012).
- [38] X. Wu, Y. Tao, L. Donga, Z. Wangb, Z. Hua, Preparation of VO_2 nanowire and their characterization, *Mater. Res. Bull.* 40 (2005) 315–321.
- [39] U.V. Sacken, J.R. Dahn, TGA/MS Studies of the thermal decomposition of NH_4VO_3 , *J. Power Sources* 26 (1989) 461–465.
- [40] M.E. Brown, B.V. Stewart, The thermal decomposition of ammonium metavanadate, *J. Therm. Anal.* 2 (1970) 287–299.
- [41] J. Twu, C.-F. Shih, T.-H. Guo, K.-H. Chen, Raman spectroscopic studies of the thermal decomposition mechanism of ammonium metavanadate, *J. Mater. Chem.* 7 (11) (1997) 2273–2277.
- [42] C. Julien, G.A. Nazri, O. Bergstrom, Raman scattering studies of microcrystalline V_6O_{13} , *Phys. Stat. Solidi B* 201 (1997) 319–326.
- [43] D. Vernardou, M. Apostolopoulou, D. Louloudakis, E. Spanakis, N. Katsarakis, E. Koudoumas, J. MacGrath, M.E. Pemble, Electrochemical properties of $\text{Opal-V}_6\text{O}_{13}$ composites, *J. Alloy Compd.* 582 (2014) 621–626.
- [44] K. Virkler, I.K. Lednev, Raman spectroscopic signature of semen and its potential application to forensic body fluid identification, *Forensic Sci. Int.* 193 (2009) 56–62.
- [45] I.L. Botto, M.B. Vassallo, E.J. Baran, G. Minelli, IR spectra of VO_2 and V_2O_5 , *Mater. Chem. Phys.* 50 (1997) 267–270.
- [46] S. Brunauer, P.H. Emmett, E. Teller, Adsorption of gases in multimolecular layers, *J. Am. Chem. Soc.* 60 (2) (1938) 309–319.
- [47] R.F. Karlak, D.S. Burnett, Quantitative phase analysis by X-ray diffraction, *Anal. Chem.* 38 (1966) 1741–1745.
- [48] A.A. Akande, K.E. Rammul, T. Moyo, N.S.E. Osman, Steven S. Nkosi, C.J. Jafta, Bonex W. Mwakikunga, Magnetism variations and susceptibility hysteresis at the metal-insulator phase transition temperature of VO_2 in a composite film containing vanadium and tungsten oxides, *J. Magn. Magn. Mater.* 375 (2015) 1–9.
- [49] J. Nogués, J. Sort, V. Langlais, V. Skumryev, S. Surinack, J.S. Munoz, M.D. Baró, Exchange bias in nanostructures, *Phys. Rep.* 422 (2005) 65–117.
- [50] K. Mbela, T. Moyo, J.Z. Msomi, M. Ozturk, N. Akdogan, Synthesis and magnetic properties of $\text{Mg}_{0.2}\text{Cr}_{1.8-x}\text{Fe}_x\text{O}_3$, *J. Magn. Magn. Mater.* 330 (2013) 159–162.
- [51] B.W. Mwakikunga, S. Motshegla, L. Sikhwivhili, Mathew Moodley, M. Scriba, Gerald Malgas, A. Simo, B. Sone, M. Maaza, Suprakas Sinha Ray, A classification and ranking system on the H_2 gas sensing capabilities of nanomaterials based on proposed coefficients of sensor performance and sensor efficiency equations, *Sens. Actuators B* 184 (2013) 170–178.
- [52] A. Simo, B. Mwakikunga, B.T. Sone, B. Julies, R. Madjoe, M. Maaza, VO_2 nanostructures based chemiresistors for low power energy consumption hydrogen sensing, *Int. J. Hydrog. Energy* 39 (2014) 8147–8157.



Room Temperature Methane (CH₄) Sensing by Vanadium Oxide (VO_x) Nanoparticles

A. A. Akande^{1,2,3,*}, K. E. Rammutla², B. P. Dhonge¹, A. G. J. Machatine³, and B. W. Mwakikunga^{1,*}

¹DST/CSIR National Centre for Nano-Structured Materials, P O Box 395, Pretoria, 0001, South Africa

²University of Limpopo, Department of Physics, P/Bag X1106, Sovenga, 0727, RSA

³School of Physics, University of Pretoria, Pretoria, 0002, South Africa

Vanadium (VO_x) nanoparticles (NPs) prepared by hydrothermal microwave method have been characterized and tested for methane (CH₄) detection. The particles structures composed of sphere-like mixed crystalline and amorphous grains with an average diameter of ≤100 nm. High BET surface area of 67 m²g⁻¹ and nano porous property of 16 nm was observed. Room temperature sensing of CH₄ gas by VO_x NPs was achieved with optimal responsivity as oppose to the performance of other fundamental metal-oxide materials. The sensor response profile follows the underlying mechanism between VO_x and CH₄.

Keywords: Methane, Sensing, Nanoparticles, Vanadium Dioxide, Vanadium Pentoxide, Microwave Synthesis.

Delivered by Ingenta to: Desiree Sam
IP: 146.64.81.115 On: Tue, 06 Feb 2018 14:03:34
Copyright: American Scientific Publishers

1. INTRODUCTION

Elevated atmospheric pollution has attracted the attention of scientist in the recent years, and has geared their interest towards building effective and inexpensive systems for detection and quantification environmentally hazardous gases.¹ Methane among others is highly explosive and flammable gas with higher potentials in causing and escalating fire in the industries and household kitchen since it is been widely used as a cooking gas. Metal oxide materials such as ZnO, SnO₂, WO₃²⁻⁶ prepared using Screen printing, RF-sputtering and Chemical Vapour Deposition (CVD) methods have been tested for the detection of CH₄ gas, but none of these materials were able to detect the CH₄ gas at low concentration (say 50 ppm and less) and at temperature near room due to their elevated transition temperature property. The report have shown that SnO₂ and ZnO can detect low concentration of CH₄ with the aid of catalyst such as antimony (Sb), platinum (Pt) but with high working temperature.^{2,4,6} This paper report on the preparation of VO_x nanoparticles by microwave hydrothermal method and their room temperature detection of CH₄ gas.

Microwave assisted synthesis is fast becoming an attractive alternative method in the materials' synthesis especially in the regime of nanoparticles synthesis.^{7,8} The conventional or traditional way of driving heat into the reacting system have shown the following disadvantages; the activation of the reactants is slow, the heat driving into the substance would first pass through

the walls of the vessels/tube in order to reach the reacting system and consequently make reaction energy intensive and less efficient.⁷ Microwave synthesis process is not limited by the thermal conductivity of the vessel, microwave energy couples directly to the entire molecules of the reacting system, leading to a rapid rise in temperature and efficient use of energy. Many reports containing higher degree of crystallinity, narrower size distributions and greater control over shape and morphology of nanostructures by microwave synthesis methods have been presented.⁸

Vanadium oxides are class of transition metals with vanadium oxidation states ranging between +1 to +5 in general. These oxidation states usually leads to the formation of a variety of binary oxides such as VO, V₂O₃, VO₂, and V₂O₅ and phases which include other members of Magneli phase (V_nO_{2n-1}) namely; V₄O₇, V₅O₉ etc., and phases with general formula (V_nO_{2n+1}) such as V₃O₇, V₄O₉ and V₆O₁₃.^{9,10} These oxide materials have most fascinating technological applications and academic interests because of their ability to show-case different electrical, optical and magnetic properties at various compositions.^{11,12} They are low mobility semiconductor with predominantly *n*-type conductivity and are classified among the groups of metal-to-insulator transition (MIT) materials by David Adler and Neville Francis Mott 1968,^{9,13} drawing their conclusion from the theoretical distinctions between metal and insulator by Bethe 1928, Sommerfeld 1928, Bloch 1929, de Boer 1937 and Peierls 1937.¹³ The two oxides of interest in this report are vanadium dioxide (VO₂) with MIT temperature (*T_C*) of 68 °C and vanadium pentoxide (V₂O₅) with MIT temperature (*T_C*) of 375 °C. Both oxides

*Authors to whom correspondence should be addressed.

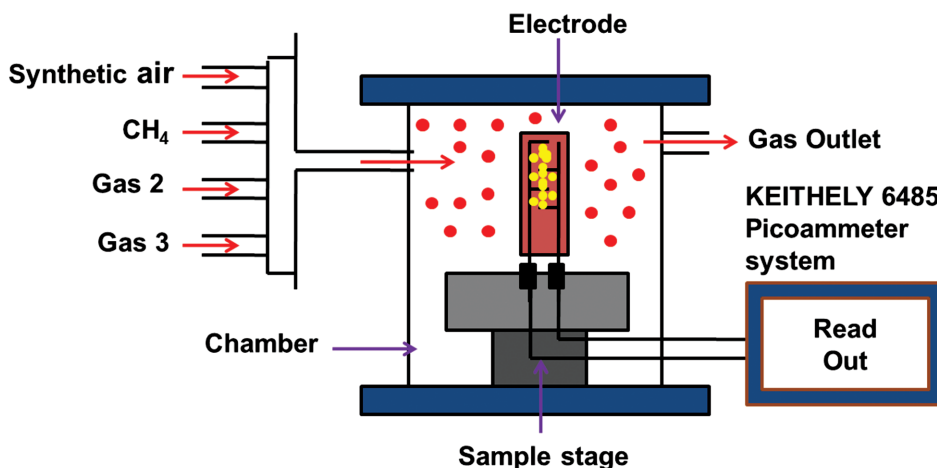


Fig. 1. Schematic diagram of KSGA565 KENOSISTEC sensing station illustrating how the gas sensing measurement was performed.

have been applied in novel devices such as thermo-chromic smart/intelligent window, electro-chromic window and electro-chemical devices. Gas sensors based on MIT/switching of VO₂ nanowire have been demonstrated,¹⁴ NO sensing capability of polycrystalline V₂O₅ phase and VO_x nanotubes type thin film has been achieved.¹⁵ Hydrogen sensing by VO₂ has also been recently demonstrated.^{16,17} VO₂ exhibits a monoclinic crystallographic structure at $T_C < 68$ °C with a band gap of 0.7 eV and tetragonal structure at $T_C > 68$ °C.⁹ The change in crystal structure and the shift in energy band between the stable metallic tetragonal phase and distorted/dimerized insulator monoclinic phase have been reported to be responsible for its MIT induced property. V₂O₅ has an orthorhombic crystallographic structure at $T_C = 375$ °C with a band gap of 2.5 eV. V₂O₅ has +5 oxidation state and forms the most stable composition among vanadium oxides.^{11,14,18}

2. EXPERIMENTAL DETAILS

About 0.5 g of NH₄VO₃ powder (purity 99.99%) was ultrasonically dissolved in 10 mL ethanol, and 5 moles of N₂H₂ reagent was added drop-wise. The mixture was transferred into 100 mL Teflon vessel and placed onto the Multiwave 3000 Microwave reactor. The reactor power was set to 600 W and the temperature was maintained at 180 °C for 20 minutes. The vessel in the reactor was allowed to cool for 25 minutes. Afterwards, the resultant mixture was collected by filtration and washed repeatedly using isopropanol and acetone in an ultrasonic bath to remove undesired impurities and to minimise particle agglomeration. The final product was dried at 100 °C for 11 hours.

The powder was characterized using a Panalytical X'pert Pro PW 3040/60 XRD equipped with Cu K α ($\lambda = 0.154$ nm) monochromatic radiation source. XRD patterns were recorded at 45.0 kV and 40.0 mA from $2\theta = 5$ to 90°. Raman spectroscopic studies were conducted using a Jobin–Yvon T64000 Raman spectrograph with a 514.5 nm excitation wavelength from an argon ion laser. The power of the laser at the sample was low enough (0.384 mW) in order to minimise localised heating of the sample. The T64000 was operated in a single spectrograph mode, with the

1800 lines/mm grating and a 100 \times objective on the microscope. Morphology studies were carried out using a LEO 1525 field emission scanning electron microscope (FESEM) and JEOL 2100 Transmission Electron Microscopy (TEM) (from Tokyo Japan) for the high resolution image.

BET analyses were carried out using Micromeritics TriStar II series Surface Area and Porosity instrument and a Micromeritics sample degassing system from USA.

Gas testing measurements were achieved using KSGA565 KENOSISTEC from Italy. The illustration below in Figure 1 is the schematic of the gas sensing station. The set-up consist of a test chamber, sensor holder, interdigitated electrode (for contacting the powder) and source meters. To carry out the measurements, VO_x powder was dispersed in ethanol and making a thick paste on the interdigitated electrode.

3. RESULTS AND DISCUSSION

Figure 2(a) shows the XRD pattern of VO_x nanoparticles (NPs) belonging to the monoclinic phase of VO₂ and orthorhombic V₂O₅. Diffractions at $2\theta = 27.8^\circ$ (011), 42.3° (211) and 65.2° (031) are characteristics of monoclinic VO₂ which was identified using PCDFWIN CAS No: 44-0252 and the broad diffraction at $2\theta = 17.4^\circ$ (200) is associated with V₂O₅ orthorhombic using PCDFWIN CAS No: 89-0611. This XRD profiles showed broad diffraction peaks denoting that the nanostructures composed of an amorphous network and crystalline region. The crystallites size of about 6 nm was calculated using Debye Scherer's model. SEM micrograph of VO_x NPS in Figure 2(b) shows formation of "sphere-like" particles (spheres consist of tiny particles) with an average diameter of ≤ 100 nm. Analysis of this SEM image revealed that the material particles' are predominantly in the range of nanometres. Figure 2(c) is the HRTEM of VO_x NPs showing diffraction planes corresponding to (200) of V₂O₅, and Figure 2(d) is the selected area electron diffraction (SAED) pattern showing that the particles composed mixed crystalline and amorphous grains. The more crystalline plane (first ring) among the four rings in the SAED is attributed to the plane (200) of V₂O₅ as suggested by the XRD profile.

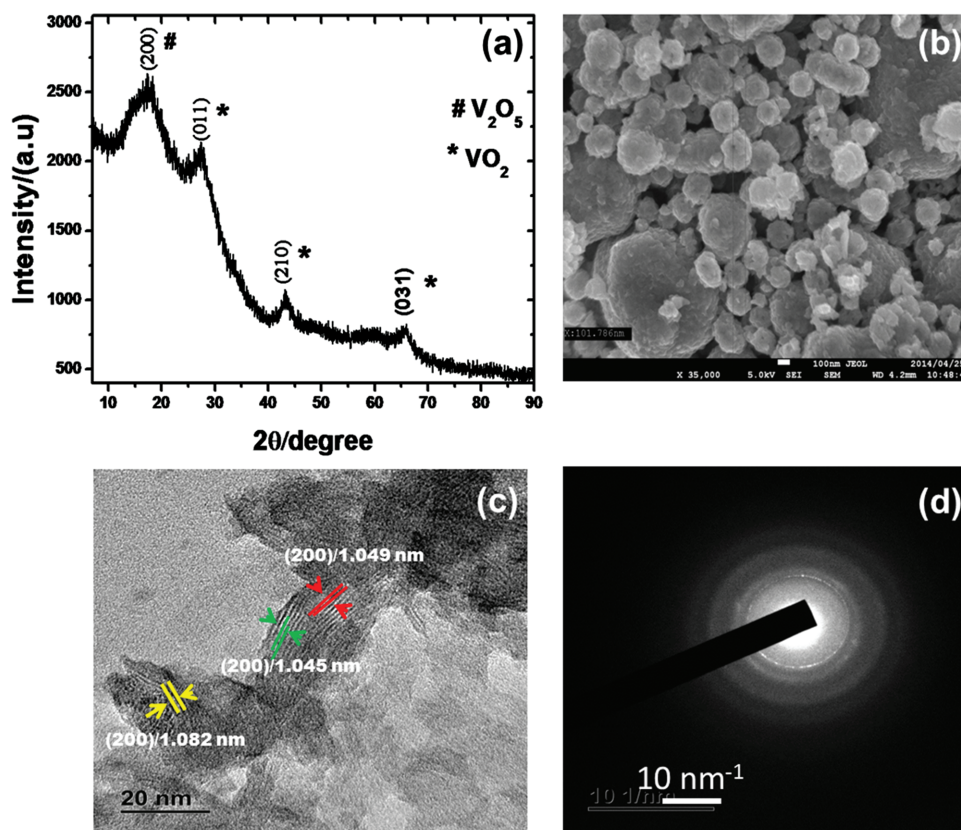


Fig. 2. (a) XRD pattern of VO_x nanoparticles, (b) SEM micrograph of VO_x nanoparticles, (c) HRTEM of VO_x NPs, (d) SAED pattern of VO_x NPs.

Raman spectrum of VO_x nanoparticles in Figure 3(a) shows Raman active modes of V₂O₅ and VO₂. A strong peak at lower frequency band 141 cm⁻¹ corresponding to the Bg symmetry while the high frequency vibration at 992 cm⁻¹ corresponds to stretching of O–V–O atoms. Vibration modes at 282, 402 and 525 cm⁻¹ are resulting from the bending mode of V–O band while the stretching mode at 692 cm⁻¹ corresponds to the motion parallel and perpendicular to ab-plane.^{18,19} These vibrations are characteristics of V₂O₅. The development of VO₂ vibration mode observed at 194 cm⁻¹ and frequency band of 142 cm⁻¹ were assigned to VO₂ by Petrov et al.²⁰ This profile showed that V₂O₅ dominates the surface of VO_x.

The specific surface area *S*_{BET} and pore size/diameter (*d*_{por}) of 67 m²g⁻¹ and *d*_{por} of 16 nm, respectively, were determined by physisorption of nitrogen according to BET theory as shown in Figure 3(b) and Eq. (1), where *p* and *p*₀ are the equilibrium and saturation pressures of the adsorbate at the temperature of adsorption, *v* is the adsorbed gas quantity, *v*_{*m*} is the monolayer adsorbed gas quantity and *c*.²¹

$$\frac{1}{v[(p_0/p) - 1]} = \frac{c - 1}{v_m c} \left(\frac{p}{p_0} \right) + \frac{1}{v_m c} \quad (1)$$

Surface area and nano porous properties revealed the potential of the material in gas and chemical sensor application. BET surface area of 67 m²g⁻¹ and average pore diameter of 16 nm obtained are large compared to that of VO₂(B) nanoneedles previously reported by Sediri et al.²²

Electrical and gas sensing properties of the pristine VO_x NPs were measured as described in the set-up in Figure 1. The sensor

test was performed by measuring the resistance of the sensor when exposed to CH₄ gas. Figure 4(a) shows variation of the current flowing through VO_x NPs for different concentrations of CH₄ gas (at room temperature). The underlying sensing mechanism between VO_x and CH₄ gas is as follows, when VO_x which is an *n*-type semiconductor is exposed to air at either changed or ambient condition, the chemisorbed oxygen at the surface of the material will acquire an electron from its conduction band to form ionic species.¹ Acquisition of electron from the conduction band of an *n*-type semiconduction would lead to a decrease in electron concentration and increase in the resistance (decrease in conduction) of the material. Introducing VO_x to a reducing species such as CH₄ gas¹ could decrease the resistance (increase the conduction) of the sensor. Figure 4(b) represents sensor response as a function of different CH₄ gas concentrations.

The sensor response is defined as

$$S(\%) = \frac{G_{\text{gas}} - G_{\text{air}}}{G_{\text{air}}} \times 100 \quad (2)$$

where *G*_{gas} and *G*_{air} are the conductance of VO_x in the presence of CH₄ (analyte gas) and air respectively. Sensor response follows Langmuir isotherm profile in that; the response increases with gas concentrations before saturation effect at 40 ppm of CH₄ concentration. Chemical reaction between CH₄ and oxygen atom in the VO_x is also assumed to be responsible for the saturation effect at high concentration of CH₄. The product of this reaction could be CO and H₂O, the sensor response shows a damping trend at higher concentration which implies that the VO_x could not detect the product of CH₄ degradation. Narrow band gap property and

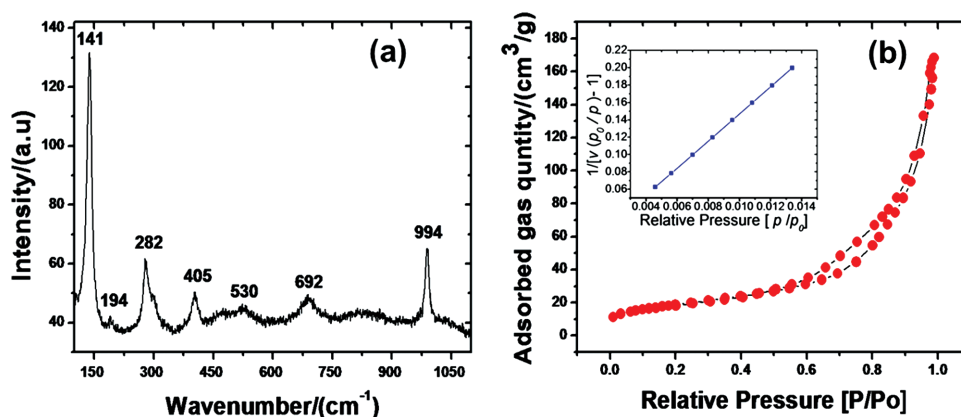


Fig. 3. (a) Raman spectrum of VO_x nanoparticles, (b) N_2 adsorption/desorption isotherms profile of VO_x nanoparticles, insert is the BET plot.

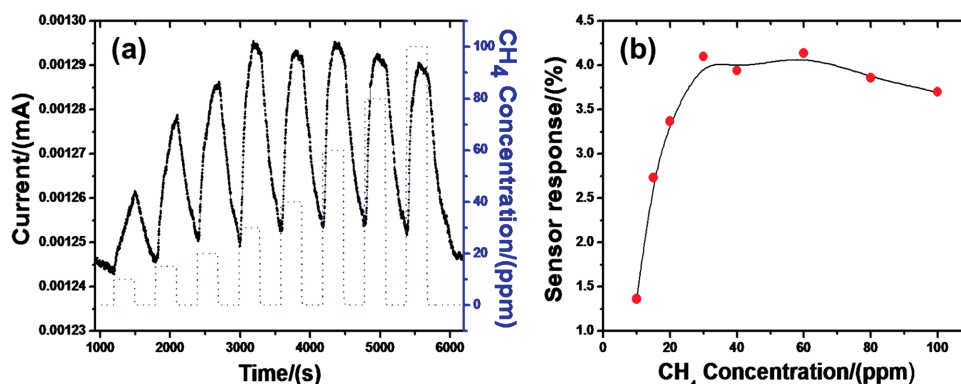


Fig. 4. (a) Variation of the current flowing through VO_x nanoparticles recorded for different concentrations of CH_4 gas. (b) Sensor response as a function of different CH_4 gas concentrations.

low MIT temperature of VO_2 compared to other transition metal-oxides may be the reason why VO_x NPs were able to detect CH_4 with high responsiveness and at room temperature.

4. CONCLUSIONS

Room temperature sensing of CH_4 gas was performed by VO_x NPs synthesized using microwave assisted hydrothermal method. The particles composed of sphere-like mixed crystalline and amorphous grains with high surface area and porosity. Room temperature sensing, low concentration detection and high sensitivity of CH_4 in the case of VO_x NPs as oppose to the performance of other fundamental transition meta-oxide may be due to the narrow band gap of VO_2 as well as its low MIT temperature property.

Acknowledgments: Authors acknowledge the support from the India-Brazil-South Africa trilateral cooperation under the National Research Foundation (NRF) grant number HGER24X.

References and Notes

1. K. Watchakun, T. Samerjai, N. Tamaekong, C. Liewhiran, C. Siriwong, V. Kruefu, A. Wisitsoraat, A. Tuantranont, and S. Phanichphant, *Sens. Act. B* 160 (2011).
2. A. Friedberger, P. Kreisl, E. Rose, G. Muller, G. K. Uhner, J. Wollenstein, and H. Botther, *Sens. Act. B Chem.* 93, 345 (2003).

3. N. J. Dayan, S. R. Sainkar, R. N. Karekar, and R. C. Aiyer, *Thin Sol. Fil.* 325, 254 (1998).
4. W. H. Zhang and W. D. Zhang, *Sens. Act. B: Chem.* 134, 403 (2008).
5. G. Sberveglieri, L. Depero, S. Groppelli, and P. Nelli, *Sens. Act. B: Chem.* 26, 89 (1995).
6. M. Sauvan and C. Pijolat, *Sens. Act. B: Chem.* 58, 295 (1999).
7. B. L. Hayes, *Aldrichimical Acta* 37, 2 (2004).
8. G. A. Kahrilas, L. M. Wally, S. J. Fredrick, M. Hiskey, A. L. Prieto, and J. E. Owens, *ACS Sustainable Chem. Eng.* 2, 3 (2013).
9. A. A. Akande, K. E. Rammuluta, T. Moyo, N. S. E. Osman, S. S. Nkosi, C. J. Jafta, and B. W. Mwakikunga, *J. Magn. Mater.* 375, (2015).
10. A. A. Akande, E. C. Liganiso, B. P. Dhonge, K. E. Rammuluta, A. Machatine, L. Prinsloo, H. Kunert, and B. W. Mwakikunga, *J. Mat. Chem. Phys.* 151, 206 (2015).
11. X. Chen, X. Wang, Z. Wang, J. Wan, J. Liu, and Y. Qian, *Nanotech.* 15 (2004).
12. M. C. Rao, *Res. J. Recent Sci.* 2, 3 (2013).
13. M. Imada, A. Fujimori, and Y. Tokura, *Rev. Modern Phys.* 70, 4 (1998).
14. E. Strelcov, Y. Lilach, and A. Kolmakov, *Nano Letters* 9, 6 (2009).
15. J. Huotari, A. L. Spetz1, and J. Lappalainen, *The 14th International Meeting on Chemical Sensors, IMCS, Nuremberg, Germany, May* (2012).
16. A. Simo, B. Mwakikunga B. T. Sone, B. Julies, R. Madjoe, and M. Maaza, *Int. J. Hydrogen Energy* 39, 15 (2014).
17. B. Mwakikunga, S. Motshhega, L. Sikhwhivilu, M. Moodley, G. Malgas, M. Scriba, and S. Sinha-Ray, *Sens. Act. B* 184 (2013).
18. B. W. Mwakikunga, E. Sidras-Haddad, and M. Maaza, *Opt. Mat.* 29 (2007).
19. S.-H. Lee, H. M. Cheong, M. J. Seong, P. Liu, C. E. Tracy, A. Mascarenhas, J. R. Pittsa, and S. K. Deb, *Sol. St. Ionics* 165 (2003).
20. G. I. Petrov and V. V. Yakovlev, *App. Phys. Lett.* 81, 6 (2002).
21. A. R. Barron, *Physical Methods in Chemistry and Nano Science, Collections Houston, Texas* (2012).
22. F. Sediri and N. Gharbi, *J. Phy. Chem. Sol.* 68 (2007).

Larger Selectivity of the V₂O₅ Nano-particles Sensitivity to NO₂ than NH₃

^{1, 2, 3} Amos Adeleke Akande, ¹ Bonex Wakufwa Mwakikunga,
² Koena Erasmus Rammutla, ³ Augusto Machatine

¹ DST/CSIR National Centre for Nano-Structured Materials, P O Box 395, Pretoria 0001, South Africa

² University of Limpopo, Department of Physics, P/Bag X1106, Sovenga, 0727, RSA

³ School of Physics, University of Pretoria, Pretoria, 0002, South Africa

¹ Tel.: +27 12 841 4771, fax: +27 12 841 2229

¹ E-mail: aaakande@csir.co.za, bmwakikunga@csir.co.za

Received: 26 March 2015 /Accepted: 31 August 2015 /Published: 30 September 2015

Abstract: V₂O₅ nanoparticles (NPs) were prepared using microwave irradiation technique and characterized using X-ray diffraction (XRD), Raman spectroscopy (RS), Field emission scanning electron microscopy (FESEM). The physisorption analysis with the aid of Brunauer-Emmimer-Teller (BET) method shows high surface area and relatively high pore diameter. The material's gas sensing capabilities was tested for NH₃ and NO₂ keeping operating temperature at 300 K. An increase in electrical resistance were observed for both NH₃ (reducing gas) and NO₂ (oxidizing gas). This increase in resistance has been explained from the fact that V₂O₅ possess both n-type and p-type conductivity with NH₃ preferring to interact with the n-type phase and NO₂ attaching to p-type adsorption sites. The sensitivity of the p-type V₂O₅ phase to NO₂ is found to be 32 times greater than the sensitivity of the n-type V₂O₅ phase to NH₃. The results show that V₂O₅ is 32 times more sensitive to NO₂ than NH₃. Copyright © 2015 IFSA Publishing, S. L.

Keywords: V₂O₅, Nano-particles, Selectivity, Sensitivity, NH₃, NO₂, Oxidizing gas, Reducing gas, n-type, p-type, Conduction band.

1. Introduction

Nanoscale materials are very suitable for gas detection at molecular level due to their inherent small size, high conductance and large surface-to-volume ratio [1]. Wide band gap semiconductor metal oxides like SnO₂, ZnO, WO₃, V₂O₅ and TiO₂ are widely investigated materials for gas sensors application because of their simplicity, easy to synthesize, cost effective and capability of detecting large number of toxic and volatile gases under different conditions [1]. Vanadium has been

extensively studied as semiconductor materials because of its ability to exhibit metal-to-insulator phase transition with respect to temperature and pressure [2-3]. Vanadium pentoxide (V₂O₅) forms the most stable oxide among other binary oxides of vanadium, it exhibits orthorhombic crystallographic structure at T_c = 375 °C with a band gap of 2.5 eV [3-4]. Sensing capability of V₂O₅ nanostructures has been achieved for nitrogen monoxide [5] and nitrogen dioxide and ethanol [5], the material has also been applied in thermo-chromic window, electrochromic window and electrochemical devices [6]. In

this current work, we report the chemiresistive properties of V_2O_5 NPs to NH_3 and NO_x gases.

2. Experimental

0.5 grams of Ammonia metavanadate NH_4VO_3 powder (purity 99.99 %) was ultrasonically dissolved in 10 mL distilled water, and 5 moles of N_2H_2 reagent was added drop-wise. The mixture was transferred into 100 mL Teflon vessel and placed onto the Multiwave 3000 Microwave reactor. The reactor power was set to 600 W, the temperature was maintained at 180 °C, and the reaction was allowed to run for 20 minutes after which the reactor cooled the vessels for 25 minutes. Afterwards, the resultant mixture was collected by filtration and washed repeatedly using isopropanol and acetone in an ultrasonic bath to remove undesired impurities and to minimise particle agglomeration. The final product was dried at 100 °C for 11 hours.

The powder was characterized using a Panalytical X' pert Pro PW 3040/60 XRD equipped with $Cu K\alpha$ ($\lambda=0.154nm$) monochromatic radiation source. XRD patterns were recorded at 45.0 kV and 40.0 mA from $2\theta = 5$ to 90°. Raman spectroscopic studies were conducted using a Jobin–Yvon T64000 Raman spectrograph with a 514.5 nm excitation wavelength from an argon ion laser. The power of the laser at the sample was low enough (0.384 mW) in order to minimise localised heating of the sample. The T64000 was operated in a single spectrograph mode, with the 1800 lines/mm grating and a 100x objective on the microscope. Morphology studies were carried out using a LEO 1525 field emission scanning electron microscope (FESEM). BET analyses were carried out using Micromeritics TriStar II series Surface Area and Porosity instrument and a Micromeritics sample degassing system from USA.

3. Gas Sensor Test

Gas testing measurements were achieved using a set-up (at the university of Cologne Germany) similar to the KSGA565 KENOSISTEC sensing measurement illustrated in Fig. 1. The sensor was prepared by dispersing V_2O_5 NPs in ethanol and making a thick paste on the interdigitated electrode and the test were performed by measuring change in electrical resistance of different concentration of the analyte using KEITHLEY picoammeter system.

4. Results and Discussion

Fig. 2 shows the XRD pattern of V_2O_5 nanoparticles (NPs) belonging to the orthorhombic phase of V_2O_5 . The broad diffractions at $2\theta = 17^\circ$ are the characteristics of the orthorhombic V_2O_5 200 reflection [PCDPDFWIN CAS No. 890611].

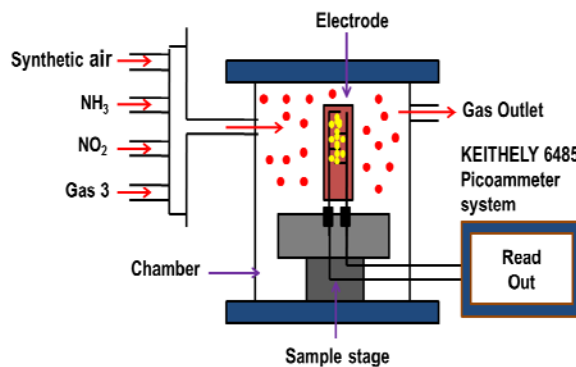


Fig. 1. Schematic diagram of KSGA565 KENOSISTEC sensing station illustrating how the gas sensing measurement was performed.

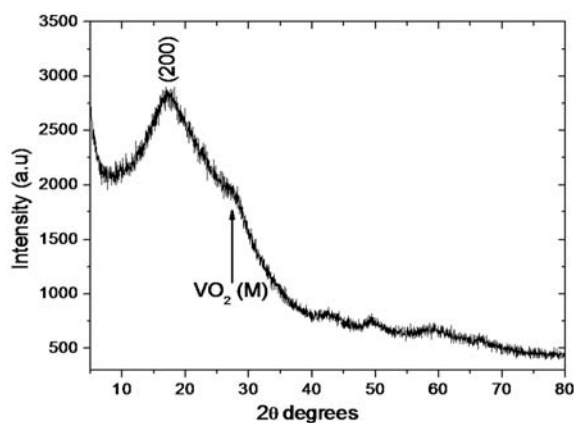


Fig. 2. XRD pattern of V_2O_5 NPs.

However, the development of VO_2 monoclinic phase was also observed at $2\theta=27.6^\circ$ [PCDPDFWIN CAS No. 710042]. The crystallite size of the particles was calculated using Debye Scherer's model and found to be 5 nm. The SEM micrograph of V_2O_5 NPs in the Fig. 3 shows formation of sphere-like colloidal particles.

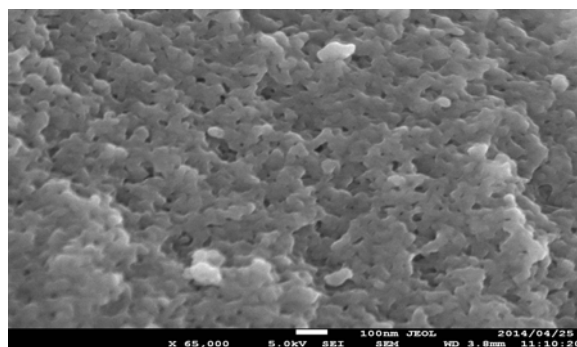


Fig. 3. SEM micrograph of V_2O_5 NPs.

Raman spectrum of V_2O_5 NPs in Fig. 4 shows Raman active modes of V_2O_5 . A strong peak at lower frequency band 141 cm^{-1} corresponding to the Bg symmetry while the high frequency vibration at 992 cm^{-1} corresponds to stretching of O-V-O atoms.

Vibration modes at 282, 402 and 525 cm^{-1} are resulting from the bending mode of V-O band while the stretching mode at 692 cm^{-1} corresponds to the motion parallel and perpendicular to ab-plane [3, 7-8]. In agreement with XRD analysis, the development of VO_2 monoclinic vibration mode was also observed at 194 cm^{-1} [9].

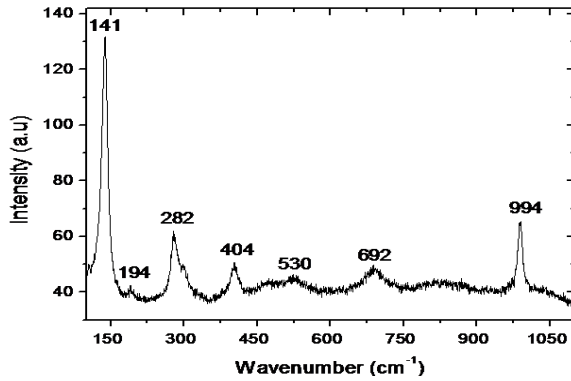


Fig. 4. Raman spectrum of V_2O_5 NPs.

The specific surface area S_{BET} and pore size/diameter (d_{por}) of 92.7 m^2g^{-1} and d_{por} of 12 nm, respectively, were determined by physisorption of nitrogen according to BET theory as shown in Fig. 5. The surface area and the nano-porous studies by SEM and BET revealed the material's potential in gas and chemical sensor application.

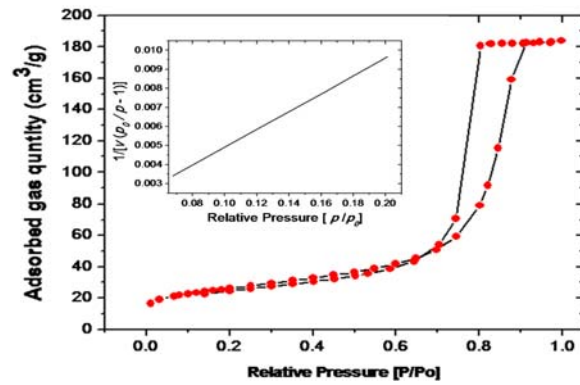
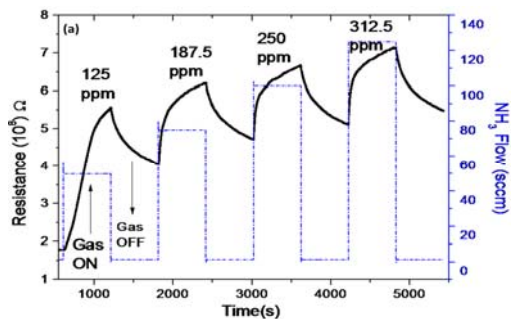
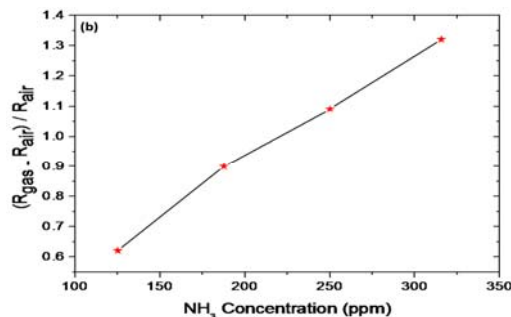


Fig. 5. N_2 adsorption/desorption isotherms profile of V_2O_5 NPs, insert is the BET plot.

The measured electrical response for different NH_3 concentrations is presented in Fig 6 (a), with operating or substrate temperature kept at 28 $^\circ\text{C}$. The material showed good response to NH_3 . Fig. 6 (b) shows linear profile for NH_3 sensitivity plot, where R_{gas} and R_{air} are the resistance of V_2O_5 NPs in the presence of the analyte gas and air respectively [10, 11]. The measured electrical response for different NO_2 concentrations is presented in Fig. 7 (a) with operating temperature kept at 28 $^\circ\text{C}$. The material showed good response for all concentrations. Increase in the electrical resistance of V_2O_5 NPs sensor upon injection of the oxidising gas NO_2 shows p-type semiconductor behaviour. Fig. 7 (b) is the NO_2 sensitivity profile.

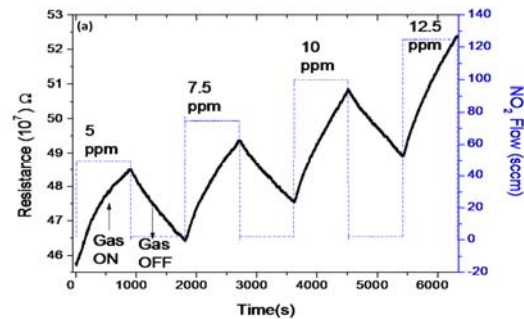


(a)

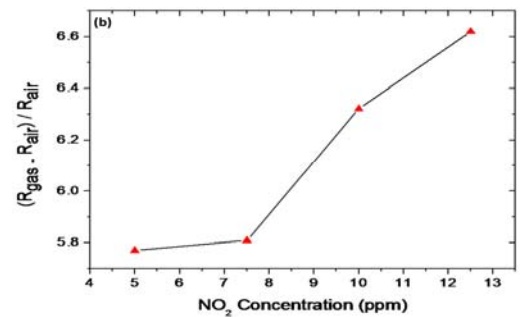


(b)

Fig. 6. (a) The electrical response of V_2O_5 NPs for different concentrations of NH_3 . (b) Sensor response as a function of different NH_3 gas concentrations.



(a)



(b)

Fig. 7. (a) The electrical response of V_2O_5 NPs for different concentrations of NO_2 . (b) Sensor response as a function of different NO_2 gas concentrations.

The proposed mechanism bases on the fact that V_2O_5 is known to exhibit both p-type and n-type conductivities [3-4]. The results show that NH_3 prefers to interact with the n-type phases of V_2O_5 . In this case the NH_3 molecule captures the adsorbed O_2^- ions from the V_2O_5 surface and oxides to NO_2 and H_2 as depicted in Fig. 8. This process robs the n-type phase of V_2O_5 of its electrons leading to less electron population in the conduction band (CB) and hence increase in resistance as shown in Fig. 6 (a).

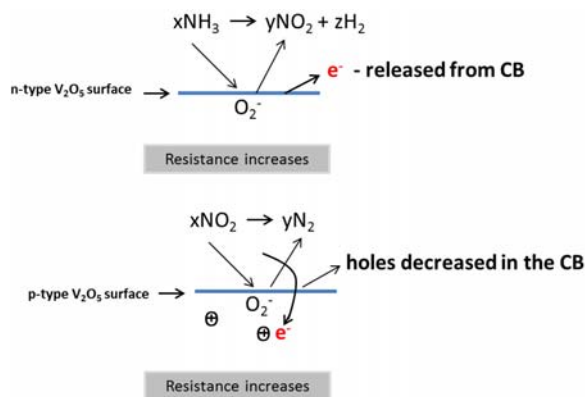


Fig. 8. Sensing mechanism of V_2O_5 NPs.

As for the proposed sensing scheme for NO_2 , the results show increase in resistance regardless of the fact that NO_2 is an oxidising gas. This is clear evidence that NO_2 prefers to interact with the p-type phase of V_2O_5 . In this case NO_2 interacts with holes or vacancies in the adsorbed O_2^- . When such a hole interacts with NO_2 , the NO_2 is broken into N_2 and adsorbed O_2^- . Only N_2 is released in the process leaving behind the O_2^- as adsorbed at the V_2O_5 surface as O_2^- . In the process the p-type phase will have gained an electron or lost a hole in the conduction. The loss of holes in the CB of a p-type V_2O_5 leads to an increase in resistance as shown in Fig. 7 (a).

It is worth noting that the magnitude of responses of V_2O_5 sensor to both NH_3 and NO_2 are many magnitude different. The sensitivity of the n-type phase to NH_3 is calculated as the slope of the response vs concentration curve in Fig. 6 (b). This works out to be $3.47 \times 10^{-3} \text{ ppm}^{-1}$. When the same sensitivity calculation is done for the p-type phase to NO_2 from Fig. 7 (b) one finds the value of 0.11. The response of the p-type phase to NO_2 is therefore 32 times greater than the sensitivity of the n-type phase to NH_3 . Therefore, this V_2O_5 sensor is 32 times more selective to NO_2 than to NH_3 . This further suggests that the V_2O_5 nanomaterials is predominantly p-type.

7. Conclusions

We report gas sensing capability of vanadium pentoxide nanoparticles synthesized using microwave

assisted techniques. The SEM image and BET nano-porous analysis revealed the large surface property of the material. Electrical response for different concentrations of these gases showed good response, and the reaction mechanism between the gases and sensor showed that V_2O_5 NPs is predominantly a p-type semiconductor with a ratio of p-type- to n-type of 32:1. This suggests that for every one electron in V_2O_5 there are 32 holes. We conclude from the results that V_2O_5 is 32 times more selective to NO_2 than to NH_3 .

Acknowledgements

Support from the India-Brazil-South Africa trilateral cooperation under the National Research Foundation (NRF) grant number HGER24X is acknowledged. Amos A. Akande also acknowledge Dr. Ella C. Linganiso for the sensing measurement.

References

- [1]. Vishah B., Samanta S., Singh A., Debnath A. K., Aman Mahajan, Bedi R. K., Aswal D. K., Gupta S. K., Chemiresistive gas sensing properties of nanocrystalline Co_3O_4 thin films, *Sensors & Actuators, B: Chemical*, Vol. 176, 2013, pp. 38-45.
- [2]. Morin F. J., Oxides Which Show a Metal-to-Insulator Transition at the Neel Temperature, *Physical Review Letters*, Vol. 3, Issue 1, 1959, pp. 34-36.
- [3]. A. A. Akande, E. C. Linganiso, B. P. Dhonge, K. E. Rammutla, A. Machatine, L. Prinsloo, H. Kunert, B. W. Mwakikunga, Phase evolution of vanadium oxides obtained through temperature programmed calcinations of ammonium vanadate in hydrogen atmosphere and their humidity, *Materials Chemistry and Physics*, Vol. 151, 2015, pp. 206-214.
- [4]. Rao M. C., Vanadium Pentoxide Cathode Material for Fabrication of all Solid State Lithium-Ion Batteries - a Case Study, *Research Journal of Recent Sciences*, Vol. 2, No. 3, 2013, pp. 67-73.
- [5]. Huotari J., Spetz A. L., Lappalainen Gas sensing properties of pulsed laser deposited vanadium oxides thin film, *Proceedings of the 14th International Meeting on Chemical Sensors (IMCS'12)*, 2012, pp 279-282.
- [6]. A. A. Akande, K. E. Rammutla, T. Moyo, N.S.E Osman, S. Nkosi, C.J. Jafta, B. W. Mwakikunga, Magnetism variations and susceptibility hysteresis at the metal-insulator phase transition temperature of VO_2 in a composite film containing vanadium oxides, *J. Magn. Magn. Mater.*, 375, 2015, pp 1-9.
- [7]. Mwakikunga B. W., Sidras-Haddad E., Maaaza M., First synthesis of vanadium dioxide by ultrasonic nebula-spray pyrolysis, *Optical Materials*, Vol. 29, 2007, pp. 481-487.
- [8]. Se-Hee Lee, Cheong H. M, Seong M., Liu J. P., Tracy C. E, Mascarenhas A., Pitts J. R., Deb S. K., Raman spectroscopic studies of amorphous vanadium oxide thin films, *Solid State Ionics*, Vol. 165, 2003, pp. 111-116.
- [9]. Petrov G. I., Yakovlev V. V., Raman microscopy analysis of phase transformation mechanisms in

- vanadium dioxide, *Applied Physics Letters*, Vol. 81, No. 6, 2002, pp. 1023-1025.
- [10]. Watchakun K., Samerjai T., Tamaekong N., Liewhiran C., Siritwong C., Kruefu V., Wisitsoraat A., Tuantranont A., Phanichphant S., Semiconducting metal oxides as sensors for environmentally hazardous gases, *Sensors & Actuators, B: Chemical*, Vol. 160, 2011, pp. 580-591.
- [11]. Yu M., Liub X., Wang Y., Zheng Y., Zhang J., M. Li, Lan W., Q. Su, Gas sensing properties of p-type semiconducting vanadium oxide nanotubes, *Applied Surface Science*, Vol. 258, 2012, pp. 9554-9558.

2015 Copyright ©, International Frequency Sensor Association (IFSA) Publishing, S. L. All rights reserved.
(<http://www.sensorsportal.com>)



SEIA' 2015

International Conference on Sensors Engineering and Electronics Instrumental Advances

21-22 November 2015
Dubai, UAE

CALL FOR PAPERS

The conference is focusing any significant breakthrough and innovation in Sensors, Electronics, Measuring Instrumentation and Transducers Engineering Advances with broadest concept, by focusing on main areas as:

- **Sensor Technology**
- **Instruments and Measuring Technology**
- **Automation and Control**

Dubai attractions: the city is known for luxury shopping, ultramodern architecture and a lively nightlife scene. Burj Khalifa, an 830 m-tall tower, dominates the skyscraper-filled skyline. At its foot lies Dubai Fountain, with jets and lights choreographed to music. On man-made islands just offshore is Atlantis, the Palm, a resort with water and marine-animal parks.

Important Dates:

Paper Submission
(2-page abstract):
15 October 2015

Notification of Acceptance:
25 October 2015

Registration:
31 October 2015

Conference Date:
21-22 November 2015



www.sensorsportal.com/HTML/CONFERENCES/SEIA_2015/

Gate Voltage Controlled Humidity Sensing Using MOSFET of VO₂ Particles

A. A. Akande, B. P. Dhonge, B. W. Mwakikunga, A. G. J. Machatine

Abstract—This article presents gate-voltage controlled humidity sensing performance of vanadium dioxide nanoparticles prepared from NH₄VO₃ precursor using microwave irradiation technique. The X-ray diffraction, transmission electron diffraction, and Raman analyses reveal the formation of VO₂ (B) with V₂O₅ and an amorphous phase. The BET surface area is found to be 67.67 m²/g. The humidity sensing measurements using the patented lateral-gate MOSFET configuration was carried out. The results show the optimum response at 5 V up to 8 V of gate voltages for 10 to 80% of relative humidity. The dose-response equation reveals the enhanced resilience of the gated VO₂ sensor which may saturate above 272% humidity. The response and recovery times are remarkably much faster (about 60 s) than in non-gated VO₂ sensors which normally show response and recovery times of the order of 5 minutes (300 s).

Keywords—VO₂, VO₂ (B), V₂O₅, MOSFET, gate voltage, humidity sensor.

I. INTRODUCTION

THE well-known phases of Vanadium oxides VO₂, V₂O₃ and V₂O₅ with V⁴⁺, V³⁺, V⁵⁺ ionic state (valence state) respectively, among other homologues series or members of the groups V_nO_{2n}, V_nO_{2n-1}, V_nO_{2n+1}, etc. have a significant impact on current research in the optical and electronic field [1]-[3]. The most interesting one among them is VO₂ because of its semiconductor-to-insulator transition around 340 K which is usually accompanied by a change in properties such as resistivity, conductivity, optical transmittance and reflectance [2]. All these properties have been reported to be preceded by phonon and electron interactions with crystal structure as it changes from low-temperature monoclinic M₁ phase (with space group P2₁/c) to high-temperature rutile phase R (with space group P4₂/mnm) and electronic band dimerization [2], [3]. However, VO₂ phase has been discovered to have many other polymorphs apart from the distorted M₁ and most stable R phases mentioned above. These other members are the meta-stable VO₂ (B), VO₂ (A), VO₂ (A_H) [4], [5] and M₂ the intermediate phase between M₁ and R phase. These phases have been generally useful in technologies such as thermal switch (thermochromic window), thermal/infrared sensors,

ultrafast switches, optical modulators (optical gating), solid oxide fuel cell electrodes, chemical and humidity sensors [6], [7]. For example, humidity sensing of vanadium particles seated on Al₂O₃-Pt interdigitated electrode configuration has been demonstrated in the previous study [1].

In this report, the effect of gate voltage to the humidity response of mixed amorphous-crystalline VO₂ (B) in MOSFET configuration will be presented.

II. METHODOLOGY

A. Material Preparation

Synthesis of VO₂ powders was achieved through microwave irradiation. The precursor NH₄VO₃ (purity 99.99%) and oxalic reagent are thoroughly dissolved in deionized water. The solution was transferred into 100 mL Teflon vessel and placed onto Multiwave 3000 microwave reactor. The reactor power, temperature and the reaction time were maintained at 600 W, 180 °C and 20 minutes, respectively. The synthesised sample was allowed to cool for 30 minutes and washed repeatedly with organic solvents in an ultrasonic bath to remove impurity and to minimize agglomeration. Finally, the sample was dried at 100 °C for 12 h.

B. Material Characterization

The characterization techniques used to analyse this material are: Panalytical X' pert Pro PW 3040/60 (XRD) with Cu K_α (λ=0.154 nm) monochromatic radiation and Jobin-Yvon T64000 Raman spectrograph (RS) with argon ion laser (power 0.384 mW) operated in 514.5 nm excitation wavelength for structural analyses and JEOL 2100 transmission electron microscopy (TEM) for the morphological studies.

C. Phisorption Test, VO₂ MOSFET Fabrication and Humidity Sensing Measurements

Adsorption and desorption isotherm to N₂ molecule was carried out using Brunauer-Emmett-Teller (BET) Micromeritics TriStar II series Surface Area, Porosity instrument and degassing system from the USA.

The VO₂ MOSFET was fabricated by ultrasonically dispersing the VO₂ particles in the organic solvent for 30 minutes and drop-casted onto drain-gate-source electrodes. The connection configuration MOSFET is developed in our group [8].

Humidity sensing measurements were conducted using KSGA565 KENOSISTEC instrument from Italy. VO₂ MOSFET was situated in the chamber and connected to the KEITHLEY source-metre incorporated in the system. The instrument set-up and sample preparation details are reported

A.A Akande holds PhD studentship candidate position at DST/CSIR National Centre for Nano-Structured Materials but registered as a PhD student at the University of Pretoria (e-mail: aaakande@csir.co.za).

B. W. Mwakikunga is a Principal Research Scientist at the DST/CSIR National Centre for Nano-Structured Materials (e-mail: bmwakikunga@csir.co.za).

B. P Dhonge is a Post-Doctoral Scientist at DST/CSIR National Centre for Nano-Structured Materials

A.G.J Machatine is a Senior Lecturer at the School of Physics University of Pretoria

elsewhere [9]. Humidity measurements were performed for relative humidity ranging from 15 to 80% at different gate voltages.

III. RESULTS AND DISCUSSION

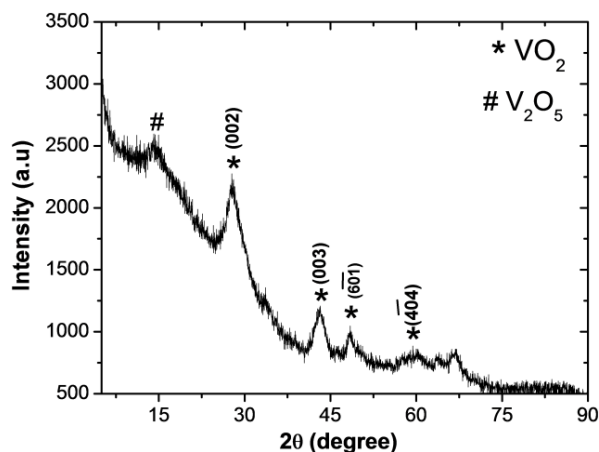


Fig. 1 XRD pattern of VO₂ particles

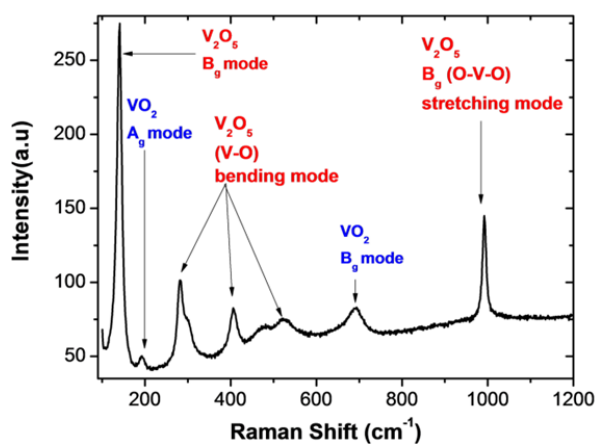


Fig. 2 Raman spectrum of VO₂ particles

The crystal structure of the VO₂ particles is shown by the XRD spectrum in Fig. 1. The spectrum clearly shows that the phase produced herein is VO₂ (B) with trace presence of V₂O₅ and amorphous phase of both V₂O₅ and VO₂ (B). The low angle peak at 15° (2θ) is the characteristic peak of V₂O₅ (PCDPDFWIN CAS No: 89-0611). This evidence shows that the precursor NH₄VO₃ has undergone reduction process in the following order: NH₄VO₃ → V₂O₅ → VO₂. This order of formation is validated by the fact that NH₄VO₃ has the vanadium ion in the V⁵⁺ state similar to that of V₂O₅. Reduction from V⁵⁺ of V₂O₅ to V⁴⁺ in VO₂ requires extra energy which is provided from calcination. Moreover, the phase VO₂ (B) has been widely reported in the literature as the preferred phase microwave synthesis and other hydrothermal techniques [4], [5]. Many phases VO₂ (B) were identified and indexed, the broad and intense peak at angle 27.8 (2θ) with (002) reflection, the peak at 43.5 (2θ) with (003) reflection and others according to the JCPDS 81 - 2392. The Raman spectrum, as shown in Fig. 2, reveals the peaks corresponding to VO₂ and

V₂O₅ vibrational modes. The peaks belonging to V₂O₅ phase seems to dominate in the spectrum because it is a very stable compared to the VO₂ phase of vanadium oxides. This means that the V₂O₅ might be formed at the surface of the core crystalline VO₂, hence Raman spectroscopy which is surface analysis technique captured more surface phonons than the core. A similar effect has been reported by Mwakikunga et al. [10] and Akande et al. [11].

The TEM image of the VO₂ particle in Fig. 3 (a) shows that the particles are composed of mixed crystalline grains and the amorphous phase. The first ring, in Fig. 3 (b), which presents the selected area electron diffraction (SAED) pattern, after the central undiffracted diffuse electron beam can be indexed to (002) Miller plane of the VO₂ (B) crystal structure. The second ring could be attributed to the second intense peak in XRD which also belongs to VO₂ (B). The TEM SAED agrees with XRD that VO₂ (B) is the dominant phase.

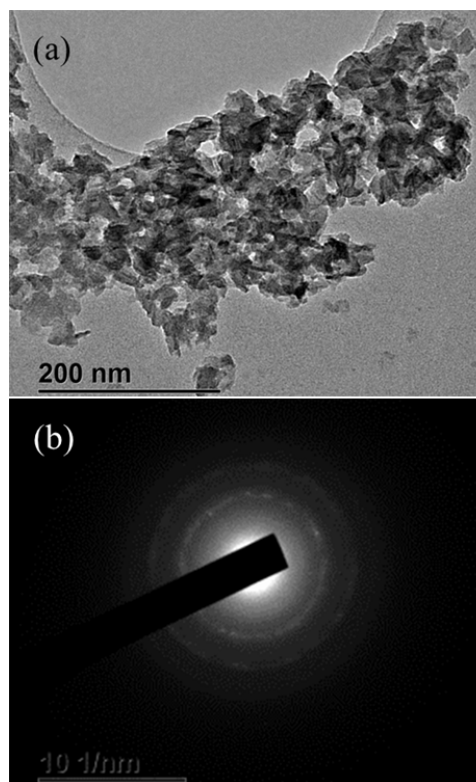


Fig. 3 (a) TEM of VO₂ particles, (b) selected area electron diffraction (SAED)

The BET surface area and physisorption adsorption/desorption isotherm shown in Fig. 4 show high detection capability of the VO₂ particles to N₂ molecules. The quantities in the figure showed improved physisorption effect compared with the one observed in the CVD synthesis of VO₂ [1]. The present surface area is found to be 67.67 m²/g compared to the maximum surface area value of about 16 m²/g in the previous finding.

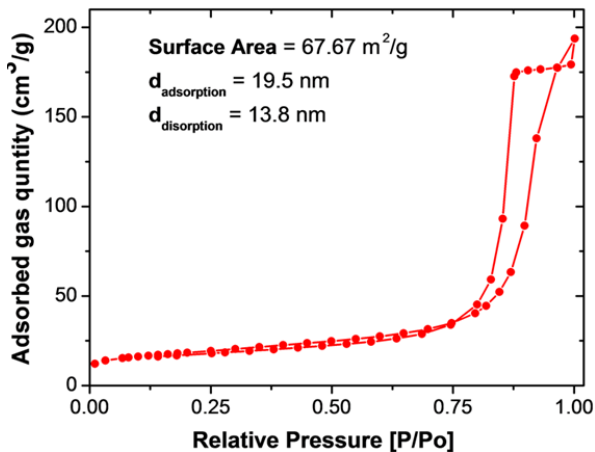


Fig. 4 N₂ molecule adsorption and desorption isotherms profile of VO₂ surface

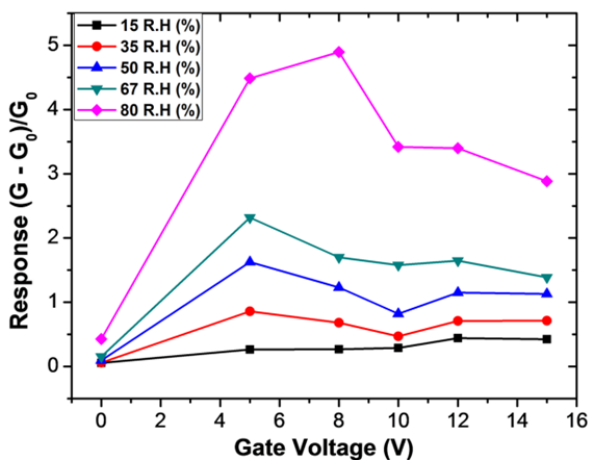


Fig. 5 Response of the VO₂ sensor to relative humidity versus the respective gate voltages

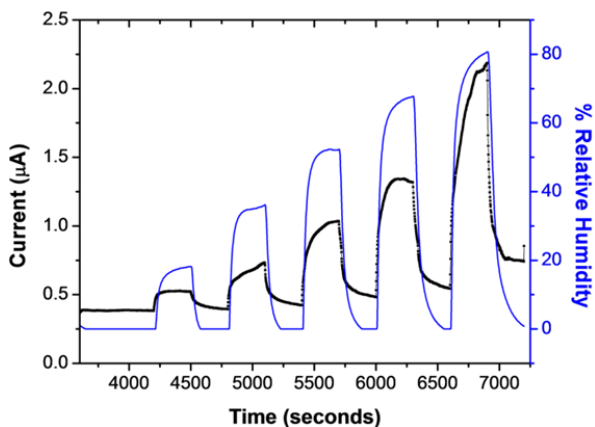


Fig. 6 Current-time curves for the sensor response to varying relative humidity concentrations, for gate of 5 V

The humidity sensing measurement was carried out at $-V$ of the drain to source voltage. The gate voltages (V_g) was varied from 0 to 15 V. The sensing device response to various humidity level for different gate voltages is shown in Fig. 5. The optimum gate voltage was found to be 5 V. The reason for

the 5-V optimum response can be attributed to an effect similar to response-temperature curves in traditional thermally-activated sensors. In such thermally-activated sensors, there exists an optimum temperature at which one gets the maximum response. At lower than this critical temperature, it is known that one gets adsorption increasing with temperature. At higher than this critical temperature, the semiconductor properties, where resistance decreases with rising temperature, dominate the adsorption effect. The analogy here is that the heater under the traditional sensor is replaced with a gate or bias voltage. At lower than the critical gate voltage, the adsorption of water vapor molecule effect dominates any other mechanisms available. At higher than this voltage the transistor is driven its pinch-off state where reduced current leads to drastic reduction in response to the adsorbing water vapor molecules. The pinch-off state is synonymous to either the Gunn Effect or the Josephson's junction effect where negative resistance has been reported for this configuration of transistors in the patent [8].

The change with respect to time in the source to drain current with various percentages of humidity at $V_g = 5$ V is shown in Fig. 6. The response time is typically 60 s and recovery time is 70 s. This is very quick response and recovery when compared to the previous VO₂(B) sensor.

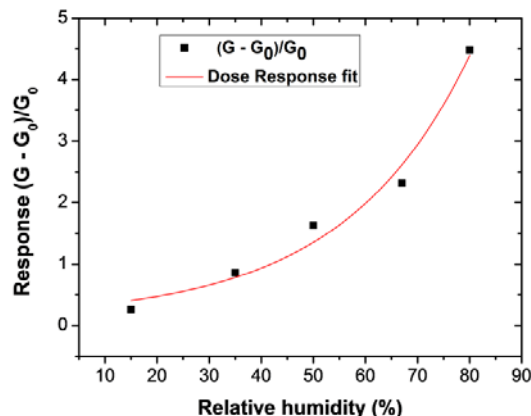


Fig. 7 Non-linear profile of the response to humidity as a function of the level of the relative humidity

When one considers the response to humidity as a function of the level of the relative humidity as shown in Fig. 7, one observes a non-linear profile which is symptomatic of S-shaped curves in dose-response characteristic equation such as that of Hill, Boltzman S - equation or the dose-response equation. When the three equation were tried for fitting, the does-response equation given by

$$G_{res} = \frac{G - G_0}{G_0} = A_1 + \frac{A_2 - A_1}{1 + 10^{(\log RH_0 - RH)p}} \quad (1)$$

where A_1 and A_2 are the lowest and highest sensor responses $\log(RH_0)$ is the logarithm of the relative humidity at 50% response whereas $EC50$ is the antilogarithm of $\log(RH_0)$ dose at which 50% response is achieved by the sensor and p is the Hill factor. From the fitting, $EC50$ value is 272%, $p = 1.26 \times$

10272 whereas $\log(RH_0)$ is 272.1, A1 and A2 are respectively 0.118 and 12096 with a correlation coefficient, R^2 , of 0.925. These results suggest that the VO_2 sensor is very resilient to humidity such that it does not saturate even when humidity approaches 100%. This sensor can then withstand rainy conditions.

IV. CONCLUSION, ON-GOING STUDIES

The nanostructured vanadium oxide was successfully synthesised and used for the humidity sensing measurements in MOSFET configuration. The gate voltage was optimized to $V_g = 5$ V. The high intensity peak of V_2O_5 vibration modes observed in Raman spectra reveals the formation of core-shell structure. The presence of V_2O_5 phase with amorphous background was also observed in XRD and TEM measurements. The BET surface area was found to be 67.67 m^2/g . The response and recovery times of the gated sensor are remarkably greater (of the order of 60-70 s) than the non-gated VO_2 sensor (which showed time of more than 300 s). The response-humidity data are non-linear and follow the typical S-curve profile. The response-dose equation fits the response-humidity data better than the Hill or Boltzmann S-curve equations and it is found that the sensor is very resilient to humidity by showing a humidity level of more than 100% where the response of the sensor could be reduced to 50%.

ACKNOWLEDGMENT

Authors acknowledge the support from the CSIR Advanced Materials for Device Applications programme (HGER27S) and the two programmes viz: India-Brazil-South Africa trilateral cooperation (HGER24X) and SA-Taiwan bilateral (HGER31X) under the National Research Foundation (NRF) grant number.

REFERENCES

- [1] A.A. Akande, E.C. Linganiso, B.P. Dhonge, K.E. Rammutla, A. Machatine, L. Prinsloo, H. Kunert, B.W. Mwakikunga, "Phase evolution of vanadium oxides obtained through temperature programmed calcinations of ammonium vanadate in hydrogen atmosphere and their humidity sensing" *J of Mat. Chem. and Phy.* 151, 206, April 2015.
- [2] A.A. Akande, K. E. Rammutla, T. Moyo, N. S.E. Osman, Steven S. Nkosi, C.J. Jafta, and Bonex W. Mwakikunga, "Magnetism variations and susceptibility hysteresis at metal-insulator phase temperature of VO_2 in a composite film containing vanadium and tungsten oxides" *J Magn. Magn. Mater.* 375, Feb. 2015.
- [3] E. Volker "The metal-to-insulator transitions of VO_2 : A band theoretical approach" *Ann. Phy Leipzig* 11 (1-6) (2002) 9
- [4] E. Strelcov, Y. Lilach, A. Kolmakov, "Gas sensor based on metal to insulator transition in VO_2 nanowire thermistor" *Nano Lett.* 9 (2009) 2322-2322
- [5] C. Wang, X. Liu, W. Xiong, Y. Zheng, "PEG-Assisted hydrothermal synthesis of VO_2 (A) nanowire with remarkable optical switching properties" International Conference on Mechanics and structural Engineering (ICMMSE 2016)
- [6] Z. Yang, C. Ko, S. Ramanathan, "Oxide Electronics Utilizing Ultrafast Metal to Insulator Transitions" *Annu. Rev. Mater. Res.* 41 (2001) 337-367
- [7] M. Maaza, O. Nemraoui, C. Sella, A. C. Beye and B. Baruch-Barak, Thermal induced tenability of surface plasmon resonance in Au- VO_2 nano-photonics, *Optics Comm.* 254 (2005) 188-195.
- [8] B. W. Mwakikunga, A field effect transistor and a gas detector including a plurality of field effect transistors, PA158013/P No. WO2014191892

- A1 PCT/IB2014/061713 also published as China (CN105474006A) Germany (DE112014002575T5) and USA (US20160116434)
- [9] A.A. Akande, B.W. Mwakikunga, K.E. Rammutla, A. Machatine, L., "Larger selectivity of the V_2O_5 nano-particles sensitivity to NO_2 than NH_3 " *J of Sensor and Trasducers* 151, 206, Sept.2015)
 - [10] B. Mwakikunga, M. Maaza, K.t. Hillie, C.J. Arendse, T. Malwela, E. Sideras Haded "From Phonon confinement to phonon splittings in flat single nanostructures, A case of $VO_2@V_2O_5$ core-shell nano-ribbons," *Raman spectr.* (2012).
 - [11] A.A. Akande "Vanadium dioxide Nanostructure Production and Applications in Sensors" MSc Thesis 2014 (Unpublished).


PAPER • OPEN ACCESS

Blue- and red-shifts of V_2O_5 phonons in NH_3 environment by *in situ* Raman spectroscopy

To cite this article: Amos Adeleke Akande *et al* 2018 *J. Phys. D: Appl. Phys.* **51** 015106

View the [article online](#) for updates and enhancements.

Blue- and red-shifts of V_2O_5 phonons in NH_3 environment by *in situ* Raman spectroscopy

Amos Adeleke Akande^{1,2} , Augusto Goncalo Jose Machatine²,
Bathusile Masina³, George Chimowa¹, Boitumelo Matsoso⁴, Kittessa Roro⁵,
Mart-Mari Duvenhage⁶, Hendrik Swart⁶, Jayita Bandyopadhyay¹,
Suprakas Sinha Ray¹ and Bonex Wakikunga¹

¹ DST/CSIR National Centre for Nano-Structured Materials, PO Box 395, Pretoria 0001, South Africa

² Department of Physics, University of Pretoria, Pretoria, 0002, South Africa

³ CSIR-National Laser Centre, PO Box 395, Pretoria, 0001, South Africa

⁴ School of Chemistry, DST-NRF Centre of Excellence in Strong Materials and the Molecular Sciences Institute, University of the Witwatersrand, Johannesburg, Wits 2050, South Africa

⁵ Energy Centre, Council for Scientific and Industrial Research, PO Box 395, Pretoria 0001, South Africa

⁶ Physics Department, University of the Free State, Free State, South Africa

E-mail: aaakande@csir.co.za (Amos A Akande) and bmwakikunga@csir.co.za (Bonex Mwakikunga)

Received 18 August 2017, revised 26 October 2017

Accepted for publication 8 November 2017

Published 5 December 2017




CrossMark

Abstract

A layer of ~ 30 nm $V_2O_5/100$ nm- SiO_2 on Si was employed in the *in situ* Raman spectroscopy in the presence of NH_3 effluent from a thermal decomposition of ammonium acetate salt with the salt heated at 100 °C. When the layer is placed at 25 °C, we observe a reversible red-shift of 194 cm^{-1} V_2O_5 phonon by 2 cm^{-1} upon NH_3 gas injection to saturation, as well as a reversible blue-shift of the 996 cm^{-1} by 4 cm^{-1} upon NH_3 injection. However when the sensing layer is placed at 100 °C, the 194 cm^{-1} remains un-shifted while the 996 cm^{-1} phonon is red-shifted. There is a decrease/increase in intensity of the 145 cm^{-1} phonon at 25 °C/ 100 °C when NH_3 interacts with V_2O_5 surface. Using the traditional and quantitative gas sensor tester system, we find that the V_2O_5 sensor at 25 °C responds faster than at 100 °C up to 20 ppm of NH_3 beyond which it responds faster at 100 °C than at 25 °C. Overall rankings of the NH_3 gas sensing features between the two techniques showed that the *in situ* Raman spectroscopy is faster in response compared with the traditional chemi-resistive tester. Hooke's law, phonon confinement in ~ 51 nm globular particles with ~ 20 nm pore size and physisorption/chemisorption principles have been employed in the explanation of the data presented.

Keywords: V_2O_5 , VO_2 , *in situ* Raman sensing, blue-shift, red-shift, selectivity, phonons

 Supplementary material for this article is available [online](#)

(Some figures may appear in colour only in the online journal)

1. Introduction

Semiconductor metal oxide gas chemo-resistive sensors have been a preferred transduction or method of detecting flammable, combustible, poisonous and toxic gases for many years



Original content from this work may be used under the terms of the [Creative Commons Attribution 3.0 licence](#). Any further distribution of this work must maintain attribution to the author(s) and the title of the work, journal citation and DOI.

now. Since its inception in 1960, when scientists discovered changes in the conductivity of semiconductor materials in the presence of gas and air [1–3], chemo-resistive technique has been a major means of transducing chemical and physical signals by converting them into a measurable one. Among other modern gas sensors or transducers such as electrochemical [4], optical [5], acoustic [6]; the metal oxide chemi-resistor is more applicable in real-life practical devices due to the characteristics such as low cost, long lifetime, fast response

time and high sensitivity [3]. However, the ability to selectively adsorb or detect a certain species or type of gas/analyte has been the limiting factor constraining the reliability of metal oxide chemi-resistors in critical application areas like environment monitoring, health diagnosis, automotive, space exploration, biomedical and pharmaceutical etc.

Raman spectroscopy is a reliable, sensitive and non-destructive method used in characterizing metal oxides and other nanomaterials [7, 8]. The Raman technique has been applied to study adsorption of molecules on the surface of metal oxides and to monitor their selective ability toward certain species of gas [9–11]. Among these studies, A_{1g} mode of SnO_2 was observed to show a huge enhancement when H_2S gas reacted with Cu doped SnO_2 nanomaterial [9]. This enhancement is observed to be absent when the material is exposed to air. The effect is reported to be reversible and the band is attributed to Cu_2S vibration, thus showing reactivity of Cu doped SnO_2 with H_2S . Nanocrystalline WO_3 powder has also been found to react with the reducing gases CH_4 and CO resulting in the growth of two broad band peaks at 1300cm^{-1} and 1600cm^{-1} which were observed to be absent in the Raman spectrum of pure WO_3 [10, 11]. Whereas, these peaks disappeared in the presence of an oxidizing gas NO_2 and thereby are attributed to the graphitic carbon peak usually present in many carbon materials [7]. This showed reactivity of CH_4 and CO with the WO_3 surface. Vanadium oxides materials are very sensitive to Raman spectroscopy [8, 12, 13] and are often characterized by it to explore their structural, metal-insulator and nanostructured properties [8]. The reason for this sensitivity is nothing less than the vanadium oxide's variation in its oxidation state and crystallographic structures which usually cause atomic or lattice displacement (distortion), causing active vibration [8, 12–18].

Vanadium pentoxide with a generic name (V_2O_5) and ionic state V^{5+} amidst other vanadium oxides (VO_2 , V_2O_3 , V_6O_{13} , V_3O_7 , etc) has been widely used for gas sensing due to its semiconductor and thermodynamic properties and atomic arrangement in the crystallographic unit cell [8, 12–18]. This material including VO_2 with V^{4+} ionic state, has been extensively applied for applications such as solar window, smart window; e.g. thermo-chromic and electrochromic devices, anti-reflecting coatings and lithium ion battery [12, 13, 17, 18]. V_2O_5 macroscopic structure (bulk), nano structure and the one whose radius is comparable with Debye length is thermodynamically favoured as orthorhombic unit cell at ambient conditions. This compound has the highest oxygen concentration among other vanadium oxide members; its crystallographic atomic arrangement provides room for corner-sharing and edge-sharing VO_6 octahedral geometry with space group D_{2h}^{13} $Pmnm$ (No. 59) layered structure and lattice parameters $a = 11.510\text{ \AA}$, $b = 3.563\text{ \AA}$ and $c = 4.369\text{ \AA}$ where b and c are frequently interchanged in orthorhombic system [17, 18]. According to the international crystallographic tables and density functional approximation records [17, 18], stoichiometric orthorhombic V_2O_5 structure should have four types of atoms in terms of their geometry coordination i.e. by their nature of bonding and bond length. One vanadium atom V and three different oxygen atoms O (1), O (2) and O (3) located

at different Wyckoff positions. V atom together with O (1) and O (3) occupy $4f$ Wyckoff position with site symmetry C_s whereas O (2) atom can occupy $2a$ Wyckoff position with site symmetry of C_{2v} [18, 19]. High symmetry orthorhombic lattice of V_2O_5 crystal structure with two formula per unit cell contains a total of 42 optical and acoustic modes. Among these 42 modes, three ground state modes are acoustic with zero frequency at high symmetry point called Γ -point.

The first order Raman active modes of this structure can be obtained from the symmetrized square of the vector representation (x, y, z) as the second rank polarizability tensor in the space group D_{2h}^{13} with 8 symmetry elements namely; E , $C_2(z)$, $C_2(y)$, $C_2(x)$, i , $\sigma(xy)$, $\sigma(xz)$ and $\sigma(yz)$ and by factor group analysis and selection rule for D_{2h}^1 point group. The infrared modes transform as (x, y, z) representation, since they are related to the electric dipole moment. Zhon *et al* [19] reported that 21 Raman active modes composed of A_g , B_{1g} , B_{2g} and B_{3g} modes may be presented in the V_2O_5 crystal while the remaining 18 modes may be due to infrared absorption (i.e. infrared active). On the other hand, the low temperature phase of VO_2 structures has space group $P2_1/(C_{2h}^5$ No. 14) and two atoms per unit cell in monoclinic crystal system. Group theory predicts 18 total modes and 15 optical zone-centre modes at wave vector $q = 0$ in the Brillouin zone (at Γ -point) from lattice mode representation by acting four symmetry elements E , $C_2(z)$, i and $\sigma(xy)$. These modes composed of A_{1g} , B_{1g} , B_{2g} and B_{3g} which were distributed in different configurations with respect to the crystal structure of the precursor compound. In this paper, we identify these vibrational modes in *in situ* Raman spectra of the V_2O_5 surface as it interacts with the NH_3 molecule as predicted from group theory. The study combined Raman spectroscopy methods, group theoretical approaches and electrophysical techniques to show the reactivity of vanadium oxide surface to NH_3 molecule at ambient temperatures and at $100\text{ }^\circ\text{C}$ by oxygen iono-sorption and lattice vibration mode assignment. The set-up could be miniaturized to find its usefulness in portable sensitive and selective chemical sensors or applied as a stationary industrial gas detector.

2. Theoretical considerations

This section includes some science of how Raman scattered photon population from a typical nanostructured surface is affected by the presence of reducing or oxidising gases. In this regard, one can use a number of basic theories providing the intensity, I , of Raman scattered photons as a function of surface characteristics. One of the most appropriate theories is the phonon confinement models generally given by [20–24].

$$I(\omega, q) = A_0 \int_0^\infty \frac{\exp(-\alpha q^2)}{[\omega - \omega(q)]^2 + (\Gamma_0/2)^2} dq \quad (1)$$

where q is the wave vector in the Brillouin zone, $\omega(q)$ is the phonon dispersion relation for the material, α is the scaling factor, Γ_0 is the full-width-at-half-maximum broadening of the Raman peak, and A_0 is the proportionality constant. The integral is performed over all ranges of the wave-vector, $q \sim 0$, which is further proportional to $\pi a/\lambda$, where λ is the

laser wavelength and a is the lattice parameter of the material. Any change in $I(\omega, q)$ should be due to less or more Raman scattered photons which means less or more phonons in the surface. This is a further signalling indicator of the chemical interactions or reactions that happen in presence of reducing or oxidising gases. The change in intensity of Raman scattered photons or phonons can be found by differentiating equation (1) with respect to both variables as follows

$$dI = A_0 \frac{\partial}{\partial \omega} \left(\int_0^\infty \frac{\exp(-\alpha q^2)}{[\omega - \omega(q)]^2 + (\Gamma_0/2)^2} dq \right) \Big|_q dq + A_0 \frac{\partial}{\partial q} \left(\int_0^\infty \frac{\exp(-\alpha q^2)}{[\omega - \omega(q)]^2 + (\Gamma_0/2)^2} dq \right) \Big|_\omega d\omega. \quad (2)$$

The first term in equation (2) gives the number of phonons of varying wavenumbers confined in the nano-particle but can only be evaluated numerically. The first part of equation (2) reduces to zero as a differential with respect to ω for the case when ω does not change, as will be seen in the experimental section this yields to null. The second term, however, can be simplified and equation (2) can then be re-written as

$$dI = A_0 \frac{[\exp(-\alpha q^2)]^2}{[\omega - \omega(q)]^2 + (\Gamma_0/2)^2} \left(\frac{2q\alpha [\exp(-\alpha q^2)]^2 [\omega - \omega(q)]^2 + (\Gamma_0/2)^2 + [\exp(-\alpha q^2)]^2 2 [\omega - \omega(q)] \frac{d\omega}{dq}}{[\omega - \omega(q)]^2 + (\Gamma_0/2)^2} \right). \quad (3)$$

In terms of the response defined from the changes in Raman peak heights and their changes, it is appropriate to evaluate the fractional change of intensity rather than merely change in intensity. The latter suffers from variations from spot to spot. Therefore, in this study we define Raman intensity response as a fractional change in intensity referenced to the Raman peak height before the analyte gas is introduced as follows:

$$\frac{dI}{I} = \frac{\frac{[\exp(-\alpha q^2)]^2}{[\omega - \omega(q)]^2 + (\Gamma_0/2)^2}}{\int_0^\infty \frac{\exp(-\alpha q^2)}{[\omega - \omega(q)]^2 + (\Gamma_0/2)^2} dq} \left(\frac{2q\alpha [\exp(-\alpha q^2)]^2 [\omega - \omega(q)]^2 + (\Gamma_0/2)^2 + [\exp(-\alpha q^2)]^2 2 [\omega - \omega(q)] \frac{d\omega}{dq}}{[\omega - \omega(q)]^2 + (\Gamma_0/2)^2} \right). \quad (4)$$

When equation (4) is further analysed in terms of the actual sensing, one can reduce it to the following shorthand version:

$$\frac{dI}{I} = f(q, \omega(q), \omega, \alpha). \quad (5)$$

Since λ is a laser wavelength, which is a constant during the Raman spectra acquisition and $q = 2\pi/\lambda$, then q is a constant and $\omega(q)$ is constant. We shall show in the experimental section that ω is also a constant. Therefore we can re-write it to

$$\frac{dI}{I} = f(\alpha). \quad (6)$$

The scaling factor α varies from materials surface to another and also depends on polarization effects apart from the number of phonons interacting with the laser photons. The number of phonons is further affected by the presence of gaseous molecules. This theoretical discussion on Raman peak intensity changes will be discussed further with experimental validation in later section.

It is also very important to discuss the theory of phonon frequency (wavenumber) changes owing to gas interaction with the material surface. There will be blue or red shifts in the vibrational frequencies due to these changes. If one imagines a linear chain model of fundamental frequency $\omega^2 = \kappa/\mu$, where κ and μ are spring constant and reduced mass of the masses on the spring, respectively, then the change in vibrational frequency, $d\omega$, should be one that depends on both the change in μ and κ . The change in κ takes place when the number of electrons per bond change, whereas the change in μ happens when active gas elements such as oxygen desorbs or adsorbs. These changes can be, mathematically, represented as follows:

$$\frac{\partial \omega}{\partial \kappa} = \frac{1}{2\sqrt{\kappa/\mu}} \quad (7)$$

and

$$\frac{\partial \omega}{\partial \mu} = \left(-\frac{\kappa}{\mu^2} \right) \frac{1}{2\sqrt{\kappa/\mu}} = \left(-\frac{\kappa}{\mu^2} \right) \frac{\partial \omega}{\partial \kappa}. \quad (8)$$

The total change in frequency can be written as

$$d\omega = \frac{\partial \omega}{\partial \mu} d\mu + \frac{\partial \omega}{\partial \kappa} d\kappa = \frac{1}{2\sqrt{\kappa/\mu}} \left(d\kappa - \frac{\kappa}{\mu^2} d\mu \right). \quad (9)$$

So, if $d\kappa > d\mu/\mu^2$, one expects a blue shift, whereas when $d\kappa < d\mu/\mu^2$ then one should expect a redshift in the Raman spectra. Both change in intensity of the phonon (equations (1)–(3)) and their frequencies (equations (4)–(6)) will be used to explain the *in situ* Raman spectra with gas sensing.

3. Experimental

A pulse laser deposition (PLD) technique was employed in this study to grow VO_x thin film on Corning glass substrates. The glass substrates were rigorously cleaned and rinsed several times (in ethanol and deionized water) with an ultrasonic bath in order to remove impurities and ensure quality. Vanadium oxide (VO₂ nanoparticles (NPs) powder with 99.9% purity) from Sigma Aldrich was converted to pellet using an

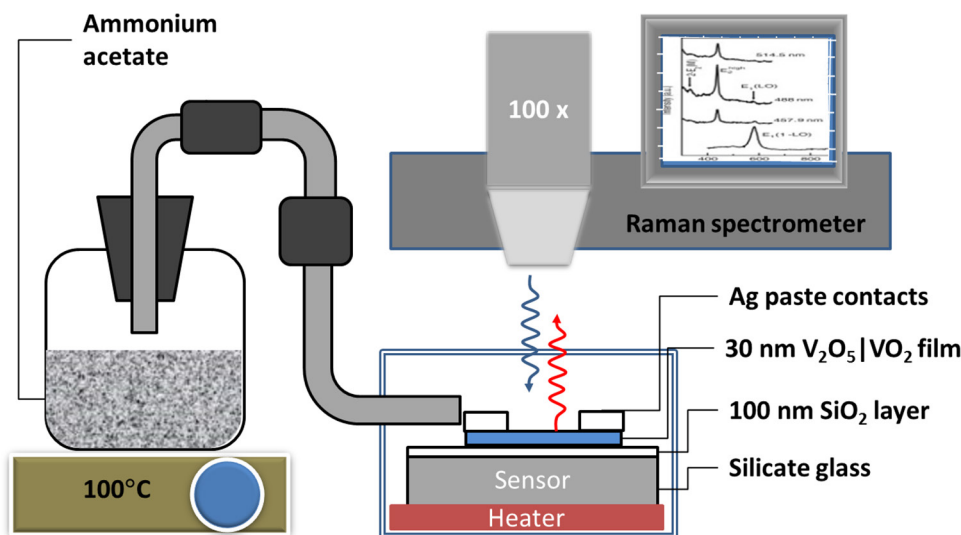


Figure 1. Schematic diagram of the *in situ* Raman measurement illustrating how the NH₃ gas sensing measurement was performed on the V₂O₅ surface.

ENERPAC P142 hydraulic cold press system made in the USA. About 5 g of VO₂ (NPs) powder was slightly dampened with methanol and transferred into a 20 mm hollow die after which a load of 100 tons was mounted on the specimen, and the resulting pellet was annealed at 500° C for ~24 h. The set-up and plasma plume dynamics of the PLD system used for this work is similar to the one reported in [25]. Nd:YAG laser beam ($\lambda = 266$ nm, $\tau = 8$ ns) was directed to the chamber by the aid of several mirrors and later focused onto the VO₂ pellet target at an incident angle of 45° using two cylindrical lenses. The minimum pulse energy was applied at 45 mJ with laser fluence of 2 J cm⁻¹ and the substrate to target distance of 5 cm was maintained during deposition. Oxygen partial pressure was set to 0.05 mbar (37 mTorr) after evacuating the chamber to the base pressure of 3.1×10^{-5} mbar, and the film was deposited for 30 min. The x-ray diffraction patterns of the film were measured at room temperature using the Panalytical XPERT PRO PW3050/50 diffractometer with CuK α radiation (45 kV, 400 mA, $\lambda = 0.1540598$ nm and $5^\circ \leq 2\theta \leq 90^\circ$). The Auriga ZEISS scanning electron microscope (SEM) was employed to study the morphology of the film and to estimate the thickness of oxide layers that are present. SAXSess Anton Paar small-angle x-ray scattering spectroscopy was employed for the particle size and pore size analysis of the film. High resolution x-ray photoelectron spectroscopy (XPS) was obtained with a PHI 5000 Versaprobe system. A low energy Ar⁺ ion gun and low energy neutralizer electron gun were used to minimize charging on the surface. A 100 μ m diameter monochromatic Al K α x-ray beam ($h\nu = 1486.6$ eV) generated by a 25 W, 15 kV electron beam was used to analyze the different binding energy peaks. The pass energy was set to 11 eV giving an analyzer resolution ≤ 0.5 eV. Multipack version 8.2 software was utilized to analyze the spectra to identify the chemical compounds and their electronic states using Gaussian–Lorentz fits.

Time of flight secondary ion mass spectroscopy (TOF-SIMS) analyses were performed using an IONTOF TOF SIMS⁵ instrument with bismuth 1+ as the primary ion source (30 kV, 1 pA pulsed at 10 kHz). These analyses were carried out

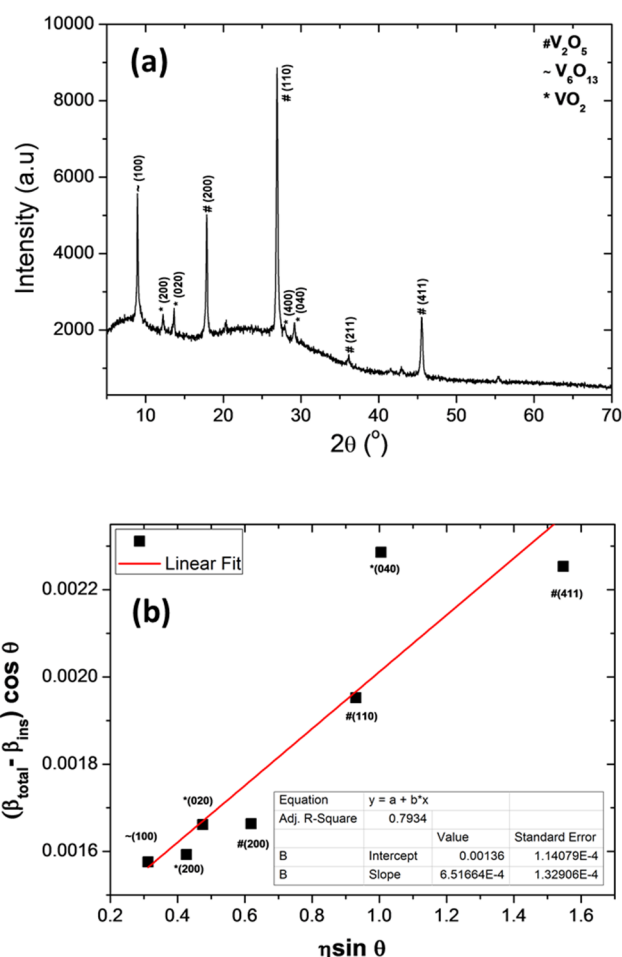


Figure 2. (a) XRD pattern of V₂O₅ film, (b) Williamson–Hull plot for the grains stain determination.

in negative secondary ion mode and under ultra-high vacuum (base pressure) of $\sim 10^{-9}$ mbar. A Cesium (1 kV, 75 nA) sputter gun was used. The analysis area was 100 \times 100 μ m² and the sputter area was 300 \times 300 μ m² at a resolution of 512 \times 512 pixels with a binning of 4 pixels.

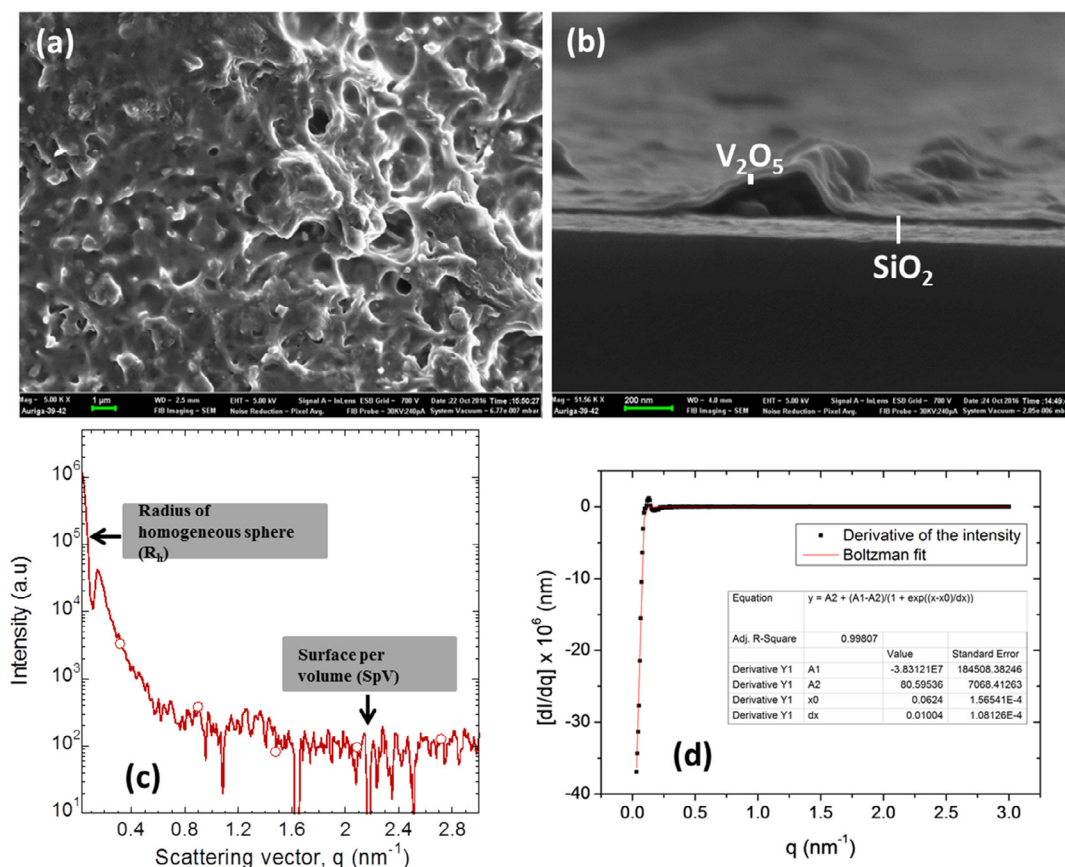


Figure 3. SEM images and SAXS spectrum of V_2O_5 film, (a) in-plane surface image, (b) cross-section image at the edge of the film showing three distinct layers, (c) SAXS analysis showing regions where the average radius of homogeneous spheres and surface per volume are extrapolated from, (d) the differential of the (I, q) data with respect to q .

Raman structural properties of the film and *in situ*-sensing measurement of NH_3 effluent produced from ammonium acetate at 100 °C was carried out using a Bruker spectrometer. A Bruker Raman Senterra spectrometer equipped with 50× optical objective and a 532nm excitation laser, at a laser power of 0.2 mW, was used for accumulating the films' spectra. The typical experimental set-up of the *in situ* Raman sensing measurement is presented in figure 1 wherein a 532nm Nd:YAG laser was directed to the film glued onto an Al_2O_3 -Pt interdigitated electrode set. The heating terminals of the interdigitated electrode are connected to a DC power supply and the whole specimen is enclosed in a transparent chamber where NH_3 effluent from the thermal decomposition of ammonium acetate was allowed flow through. Conductometric sensing measurements were conducted using KSGA565 KENOSISTEC sensing station set-up from Italy. The film surface was wire bonded by silver paste in two terminals configurations to allow connection with the KSGA565-KEITHLEY source meter, after which the currents across the film were measured for different concentrations of NH_3 gas.

4. Results and discussion

Figure 2(a) shows the XRD pattern of the film, the pattern shows that the film is predominantly composed of V_2O_5 , according to the Institute for crystallographic and diffraction database, with a powder diffraction number of (PDF 41-1426)

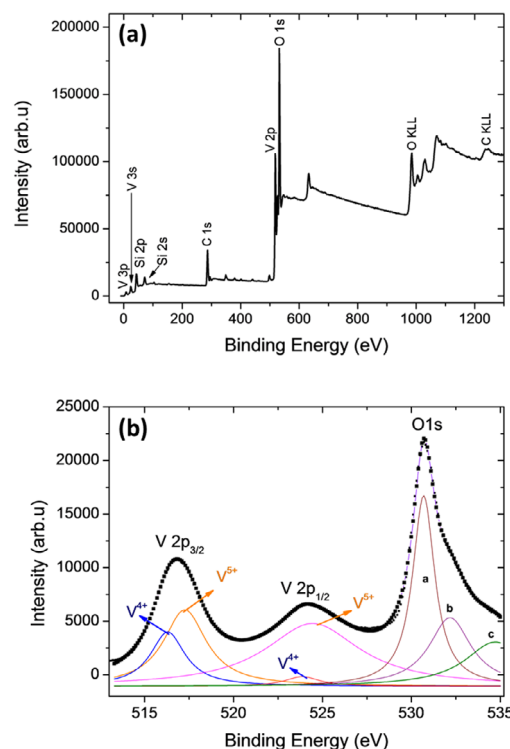


Figure 4. XPS spectra of the V_2O_5 film, (a) broad survey scan spectrum, (b) higher resolution deconvoluted core level spectrum of V-2p and O-1s for the V_2O_5 film.

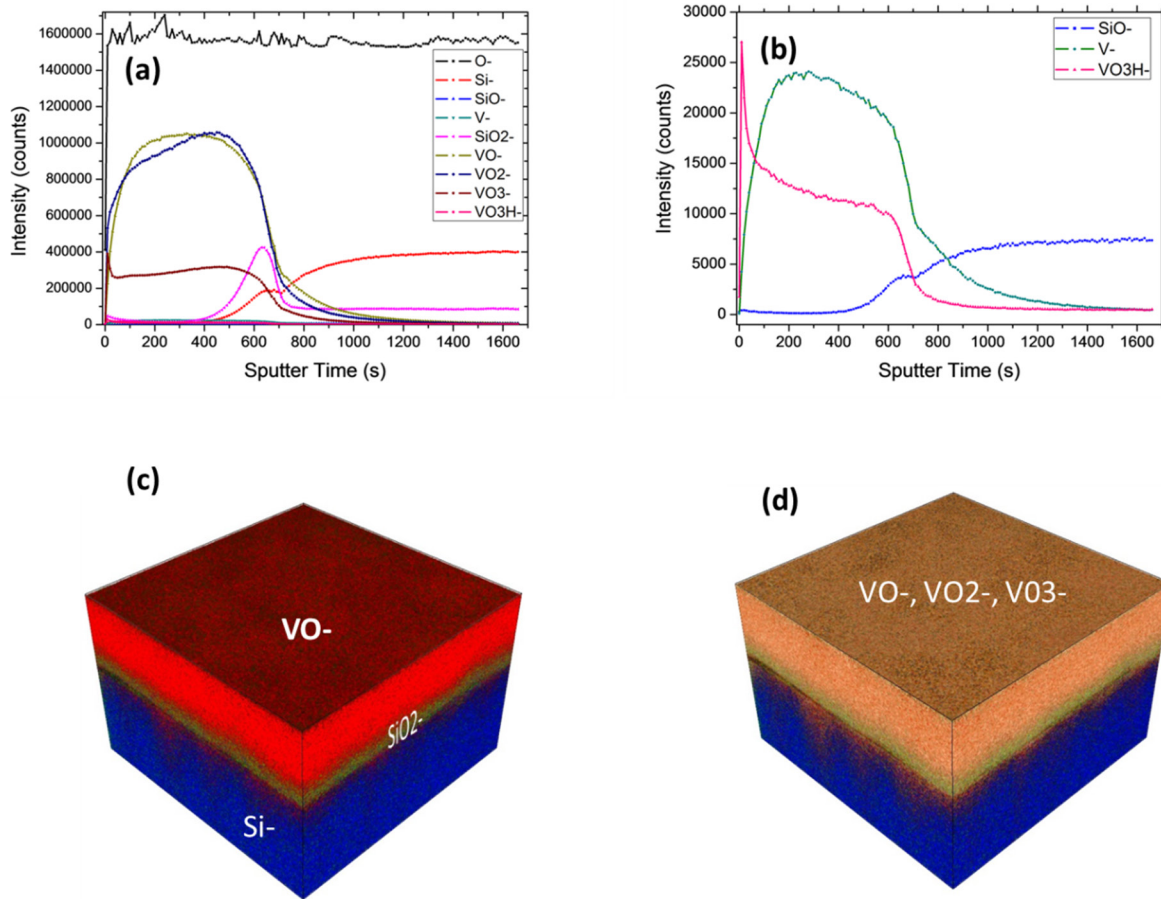


Figure 5. (a) TOF-SIMS depth profile of the negative ions of V, VO, Si and SiO species available in the film, (b) is the TOF-SIMS depth profile spectrum showing the low counts SiO-, V- and VO3H- species in (a), (c) 3D overlays image of the ions of the film consisting of Si-, SiO₂- and VO, (d) 3D overlays image of the entire film displaying VO-, VO₂- and VO₃- as the surface ions.

but with trace phases of VO₂ and V₆O₁₃ according to (PDF 76-0676) and (PDF 27-1318), respectively. This x-ray spectrum has been matched with the Rietveld structure refinement method with the Bragg positions showing strong correlation with the V₂O₅ structure; this report is given in the supplementary material (SM) (stacks.iop.org/JPhysD/51/015106/mmedia). The average crystallite size *L* and lattice micro/nano strain ϵ of the film were calculated using the well-known Scherrer's and Williamson–Hall formula (presented in the SM) [26, 27] and were found to be ~70nm and $0.000651 \pm 1.32 \times 10^{-4}$, respectively. Figure 2(b) is the plot of the Williamson–Hall assumption for lattice strain determination. The film morphology are presented in figure 3 with (a) showing the in-plane formation of clusters of particles with pores at the surface and (b) the cross section at the edge of the film showing that the film is ~30nm in thickness. Figure 3(c) presents a small-angle-x-ray-scattering (SAXS) plot of scattering intensity versus the wave vector for the V₂O₅ layer. From the software on the SAXS instrument based on Guinier *et al*'s formulations, the morphology of the layer is interpreted to be composed of nearly spherical particles from the linearity of the extreme side of the small wave vector and this gives a mean particle diameter of 51.15 ± 0.60 nm. This translates to a surface-to-volume ratio estimated at 8.25 ± 628.60

$\text{m}^2 \text{cm}^{-3}$ estimated at the wave vector of 2nm^{-1} end of the spectrum. Figure 3(d) presents a differential of the spectrum in figure 3(c) which is derived from the well know intensity–wave vector–radial distance equation [28]

$$I = c \int_0^\infty n(r) f(q, r) S(q, r) dr \quad (10)$$

where $n(r)$ is the normal particle size distribution curve such as the Gaussian, Loretzian or lognormal and the like, $f(q, r)$ is the form factor and $S(q, r)$ is the structure factor. For materials without dopants like in our present case, the form factor is unity and similarly the structure factor. Therefore, a differential of the (q, I) data with respect to q of equation (10) gives a plot of the S -curve type as given in figure 3(d). When a Boltzmann's S -curve equation is fitted to the differential curve, the central q_0 and its standard deviation are found to be $0.06 \pm 1.58 \times 10^{-4}$ which when converted from the reciprocal space, q , to the real space, r , gives the mean diameter, r_0 , of about 50nm which confirms the software-obtained value of the particle size. We can conclude the average particle size by SAXS to be 51 nm for this 30nm layer which, when hexagonal close packing of these particles is considered, forms pores of mean diameter of about 20nm. Phonon confinement is therefore possible because of the tight pore size rather than particle size.

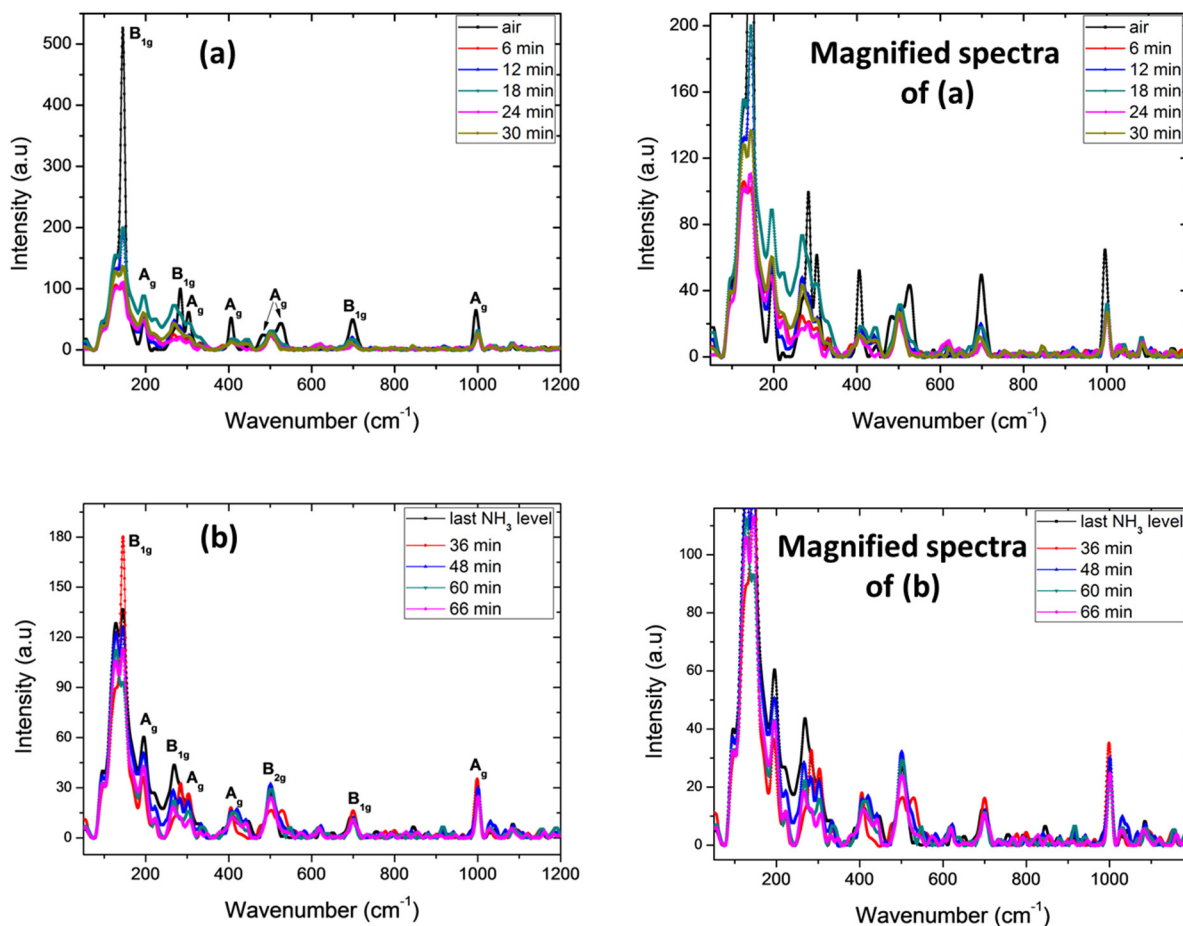


Figure 6. (a) Raman spectra at 25 °C of V₂O₅ film in air, and covered with NH₃ molecule recorded at 6 min intervals, (b) Raman spectra at 25 °C of V₂O₅ film recovering from NH₃ molecule recorded at 6 and 12 min intervals.

XPS spectrum of the surface of the V₂O₅ film is represented in figure 4 with (a) displaying the overall core level XPS survey spectrum and (b) showing Lorentzian–Gaussian deconvoluted core level spectrum of V-2p and O-1s for the V₂O₅ film. The ½ spin–orbit doublet component of the V-2p photoelectron was found to be 524.9 eV for V⁵⁺ and 523.6 eV for V⁴⁺ state while the 3/2 spin–orbit component after further Lorentzian- Gaussian dividing peak analysis gives 517.25 and 516.2 eV for V⁵⁺ and V⁴⁺ respectively [29, 30]. The oxygen O1s is deconvoluted into three peaks, 531, 533 and 535 eV which can be assigned to adsorbed oxygen (a), single bonded oxygen (b) and double bonded oxygen (c) respectively. The TOF SIMS measurement has been used to unveil the chemical elements that are present in V₂O₅ film as a function of sputter-depth, the results are presented in figure 5 where (a) shows depth profile of the negative ions of V, VO, Si and SiO species, (b) is the magnified spectrum of SiO-, V- and VO3H-species and (c) and (d) are the overlay images of all the compounds present in the film. The spectra of ions with depth in figure 5(a) and their image overlays in figure 5(c) shows that vanadium oxides species dominate the film surface to ~500 s sputter time. This analysis is in good agreement with the above XPS results in that VO₂ (V⁴⁺) and V₂O₅ (V⁵⁺) were seen to be more at the surface. This is also true for XRD analysis that shows diffraction peaks for VO₂ (V⁴⁺), V₂O₅ (V⁵⁺)

and V₆O₁₃ which happen to be V⁴⁺ and V⁵⁺ mixed oxide. The TOF-SIMS spectrum in figure 5(a) and overlays images in figure 5(c) also made it possible to understand the V₂O₅ film layers in the SEM cross-section image in figure 3(b) and estimate the film thickness. It was found that in ~500 s sputter time ~30 nm vanadium oxides layer was sputtered completely and thereafter the gun penetrated into the interface region in ~700 s sputter time which is found to be rich in SiO₂. This SiO₂ layer has been estimated to be ~100 nm from the cross-section SEM image.

4.1. In situ Raman spectroscopy with gas sensing at 25 °C

Figure 6 shows the effect of atmosphere changes in the surface of V₂O₅ film when subjected to the effluent of NH₃ from the compound of ammonium acetate. Figure 6(a) illustrates the change in Raman spectra of the film when exposed to the molecule at different times (with intervals of 6 min) and to air (as a control spectrum) at 25 °C, while figure 6(b) represents the change in the Raman spectrum of the film when recovering from NH₃. In these profiles, the authors observed that the modes at low-frequency Raman line region of V₂O₅, earlier classified as rigid-layer modes [13] with bending vibration characteristics, were mostly unaltered in wavenumber when the film was subjected to the NH₃ effluent. Interestingly, the

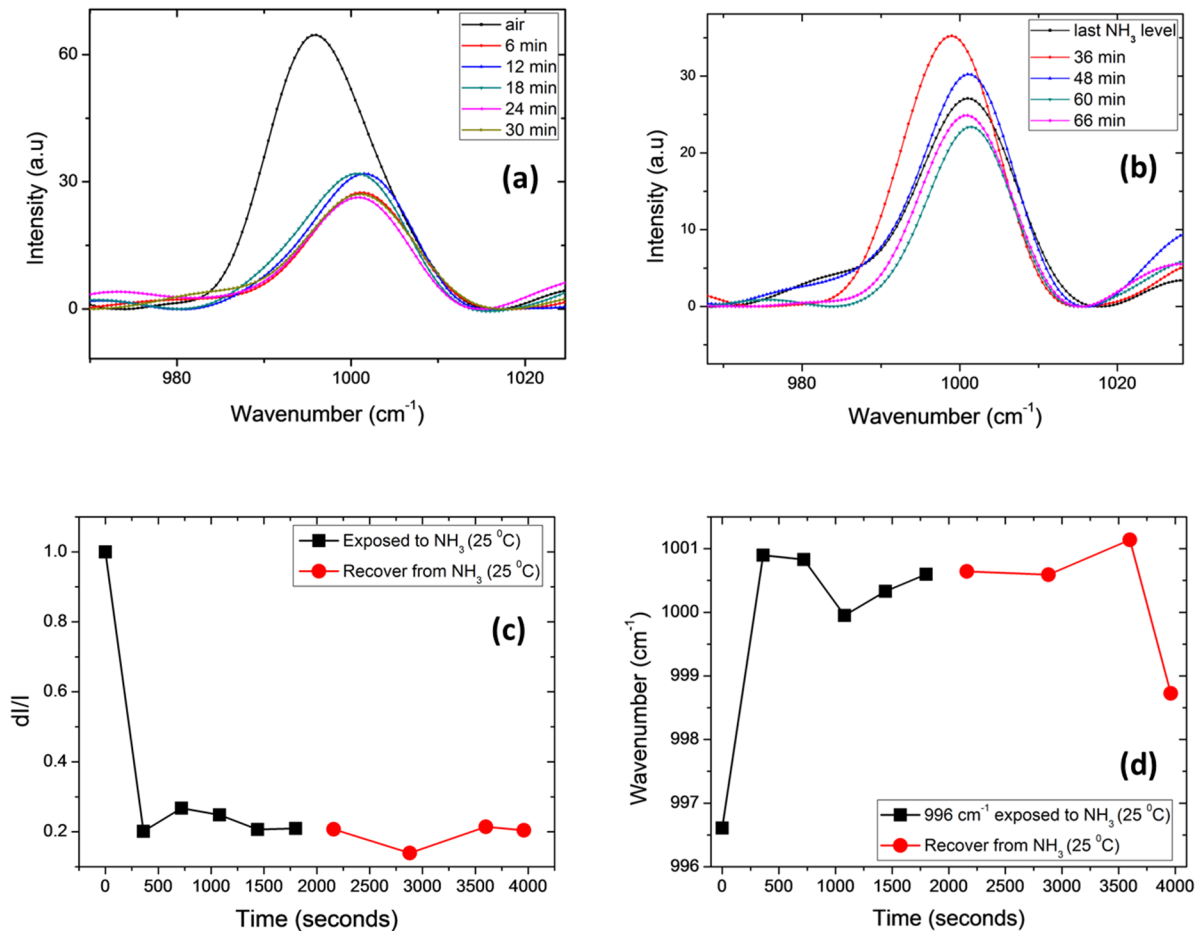


Figure 7. (a) Magnified images of 996 cm^{-1} Raman lines when the film is exposed to NH_3 at 25°C , (b) magnified images of 996 cm^{-1} Raman lines when the film is recovering from NH_3 at 25°C , (c) Gaussian fitted data of the heights of low-frequencies 143 cm^{-1} Raman lines when the film is exposed to and recovering from NH_3 at 25°C , (d) Gaussian fitted data of peak-positions of high-frequencies 996 cm^{-1} Raman lines when the film is exposed to and recovering from NH_3 at 25°C .

one at 194 cm^{-1} which shows a shift to low-frequency Raman line was observed to redshift. On the other hand, at the higher-frequency side of the Raman spectra, the 996 cm^{-1} stretching mode displayed significant shift towards high frequency of the Raman line (blueshift) in all spectra (shown in figure 7(a)). The reverse effect was observed when recovering the film from effluent of NH_3 in figures 6(b) and 7(b), where both blueshifted 996 cm^{-1} and redshifted 194 cm^{-1} modes showed some recovery potential.

In accordance with equation (6) where the change in Raman line position $d\omega$, as a function of both elastic constant of the bonds, κ , and reduced mass of the atoms around these bonds, μ , is given by $d\omega \propto d\kappa - (\kappa/\mu^2)d\mu$. In the present system case: $1/\mu = (1/m_O) + (1/m_V)$ or $\mu = m_O m_V / (m_O + m_V)$. The increase in κ could be ascribed to acceptance of an electron by the V_2O_5 surface from the NH_3 effluent and vice versa, whereas an increase in μ could be ascribed to the acceptance of atoms from the gas by the V_2O_5 surface. Changes in κ should be prevalent at 25°C where adsorption is more likely to happen, while an increase in μ is likely to happen at high temperatures where chemisorption due to breakage of NH_3 bonds is preferred.

Since the 996 cm^{-1} phonon is being blue-shifted [i.e. $d\omega > 0$] when exposed to NH_3 , one expects that $d\kappa > d\mu/\mu^2$. This means that the change in elastic κ is larger than the

change in μ . This suggests that V–O bond gains electrons from NH_3 . On the other hand, the observation that the 194 cm^{-1} phonon is being red-shifted when NH_3 is introduced means that $d\kappa < d\mu/\mu^2$. This could indicate that the V–O–V or O–V–O bonds prevalent in the VO_2 system are losing electrons to the NH_3 at 25°C . This surprising result leads to the conclusion that bonds that have many electrons tend to gain more electrons whereas those bonds that have less electrons tend to lose even the few electrons that they have. This phenomenon is similar to an observation made during the halogenation of organic alkanes with HCl or HF or HBr in 1890s by a scientist known as Markovnikov, who observed that the H atom preferred to attach itself to carbon with the highest number of H atoms [31, 32].

A decrease in intensities of 145 cm^{-1} low-frequency Raman line of V_2O_5 were also observed as a function of NH_3 effluent exposure (figure 6(a)) [33], but a reverse effect is observed when recovering the surface from NH_3 exposure in that the intensities increased slowly and saturate (figure 6(b)) with less potential when recovering from the NH_3 effluent. The profiles in figures 7(c) and (d) are representative of the change in intensity (dI/I) of the 145 cm^{-1} Raman lines and wavenumber (ω) peak-positions of 996 cm^{-1} Raman line at 25°C . These line profiles show that the intensities of 145 cm^{-1} phonon

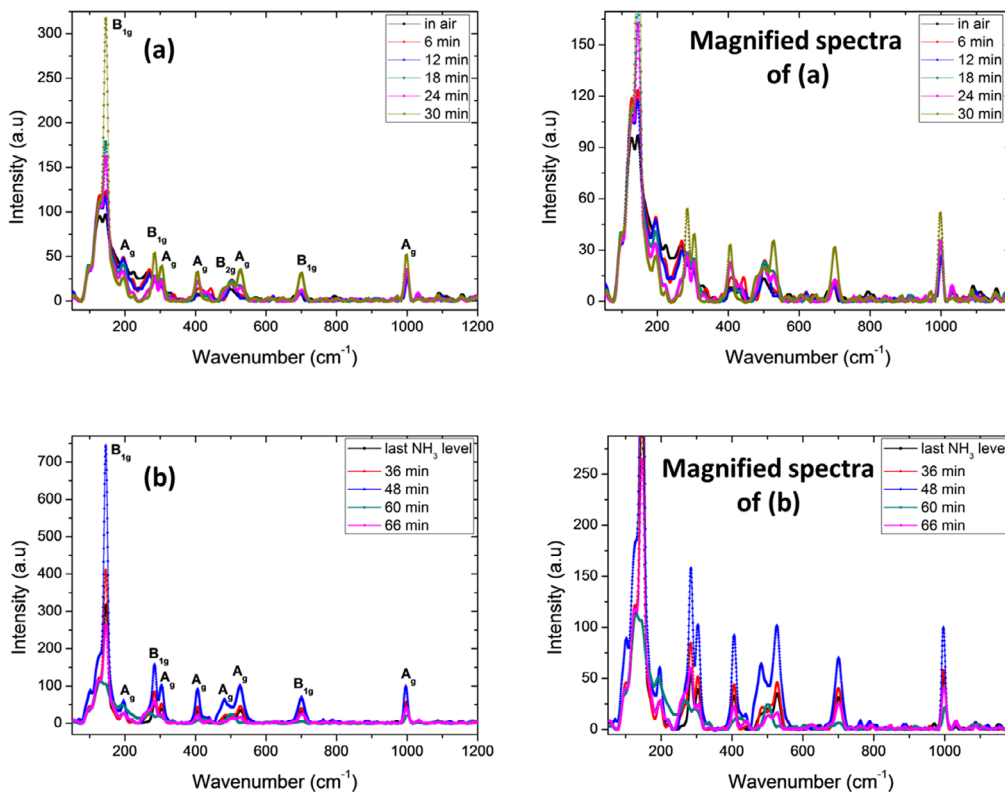


Figure 8. (a) Raman spectra at 100 °C of V₂O₅ film in air, and covered with NH₃ molecule recorded at 6 min intervals, (b) Raman spectra at 100 °C of V₂O₅ film recovering from NH₃ molecule recorded at 6 and 12 min intervals.

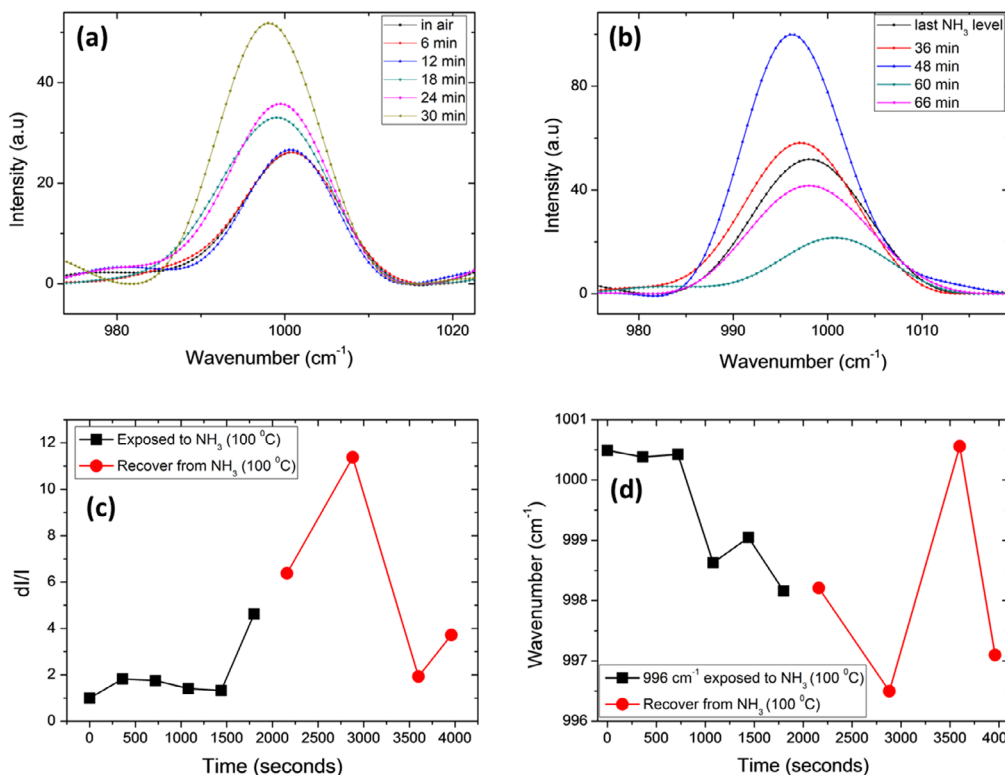


Figure 9. (a) Magnified images of 996 cm⁻¹ Raman lines when the film is exposed to NH₃ at 100 °C, (b) magnified images of 996 cm⁻¹ Raman lines when the film is recovering from NH₃ at 100 °C, (c) Gaussian fitted data of the heights of low-frequencies 143 cm⁻¹ Raman lines when the film is exposed to and recovering from NH₃ at 100 °C, (d) Gaussian fitted data of peak-positions of high-frequencies 996 cm⁻¹ Raman lines when the film is exposed to and recovering from NH₃ at 100 °C.

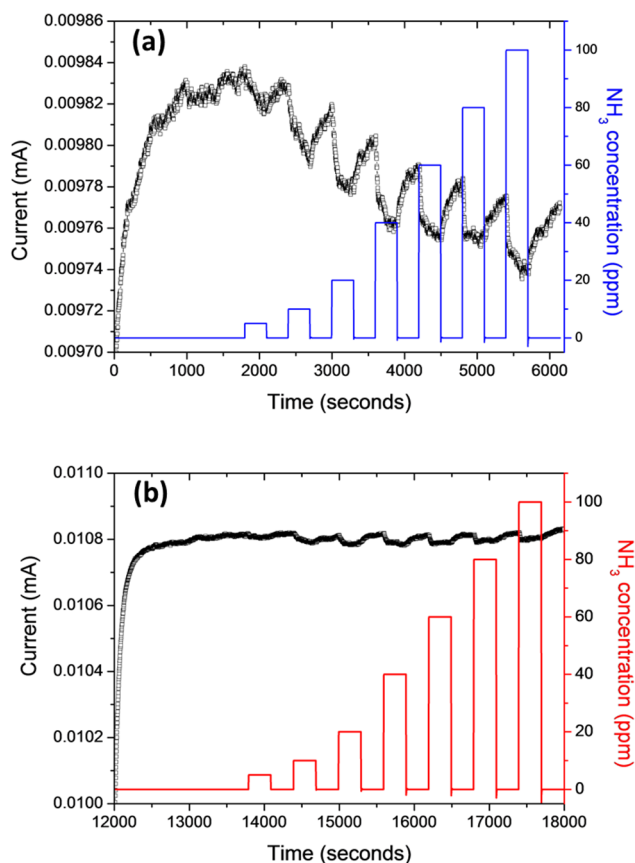


Figure 10. Conductometric sensing signal for NH_3 , (a) at room temperature, (b) at $100\text{ }^\circ\text{C}$.

decrease and saturate with time during exposure, and experience difficulty in recovery due to the lack of vents in the home made gas sensing cell shown in figure 1. This decrease in Raman scattered intensities in the presence of molecules may also be due to the absorption of laser light of free electrons created as a result of the interaction between V_2O_5 and NH_3 [10]. The Raman fingerprint position of 996 cm^{-1} phonon recorded more significant blueshift (4 cm^{-1}) before saturation when exposed to the NH_3 molecule with relatively high potential of recovery than the redshift of the 194 cm^{-1} (2 cm^{-1}) as shown in figure 7(d).

4.2. In situ Raman spectroscopy with gas sensing at $100\text{ }^\circ\text{C}$

In the same manner, figure 8(a) displays the Raman spectra of the film when exposed to the effluent of the NH_3 molecule at different times (with interval of 6 min) and to air (as control spectrum) at $100\text{ }^\circ\text{C}$, while figure 8(b) shows the change in Raman spectra of the film when recovering from the molecule. Figures 9(a) and (b) are the magnified spectra of 996 cm^{-1} Raman lines when the surface is exposed to and recovering from NH_3 at $100\text{ }^\circ\text{C}$ while the profiles in figures 9(c) and (d) are the change in intensity (dI/I) of 145 cm^{-1} Raman line and wavenumber peak-position of 996 cm^{-1} at $100\text{ }^\circ\text{C}$. The fact that the phonons are thermally mediated, coupled with the possibility of less scattering of light at the less-dense environment, may be responsible for the change observed at $100\text{ }^\circ\text{C}$ relative to the effects observed in the case of room temperature measurements ($25\text{ }^\circ\text{C}$). It is true that the way and manner

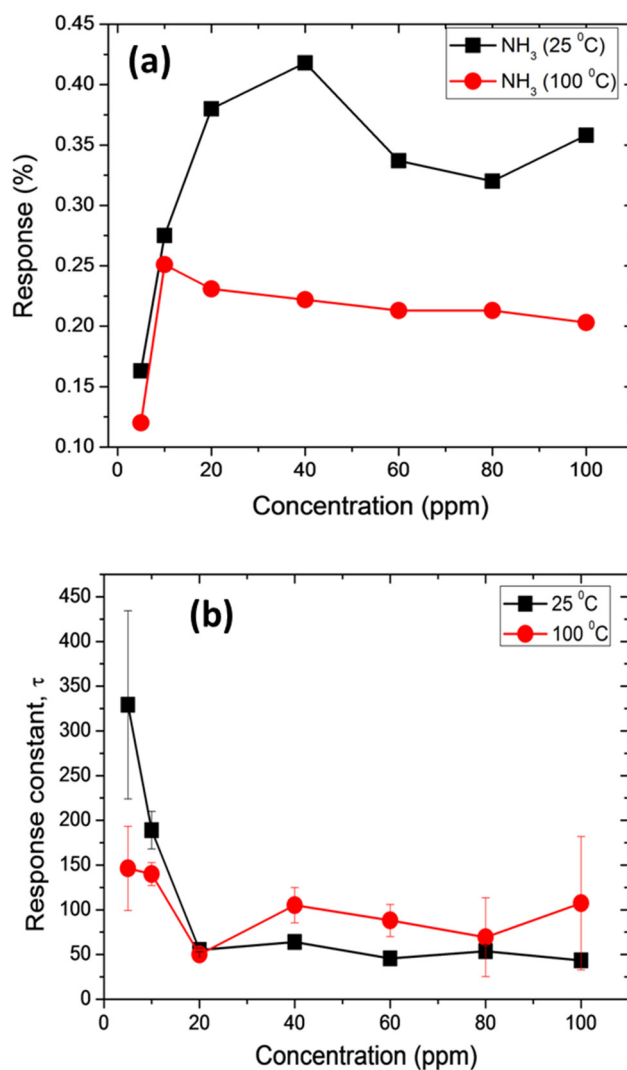


Figure 11. (a) Response curve as a function of different NH_3 gas concentrations, (b) plot of the response time constant for different concentrations of NH_3 gas.

in which the NH_3 molecule sits on the V_2O_5 will greatly influence the charge distribution between them [24]. In addition to the V_2O_5 crystal, geometrical structure and space group discussed in the introduction, V_2O_5 is a layered structure having distorted square pyramids of VO_5 which share edges and corners with the apex of the V–O configuration having a much shorter bond length compared to other bonds. This short bond length corresponds to a double bond attachment [17, 34]. One may propose that hydrogen atoms in an NH_3 molecule in a trigonal pyramid structure preferred to attach themselves to the vanadyl oxygen (i.e the one with double bond and shorter length). If so, that may cause the molecule to give away some of their charges to the $\text{V}=\text{O}$ layer and consequently increase the spring constant which leads to a blueshift in the Raman spectrum. Thus, the remnants of the NH_3 dissociation that are lying in the chamber may regroup and attach themselves to the bonded hydrogen atom and revert back to the NH_3 molecule when recovering V_2O_5 film from the coverage.

Other Raman frequency modes of V_2O_5 observed were $225, 270, 283, 305, 335, 406, 503, 614$ and 700 cm^{-1} at $25\text{ }^\circ\text{C}$ and $100\text{ }^\circ\text{C}$, and they all belong to the vibration

Table 1. Summary of Raman signatures versus chemi-resistive sensing of NH₃ molecule at the V₂O₅ surface.

Sensing properties due to Raman signatures			
Temp °C	Derivative (dI/I) of 143 cm ⁻¹		Change in wavenumber ($\Delta\omega$) of 996 cm ⁻¹
	Response	Response τ (s)	Response
25	-0.799	300	4
100	3.6	1400	-3.2
Sensing properties due to Chemi-resistive test			
Temp °C	Chemi-resistive at 40 ppm		
	Response	Response τ (s)	
25	0.419	59	
100	0.222	105	

modes of V₂O₅ except the modes at 194 cm⁻¹ and 614 cm⁻¹ which are Raman fingerprint positions for the VO₂ structure [13, 19, 26, 35, 36]; this shows that VO₂ crystallites are not participating in the reactivity of NH₃ effluent molecule.

4.3. Comparison of *in situ* Raman spectroscopy-gas-sensor tester and the traditional chemi-resistive gas-sensor testing station

Figure 10 shows electrical measurements of the V₂O₅ film in the presence and absence of NH₃ gas via the set-up described in the experimental section and previously reported [14, 37]. Figure 10(a) is the transient time-conductometric signals of the film when exposed to NH₃ gas at room (25 °C) and figure 10(b) is the signals at 100 °C. The profile shows a decrease in conduction of the film in the presence of NH₃ gas at 25 °C and 100 °C for every concentration. The sensor response and response time constant calculations for different concentrations of NH₃ gas are given as follows:

$$\frac{i}{i_0} = \exp \frac{t}{\tau_1} \quad 0 \leq t \leq t_1 \quad (11)$$

$$\frac{i}{i_0} = \exp \frac{t}{\tau_1} \times \exp \frac{t-t_1}{\tau_2} \quad t_1 < t \leq t_2 \quad (12)$$

where i_0 is the initial current of the sensor in synthetic air (flowing through the chamber), t_1 is the time for i_0 value, i is either the current when the target gas is turned on or off and t_2 is the time at which the sensor recover to its original value. The quantity τ_1 and τ_2 are the time constants for response and recovery steps, these parameters were calculated by fitting the first order exponential function in equations (11) and (12). Figure 11(a) shows a response profile which was calculated from equation (11). The pattern shows better adsorption for all concentrations of the NH₃ gas at 25 °C compared to the one at 100 °C. A response time constant plot was extracted from the same equation(11) as shown in figure 11(b). The response time constant in this paper is defined as the time it takes the sensor to reach 63% i.e $1 - e^{-1}$ of its maximum after exposed to the gas [15, 38, 39]. This result also showed that the responses at 25 °C are faster than that of 100 °C but responses at 100 °C showed stability compared with ones at 25 °C. There is a cross-over in the response time at 20 ppm where the response time is found to be 50 s.

When one compares both the *in situ* Raman spectroscopy gas sensor tester and the traditional conductometric sensing as summerized in the table 1 below, firstly one can infer that at 25 °C the change in the wavenumber of 996 cm⁻¹ (with + shift or blue shift of 4 cm⁻¹) is greater than at 100 °C (with - shift or red shif of 3.2 cm⁻¹) and that the two temperatures showed significant and comparable recovery. On the other hand, the response according to the fractional change in intensity at 25 °C is great (with downward turn or -0.799) compared with the 0.419 of the chemi-resistive test and the one at 100 °C (with upward turn or +3.6) is large compared with the 0.222 of the chemiresistive test. This showed that the *in situ* Raman spectroscopy gas-sensor tester is more responsive than the chemi-resistive sensor especially when considering the fact that the NH₃ effluent concentration in the chamber may be less or even far less than 40 ppm. Also, when one compares the two response time constants, the chemi-resistive sensor showed faster response compared with the *in situ* Raman spectroscopy gas sensor-tester. Again a low concentration of the effluent NH₃ in the *in situ* Raman gas sensing chamber may be the cause. This study shows that apart from using the response due to the fractional change in Raman intensity and chemi-resistive signal, Raman wavenumber (frequency) shift can be employed to selectively monitor gas leakages in the environment or to monitor decomposition of gases in industry during gas processing.

5. Conclusions

In summary, *in situ* Raman spectroscopy has been employed to monitor the reactivity of NH₃ effluence produced from ammonium acetate salt decomposed at 100 °C at the surface of 30 nm layers (with spherical particle of ~51 nm and pores of ~20 nm) of V₂O₅ film deposited by PLD techniques. The results showed a recoverable red shift in the 194 cm⁻¹ phonons and blue shift in the 996 cm⁻¹ phonons upon the interaction of the molecule at ambient temperature (25 °C) and 100 °C. Adsorption effects (increase in intensity) of 145 cm⁻¹ phonons were also observed at these two temperatures. The Raman scattered adsorption effect has been explained using phonon confinement models by taking fractional change in intensity into account while the blue or red shift in the wavenumber (frequency) is related to the change in elastic constant and the reduced mass of the sensing surface *in situ* with NH₃ ambience. The adsorption effect is related to more and/or less Raman scattered photons

while frequency shift is explained as a decrease in the elastic constant (acceptance of charges from the molecule) when blue shifted and decrease in elastic constant (donation of charges) or increase in reduced mass (chemisorption) when red shifted. Acceptance of charges by the V_2O_5 surface from the molecule is observed to be prevalent at the ambient temperature while an increase in the reduced mass is observed at 100 °C. This is considered to be true since the breaking of chemical bonds or decomposition of NH_3 could only take place at a temperature higher than that of the ambient temperature.

Comparison and rankings of *in situ* Raman spectroscopy gas-sensor tester with the traditional chemi-resistive sensor tester showed that the *in situ* Raman spectroscopy sensor tester is excellent. Additionally, the significant recoverable blue shift and red shift observed when NH_3 interacts with the surface may be considered an outstanding feature of *in situ* Raman spectroscopy on selective monitoring of gas leakage in the environment or to monitor decomposition in industry during gas processing. Hopefully the technique will be helpful in advancing or upgrading the design of chemical sensors for environmental or industrial pollution monitoring.

6. Future plans

The effect of electron capture from the V–O–V bond and the same being donated to the V = O bonds can also be seen with XPS. This can be accomplished through (1) analysis of XPS spectra or (2) *in situ* XPS with NH_3 gas injection. In (1) the analysis through peak deconvolution shows several chemical states of vanadium: V^{4+} and V^{5+} and oxygen: O_{2-} or O_1s but that the three oxygen peaks (about 531, 533 and 535 eV) can be assigned to adsorbed oxygen (a), single bonded oxygen (b) and double bonded oxygen (c), respectively. It is more likely that upon NH_3 injection, the NH_3 and adsorbed oxygen interaction gives electrons to the double bond with a higher probability than to a single bond in the V_2O_5 chemical structure. This XPS explanation concurs very well with the experimental observation from our current Raman spectroscopy where we observe a relaxation of the V–O–V bond leading to red-shift in the peak and the stiffening of the V = O bond which shows a blue shift. As for (2), in order to verify the analysis in (1), there is a need to perform *in situ* XPS with a few ppm's of NH_3 in the XPS chamber and monitoring the evolution of the V and O peaks. To perform such an experiment, one would need to incorporate a gas chamber to the XPS set-up. Currently we do not have XPS facility in our laboratory; the XPS data included in this manuscript was acquired from another institute.

Acknowledgments

A A Akande acknowledges CSIR National Centre for Nano-Structured Materials for PhD Studentship position (project number HGER27S and HGER50S) and the National Research Foundation through KIC150917142805 travel grant. He also acknowledges the assistance of Bafana Moya of National Laser Centre during PLD experiments and Egger Sharon of National Centre for Nano-Structured Materials Characterization Facility for SEM Cross section.

ORCID iDs

Amos Adeleke Akande  <https://orcid.org/0000-0002-3691-9233>

References

- [1] Seiyama T and Kato A 1962 A new detector for gaseous components using semiconductive thin films *Anal. Chem.* **34** 1502
- [2] Brattain W H and Bardeen J 1953 Surface properties of germanium *Bell Syst. Tech. J.* **32** 1–41
- [3] Neri G 2015 Fifty years of chemoresistive gas sensors *Chemosensors* **3** 1–20
- [4] Kasalizadeh M, Khodadadi A A and Mortazavi Y 2013 Coupled metal oxide-doped Pt/SnO₂ semiconductor and yttria-stabilized zirconia electrochemical sensors for detection of VOCs *J. Elec. Soc.* **1160** B218–24
- [5] Lee Y W, Kim E, Shin B and Lee S 2012 High performance optical gating in junction device based on vanadium dioxide thin film grown by sol-gel method *J. Electr. Eng. Technol.* **7** 784–8
- [6] Hoummady M, Campitelli A and Wlodarski W 1997 Acoustic wave sensors: design, sensing mechanisms and applications *Smart Mater. Struct.* **6** 647
- [7] Chu P K and Li L 2015 Characterization of amorphous and nanocrystalline carbon films *J Mater. Chem. Phys.* **96** 253–77
- [8] Akande A A, Liganiso E C, Dhonge B P, Rammutla K E, Machatine A, Prinsloo L, Kunert H and Mwakikunga B W 2015 Phase evolution of vanadium oxides obtained through temperature programmed calcinations of ammonium vanadate in hydrogen atmosphere and their humidity sensing properties *J. Mater. Chem. Phys.* **151** 206–14
- [9] Pagnier T, Boulova M, Galerie A, Gaskov A and Lucazeau G 2000 Reactivity of SnO₂–CuO nanocrystalline materials with H₂S: a coupled electrical and Raman spectroscopy study *Sensors Actuators B* **71** 134–9
- [10] Boulova M, Gaskov A and Lucazeau G 2001 Tungsten oxide reactivity versus CH₄, CO and NO₂ molecules studied by Raman spectroscopy *Sensors Actuators B* **81** 99–106
- [11] Govender M, Motaung D E, Mwakikunga B W, Umapathy S, Sil S, Prasad A K, Machatine A G J and Kunert H W 2013 Operating temperature effect in WO₃ film for gas sensing *2013 IEEE SENSORS* pp 1–4
- [12] Lee S-H, Cheong H M, Seong M J, Liu P, Tracy C E, Mascarenhas A, Pitts J R and Deb S K 2003 Raman spectroscopic studies of amorphous vanadium oxide thin films *Solid State Ion.* **165** 111–6
- [13] Julien C, Nazari A G and Bergstrom O 1997 Raman scattering studies of microcrystalline V₆O₁₃ *Phys. Status Solidi b* **201** 319–25
- [14] Akande A A, Rammutla K E, Dhonge B P, Machatine A G J and Mwakikunga B W 2016 Room temperature methane (CH₄) sensing by vanadium oxide (VO_x) nanoparticles *Adv. Sci. Lett.* **22** 901–4
- [15] Mwakikunga B et al 2013 A classification and ranking system on the H₂ gas sensing capabilities of nanomaterials based on proposed coefficients of sensor performance and sensor efficiency equations *Sensors Actuators B* **184** 170–8
- [16] Simo A, Mwakikunga B, Sone B T, Julies B, Madjoe R and Maaza M 2014 VO₂ nanostructures based chemiresistors for low power consumption hydrogen sensing *Int. J. Hydrog. Energy* **39** 8147–57

- [17] Rao M C 2013 Structural stoichiometry and phase transitions of MoO₃ thin films for solid state microbatteries *Res. J. Recent Sci.* **2** 67–73
- [18] Laubach S, Schmidt P C, Thißen A, Fernandez-Madrigal F J, Wu Q, Jaegermann W, Klemm M and Horn S 2007 Theoretical and experimental determination of the electronic structure of V₂O₅, reduced V₂O_{5-x} and sodium intercalated NaV₂O₅, *Phys. Chem. Chem. Phys.* **9** 2564
- [19] Zhon B and He D 2008 Raman spectrum of vanadium pentoxide from density-functional perturbation theory *J. Raman Spectrosc.* **29** 1475–81
- [20] Adu K W, Gutiérrez H R, Kim U J, Sumanasekera G U and Eklund P C 2005 Confined phonons in Si nanowires *Nano Lett.* **5** 409–14
- [21] Arora A K, Rajalakshmi M, Ravindran T R and Sivasubramanian V 2007 Raman spectroscopy of optical phonon confinement in nanostructured materials *J. Raman Spectrosc.* **38** 604–17
- [22] Fauchet P M and Campbell I H 1988 Raman spectroscopy of low-dimensional semiconductors *Crit. Rev. Solid St. Mater. Sci.* **14** s79–s101
- [23] Mwakikunga B W, Maaza M, Hillie K T, Arendse C J, Malwela T and Sideras-Haddad E 2012 From phonon confinement to phonon splitting in flat single nanostructures: a case of VO₂@V₂O₅ core-shell nano-ribbons *Vib. Spectrosc.* **61** 105–11
- [24] Mwakikunga B W, Sideras-Haddad E, Forbes A and Arendse C J 2008 Raman spectroscopy of WO₃ nano-wires and thermo-chromism study of VO₂ belts produced by ultrasonic spray and laser pyrolysis techniques *Phys. Status Solidi a* **205** 150–4
- [25] Masina B N, Lafane S, Wu L, Akande A A, Mwakikunga B, Abdelli-Messaci S, Kerdja T and Forbes A 2015 Phase-selective vanadium dioxide (VO₂) nanostructured thin films by pulsed laser deposition *J. Appl. Phys.* **118** 165308
- [26] Akande A A 2014 Vanadium dioxide nanostructure and applications in sensors *MSc Thesis* University of Limpopo (Unpublished)
- [27] Sajilal K and Moses Ezhil Raj A 2016 Effect of thickness on physico-chemical properties of p-NiO (bunsenite) thin films prepared by the chemical spray pyrolysis (CSP) technique *Optik* **127** 1442–9
- [28] Huang E *et al* 2002 Pore size distributions in nanoporous methyl silsesquioxane films as determined by small angle x-ray scattering *Appl. Phys. Lett.* **81** 2232–4
- [29] Yu Q, Li W, Liang J, Duan Z, Hu Z, Liu J, Chen H and Chu J 2013 Oxygen pressure manipulations on the metal-insulator transition characteristics of highly (011)-oriented vanadium dioxide films grown by magnetron sputtering *J. Phys D: Appl. Phys.* **46** 055310
- [30] Zang P, Huang T, You Q, Zang J, Li W, Wu J, Hu Z and Chu J 2015 Effects of crystal orientation on electronic band structure and anomalous shift of higher critical point in VO₂ thin films during the phase transition process *J. Phys D: Appl. Phys.* **48** 485302
- [31] Kerber R 2002 Markovnikov's rule in history and pedagogy *Found. Chem.* **4** 61–72
- [32] Xu C, Ma C, Xiao F, Chen H and Dai B 2016 Catalyst-free hydrochlorination protocol for terminal arylalkynes with hydrogen chloride *Chin. Chem. Lett.* **27** 1683–5
- [33] Tepper B, Richer B, Dupuis A C, Kuhlbeck H, Hucho C, Schilbe P, Yarmo A M and Freund H J 2002 Adsorption of molecular and atomic hydrogen on vacuum-cleaved V₂O₅ (001) *Surf. Sci.* **496** 64–72
- [34] Sipr O, Simunek A, Bocharov S, Kirchner Th and Drager G Geometric and electronic structure effects in polarized V K-edge absorption near-edge structure spectra of V₂O₅ *Phys. Rev. B* **60** 14115
- [35] Petrov G I and Yakovlev V V 2002 Raman microscopy analysis of phase transformation mechanisms in vanadium dioxide *Appl. Phys. Lett.* **81** 1023
- [36] Pan M, Liu J, Zhong H, Wang S, Li Z, Chen X and Lu W 2004 Raman study of phase transition in VO₂ thin film *J. Cryst. Growth* **268** 178–83
- [37] Akande A A, Mwakikunga B W, Rammutla K E and Machatine A 2015 Larger selectivity of the V₂O₅ nano-particles sensitivity to NO₂ than NH₃ *Sens. Trans.* **192** 61–5
- [38] Soleimanpour A M, Jayatissa A H and Sumanasekera G 2013 Surface and gas sensing properties of nanocrystalline nickel oxide thin film *Appl. Surf. Sci.* **276** 291–7
- [39] Johnson J L, Behnam A, An Y, Pearton S J and Ural A 2011 Experimental study of graphitic nanoribbon films for ammonia sensing *J. Appl. Phys.* **109** 124301